Tunneling processes through magnetic impurities on superconducting surfaces: Yu-Shiba-Rusinov states and the Josephson effect

Haonan HUANG

故不积跬步，无以至千里，不积小流，无以成江海。

骐骥一跃，不能十步，驽马十驾，功在不舍。

— 荀子(约公元前313年－公元前238年)

For unless a person adds steps and half-steps to each other, he cannot go a thousand *li*;

unless little streams are gathered, rivers and seas cannot be formed.

A fast horse in one leap cannot go a thousand paces;

but an old broken down nag can do it in ten days—its merit consists in not losing time.

— Xunzi (ca. 313 – 238 BCE)

— Translated by Homer H. Dubs in *The Works of Hsüntze* (1928)

Acknowledgements

This PhD study was a fascinating journey, not only because of the intriguing scientific topic, but also thanks to the support and friendships from my colleges and friends, without which this thesis would not have been possible.

First of all, I would like to thank Prof. Klaus Kern for giving me the opportunity to join the Nanoscale Science Department at the Max Planck Institute for Solid State Research in Stuttgart as a PhD student. The scientific infrastructure he established in the department including the precision laboratory, the stock of spare parts and the close relationship with the engineers were indispensable for all works done in this thesis. It was truly enjoyable to work in his department with the scientific freedom and open exchange of ideas.

I would like to express my special gratitude to Dr. Christian R. Ast for supervising my work. His experimental expertise helped me conquer a lot of obstacles, his insightful theoretical understanding on multiple topics sparkled many inspiring discussions and his iterations of paper revision taught me important aspects of scientific writing. From him, I learned way more than what I can express here.

I want to thank Prof. Vincenzo Savona, Prof. Harald Brune, Prof. Jose Ignacio Pascual and Dr. Tristan Cren as members of my thesis committee for reviewing my PhD work.

I am grateful to the mK-STM team, including Dr. Markus Etzkorn for the short introduction at the beginning, Dr. Jacob Senkpiel who passed me a lot of hands-on experience on the mK-STM, and Dr. Sujoy Karan who worked together with me in the lab. We all love (and hate) the beast in box one but it was always a pleasure working together. I would also like to thank the rest of the people in the group, including Dr. Robert Drost, Piotr Kot, Maximilian Uhl, Janis Siebrecht, Dr. Andreas Topp and Ahmed Saleh not only for sitting through the Monday group meetings together (always begin by exchanging pleasantries over the weekend), but also for the interesting discussions and mutual help on the machines. I would like to thank Janis Siebrecht especially for his terrific input on the German language part of this thesis within the shortest possible time.

Dr. Ciprian Padurariu, Dr. Björn Kubala and Prof. Joachim Ankerhold have my sincere thanks for their theoretical support. The intense discussions way into the evenings with them in Ulm

Acknowledgements

Abstract

Magnetic impurities generate a wealth of phenomena on surfaces. On metals, conducting electrons screen the magnetic moment at low temperature, giving rise to the Kondo effect. On superconductors, the Yu-Shiba-Rusinov (YSR) states emerge inside the superconducting gap due to the exchange coupling. In this thesis, we use a scanning tunneling microscope (STM) with a base temperature of $10\,\mathrm{mK}$ to study magnetic impurities on surfaces. This thesis contains two parts, the interplay between magnetic impurities and superconductivity as well as the tunneling processes between YSR states.

Concerning the interplay between magnetic impurities and superconductivity, the single impurity Anderson model (SIAM) offers a consistent picture, in which the impurity substrate coupling Γ is a central parameter of experimental relevance. For YSR phenomena, the mean field approximation is usually sufficient which gives analytical results for a quantitative interpretation of the experimental data. We tune Γ by the atomic forces in the junction and quantitatively identify the key role of Γ in the YSR energy. We further investigate multiple Andreev reflections (MARs) involving a single YSR state, confirming the absence of a spin forbidden family of MARs thereby proving the spin non-degeneracy of the YSR states experimentally.

The presence of YSR impurities not only gives rise to peaks in the tunneling spectra, but also influences the superconducting ground state. At small Γ, the impurity spin is unscreened, which results in a π phase shift in the Josephson transport due to the unpaired spin. At large Γ, the impurity spin is screened and the phase is 0. The change of the YSR ground state when varying Γ qualifies as a quantum phase transition (QPT). We observe a significant step in the Josephson current when tuning Γ across the QPT, which signals the $0 - \pi$ transition and the change of the ground state, justifying the QPT.

We then go beyond the mean field approximation and include correlation effects in the SIAM to fit the Kondo effect. To reveal the Kondo effect from the YSR impurity, magnetic fields above the critical field are applied to quench superconductivity. We demonstrate the relation between the Kondo effect and the YSR states connected by the SIAM and present the scaling between the YSR energy and the Kondo temperature. Despite the close relation between the two phenomena, the correlation effects are not necessary to explain various YSR phenomena even on a quantitative level as shown previously. Therefore, the question remains that to which extent the correlation effects persist in the superconducting state. On this, we show that the correlation effects, although largely invisible in the superconducting spectra, manifest

Abstract

clearly as an offset current in the YSR measurements.

Conventionally, the STM tip only serves as a probe to unravel the sample properties. However, in principle the tip, sample and junction form one quantum system. With the capability to controllably introduce YSR states of desired properties on the tip apex (the YSR-STM), we construct a minimal tunnel junction between two discrete levels, a YSR state on the sample and a YSR state on the tip apex. The tunneling between two YSR states, *Shiba-Shiba tunneling*, features sharp peaks in the current, the area of which reveals the relaxation dynamics and the intrinsic lifetime of the YSR states. Apart from being discrete levels, the YSR states have spin degree of freedom due to the spin non-degeneracy discussed previously. We show that the spin plays an important role in Shiba-Shiba tunneling and we find a behavior that is consistent with paramagnetic impurities.

To conclude, this thesis presents multiple experimental aspects of a single YSR state quantitatively and consistently explained by the SIAM, both on the mean field level and in the fully correlated situation. The possibility to functionalize the STM tip with a YSR state opens more possibilities, and we show the tunneling between two YSR states as a first application, laying the basis for possible extension of the YSR-STM to more scenarios.

Key words: *Yu-Shiba-Rusinov states (YSR), Kondo effect, Scannning Tunneling Microscopy (STM), Yu-Shiba-Rusinov Scanning Tunneling Microscopy (YSR-STM), Shiba-Shiba Tunneling, Josephson Effect, Quantum Phase Transition (QPT), $0 - \pi$ Transition, Single Impurity Anderson model (SIAM), Numerical Renormalization Group (NRG) Theory, Multiple Andreev Reflections (MARs)*

Zusammenfassung

Magnetische Störstellen erzeugen eine Vielzahl von Phänomenen auf Oberflächen. In Metallen schirmen die Leitungselektronen bei niedrigen Temperaturen das magnetische Moment ab, was zum Kondo-Effekt führt. In der Bandlücke von Supraleitern bilden sich Yu-Shiba-Rusinov (YSR)-Zustände aufgrund der Austauschwechselwirkung. In dieser Dissertation wird ein Rastertunnelmikroskop (RTM) mit einer Basistemperatur von 10mK genutzt, um magnetische Störstellen auf Oberflächen zu untersuchen. Diese Dissertation besteht aus zwei Teilen, nämlich der Wechselwirkung von magnetischen Störstellen mit der Supraleitung sowie den Tunnelprozessen zwischen YSR-Zuständen.

Bezüglich der Wechselwirkung zwischen magnetischen Defekten und Supraleitung bietet das Single Impurity Anderson Model (SIAM) eine schlüssige Darstellung, in welcher die Kopplung des Defekts mit dem Substrat, bezeichnet mit Γ, ein zentraler Parameter mit experimenteller Bedeutung ist. Für YSR-Phänomene ist die Molekularfeldnäherung, welche analytische Ergebnisse für die quantitative Interpretation der Messdaten liefert, normalerweise ausreichend. Durch die Nutzung atomarer Kräfte im Tunnelkontakt wird Γ verändert und dessen zentrale Rolle für die YSR-Energie quantitativ ermittelt. Außerdem werden Multiple Andreev-Reflektionen (MAR), die einen einzelnen YSR-Zustand involvieren, untersucht, und die Abwesenheit einer Spin-verbotenen Familie von MAR bestätigt und somit die Nicht-Entartung des Spins der YSR-Zustände experimentell belegt.

Das Vorhandensein von YSR-Störstellen führt nicht nur zu Peaks in den Tunnelspektren, sondern beeinflusst auch den supraleitenden Grundzustand. Bei kleinen Γ wird der Spin des Defekts nicht abgeschirmt, was aufgrund des ungepaarten Spins zu einem π-Phasensprung im Josephson-Transport führt. Bei großen Γ wird der Spin des Defekts abgeschirmt und die Phase ist 0. Der Wechsel des YSR-Grundzustands mit sich änderndem Γ berechtigt die Bezeichnung als Quanten-Phasenübergang (QPT). Wir beobachten einen signifikanten Schritt im Josephson-Strom, wenn Γ über den QPT bewegt wird, was einen $0 - \pi$-Übergang, sowie eine Änderung des Grundzustands signalisiert und damit den QPT belegt.

Weiterhin werden über die Molekularfeldnäherung hinaus Korrelationseffekte im SIAM einbezogen, um den Kondo-Effekt zu fitten. Um den Kondo-Effekt vom YSR-Defekt hervorzuheben, werden magnetische Felder oberhalb des kritischen Feldes angelegt, um die Supraleitung zu quenchen. Wir zeigen den Zusammenhang zwischen Kondo-Effekt und YSR-Zuständen durch Verbindung mit dem SIAM und präsentieren die Skalierung zwischen YSR-Energie und Kondo-Temperatur. Trotz der engen Beziehung zwischen den zwei Phänomenen sind

Zusammenfassung

Korrelationseffekte nicht notwendig, um die verschiedenen YSR-Phänomene zu erläutern–
selbst auf einer quantitativen Ebene, wie es zuvor gezeigt wurde. Daher bleibt die Frage, in-
wiefern Korrelationseffekte im supraleitenden Zustand persistieren. Hierzu zeigen wir, dass
Korrelationseffekte– wenn auch großteils nicht sichtbar in supraleitenden Spektren– sich klar
als Offset-Strom in den YSR-Messungen manifestieren.

Konventionell fungiert die RTM-Spitze nur als Sonde, um die Eigenschaften der Probe auf-
zudecken. Prinzipiell bilden die Spitze, Probe und der Tunnelkontakt aber ein Quantensy-
stem. Mit der Fähigkeit, kontrolliert YSR-Zustände mit den gewünschten Eigenschaften am
Scheitel der Spitze zu erzeugen (d.h. dem YSR-RTM), wird ein minimaler Tunnelübergang
zwischen zwei diskreten Levels, nämlich einem YSR-Zustand auf der Probe und einem YSR-
Zustand am Scheitel der Spitze, geschaffen. Das Tunneln zwischen zwei YSR-Zuständen,
das Shiba-Shiba-Tunneling, weist scharfe Peaks, deren Fläche die Relaxationsdynamik und
intrinsische Lebensdauer der YSR-Zustände offenbaren, im Strom auf. Abgesehen von der
Tatsache, dass die YSR-Zustände diskret sind, haben sie einen Freiheitsgrad im Spin aufgrund
des nichtentarteten Zustands. Es wird gezeigt, dass der Spin eine wichtige Rolle im Shiba-
Shiba-Tunnelvorgang spielt und ein Verhalten gefunden, das mit dem von paramagnetischen
Defekten übereinstimmt.
Zusammenfassend präsentiert diese Dissertation viele experimentelle Aspekte eins einzelnen
YSR-Zustands quantitativ, welche konsistent mit dem SIAM erklärt werden können, sowohl im
Rahmen des Molekularfeld-Ansatzes, wie auch in einem komplett korrelierten Zusammen-
hang. Die Möglichkeit, die RTM-Spitze mit einem YSR-Zustand zu funktionalisieren, eröffnet
neue Möglichkeiten und das Tunneln zwischen zwei YSR-Zuständen wird als eine erste An-
wendung gezeigt, wodurch die Grundlage für eine mögliche Erweiterung des YSR-RTMs für
weitere Szenarien gelegt wird.

Stichwörter: *Yu-Shiba-Rusinov-Zustände (YSR), Kondo-Effekt, Rastertunnelmikroskopie (RTM),
Shiba-Shiba-Tunnelprozesse, Josephson-Effekt, Quanten-Phasenübergang (QPT), $0 - \pi$ Über-
gang, Single Impurity Anderson Model (SIAM), Theorie der Numerical Renormalization Group
(NRG), Multiple Andreev-Reflektionen (MAR)*

Contents

Contents

Contents

List of Figures

List of Tables

Abbreviations

AC	Alternating current
BCS	Bardeen, Cooper and Schrieffer
$c, c^\dagger$	Electron annihilation and creation operators
$\gamma, \gamma^\dagger$	Bogolibov quasiparticle annihilation and creation operators
DC	Direct current
DCB	Dynamic Coulomb blockade
Δ	Superconducting order parameter
DOS	Density of states
DR	^{3}He $-$ ^{4}He dilution refrigerator
e	Elementary electric charge
E_c	Charging energy of the junction
E_F	Fermi energy
E_J	Josephson coupling energy
$E(\phi)$	Energy phase relation
ϵ	YSR energy
$f(E) = \frac{1}{e^{E/k_B T}+1}$	Fermi–Dirac distribution function
FWHM	Full-width at half-maximum
$G_0 = \frac{2e^2}{h}$	Conductance quantum
G_N	Normal state conductance
h	Planck constant
$\hbar = h/2\pi$	Reduced Planck constant
HWHM	Half-width at half-maximum
η	Dynes' parameter in the Green's function theory
I	Current
I_c	Josephson critical current
I_s	Josephson switching current
k_B	Boltzmann constant
MARs	Multiple Andreev reflections
MBS	Majorana bound states
MF	Mean field approximation
mK-STM	Milikelvin STM
ML	Monolayer

Abbreviations

μ_B	Bohr magneton
NRG	Numerical renormalization group theory
ν_0	Normal state density of states
P(E)	Probability function for the tunneling charge to exchange energy with the environment
QPT	Quantum phase transition
$R_N = 1/G_N$	Normal state resistance
RT	Room temperature
SC	Superconductivity
sgn(x)	Sign function
Shiba-Shiba tunneling	The tunneling between Yu-Shiba-Rusinov states
SIAM	Single impurity Anderson model
SPM	Scannning probe microscopy
STM	Scannning tunneling microscopy/microscope
STS	Scannning tunneling spectroscopy
σ	Spin
T	Temperature
T_c	Critical temperature of a superconductor
T_K	Kondo temperature
$\tau = G_N/G_0$	Normal state transmission
UHV	Ultra high vacuum
V	Bias voltage
YSR	Yu-Shiba-Rusinov state
YSR-BCS tunneling	The tunneling between a YSR state and a clean BCS superconductor
YSR-STM	An STM with the tip functionalized by a YSR state

1 Introduction

The interplay between magnetic impurities and the host materials has stimulated the interest of researchers since more than half a century ago. In the 1960s, L. Yu, H. Shiba and A. I. Rusinov showed theoretically that bound states emerge inside the superconducting gap when a magnetic impurity is coupled to a superconductor [1–3], later called the Yu-Shiba-Rusinov (YSR) states after the names of the three pioneers. In the same decade, J. Kondo provided a satisfactory theoretical explanation about the anomalous increase of the resistivity near zero temperature in normal conducting metals containing magnetic impurities [4], a phenomenon later named after him as the Kondo effect.

Around that time (December 1959 to be precise), Richard Feynman gave a lecture titled *There's Plenty of Room at the Bottom* where he imagined the possibility of manipulating and controlling matters at the atomic scale. Despite its wide reception now, this idea went largely unnoticed at the time, sounding nothing more than a fantasy. In fact, Richard Feynman chose words very carefully "The principles of physics, as far as I can see, do not speak against the possibility of maneuvering things atom by atom" [5].

Indeed, in the introduction of his pioneering work on the YSR states [1], L. Yu had to admit that the reason for considering only a single magnetic impurity was merely for simplicity and further investigation would be necessary to determine to which extent the discussion would remain valid for real superconductors containing many impurities. Perhaps even more difficult than resolving atoms, measuring the YSR state and the Kondo effect on a single impurity level would require spectroscopic capabilities at the atomic scale which could also not be possibly foreseen at the time.

The introduction of the numerical renormalization group (NRG) technique in 1975 by K. G. Wilson [6] marked the milestone of the theory development regarding the quantum impurity problems. The Kondo problem was conclusively solved numerically by the NRG theory [6, 7], which was later generalized to the single impurity Anderson model (SIAM) [8, 9] and applied to the magnetic impurities on superconductors [10, 11], demonstrating the connection between the YSR and the Kondo physics decisively. Despite the success in theory which remained more

or less state-of-art until now, the experiments still waited for the the right technology.

The groundbreaking development of the scanning tunneling microscope (STM) in 1981 by Gerd Binnig and Heinrich Rohrer offered unprecedented possibility not only to "see" and manipulate the atoms by using an atomically sharp tip, realizing what Feynman dreamed, but also to measure the spectrum. Within only two years from the first development, the ultra-high vacuum (UHV) was achieved and the atomic resolution was demonstrated for the (1×2) reconstruction of the Au(110) surface [12] and the (7×7) reconstruction of the Si(111) surface [13]. The second function to measure the spectrum, the so-called scanning tunneling spectroscopy (STS), was also demonstrated at a similar speed [14]. All of these were done at the room temperature.

It was clear, though, that the true power of the STM came from combining the spatial resolution with the spectroscopy capabilities allowing for resolving the wavefunction and density of states locally. Nevertheless, it took about 15 years for the technology to mature and to bring the STM to cryogenic temperatures with sufficient mechanical stability and energy resolution to realize this [15].

The year 1997 witnessed an experimental breakthrough where A. Yazdani *et al.* showed for the first time the observation of the YSR states on a single Mn and Gd atom on a superconducting Nb(110) surface. Just one year later, J. Li *et al.* [16] and V. Madhavan *et al.* [17] almost simultaneously measured the spectroscopy feature of the Kondo effect around a single magnetic impurity. All these experiments were performed around $T = 4K$ with an STM equipped with a [4]He cryostat. Since then, the field of magnetic impurities on surfaces including the YSR states [18–29] and the Kondo effect [29–39] literally revived.

Nevertheless, the precise measurement of the YSR states as sharp levels posed great challenge for the energy resolution of the STM. The use of superconducting tips [40–42] and the low temperature of 0.4 K with a single-shot [3]He cryostat for high resolution measurements of the YSR states in 2008 was a breakthrough [43]. Following this idea of superconducting tips, K. J. Franke *et al.* demonstrated the connection between the YSR states and the Kondo effects at 4.5 K for the first time in 2011 [44], which has been discussed more times since then [45, 46].

Before 2011, only a few STM groups in the world [40, 47–51] had tried to go to tens of mK temperatures using the dilution refrigerator (DR) technology. Although measurements at milikelvin temperatures were demonstrated, high resolution STS was still not routinely done [52] because the temperature is not the only (perhaps not even the most important) factor influencing the energy resolution.

In 2011, an STM with a DR having a base temperature of 10 mK with UHV and high magnetic field capabilities was developed in this group at the Max Planck Institute for Solid State Research (the mK-STM) [53, 54] , which over the years achieved extremely high spectroscopic energy resolution down to the few μV range thanks to the multiple improvements including the construction of the Precision Laboratory [55]. The experimental work in this thesis comes

from the mK-STM.

With the ultra-low temperature and high energy resolution, we are ready to explore the YSR and Kondo physics with great quantitative detail, especially concerning YSR impurities with tunable energy upon tip approach. Furthermore, we demonstrate the YSR-STM where the STM tip can be reliably functionalized with YSR states of various and desired properties, including one that moves across the quantum phase transition (QPT) upon tip approach achieving tunable $0-\pi$ transition. We then use the YSR tip to study the tunneling processes between YSR states (*Shiba-Shiba tunneling*). Shiba-Shiba tunneling, basically the tunneling between discrete levels, features unprecedented sharpness (perhaps at the quantum limit) of the spectroscopic features.

In this thesis, we utilize superconducting vanadium and intrinsic magnetic impurities on the V(100) surface and on the vanadium tip. Chapter 2 contains the theoretical backgrounds regarding the YSR states, the Kondo effect and the tunneling processes. In Chapter 3, the technical aspects of the mK-STM are discussed.

Different aspects of the experiments on the tunneling between a YSR state and a clean superconductor are presented in Chapters 4, 5 and 6, where the SIAM under the mean field approximation yields excellent agreement with the measurements. In Chapter 4, YSR states with varying energy upon tip approach are investigated, establishing the role of the impurity-substrate coupling as the key parameter connecting the YSR energy and the normal state transmission. In Chapter 5, the tunneling spectra at high conductance are shown demonstrating the interplay between the YSR states and the multiple Andreev reflections (MARs). In Chapter 6, the supercurrent reversal at the QPT of a YSR state is presented. The step behavior in the Josephson current is shown, which originates from the $0-\pi$ transition and the quantum interference between two tunneling channels.

Chapter 7 goes beyond the mean field approximation and shows the connection between the YSR states and the Kondo effect. The NRG technique is employed for the full solution of the SIAM, which is applied to fit the Kondo spectra and confirm the scaling between the YSR energy and the Kondo temperature experimentally.

In the previous chapters, the YSR state is either on the sample or on the tip, with only one YSR state inside the junction. In Chapter 8, we move the YSR tip onto a YSR state on the sample and investigate the tunneling between the YSR states, the Shiba-Shiba tunneling. We first show that the Shiba-Shiba tunneling features sharp peaks in the current and the conductance dependency of the peak area is a direct measure of the intrinsic lifetime. We then show that the spin plays an important role in the Shiba-Shiba tunneling and the ratio between the thermal and direct processes reflects the relative spin orientation.

In Chapter 9, we conclude the thesis and offer an outlook regarding the Shiba-Shiba tunneling and the YSR-STM.

2 Theoretical background

This chapter serves as the theoretical background for this thesis. The Green's function theory is an essential tool for calculating the tunneling properties (for instance the dI/dV spectrum), especially when the simple convolution of electronic density of states (see Section 3.1.2) is not sufficient (for example when superconductivity or higher order processes are involved). The general procedure for simulating the tunneling spectrum is to first obtain the Green's functions for the two isolated electrodes from their respective Hamiltonian (in equilibrium), and then insert them to the non-equilibrium Green's function formalism to calculate the tunneling current when a bias voltage is applied (out of equilibrium). In reality, the tunneling spectrum is further modified by the $P(E)$ function which takes into account the interaction with the environment through photon emission and absorption.

The first part of this chapter concerns the situation of a single electrode. We will introduce the equilibrium Green's function theory and the theory of superconductivity. Then we will discuss two phenomena regarding the magnetic impurities on the substrate, the Yu-Shiba-Rusinov (YSR) states and the Kondo effect, and show their connection in the single impurity Anderson model (SIAM).

In the second part of this chapter, the tunneling between two electrodes will be discussed, connecting the objects of interest in the first part with the transport measurements in the tunnel junction. The non-equilibrium Green's function formalism and the $P(E)$ theory will be presented and subsequently applied to the tunneling processes between superconductors.

2.1 The Green's function theory

The Green's function for a general single-particle problem is defined as

$$G_0(\omega) = \frac{1}{\omega - H_0},$$

(2.1)

where H_0 is the Hamiltonian of the system and ω is the energy. Here, we let $\hbar = 1$ and thus ω and E are exchangeable.

For interacting systems with $H = H_0 + V$ where H_0 is a single-particle Hamiltonian with a known Green's function G_0 and V is the interaction part, the full Green's function G can be obtained by the Dyson's equation

$$G = G_0 + G_0 \Sigma G, \tag{2.2}$$

or

$$G = \frac{1}{G_0^{-1} - \Sigma(\omega)} = \frac{1}{\omega - H_0 - \Sigma(\omega)}, \tag{2.3}$$

where $\Sigma(\omega)$ is the self-energy, which contains the information of the interaction.

The retarded and advanced Green's functions are defined as

$$G^{r,a}(\omega) = G(\omega \pm i\eta), \tag{2.4}$$

where η is a small positive parameter chosen close to zero and the $+$ and $-$ signs are for the retarded and advanced Green's functions respectively.

The density of states can be calculated from the retarded or advanced Green's function

$$\rho(\omega) = \mp \frac{1}{\pi} \text{Im} G^{r,a}(\omega), \tag{2.5}$$

which corresponds to the diagonal terms if the Green's function is a matrix.

2.2 Superconductivity

In some materials, the electrical resistance vanishes below a certain critical temperature T_c, a phenomenon called superconductivity. Superconductivity was first observed in solid mercury at liquid helium temperature by Heike Kamerlingh Onnes in 1911 at the University of Leiden [56]. Since then, many simple elements have been found to be superconducting at low temperature, including lead, aluminum, niobium, as well as vanadium.

In the early days, superconductors were thought to be just ideal conductors having zero resistivity, until the discovery of the exclusion of magnetic flux in superconductors by Walther Meissner and Robert Ochsenfeld in 1933 [57], which is often referred to as the Meissner effect. This means that independent of the history of the sample, the magnetic field inside a superconductor is zero (given that the applied magnetic field is not too strong to quench superconductivity), showing that the transition into a superconducting state is indeed a phase transition [58].

Since the discovery of superconductivity, great efforts have been made to obtain a better theoretical understanding. Several theories were developed, from the classical London equations

(1935) to the phenomenological Ginzburg–Landau theory (1950) [59].

One crucial step forward was the development of a fully microscopic theory of superconductivity in 1957 by John Bardeen, Leon Neil Cooper and John Robert Schrieffer [60], which is usually abbreviated as BCS theory. The BCS theory proposes that two electrons with opposite spin and momentum pair up via phonon mediated attractions forming a Cooper pair. We will cover this in more detail in the following section.

Everything seemed to be understood until the discovery of high-T_c superconductors in 1986 (lanthanum barium copper oxide, LBCO, $T_c \sim 30\,\mathrm{K}$) [61]. In just one year, researchers increased T_c to 93 K above liquid nitrogen temperature by replacing lanthanum with yttrium [62], and T_c has risen further since. Such high-T_c superconductors have many properties that cannot be explained by BCS theory (therefore called unconventional superconductors) and many new mechanisms are being proposed, though definitive consensus has not been reached yet.

Despite theoretical challenges, the family of superconductors grows fast in recent years. In 2008, $T_c = 26\,\mathrm{K}$ was shown in fluorine-doped LaFeAsO [63], bringing iron-based layered superconductors to the high-T_c family, and since then T_c of related materials has risen rapidly [64, 65]. In 2018, unconventional superconductivity was discovered in twisted bilayer graphene [66].

In the scope of this thesis, we will focus only on the conventional superconductors for which BCS theory provides satisfactory predictions. The superconductor we use for our experiments is vanadium, which is a simple BCS superconductor. In the outlook, we will discuss possible extensions of this thesis to unconventional superconductivity.

2.2.1 BCS theory

The general Hamiltonian of interacting electrons is

$$H = \sum_{k,\sigma} \xi_k c_{k\sigma}^\dagger c_{k\sigma} + \sum_{\substack{k,k',q \\ \sigma,\sigma'}} V_{k,k',q} c_{k+q,\sigma}^\dagger c_{k'-q,\sigma'}^\dagger c_{k',\sigma'} c_{k,\sigma}, \tag{2.6}$$

where c and $c^\dagger$ are the electron annihilation and creation operators, k is the momentum, q is the momentum transfer, σ is the spin, V is the scattering potential capturing all electron-electron interactions and $\xi_k = \frac{\hbar^2 k^2}{2m} - \mu$ is the kinetic energy with respect to the chemical potential μ. It has been shown by Leon Neil Cooper in 1956 [67] that if for some reason there is an attractive interaction between two electrons above the Fermi sea, there exists a bound state, no matter how weak the interaction is. Since the most favorable binding happens when two electrons have opposite momentum k and we further assume singlet pairing, Eq. 2.6 can be reduced to

$$H_{\mathrm{BCS}} = \sum_{k,\sigma} \xi_k c_{k\sigma}^\dagger c_{k\sigma} + \sum_{k,k'} V_{kk'} c_{k\uparrow}^\dagger c_{-k\downarrow}^\dagger c_{-k'\downarrow} c_{k'\uparrow}. \tag{2.7}$$

Eq. 2.7 is a many-body Hamiltonian, so further simplification is desirable for its solution. One possibility is the mean-field approximation [2]

$$H_{\text{BCS,MF}} = \sum_{k,\sigma} \xi_k c_{k\sigma}^\dagger c_{k\sigma} - \sum_k \left(\Delta_k c_{k\uparrow}^\dagger c_{-k\downarrow}^\dagger + \Delta_k^* c_{-k\downarrow} c_{k\uparrow} \right), \tag{2.8}$$

where Δ_k is the superconducting order parameter satisfying the self-consistency conditions

$$\begin{aligned} \Delta_k &= -\sum_{k'} V_{kk'} \langle c_{-k'\downarrow} c_{k'\uparrow} \rangle, \\ \Delta_k^* &= -\sum_{k'} V_{kk'}^* \langle c_{k'\uparrow}^\dagger c_{-k'\downarrow}^\dagger \rangle. \end{aligned} \tag{2.9}$$

To diagonalize this Hamiltonian, we introduce the Nambu spinor $(c_{k\uparrow}^\dagger, c_{-k\downarrow})$ as the basis. Then the Hamiltonian can be written as

$$H_{2\times2} = \begin{pmatrix} \xi_k & -\Delta_k \\ -\Delta_k^* & -\xi_{-k} \end{pmatrix}, \tag{2.10}$$

which is a 2×2 matrix in Nambu space. We can also extend the pairing terms to both spin species at momentum k and write the Hamiltonian with the spinor $(c_{k\uparrow}^\dagger, c_{-k\downarrow}, c_{k\downarrow}^\dagger, -c_{-k\uparrow})$. This will result in the full 4×4 Nambu space as

$$H_{4\times4} = \frac{1}{2} \begin{pmatrix} \xi_k & -\Delta_k & 0 & 0 \\ -\Delta_k^* & -\xi_{-k} & 0 & 0 \\ 0 & 0 & \xi_k & -\Delta_{-k} \\ 0 & 0 & -\Delta_{-k}^* & -\xi_{-k} \end{pmatrix}, \tag{2.11}$$

which is block-diagonalized into two 2×2 matrices. Assuming $|\Delta_k| = |\Delta_{-k}|$, it reduces to Eq. 2.10 effectively. Actually, even in more complicated situations, if the spin-orbit coupling and the spin-flip scattering are absent, the 4×4 matrix is always block-diagonalized and it is sufficient to only study the 2×2 matrix [68]. Consequently in the following part of this section, we will go back to the 2×2 case.

The diagonalization is straightforward assuming $\xi_k = \xi_{-k}$, yielding eigenvalues $\pm E_k$ with $E_k = \sqrt{\xi_k^2 + |\Delta_k|^2}$. For the eigenvectors, a unitary Bogoliubov transformation that diagonalizes the matrix in Eq. 2.10 casts the original electron creation and annihilation operators into a superposition of them:

$$\begin{pmatrix} \gamma_{k\uparrow} \\ \gamma_{-k\downarrow}^\dagger \end{pmatrix} = \begin{pmatrix} u_k^* & -v_k \\ v_k^* & u_k \end{pmatrix} \begin{pmatrix} c_{k\uparrow} \\ c_{-k\downarrow}^\dagger \end{pmatrix}, \tag{2.12}$$
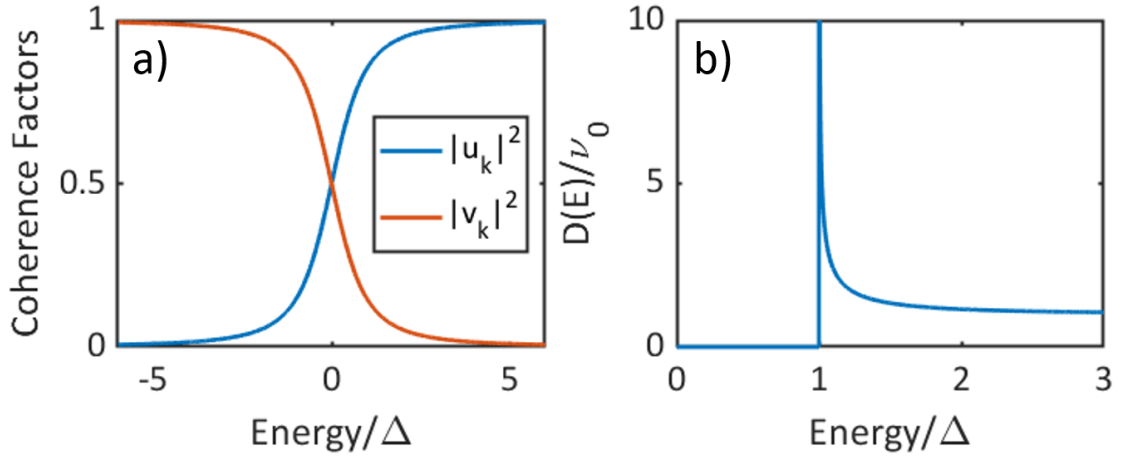
Figure 2.1 – **The BCS theory.** a) The coherence factors $|u_k|^2, |v_k|^2$ at different energy. Near the Fermi level (zero energy here), the Bogoliubov quasiparticles are a mixture of electrons and holes. b) The quasiparticle density of states as a function of the excitation energy features a gap and a divergence at the gap edge.

satisfying

$$|u_k|^2 = \frac{1}{2}\left(1 + \frac{\xi_k}{E_k}\right), |v_k|^2 = \frac{1}{2}\left(1 - \frac{\xi_k}{E_k}\right), u_k v_k = \frac{\Delta_k}{2E_k},$$

$$H_{\text{BCS,MF}} = \sum_{k,\sigma} E_k \gamma_{k\sigma}^\dagger \gamma_{k\sigma}.$$

(2.13)

The resulting diagonalized quasiparticles are called Bogoliubov quasiparticles, being a superposition of electrons and holes. Notice that far above the Fermi energy ($\xi_k \gg |\Delta_k|$), $|u_k|^2 \to 1, |v_k|^2 \to 0$, meaning that the quasiparticles there are mainly electron-like. Deep inside the Fermi sea ($\xi_k \ll -|\Delta_k|$), $|u_k|^2 \to 0, |v_k|^2 \to 1$, meaning that the quasiparticles there are mainly hole-like. At the Fermi energy ($\xi_k = 0$) however, $|u_k|^2 = |v_k|^2 = 1$, the quasiparticles consist of electron part and hole part with the same amplitude. This is visualized in Fig. 2.1 a). The concept of Bogoliubov quasiparticles is important for the discussion of Yu-Shiba-Rusinov states later.

Quasiparticle density of states

The density of states of Bogoliubov quasiparticles is

$$D(E) = \frac{1}{N} \sum_k \delta(E - \sqrt{\xi_k^2 + |\Delta_k|^2})$$

$$= \begin{cases} 0 & \text{for } 0 < E < \Delta, \\ \nu_0 \frac{E}{\sqrt{E^2 - \Delta^2}} & \text{for } E > \Delta, \end{cases}$$

(2.14)

9

in which the normal state density of states ν_0 and the superconducting order parameter Δ are assumed to be constant. This is plotted in Fig. 2.1 b), and it is clear that there is a gap near zero energy accompanied by a divergence of the density of states at the gap edge (the so-called coherence peaks). It is tempting to relate Eq. 2.14 directly with the spectrum measured in tunneling experiments and indeed they look similar. However, since electrons rather than quasiparticles tunnel across the junction, it is *a priori* not clear whether the tunneling spectrum measures indeed the quasiparticle density of states. Therefore, we will introduce the BCS Green's function in the following as a basis for calculating the transport properties later.

2.2.2 The Green's function for a BCS superconductor

The BCS Green's function can be calculated from the Hamiltonian (Eq. 2.10) via Eq. 2.1 integrating over k-space:

$$g_{\text{BCS}}(\omega) = \frac{-\pi\nu_0}{\sqrt{\Delta^2 - \omega^2}} \begin{pmatrix} \omega & -\Delta \\ -\Delta & \omega \end{pmatrix}, \tag{2.15}$$

where ν_0 is the normal state density of states at the Fermi level. Notice that here the Green's function is in 2×2 Nambu space, and the Green's function in the 4×4 case can be derived using the Hamiltonian in Eq. 2.11 instead. The off-diagnoal terms are defined to be the anomalous Green's function

$$F(\omega) = G_{12}(\omega) = G_{21}(\omega). \tag{2.16}$$

Therefore, the anomalous Green's function for a BCS superconductor is $F_{\text{BCS}}(\omega) = \frac{\pi\nu_0\Delta}{\sqrt{\Delta^2 - \omega^2}}$.

Via Eqs. 2.4 and 2.5, the density of states can be derived from the diagonal parts of the Green's function. In principle, the density of states in Nambu space has electron and hole components (ρ_{11} and ρ_{22} respectively), but due to electron hole symmetry here, $\rho_{11} = \rho_{22}$. For $\eta \to 0$, the result reduces to Eq. 2.14. Increasing η will broaden the spectrum and remove the divergence at $\omega = \pm\Delta$ (Fig. 2.2).

2.2.3 Tight binding model for superconductivity

The BCS Hamiltonian is usually written in k-space as in Eq. 2.8, which is a convenient choice for homogeneous superconductors. However, if translational invariance is broken due to the presence of impurities, it might be beneficial to rewrite the Hamiltonian in real space in a tight-binding manner. The inclusion of impurities will be covered in the next section. Here we provide the tight-binding Hamiltonian for a clean BCS superconductor in the mean field approximation that gives rise to the BdG equations [68, 69]:

$$H_{\text{BCS}} = \sum_{i,\sigma}(\epsilon_i - \mu)c^\dagger_{i\sigma}c_{i\sigma} - t\sum_{\langle i,i'\rangle,\sigma} c^\dagger_{i\sigma}c_{i'\sigma} - \sum_i \left(\Delta_i c^\dagger_{i\uparrow}c^\dagger_{i\downarrow} + \Delta_i^* c_{i\downarrow}c_{i\uparrow}\right). \tag{2.17}$$

Figure 2.2 – **The BCS density of states with different η in the Green's function theory.** A large η softens the coherence peaks at the gap edge and also fills up the gap.

Here, i is the site index, σ is the spin index, ϵ_i is the on-site energy on site i, μ is the chemical potential, t is the hopping between nearest-neighbor sites i and i' and Δ_i is the superconducting order parameter on site i. Consider a one dimensional chain with nearest-neighbor hopping. We cast this Hamiltonian H_{BCS} into the matrix form under the basis A [70]:

$$A_i = \left(c_{i\uparrow}^\dagger, c_{i\downarrow}^\dagger, c_{i\uparrow}, c_{i\downarrow} \right), A_i^\dagger = \begin{pmatrix} c_{i\uparrow} \\ c_{i\downarrow} \\ c_{i\uparrow}^\dagger \\ c_{i\downarrow}^\dagger \end{pmatrix},$$

$$H_{\text{BCS}} = \begin{array}{c} \\ c_{0\uparrow}^\dagger \\ c_{0\downarrow}^\dagger \\ c_{0\uparrow} \\ c_{0\downarrow} \\ c_{1\uparrow}^\dagger \\ c_{1\downarrow}^\dagger \\ c_{1\uparrow} \\ c_{1\downarrow} \\ \dots \end{array} \begin{array}{cccccccc} c_{0\uparrow} & c_{0\downarrow} & c_{0\uparrow}^\dagger & c_{0\downarrow}^\dagger & c_{1\uparrow} & c_{1\downarrow} & c_{1\uparrow}^\dagger & c_{1\downarrow}^\dagger & \dots \\ \begin{pmatrix} 0 & 0 & 0 & -\Delta & -t & 0 & 0 & 0 & \dots \\ 0 & 0 & \Delta & 0 & 0 & -t & 0 & 0 & \dots \\ 0 & \Delta^* & 0 & 0 & 0 & 0 & t & 0 & \dots \\ -\Delta^* & 0 & 0 & 0 & 0 & 0 & 0 & t & \dots \\ -t & 0 & 0 & 0 & 0 & 0 & 0 & -\Delta & \dots \\ 0 & -t & 0 & 0 & 0 & 0 & \Delta & 0 & \dots \\ 0 & 0 & t & 0 & 0 & \Delta^* & 0 & 0 & \dots \\ 0 & 0 & 0 & t & -\Delta^* & 0 & 0 & 0 & \dots \\ \dots & \dots & \dots & \dots & \dots & \dots & \dots & \dots & \dots \end{pmatrix} \end{array},$$

(2.18)

assuming $\epsilon_i \equiv 0, \mu = 0, \Delta_i \equiv \Delta$. Notice that for a superconductor, the basis has dimension four for each site instead of one for a normal metal (corresponding to the 4×4 Nambu space in k-space). As discussed, in the absence of spin-orbit coupling and spin-flip transitions, the matrix can be block-diagonalized, reducing the dimension to two per site, reducing the
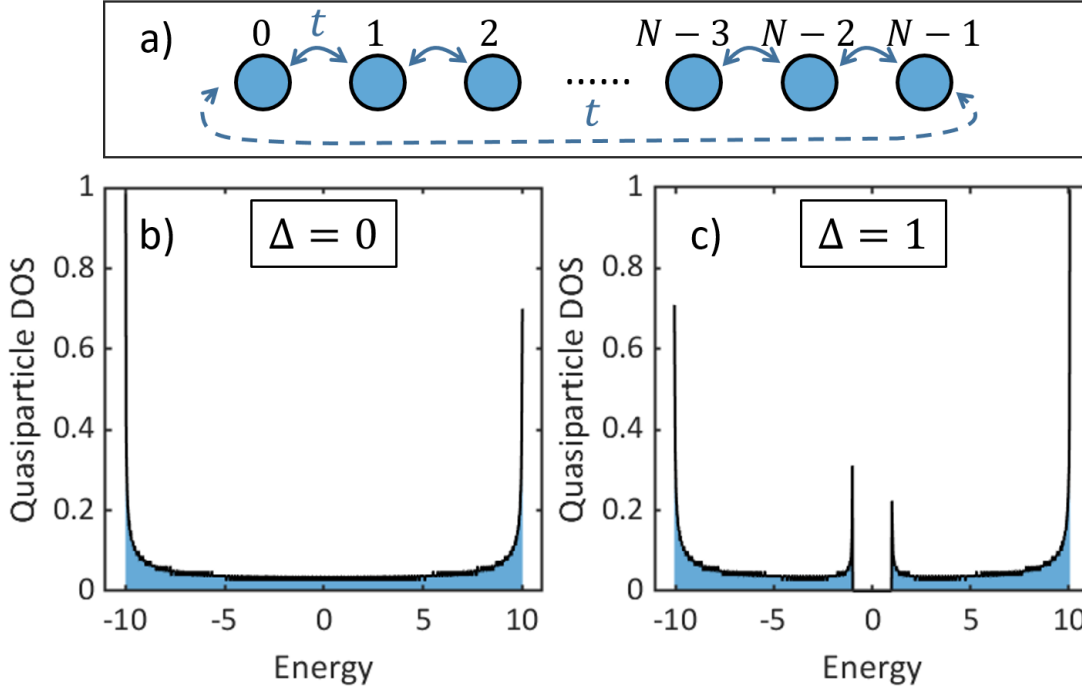
Figure 2.3 – **Density of states calculation of a 1D tight binding chain.** There are $N = 4000$ sites in total, with the hopping parameter $t = 5$. a) A visualization of the 1D chain. Periodic boundary conditions are used. b) Calculation without superconductivity showing the characteristic density of states for a 1D system. c) Calculation including superconductivity with $\Delta = 1$. A gap opens up in the energy range $[-\Delta, \Delta]$.

computational effort.

From the diagonalization of the matrix in Eq. 2.18, we can get the energy eigenvalues, whose histogram provides the total quasiparticle density of states (the local density of states on each site will be discussed later in Eq. 2.29). A typical 1D calculation is shown in Fig. 2.3. In the normal conducting situation (Fig. 2.3 b)), the density of states is continuous, diverging at the band edges which is characteristic of a 1D system. When superconductivity is introduced through a non-zero Δ (Fig. 2.3 c)), a gap opens near the Fermi level and the density of states diverges at the gap edges, in agreement with the analytical formula Eq. 2.14. As a side note, the asymmetry with respect to the energy is purely artificial due to finite size and binning.

2.3 Magnetic impurities on surfaces

Impurities are often seen as unwanted objects and tremendous effort is made to remove them as much as possible. They produce unsatisfactory products in chemical industry, increase resistivity in metals for electrical applications, destroy spin coherence in quantum technology and cause health concerns in pharmaceuticals and food. From another point of view, however, this just shows the critical influence of impurities on the properties of substances. Besides

removing unwanted impurities, introducing desirable impurities in a controlled way is as important in modern technology. One notable instance is the multibillion-dollar semiconductor industry, which relies on the spatially precise implantation of impurities to semiconductors to modify electrical properties and to build integrated circuits.

Among various types of defects, magnetic impurities are of special interest because they carry unpaired spins which not only give rise to classical magnetic moments but also complex quantum effects like coherence and entanglement. One example would be the nitrogen-vacancy center in the diamond lattice which is used in quantum sensing and quantum computing exploiting its spin properties.

For a long time, due to their atomic size, impurities could only be studied as an ensemble through macroscopic measurements like transport or spectroscopy. The advances in surface-sensitive techniques, especially scanning probe microscopy (SPM) which we will cover later, enable measuring and even manipulating single impurities, raising much interest in the field. As a side note, the discussion in this section is equally valid for impurities buried in a bulk material, and the emphasis on the surface is a tribute to surface-sensitive techniques that contribute to single impurity experiments.

When magnetic impurities are placed on a normal metal, the Kondo effect may appear. When they are placed on a superconductor, Yu-Shiba-Rusinov states are created. Both quantum impurity problems can be fully solved numerically by the numerical renormalization group (NRG) theory within the single impurity Anderson model (SIAM). We will cover these in detail in the following.

2.3.1 Yu-Shiba-Rusinov states

In their pioneering works in the 1960s, L. Yu, H. Shiba and A. I. Rusinov theoretically discussed the situation when a classical spin is placed on a superconductor. They found that bound states inside the superconducting gap emerge, [1–3] which were later called the Yu-Shiba-Rusinov (YSR) states, or Shiba states. Their derivations are based on the mean field approximation neglecting correlations due to the quantum nature of the spin, which turns out to work surprisingly well for explaining experimental data. We will follow the mean-field approximation here and in Chapters 4, 5 and 6, while we go beyond and solve the full Hamiltonian using the numerical renormalization group theory in section 2.3.3 and in Chapter 7.

The classical YSR Hamiltonian

The YSR states can be modeled in different ways. One possibility is the SIAM with superconductivity, which will be introduced in section 2.3.3. The SIAM can be solved analytically in the mean field approximation, which will be derived in Chapter 4. Here, we follow the classical YSR model [19, 69, 71] which is largely equivalent to the SIAM in the mean field approximation (though simpler because the SIAM contains more features). We extend the BCS Hamiltonian

in Eq. 2.8 to include a magnetic impurity in the mean field approximation (or classical spin approximation):

$$H_{\text{imp}} = \sum_\sigma (JS\sigma + U) c_{0\sigma}^\dagger c_{0\sigma},$$

$$
\begin{aligned}
H_{\text{YSR}} &= H_{\text{BCS}} + H_{\text{imp}} \\
&= \sum_{k,\sigma} \xi_k c_{k\sigma}^\dagger c_{k\sigma} - \sum_k \left(\Delta_k c_{k\uparrow}^\dagger c_{-k\downarrow}^\dagger + \Delta_k^* c_{-k\downarrow} c_{k\uparrow} \right) + \sum_\sigma (JS\sigma + U) c_{0\sigma}^\dagger c_{0\sigma},
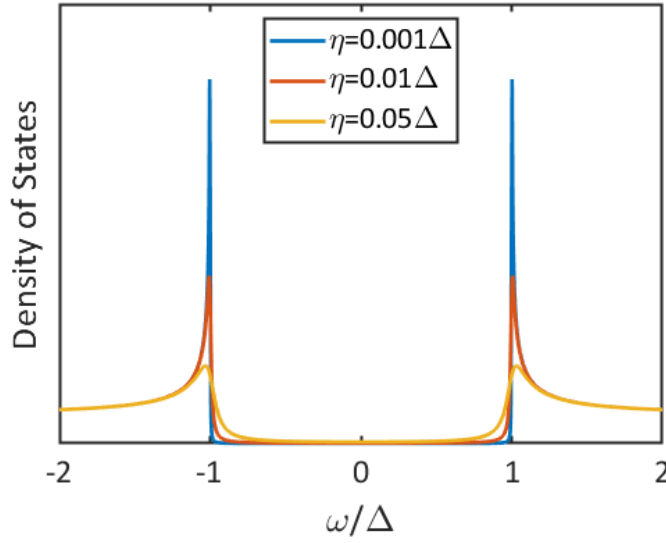\end{aligned}
\tag{2.19}
$$

where J is the exchange coupling, S is the spin and U is the nonmagnetic scattering strength. This can be solved within the Green's function formalism [2, 71, 72] and one solution is presented below.

The Green's function for a YSR state

We can include the magnetic impurity (Eq. 2.19) by applying the Dyson's equation (Eq. 2.2) on the BCS Greens' function (Eq. 2.15) setting the self-energy $\Sigma = JS + U\tau_z$ with τ_z being the Pauli z matrix in Nambu space, and the resulting YSR Green's function in 2×2 Nambu space is [19, 72]

$$
\begin{aligned}
g_{\text{YSR}}(\omega) = \frac{\pi\nu_0}{2\omega\alpha - (1 - \alpha^2 + \beta^2)\sqrt{\Delta^2 - \omega^2}} \\
\times \begin{pmatrix} \omega + (\alpha + \beta)\sqrt{\Delta^2 - \omega^2} & -\Delta \\ -\Delta & \omega + (\alpha - \beta)\sqrt{\Delta^2 - \omega^2} \end{pmatrix},
\end{aligned}
\tag{2.20}
$$

with dimensionless parameters $\alpha = \pi\nu_0 JS$ and $\beta = \pi\nu_0 U$ where ν_0 is the normal-state density of state at the Fermi level. When $\alpha = 0, \beta = 0$, Eq. 2.20 reduces to Eq. 2.15.

The pole of Eq. 2.20 (the solution of $2\omega\alpha - (1 - \alpha^2 + \beta^2)\sqrt{\Delta^2 - \omega^2} = 0$ with respect to ω) yields the energy of the bound state inside the gap, called the YSR energy

$$\epsilon_0 = \text{sgn}(\alpha)\Delta \frac{1 - \alpha^2 + \beta^2}{\sqrt{(1 - \alpha^2 + \beta^2)^2 + 4\alpha^2}}, \tag{2.21}$$

where sgn is the sign function. When α increases from zero, ϵ_0/Δ decreases from 1 until it reaches zero when $\alpha = \sqrt{1 + \beta^2}$. It further decreases and approaches -1 for $\alpha \to +\infty$. The zero crossing denotes a quantum phase transition (QPT), although it is not clear here in the mean field picture, why this is a phase transition. After we introduce the Kondo effect, we will revisit this and provide a many-body picture of the YSR states (section 2.3.3), where the change of the ground state will become clear.

With Eq. 2.20, we can already calculate the full YSR density of states via Eqs. 2.4 and 2.5. Here, the YSR density of states consists of electron and hole components ($\rho_{\text{YSR},11}$ and $\rho_{\text{YSR},22}$, respectively), plotted in Fig. 2.4. It can be seen that the superconducting gap at $\omega \in [-\Delta, \Delta]$ is preserved, while the coherence peaks vanish. The peak inside the gap is the YSR state, whose
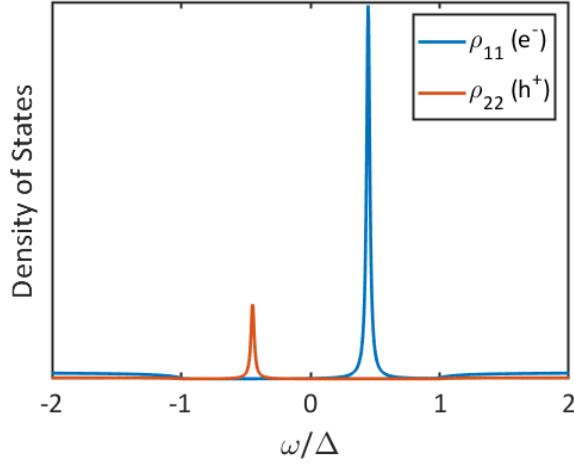
Figure 2.4 – **The YSR density of states.** $\alpha = \beta = \Delta = 1, \eta = 0.015$ in the calculation. The Lorentzian peak inside the gap is the YSR state. Since $\beta \neq 0$, the electron hole symmetry is broken, the electron and hole parts have different spectral weight. Notice that the energy axis of the hole part is flipped in the plot.

width is proportional to η (see later discussion). The electron and hole parts are asymmetric if β is non-zero. The energy axis is flipped for the hole part in the plot because holes tunnel in the other direction, but keep in mind that there is only one YSR energy in 2×2 Nambu space.

The Green's function near the pole can be simplified as [19]

$$g_{\text{YSR}}(\omega) = \frac{1}{\omega - \epsilon_0} \begin{pmatrix} u^2 & uv \\ uv & v^2 \end{pmatrix},$$

(2.22)

with u^2, v^2 being the electron and hole parts satisfying

$$u^2, v^2 = \frac{2|\alpha|\pi \nu_0 \Delta (1 + (\alpha \pm \beta)^2)}{\left((1 - \alpha^2 + \beta^2)^2 + 4\alpha^2 \right)^{3/2}}.$$

(2.23)

If the potential scattering U is non-zero (given that $JS \neq 0$), the electron-hole symmetry is broken and $u^2 \neq v^2$.

The corresponding retarded and advanced Green's functions are

$$g_{\text{YSR}}^{r,a}(\omega) = \frac{1}{\omega \pm i\eta - \epsilon_0} \begin{pmatrix} u^2 & uv \\ uv & v^2 \end{pmatrix}.$$

(2.24)

According to Eq. 2.5, the density of states near the YSR state is

$$\rho_{\text{YSR},11}(\omega) = \frac{1}{\pi} \frac{u^2 \eta}{(\omega - \epsilon_0)^2 + \eta^2},$$

$$\rho_{\text{YSR},22}(\omega) = \frac{1}{\pi} \frac{v^2 \eta}{(\omega - \epsilon_0)^2 + \eta^2},$$

(2.25)

which is a Lorentzian function with width η centered at ϵ_0, meaning that the YSR state is a Bogoliubov quasiparticle level being a superposition of electron and hole parts.

We have derived the analytical formulae regarding the properties of the YSR states using the Green's function theory. Nevertheless, there are two unsolved issues. First, these calculations only consider the properties on the impurity site containing no information about the spatial extension. Second, the self-consistency condition for the order parameters (Eq. 2.9) have not been taken into account. To answer these questions, we will investigate YSR states using the tight binding model numerically in the following part, and compare with the analytical results.

YSR state in the tight binding model

Since H_{imp} in Eq. 2.19 is written in real space, we just insert the tight binding version of H_{BCS} from Eq. 2.17 into Eq. 2.19 to construct the YSR Hamiltonian in real space:

$$H_{\mathrm{YSR}} = \sum_{i,\sigma}(\epsilon_i - \mu)c_{i\sigma}^\dagger c_{i\sigma} - t\sum_{\langle i,i'\rangle,\sigma} c_{i\sigma}^\dagger c_{i'\sigma} - \sum_i \left(\Delta_i c_{i\uparrow}^\dagger c_{i\downarrow}^\dagger + \Delta_i^* c_{i\downarrow} c_{i\uparrow}\right)$$
$$+ \sum_\sigma (JS\sigma + U)c_{0\sigma}^\dagger c_{0\sigma}. \tag{2.26}$$

Largely similar to Eq. 2.18, the matrix form of the above Hamiltonian in a 1D chain looks like:

$$H_{\mathrm{YSR}} = \begin{array}{c} \\ c_{0\uparrow}^\dagger \\ c_{0\downarrow}^\dagger \\ c_{0\uparrow} \\ c_{0\downarrow} \\ c_{1\uparrow}^\dagger \\ c_{1\downarrow}^\dagger \\ c_{1\uparrow} \\ c_{1\downarrow} \\ \dots \end{array} \begin{array}{c} \begin{array}{cccccccccc} c_{0\uparrow} & c_{0\downarrow} & c_{0\uparrow}^\dagger & c_{0\downarrow}^\dagger & c_{1\uparrow} & c_{1\downarrow} & c_{1\uparrow}^\dagger & c_{1\downarrow}^\dagger & \dots \end{array} \\ \left(\begin{array}{ccccccccc} U+JS & 0 & 0 & -\Delta & -t & 0 & 0 & 0 & \dots \\ 0 & U-JS & \Delta & 0 & 0 & -t & 0 & 0 & \dots \\ 0 & \Delta^* & -(U+JS) & 0 & 0 & 0 & t & 0 & \dots \\ -\Delta^* & 0 & 0 & -(U-JS) & 0 & 0 & 0 & t & \dots \\ -t & 0 & 0 & 0 & 0 & 0 & 0 & -\Delta & \dots \\ 0 & -t & 0 & 0 & 0 & 0 & \Delta & 0 & \dots \\ 0 & 0 & t & 0 & 0 & \Delta^* & 0 & 0 & \dots \\ 0 & 0 & 0 & t & -\Delta^* & 0 & 0 & 0 & \dots \\ \dots & \dots & \dots & \dots & \dots & \dots & \dots & \dots & \dots \end{array}\right) \end{array}. \tag{2.27}$$

The diagonalization of Eq. 2.27 yields energy eigenvalues E_n and corresponding eigenvectors

$$\phi^n = \begin{pmatrix} u_{i\uparrow}^n \\ u_{i\downarrow}^n \\ v_{i\uparrow}^n \\ v_{i\downarrow}^n \end{pmatrix}, \tag{2.28}$$

with n indexing the energy eigenvalue and i being the site index. The local density of states of

spin σ at site i is [68]

$$\rho_{i\sigma}(E) = \sum_n \left(|u_{i\sigma}^n|^2 \delta(E_n - E) + |v_{i\sigma}^n|^2 \delta(E_n + E) \right). \tag{2.29}$$

With Eq. 2.29, we can calculate the local density of states at the impurity site (the blue curve in Fig. 2.5 b)). There is a pair of YSR states inside the gap with asymmetric intensity due to non-zero U. At the middle of the chain, the local density of states recovers the clean BCS limit (the red curve in Fig. 2.5 b)). The decay of the YSR intensity away from the impurity site is shown in Fig. 2.5 c), where the peak asymmetry also oscillates away from the impurity site.

One important feature is that, when JS increases, the YSR energy crosses zero, which is the quantum phase transition. The numerical result from the tight binding model agrees quantitatively with the analytical formula in Eq. 2.21, shown in Fig. 2.5 d). We further define the YSR asymmetry

$$A = \frac{h_{\mathrm{R}} - h_{\mathrm{L}}}{h_{\mathrm{R}} + h_{\mathrm{L}}}, \tag{2.30}$$

where $h_{\mathrm{R,L}}$ are the peak intensities for the right and left YSR peaks, respectively. One feature regarding the asymmetry is that across the quantum phase transition, the peak asymmetry reverses, shown in Fig. 2.5 e), also agreeing with the analytical formula in Eq. 2.23. However, this reversal might not be always observed in the spectrum where the tunneling happens between the YSR state and a superconductor. The higher order tunneling processes also change and reverse the spectroscopic asymmetry which might obscure this reversal.

Self-consistency and the local order parameter

In the previous discussion, we let $\Delta_i \equiv \Delta$ be a fixed input parameter. However, Δ_i is subject to the following self-consistency condition in the tight binding model at finite temperature T [68, 70]

$$\Delta_i = \frac{V}{2} \sum_n (-u_{i\uparrow}^n v_{i\downarrow}^{n*} + u_{i\downarrow}^n v_{i\uparrow}^{n*}) \tanh\left(\frac{E_n}{2 k_{\mathrm{B}} T}\right), \tag{2.31}$$

where V is the superconducting pairing potential and k_{B} is the Boltzmann factor. The proper way for a self-consistent calculation is to go back and forth between Eq. 2.31 and Eq. 2.27 until convergence is reached. In the presence of a magnetic impurity, this results in a non-uniform superconducting order parameter near the impurity (Fig. 2.6 b)). This also changes slightly the behavior of the YSR energy (Fig. 2.6 a)).

One observation that has been widely discussed is that the local order parameter on the impurity site changes sign at the quantum phase transition (Fig. 2.6 c)), while the size of the superconducting gap in the density of states stays nearly constant (Fig. 2.6 d)). However, contrary to the common belief, the local order parameter is only a theoretical quantity which is not directly measurable in the Josephson experiments, which we will discuss later in this chapter.
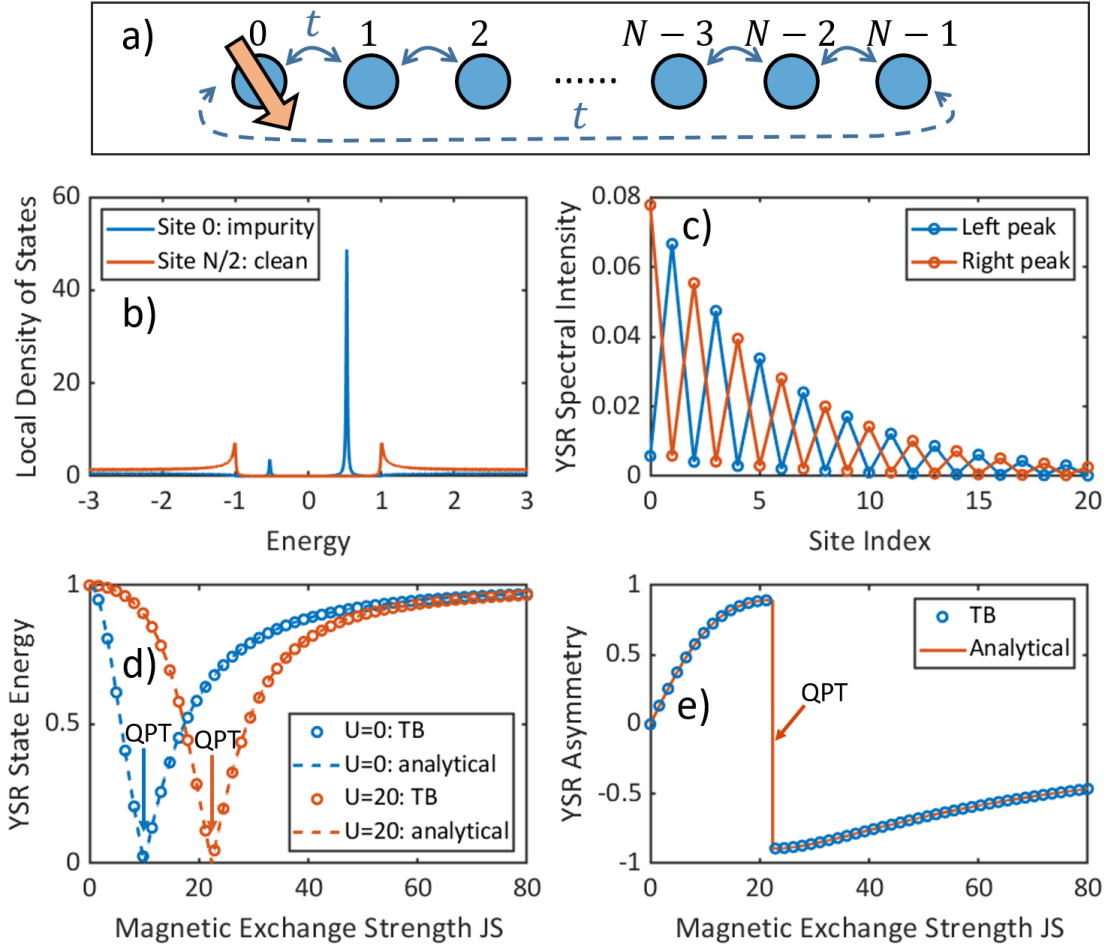
Figure 2.5 – **The YSR state in a 1D tight binding chain.** $t = 5, \Delta = 1$ for all calculations. In b), $N = 2000$ sites are used. In c)-e), $N = 500$ sites are used. a) Schematics of the the 1D chain. The magnetic impurity is located at site 0. b) The local density of states calculation with parameters $JS = 17, U = 20$ and broadening $\eta = 0.01$. c) The spatial variation of the YSR state for the same parameters as in b). d) The dependency of the YSR energy on the magnetic exchange strength JS for different U. The numerical result from the tight binding model agrees well with the analytical solution in Eq. 2.21. The point where the YSR energy crosses zero (QPT) is labeled with arrows. e) The dependency of the YSR asymmetry $A = \frac{h_R - h_L}{h_R + h_L}$ on JS for $U = 20$, agreeing well with the analytical solution in Eq. 2.23.
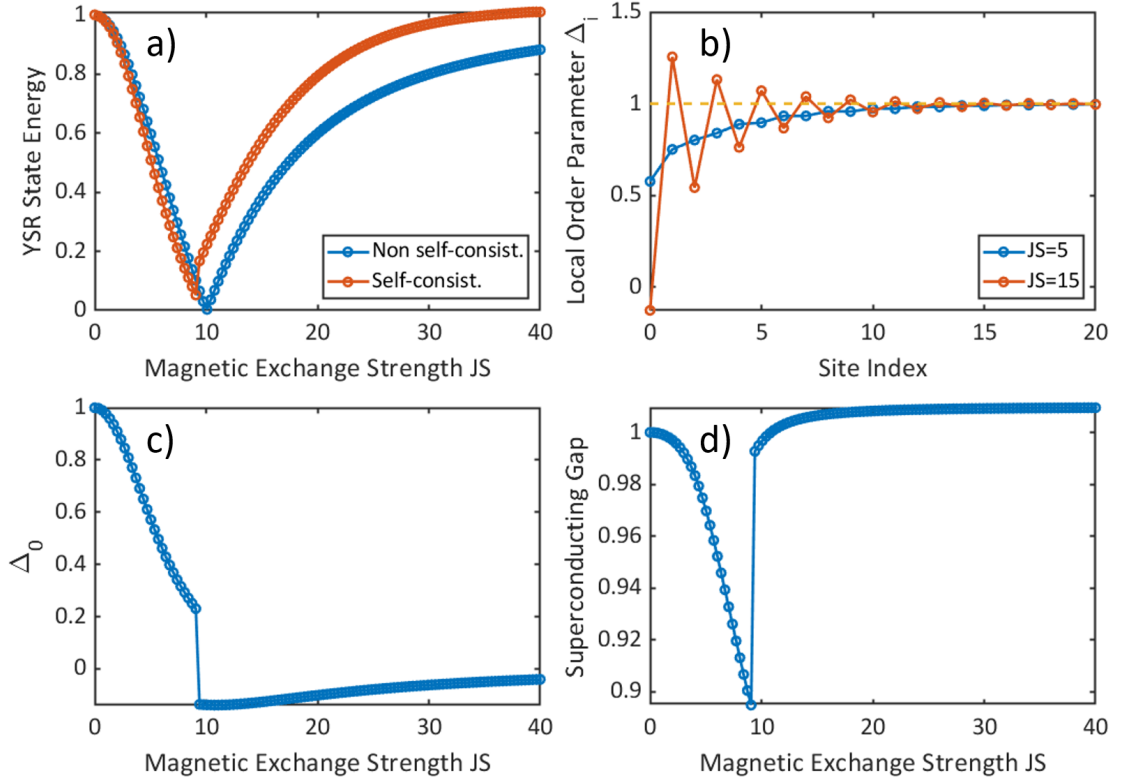
Figure 2.6 – **Self-consistent calculation.** Except for the blue curve in panel a), everything is calculated self-consistently with the pairing potential $V = 8.532$ chosen such that the resulting $\Delta \approx 1$ in the case of a clean superconductor and $k_B T = 0.01$. $N = 200$ sites are used, $U = 0$, $t = 5$. a) The self-consistency condition for the order parameter shifts the evolution of the YSR energy with respect to JS. b) The local order parameter varies near the impurity (site 0) and recovers the bulk value away from the impurity. c) Variation of the local order parameter at the impurity site with respect to JS. There is a change of sign at the QPT. d) The superconducting gap in the spectrum, however, remains nearly constant despite the inclusion of self-consistency. The gap is estimated from the lowest lying eigenenergy except the YSR states.

2.3.2 The Kondo effect

Some metals develop superconductivity at low temperature, with a sharp decrease of their resistivity to zero below the critical temperature, while others remain normal conducting (like copper, gold and silver). The resistivity of these normal conducting metals generally decreases as the temperature is lowered due to less phonon scattering, until it saturates at some residual value from static defect scattering. However, when magnetic impurities are introduced into these metals, the resistivity anomalously increases as the temperature is further lowered [73] (Fig. 2.7 a)). Such a phenomenon was experimentally discovered in the 1930s [74, 75], but not until 1964 was a satisfactory theoretical explanation provided by Jun Kondo[4], after whom the phenomenon was named. The essential mechanism is that while the local magnetic moment is essentially free for $T \gg T_K$ (the weak coupling regime, where T_K is the Kondo temperature), when $T \ll T_K$ (the strong coupling regime where perturbation theories fail) the conduction

electrons screen the impurity spin forming a nonmagnetic many-body Kondo singlet state, which results in a sharp peak near the Fermi energy in the density of states [7] (Fig. 2.7 b)).

One definition of the Kondo temperature T_K that is widely used experimentally is the half-width at half-maximum (HWHM) of the spectral peak at zero temperature $\Gamma_{HWHM} = k_B T_K$ [36, 76], which can be extended to a finite temperature in the Fermi liquid model (only valid for $T < T_K$) $2\Gamma_{HWHM} = \sqrt{(\alpha k_B T)^2 + (2 k_B T_K)^2}$ with $\alpha = 5.4$ measured experimentally [34, 36, 76].

However, the Kondo peak usually has more complicated shapes than what is shown in Fig. 2.7 b), requiring further fitting to extract Γ_{HWHM}. This can be done by fitting the phenomenological Fano function [32, 34, 36, 77] or Frota function [38, 76, 78, 79]. The parameters in the Fano and Frota functions relate to the HWHM by [15, 76] $\Gamma_{HWHM} = \Gamma_{Fano}$, $\Gamma_{HWHM} = 2.542\Gamma_{Frota}$.

Keep in mind that the Kondo effect is not a phase transition like superconductivity but a smooth transition and therefore there exist multiple definitions of T_K theoretically [6, 80–84], which might deviate for up to a factor of 5 from the above commonly used experimental definition. Moreover, the fit functions above only work in the strong coupling regime ($T \ll T_K$) and none of them quantitatively reflects all features of the spectrum, let alone predicting the evolution of the spectrum with the temperature or the external magnetic field. For this, the numerical renormalization group theory provides a better and precise solution (see Chapter 7) allowing for more reliable T_K extraction.

Advances in experimental techniques opens up new opportunities for the microscopic investigation of the Kondo effect down to the atomic scale. In 1998, the Kondo effect was first observed on single atoms using scanning tunneling microscopy [16, 17]. Since then, the field has gained more and more attention and the Kondo effect on single magnetic atoms and molecules has been detected in various systems [30–34, 36].

2.3.3 The single impurity Anderson model and the numerical renormalization group theory

The YSR and Kondo physics are closely related (the only difference is the presence of superconductivity in the YSR case) and can thus be unified in the same parameter space under the single impurity Anderson model (SIAM). In the following part, we will show that the SIAM indeed reproduces both phenomena, and the YSR energy depends universally on the ratio between the Kondo temperature and the superconducting order parameter T_K/Δ, which will be discussed in more detail in Chapter 7.

Both the YSR states and the Kondo effect belong to the quantum impurity problem, where an impurity with a small degree of freedom (spin for instance) couples to the continuum of states in the substrate, where both need to be considered quantum mechanically. Solving quantum impurity problems is non-trivial, since perturbation theory fails in many cases (for instance for the Kondo effect below T_K). The numerical renormalization group (NRG) theory presents a numerical solution to such problems, offering a full solution to the SIAM.
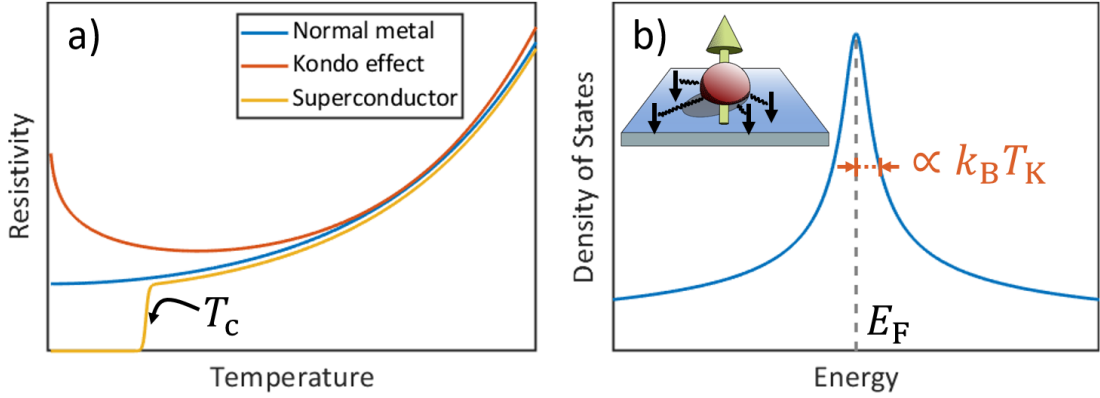
Figure 2.7 – **The Kondo effect.** a) Low temperature behavior of the resistivity of different materials. In a superconductor, the resistivity drops to zero below the critical temperature T_c. In a normal metal, the resistivity decreases with decreasing temperature and then saturates. When a normal metal is doped with magnetic impurities, an anomalous increase of resistivity when the temperature is further lowered emerges, which is the Kondo effect. b) The characteristic Kondo resonance peak in the density of states near the Fermi energy. The inset shows a schematics of the Kondo screening.

The Numerical Renormalization Group (NRG) theory

The NRG theory is a numerical approach developed by Kenneth Geddes Wilson in 1975, [6] originally for solving the Kondo problem and later also for solving the SIAM [8, 9]. The general strategy is to discretize the continuous conduction band with a logarithmically spaced set of intervals, reducing the continuum to discrete states. Then the original Hamiltonian is mapped onto an 1D chain (the so-called "Wilson chain"), which is subsequently diagonalized iteratively. Further analysis of the energies or matrix elements provides information about the system, including the density of states[81].

The "NRG Ljubljana" package is an open-source NRG implementation developed by Rok Žitko for calculating quantum impurity problems [85]. The NRG simulations performed in this thesis (including the simulations of the SIAM presented in the following and in Chapter 7) are done using this code.

The basic SIAM

The single impurity Anderson model (SIAM) writes [86]

$$
\begin{aligned}
H_{\mathrm{SIAM}} &= H_{\mathrm{band}} + H_{\mathrm{imp}} + H_{\mathrm{c}}, \\
H_{\mathrm{band}} &= \sum_{k\sigma} \xi_k c_{k\sigma}^\dagger c_{k\sigma}, \\
H_{\mathrm{imp}} &= \epsilon_d n + U n_\uparrow n_\downarrow, \\
H_{\mathrm{c}} &= \sum_{k\sigma} V_k (c_{k\sigma}^\dagger d_\sigma + \mathrm{H.c.}),
\end{aligned}
\tag{2.32}
$$

with H_{band} containing the bulk band dispersion ξ_k, H_{imp} being the impurity Hamiltonian with on-site energy ϵ_d, on-site Coulomb repulsion U and the number operator n, and H_c containing the hybridization V_k between the impurity and the substrate. Assuming constant density of states ρ and constant hybridization strength, we define $\Gamma = \pi \rho |V_{k_F}|^2$. The number of parameters in the SIAM is three (ϵ_d, U, Γ). For convenience, we let $\delta = \epsilon_d + U/2$ such that $\delta = 0$ reflects the electron-hole symmetric case. In the following discussions, the parameters are thus δ, U, Γ.

The SIAM has a rich phase diagram, but here we only focus on the regime $U \gg \Gamma$ and $|\delta| < U/2$ where the Kondo effect is reproduced. If $|\delta| > U/2$, the impurity will either be filled with two electrons with opposite spin, or completely empty at low temperature and thus be non-magnetic. If $|\delta| < U/2$, a sharp Kondo resonance emerges near the Fermi energy (see the spectral function calculation using NRG in Fig. 2.8 b)). In this Kondo regime, the SIAM density of states also features two impurity levels at ϵ_d and $\epsilon_d + U$ (Fig. 2.8 a)). For $\delta = 0$, the two impurity levels are at $\pm\frac{U}{2}$, and the SIAM Hamiltonian is electron-hole symmetric, resulting in symmetric density of states (including the Kondo peak and the YSR states, which will be introduced later). The asymmetry of the Kondo peak can be modeled by a non-zero δ, which will be discussed in Chapter 7 in more detail.

The Schrieffer-Wolff transformation relates the SIAM to the Kondo impurity model [87], and thus the Kondo temperature T_K can be written as [86, 88]:

$$
\begin{aligned}
T_K &= D_{eff} \sqrt{\rho J} \exp(-\frac{1}{\rho J}), \\
\rho J &= \frac{2\Gamma}{\pi}(\frac{1}{-\epsilon_d} + \frac{1}{U + \epsilon_d}) = \frac{8\Gamma}{\pi U}\frac{1}{1 - 4(\delta/U)^2}, \\
D_{eff} &= \begin{cases} \text{a constant on the order of } D & \text{if } U \gg D, \\ 0.364\sqrt{|\epsilon_d(\epsilon_d + U)|} = 0.182 U \sqrt{1 - 4(\delta/U)^2} & \text{if } U \ll D, \end{cases}
\end{aligned}
\tag{2.33}
$$

where J is the exchange coupling and D is the electronic band width which is set to 1 in all simulations, meaning that all energy scales are referenced to D. Here, the Kondo temperature T_K is directly in the unit of energy, while experimentally T_K is more often a temperature and the corresponding energy is $k_B T_K$. The condition for the above formula is $U \gg \pi\Gamma$, $\epsilon_d \ll -\pi\Gamma$ and $\epsilon_d + U \gg \pi\Gamma$ (that both impurity levels are away from the Fermi energy for at least $\pi\Gamma$ which is the spread of the levels, such that the system is not in the valence fluctuation regime). If we rewrite it in δ, it means that $|\delta| < U/2$ with the distance to $U/2$ much larger than $\pi\Gamma$. In this limit, $\rho J \ll \frac{2\Gamma}{\pi}\frac{1}{\pi\Gamma} = \frac{2}{\pi^2} < 1$, automatically satisfying the small ρJ requirement for the Schrieffer-Wolff transformation [87] also for asymmetric cases.
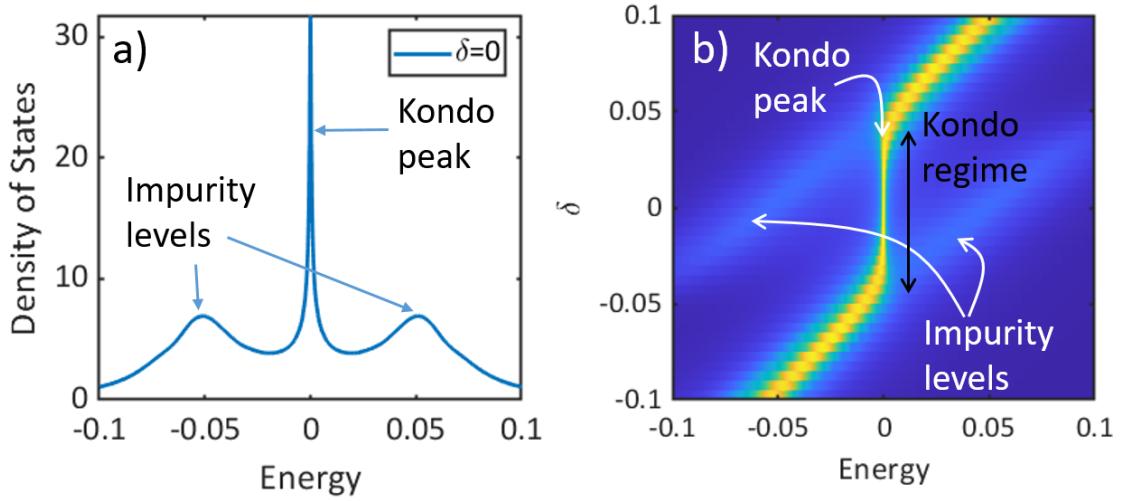
Figure 2.8 – **The density of states of the SIAM with different δ.** $U = 0.1, \Gamma = 0.01$. a) The electron-hole symmetric case $\delta = 0$. b) The color plot of the density of states with $\delta \in [-0.1, 0.1]$, or $[-U, U]$, showing the Kondo regime when $|\delta| < \frac{U}{2}$ and impurity levels at ϵ_d and $\epsilon_d + U$.

The SIAM in the magnetic field

In addition to the basic SIAM Hamiltonian (Eq. 2.32), we can consider the external magnetic field by adding a Zeeman term:

$$H_{\text{SIAM,B}} = H_{\text{SIAM}} + g\mu_{\text{B}}BS_z. \tag{2.34}$$

When increasing the magnetic field, the Kondo resonance splits (Fig. 2.9). Here, it is convenient to absorb the prefactors into B and measure it in the unit of the Kondo temperature T_{K}. In a small magnetic field, the Kondo peak only reduces in height, while the real splitting starts around $B = 3T_{\text{K}}$ (Fig. 2.9 a))[86]. This shows that, in the absence of a magnetic anisotropy, the magnetic field at which the Kondo peak starts to split is an indication of the Kondo temperature.

The SIAM with superconductivity

Instead of the magnetic field, superconductivity (Eq. 2.8) also can be introduced to study the YSR states within the SIAM:

$$H_{\text{SIAM,SC}} = H_{\text{SIAM}} - \sum_k \left(\Delta c_{k\uparrow}^\dagger c_{-k\downarrow}^\dagger + \Delta^* c_{-k\downarrow} c_{k\uparrow} \right). \tag{2.35}$$

The resulting density of states contains features of different energy scales (Fig. 2.10). At high energy, there are impurity levels (Fig. 2.10 a)). At low energy, there is a superconducting gap
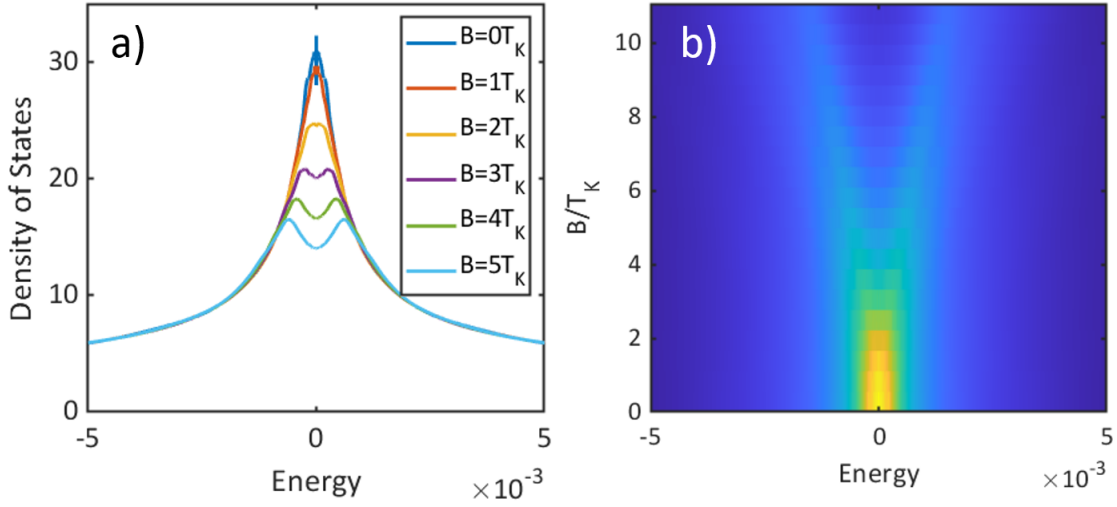
Figure 2.9 – **The density of states of the SIAM in a magnetic field showing the splitting of the Kondo peak.** $U = 0.1, \Gamma = 0.01$. a) Density of states zoomed in to the Kondo peak, which splits up with increasing magnetic field. b) Color plot of the density of states sweeping the magnetic field, showing that the splitting starts at a finite magnetic field.

on top of the Kondo peak near the Fermi energy (Fig. 2.10 b)). In the superconducting gap, one pair of YSR states is observed (Fig. 2.10 c)). Both the Kondo peak and the YSR states show electron-hole asymmetry if $\delta \neq 0$ (Figs. 2.10 b,c) and Fig. 2.11 b)). With increasing Γ, the YSR energy will move across zero (the QPT), with reversed asymmetry (Figs. 2.11 a,b)).

YSR states from a many-body point of view

In a many-body point of view, a YSR state consists of the ground state and one excited state. Without superconductivity, the low energy physics of the SIAM is governed by T_{K}. At low temperature, the impurity spin is screened, resulting in a non-magnetic singlet ground state. Adding superconductivity will open a gap at the Fermi level, depleting the conduction electrons nearby. If superconductivity dominates, there will not be any conduction electrons at the Fermi level available for Kondo screening and the impurity spin will remain unscreened (the free-spin regime) as the ground state, while the screened case is the excited state. If superconductivity is weak, the Kondo screening dominates (the screened regime), while the free-spin state becomes the excited state. The change in the YSR energy accompanies this competition between T_{K} and Δ (Fig. 2.11 c)), and the change of the ground state (exchanging the ground state and the excited state) justifies the classification as QPT. It turns out that within the SIAM, the YSR energy (normalized by Δ) depends universally on T_{K}/Δ, irrespective of the SIAM parameters (U, δ etc.). The QPT happens at $T_{\mathrm{K}}/\Delta = 0.2 \sim 0.3$ [81, 88]. For a detailed discussion see Chapter 7.

One remark is that the dependency of the YSR energy and asymmetry on Γ calculated using
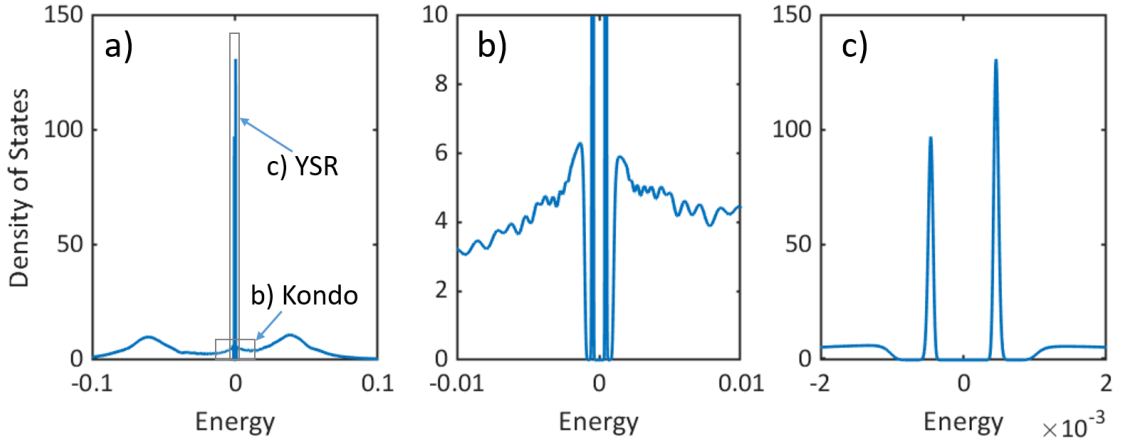
Figure 2.10 – **The density of states of the SIAM with superconductivity showing the coexistence of YSR and Kondo physics.** $U = 0.1, \Gamma = 0.007, \delta = -0.01, \Delta = 0.001$. a) The density of states in the full range showing the two impurity levels. b) and c) are zoom-ins to a), regions of which are denoted in a). b) There is a superconducting gap on top of the Kondo peak. c) YSR states exist inside the superconducting gap.

the fully correlated NRG theory (Figs. 2.11 a), b)) is qualitatively very close to the mean field calculation (c.f. Figs. 2.5 d), e)). Although in the mean field calculation, the x-axis is JS, the two calculations are comparable recalling that Γ in the SIAM is proportional to J in the Kondo impurity model (Eq. 2.33). Such resemblance indicates that, unlike the Kondo effect where correlation effects play an indispensable role, the YSR physics is largely already captured by the simple mean-field approximation, which is largely due to the presence of the energy gap similar to impurity states in a doped semiconductor. This justifies the use of the mean-field model in Chapters 4,5 and 6.

2.4 Fundamental theories on tunneling processes

To probe the objects of interest discussed before, we need another electrode to form a tunnel junction. To simulate transport properties through the tunnel junction, the non-equilibrium Green's function formalism is a flexible and essential tool. This will be covered in the first part of this section.

In reality, the tunnel junction interacts with the electromagnetic environment through the $P(E)$ function, which is a dominant broadening mechanism at very low temperature (or when the thermal broadening is absent like in the tunneling between discrete levels, which is the case in Chapter 8). This will be covered in the second part of this section.
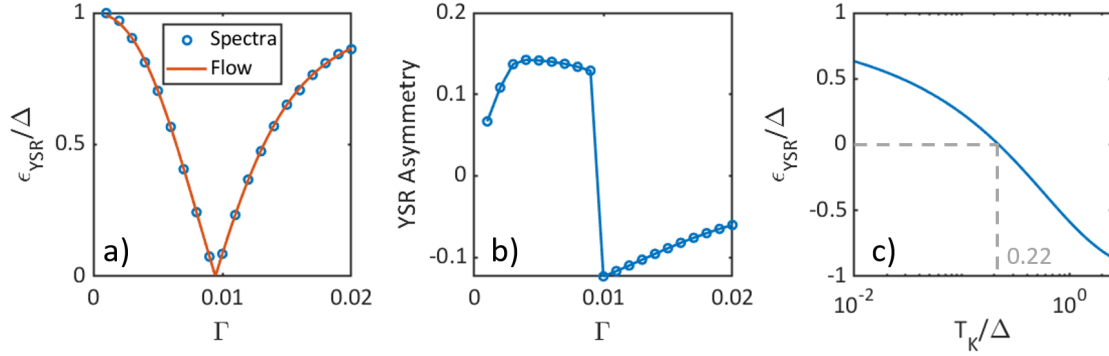
Figure 2.11 – **The YSR quantum phase transition.** $U = 0.1, \delta = -0.01, \Delta = 0.001$. a) With increasing Γ, the YSR energy crosses zero (the QPT). The circles are the YSR energies extracted from the density of states calculation, while the solid line contains the energies extracted directly from the renormalization-group flow diagrams in the NRG, which is more accurate. b) The YSR asymmetry (extracted from the density of states calculation) reverses at the QPT. c) The universal dependence of the YSR energy on T_K/Δ. The QPT happens around $T_K/\Delta = 0.22$, consistent with literature values [81, 88] around $0.2 \sim 0.3$.

2.4.1 Non-equilibrium Green's function formalism

Up till now, our discussion on the Green's function was concerned with a single electrode. Once we add a second electrode and apply a bias voltage, the system will be driven out of equilibrium, where the Keldysh formalism [89] is needed. It is thus an essential tool to simulate various electronic transport problems. Here, we are interested in modeling tunnel junctions. The following discussions follow mainly Refs. [90–92].

For a metallic junction in the tunneling regime, the tunneling current given by the Keldysh formalism is basically the usual Bardeen tunneling formula (Eq. 3.2) [92]. In this thesis, the only metallic junction is in the Kondo measurements in Chapter 7, where the dI/dV spectrum is simply proportional to the density of states (because the other electrode is metallic and normal conducting having constant density of states), and thus there is no need to invoke the Green's function technique there. In all other parts of this thesis, the tunnel junction is formed between two superconductors, and thus we focus here on the Green's function formalism for superconducting junctions.

The tunnel junction between two superconductors can be described by the Hamiltonian [90, 91]

$$H(\tau) = H_L + H_R + \sum_\sigma \left(t e^{i\phi(\tau)/2} c^\dagger_{L\sigma} c_{R\sigma} + t^* e^{-i\phi(\tau)/2} c^\dagger_{R\sigma} c_{L\sigma} \right), \tag{2.36}$$

with $H_{L,R}$ being the respective Hamiltonian for the left and right electrode, t being the tunnel coupling, σ being the spin, τ being the time, $\phi(\tau)$ being the superconducting phase given by the Josephson relation (see Eq. 2.67) $\phi(\tau) = \phi_0 + \frac{2\omega_0\tau}{\hbar}, \omega_0 = eV$ and V being the bias voltage applied across the junction.

In the time domain, the tunneling current writes

$$I(\tau) = \frac{e}{\hbar} \text{Tr}[\tau_z(\hat{t}(\tau)G_{RL}^{+-}(\tau,\tau) - G_{LR}^{+-}(\tau,\tau)\hat{t}^\dagger(\tau))], \tag{2.37}$$

where τ_z is the Pauli z matrix in Nambu space, Tr is the trace in Nambu space, and $\hat{t}(\tau) = \begin{pmatrix} te^{i\phi(\tau)/2} & 0 \\ 0 & -t^* e^{-i\phi(\tau)/2} \end{pmatrix}$ is the hopping matrix. The lesser Green's function $G^{+-}(\tau,\tau)$ in the Keldysh formalism is defined by a (2×2) matrix:

$$G_{ij}^{+-}(\tau,\tau') = i \begin{pmatrix} \langle c_{j\uparrow}^\dagger(\tau')c_{i\uparrow}(\tau) \rangle & \langle c_{j\downarrow}(\tau')c_{i\uparrow}(\tau) \rangle \\ \langle c_{j\uparrow}^\dagger(\tau')c_{i\downarrow}^\dagger(\tau) \rangle & \langle c_{j\downarrow}(\tau')c_{i\downarrow}^\dagger(\tau) \rangle \end{pmatrix}. \tag{2.38}$$

Plugging Eq. 2.38 into Eq. 2.37, we get

$$I(\tau) = \frac{e}{\hbar} (te^{i\omega_0\tau/\hbar}G_{RL,11}^{+-} - t^* e^{-i\omega_0\tau/\hbar}G_{LR,11}^{+-} + t^* e^{-i\omega_0\tau/\hbar}G_{RL,22}^{+-} - te^{i\omega_0\tau/\hbar}G_{LR,22}^{+-}). \tag{2.39}$$

The involved Green's functions satisfy:

$$G_{RL}^{+-}(\tau,\tau) = \int d\tau_1[G_{RR}^r(\tau,\tau_1)\hat{t}^\dagger(\tau_1)g_L^{+-}(\tau_1-\tau) + G_{RR}^{+-}(\tau,\tau_1)\hat{t}^\dagger(\tau_1)g_L^a(\tau_1-\tau)], \tag{2.40}$$

$$G_{LR}^{+-}(\tau,\tau) = \int d\tau_1[g_L^{+-}(\tau-\tau_1)\hat{t}(\tau_1)G_{RR}^a(\tau_1,\tau) + g_L^r(\tau-\tau_1)\hat{t}(\tau_1)G_{RR}^{+-}(\tau_1,\tau)], \tag{2.41}$$

with g being an unperturbed Green's function and G being a full Green's function. It is possible to numerically calculate the tunneling current for arbitrary Green's functions, given a few more equations. The full calculation at arbitrary transmissions, however, is highly non-trivial, and we use the code developed by our collaborator Juan Carlos Cuevas for such simulations. For a superconducting junction, the simulation gives full account of the multiple Andreev reflections which will be discussed later. Here, we only discuss the current in the tunneling regime (low transmission limit), where everything is analytical and we can calculate using simple convolutions.

The tunneling current in the low transmission regime

We approximate all Green's functions of one electrode to be the unperturbed ones $G_{RR}^{+-} = g_R^{+-}$, $G_{RR}^{r,a} = g_R^{r,a}$, and therefore Eqs. 2.40 and 2.41 change to

$$G_{RL}^{+-}(\tau,\tau) = \int d\tau_1[g_R^r(\tau,\tau_1)\hat{t}^\dagger(\tau_1)g_L^{+-}(\tau_1-\tau) + g_R^{+-}(\tau,\tau_1)\hat{t}^\dagger(\tau_1)g_L^a(\tau_1-\tau)], \tag{2.42}$$

$$G_{LR}^{+-}(\tau,\tau) = \int d\tau_1[g_L^{+-}(\tau-\tau_1)\hat{t}(\tau_1)g_R^a(\tau_1,\tau) + g_L^r(\tau-\tau_1)\hat{t}(\tau_1)g_R^{+-}(\tau_1,\tau)], \tag{2.43}$$

Given the relations between retarded (G^r), advanced (G^a), lesser (G^{+-}) and greater (G^{-+}) Green's functions

$$G^a - G^r = G^{+-} - G^{-+}, \tag{2.44}$$

$$g^{+-} = (g^a - g^r)f(\omega), \tag{2.45}$$

$$g^{-+} = -(g^a - g^r)(1 - f(\omega)), \tag{2.46}$$

where $f(\omega) = \frac{1}{e^{\omega/k_B T}+1}$ is the Fermi function, the following result for the DC current can be obtained after a Fourier transform

$$I_0 = \frac{e|t|^2}{h} \int_{-\infty}^{+\infty} d\omega [g_{L,11}^{+-}(\omega)g_{R,11}^{-+}(\omega + \omega_0) - g_{L,22}^{+-}(\omega)g_{R,22}^{-+}(\omega - \omega_0)$$
$$- g_{R,11}^{+-}(\omega)g_{L,11}^{-+}(\omega - \omega_0) + g_{R,22}^{+-}(\omega)g_{L,22}^{-+}(\omega + \omega_0)]. \tag{2.47}$$

This expression can be further simplified considering Eq. 2.5:

$$I_0 = \frac{4\pi^2 e|t|^2}{h} \int_{-\infty}^{+\infty} \left[\rho_{L,11}(\omega)\rho_{R,11}(\omega + \omega_0) + \rho_{L,22}(\omega + \omega_0)\rho_{R,22}(\omega)\right] \times$$
$$\left(f(\omega) - f(\omega + \omega_0)\right) d\omega, \tag{2.48}$$

which is very similar to the Bardeen tunneling formula (Eq. 3.2), except that the current consists of both electron (the 11 term) and hole parts (the 22 term).

2.4.2 The $P(E)$ theory

With the Green's function theory, the tunneling current can be calculated, which already includes the thermal broadening $\propto k_B T$ in metallic junctions. Besides that, in reality, the measured spectra are further broadened due to the energy exchange with the environment via photons (Fig. 2.12 a)). A spectral peak will develop a shoulder at the low (high) energy side because of the photon absorption (emission) process during tunneling. This can be modeled by an additional convolution with the $P(E)$ function, which describes the probability for a tunneling electron to exchange energy with the environment [93–95]:

$$\vec{\Gamma}(V) = \frac{1}{e^2 R_T} \int_{-\infty}^{\infty} \int_{-\infty}^{\infty} dEdE' \rho_t(E)\rho_s(E' + eV)f(E)[1 - f(E' + eV)]P(E - E'). \tag{2.49}$$

Here $\vec{\Gamma}(V)$ is the forward tunneling probability, $\rho_{t,s}$ are the density of states of the tip and sample and $f(E) = \frac{1}{e^{E/k_B T}+1}$ is the Fermi function. Exchanging the electrons and holes will provide the equation for backwards tunneling probability $\overleftarrow{\Gamma}(V)$, and the total tunneling current (for electron tunneling) is

$$I(V) = e\left(\vec{\Gamma}(V) - \overleftarrow{\Gamma}(V)\right). \tag{2.50}$$
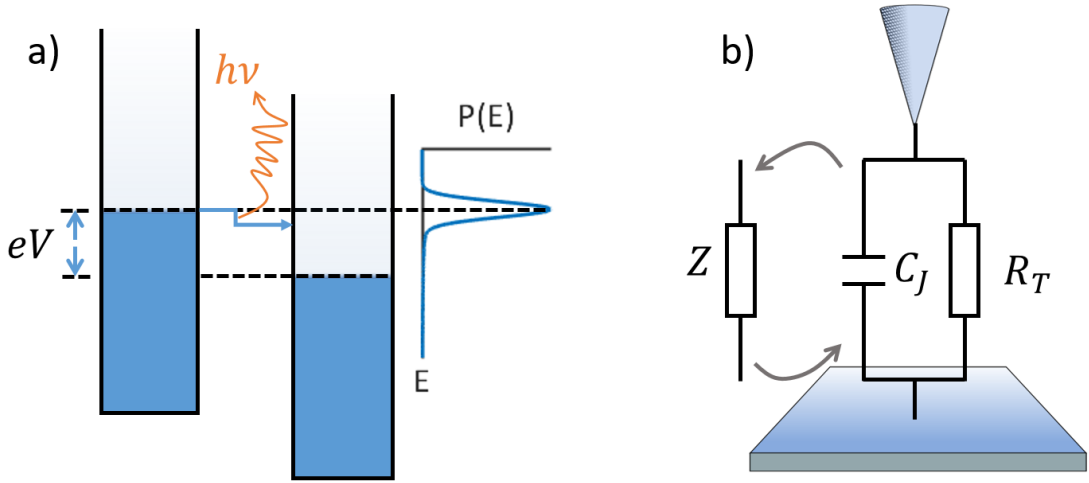
Figure 2.12 – **The $P(E)$ function.** a) The schematics of a generic tunnel junction showing the energy loss to the environment via photon emission, which is captured by the $P(E)$ function. b) In the $P(E)$ theory, the environment is treated as an impedance in parallel to the junction capacitance C_J.

The derivation of the $P(E)$ function

In the discussion in this part, we follow Refs. [96–98]. In essence, the interaction with the environment is mediated through the phase fluctuation $\tilde{\phi}$ across the junction, and we introduce the phase-phase correlation function

$$J(t) = \langle [\tilde{\phi}(t) - \tilde{\phi}(0)]\tilde{\phi}(0) \rangle. \tag{2.51}$$

The $P(E)$ function can be written as [98]

$$P(E) = \frac{1}{2\pi\hbar} \int\limits_{-\infty}^{\infty} dt \exp\left(J(t) + \frac{iEt}{\hbar}\right). \tag{2.52}$$

Now we further decompose the correlation function $J(t)$ to the environmental impedance part $J_0(t)$ and the capacitive noise part $J_N(t)$

$$J(t) = J_0(t) + J_N(t), \tag{2.53}$$

and thus the final $P(E)$ function is a convolution of the corresponding two parts

$$P(E) = \int\limits_{-\infty}^{\infty} dE' P_0(E - E') P_N(E'). \tag{2.54}$$

The $P_N(E)$ function, which is the capacitive noise contribution, is a simple Gaussian function:

$$P_N(E) = \frac{1}{\sqrt{4\pi E_c k_B T}} \exp\left(-\frac{E^2}{4E_c k_B T}\right) \tag{2.55}$$

where E_c is the charging energy of the junction given by

$$E_c = \frac{Q^2}{2C_J}, \tag{2.56}$$

with Q being the charge of the carriers in the leads and C_J being the junction capacitance. For a normal conducting junction $Q = e$, while for a superconducting junction where Cooper pair tunneling dominates $Q = 2e$.

The more complicated $P_0(E)$ function is related to the energy exchange with the environment. We can calculate it using [97, 98]

$$J_0(t) = \int_{-\infty}^{\infty} \frac{d\omega}{\omega} \frac{\operatorname{Re} Z_t(\omega)}{R_Q} \frac{\exp(-i\omega t) - 1}{1 - \exp(-\beta \hbar \omega)}, \tag{2.57}$$

where $\beta = 1/k_B T$, T is the temperature, R_Q is the resistance quantum which is $h/2e^2$ for the normal conducting case and $h/4e^2$ for superconducting case (according to Ref. [98], there is an additional factor of two outside of the integral in the superconducting case). $Z_t(\omega)$ is the total impedance

$$Z_t(\omega) = \frac{1}{i\omega C_J + Z^{-1}(\omega)}, \tag{2.58}$$

considering a junction capacitance C_J in parallel with the external impedance $Z(\omega)$ (Fig. 2.12 b)).

In real simulations the following integration equation is often used instead for computational efficiency

$$P_0(E) = I(E) + \int_{-\infty}^{\infty} d\omega K(E, \omega) P_0(E - \hbar\omega), \tag{2.59}$$

with the inhomogeneity $I(E) = \frac{1}{\pi\hbar} \frac{D}{D^2 + E^2/\hbar^2}$ and the integral kernel $K(E, \omega) = \frac{E/\hbar}{D^2 + E^2/\hbar^2} k(\omega) + \frac{D}{D^2 + E^2/\hbar^2} \kappa(\omega)$. Here,

$$
\begin{aligned}
D &= \frac{\pi}{\beta\hbar} \frac{\operatorname{Re} Z_t(0)}{R_Q}, \\
k(\omega) &= \frac{1}{1 - \exp(-\beta\hbar\omega)} \frac{\operatorname{Re} Z_t(\omega)}{R_Q} - \frac{1}{\beta\hbar\omega} \frac{\operatorname{Re} Z_t(0)}{R_Q}, \\
\kappa(\omega) &= -\frac{1}{1 - \exp(-\beta\hbar\omega)} \frac{\operatorname{Im} Z_t(\omega)}{R_Q} - \frac{2}{\hbar\beta} \sum_{n=1}^{\infty} \frac{\nu_n}{\nu_n^2 + \omega^2} \frac{Z_t(-i\nu_n)}{R_Q},
\end{aligned}
\tag{2.60}
$$

where the Matsubara frequencies ν_n are defined to be $\hbar\nu_n = 2n\pi/\beta$.

Now, the $P(E)$ function only depends on the temperature T, the junction capacitance C_J, and the external impedance $Z(\omega)$. The expression for $Z(\omega)$ differs for different models, and two commonly used ones are [96, 98, 99]

$$Z(\omega) = \begin{cases} R_{\mathrm{env}} & \text{(ohmic impedance)}, \\ R_{\mathrm{env}} \frac{1+\frac{i}{\alpha}\tan(\frac{\pi}{2}\frac{\omega}{\omega_0})}{1+i\alpha\tan(\frac{\pi}{2}\frac{\omega}{\omega_0})} & \text{(infinite transmission line model)}, \end{cases} \tag{2.61}$$

where R_{env} is the effective DC resistance for the environmental impedance which in many cases can be set to the vacuum impedance of 376.73Ω (although this can change in principle), and then the simple ohmic impedance model does not contain any free parameter. The infinite transmission line model introduces two more free parameters: α is the effective damping parameter and ω_0 is the principal resonance frequency.

Properties of the $P(E)$ function

The behavior of $P_N(E)$ is straightforward, since it is a simple Gaussian function (Eq. 2.55). It is symmetric and usually dominates the width of the final $P(E)$ function (Fig. 2.13). The full-width-at-half-maximum (FWHM) is $4\sqrt{\ln 2}\sqrt{E_c k_{\mathrm{B}} T}$, proportional to $\sqrt{\frac{T}{C_J}}$. This means that the $P(E)$ broadening decreases with decreasing temperature or increasing junction capacitance.

$P_0(E)$ describes the energy exchange with the environment. First, it satisfies the sum rule $\int_{-\infty}^{\infty} dE P_0(E) = 1$, which the final $P(E)$ function also inherits because $P_N(E)$ is also normalized

$$\int_{-\infty}^{\infty} dE P(E) = 1. \tag{2.62}$$

Second, since it is more likely to emit a photon than to absorb one from the environment at low temperature, $P_0(E)$ is asymmetric (Fig. 2.13). It satisfies the so-called detailed balance symmetry

$$P_0(-E) = e^{-\beta E} P_0(E), \tag{2.63}$$

in which the imbalance between absorption and emission is actually the signature of a quantum mechanical process.

Phenomena related to the $P(E)$ function

For a more detailed discussion of the relation between the $P(E)$ function and the following three phenomena see Ref. [95].

Spectral broadening Since the $P(E)$ function is an additional convolution in the tunneling current formula (Eq. 2.49), it broadens the spectra. Since the FWHM of the $P(E)$ function is proportional to $\sqrt{T}$ instead of T as in the normal Fermi broadening, it becomes important for temperatures below 1K. In addition, since the FWHM of the $P(E)$ function is inversely

Figure 2.13 – **The two components of a** $P(E)$ **function.** The $P(E)$ function consists of the asymmetric part $P_0(E)$, which captures the energy exchange with the environment, and the symmetric part $P_N(E)$, which reflects the capacitive noise. $P_N(E)$ usually dominates the broadening of the $P(E)$ function. The calculation is done with an ohmic impedance with parameters $C_J = 5\,\text{fF}$, $T = 15\,\text{mK}$.
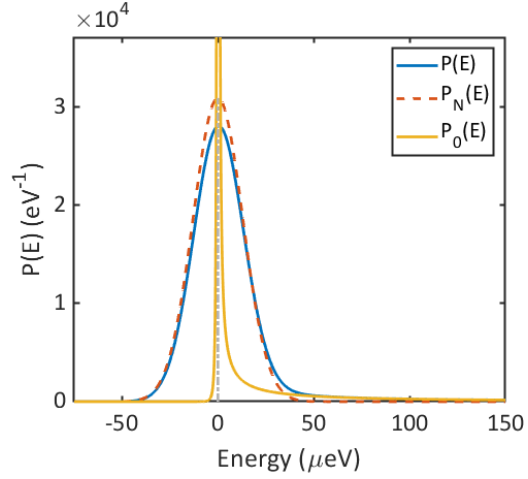
proportional to $\sqrt{C_J}$, increasing the junction capacitance can reduce the $P(E)$ broadening and thus increase the energy resolution.

The dynamic Coulomb blockade (DCB) Consider electron tunneling through a metallic junction at a bias voltage close to zero. The energy loss through photon emission can be so high that the final state is no longer above the Fermi level. Since the electron cannot tunnel into an already filled state, the tunneling probability is reduced, resulting in a dip in the dI/dV spectrum near zero bias.

The Josephson effect Two superconductors connected by a weak link is called the Josephson junction, which can support a DC current with zero voltage. If the junction is voltage biased, the DC spectral feature locates near zero bias and is a direct imprint of the asymmetry of the $P(E)$ function. The energy exchange with the environment actually facilitates the Cooper pair tunneling, such that in the context of the Josephson effect, the DCB is also referred to as an anti-blockade. This will be covered later in section 2.5.3 in more detail.

2.5 Tunneling processes between superconductors

In the last section of this chapter, we would like to apply the introduced theoretical machinery to the tunnel junction between two superconductors, because this thesis will mainly deal with such junctions. Before that, we first define the transmission

$$\tau = G_N/G_0 \tag{2.64}$$

to be the normal state conductance G_N normalized by the conductance quantum $G_0 = \frac{2e^2}{h}$. Since the conductance quantum is the maximum conductance possible in a single channel junction, $0 \leq \tau \leq 1$.
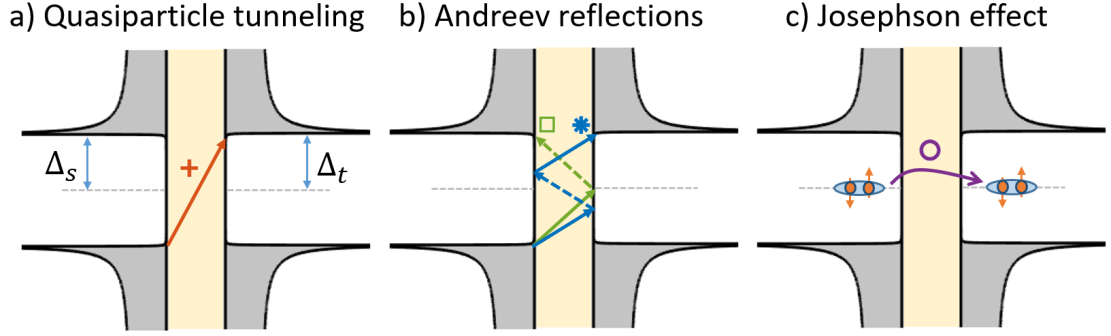
Figure 2.14 – **Tunneling processes between superconductors.** a) Direct quasiparticle tunneling with one charge transferred per tunneling event. b) Andreev reflections, where electrons (solid lines) are reflected as holes (dashed lines), transferring multiple charges. The green arrows label the second order process, and the blue arrows label the third order process. c) The Josephson effect, where Cooper pairs tunnel.

There are three types of tunneling processes between two superconductors: quasiparticle tunneling, (multiple) Andreev reflections (MARs) and the Josephson effect (Fig. 2.14).

2.5.1 Quasiparticle tunneling

Direct quasiparticle tunneling is a first order tunneling process, which is linearly proportional to τ. It can be described by Eq. 2.48 as a simple convolution of the tip and sample density of states. For the tunneling between two clean superconductors, it gives rise to the coherence peaks at $eV = \pm(\Delta_s + \Delta_t)$, with $\Delta_{s,t}$ being the superconducting order parameters for the sample and the tip, respectively (Fig. 2.14 a)). Notice that at high transmission, the dI/dV peak of quasiparticle tunneling will deviate from a linear dependence on τ and become sublinear due to tunnel broadening, where Eq. 2.48 is no longer valid.

The YSR-BCS tunneling If one electrode (with order parameter Δ_s) contains a YSR state with energy ϵ_0 while the other electrode is a clean superconductor with order parameter Δ_t, there will be a pair of direct tunneling peaks ($d_{\pm}$) in the dI/dV spectrum at $eV = \pm|\Delta_t + \epsilon_0|$ and a pair of thermal assisted tunneling peaks ($t_{\pm}$) at $eV = \pm|\Delta_t - \epsilon_0|$, where $+,-$ denote the peaks at positive and negative bias voltage, respectively.

At low transmission, the dI/dV peaks scale linearly with τ, called the linear regime. At higher transmission, higher order processes starts to dominate and the peak depends sublinearly [19].

The simulation of the tunneling spectra in the linear regime (Fig. 2.15) can be done by plugging in the YSR Green's function (Eq. 2.20) and the BCS Green's function (Eq. 2.15) into the expression for the tunneling current (Eq. 2.48). The peaks have prominent negative differential conductance part, and the coherence peaks at $eV = \pm(\Delta_s + \Delta_t)$ vanishes. It can be shown that

Figure 2.15 – **The simulated YSR-BCS tunneling spectrum.** At low temperature, only the direct tunneling peaks ($d_\pm$) exist (red curve), while at higher temperature, the thermal processes ($t_\pm$) emerge (yellow curve). Notice that in the presence of the YSR state, the coherence peaks at $eV = \pm(\Delta_s + \Delta_t)$ vanish (compare with the clean junction situation in the blue curve). The spectra are offset for clarity.
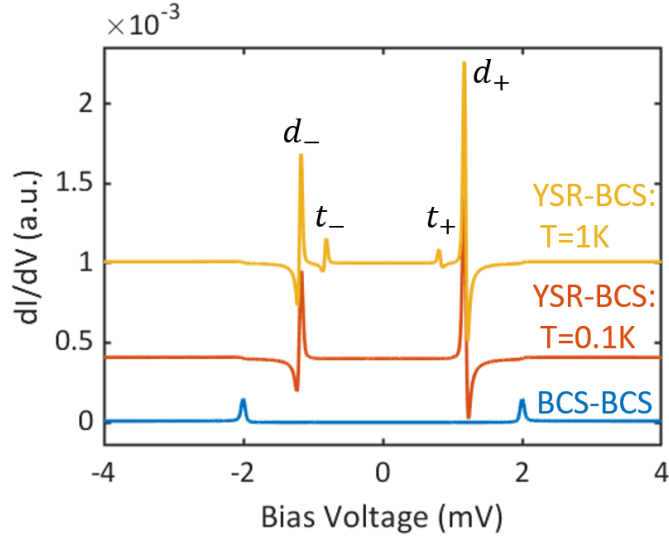
the ratio between the thermal and direct peaks is the Boltzmann factor [19, 100]

$$\frac{t_+}{d_-} = \frac{t_-}{d_+} = \exp\left(-\frac{|\epsilon_0|}{k_B T}\right), \tag{2.65}$$

and it is clear that for $T \to 0$, the thermal peaks $t_\pm$ will vanish, which is the case in our experiments at milikelvin temperatures, unless otherwise stated. As an important note, Eq. 2.65 only holds at the low conductance limit (the linear regime).

One practical aspect is that, to extract the YSR energy from the peak position, we need to subtract the Δ of the other electrode.

The YSR-YSR tunneling If both electrodes contain YSR states (with YSR energy $\epsilon_{s,t}$), there will be a pair of direct tunneling features at $eV = \pm|\epsilon_s + \epsilon_t|$ and a pair of thermal assisted tunneling features at $eV = \pm|\epsilon_s - \epsilon_t|$, which we call the Shiba-Shiba tunneling processes. The Shiba-Shiba tunneling is the elementary tunneling process between single levels, which will be covered in detail in Chapter 8.

2.5.2 Andreev reflections

Electrons traveling towards a superconductor might be reflected back as a hole, which is called an Andreev reflection. In this case, two net charges are transferred across the junction (the green process in Fig. 2.14 b)), and thus it is a second order process scaling with τ^2. If both electrodes are superconducting, Andreev reflections can happen multiple times in series, which are then called multiple Andreev reflections (MARs) (one example is the blue process in Fig. 2.14 b), which is a third order process scaling with τ^3). The bias voltages of the dI/dV peak for a few lowest order MARs are shown in Table 2.1, together with the scaling with respect to τ.

order	2	3	4	5	...
$eV = \pm$	$\Delta_{s,t}$	$\frac{\Delta_s + \Delta_t}{3}$	$\frac{\Delta_{s,t}}{2}$	$\frac{\Delta_s + \Delta_t}{5}$	...
scaling	$\propto \tau^2$	$\propto \tau^3$	$\propto \tau^4$	$\propto \tau^5$	...

Table 2.1 – **MARs between two BCS superconductors.** Only a few lowest order processes are shown.

Basically $eV = \pm \frac{\Delta_{s,t}}{n}$ and $eV = \pm \frac{\Delta_s + \Delta_t}{2n+1}$ for integer $n \geq 1$. The higher order the MARs is, the smaller bias voltage it is located and the higher transmission at which it emerges. Here, all MAR processes are below $|eV| = \Delta_{s,t}$.

The Andreev reflections including the YSR states If one electrode contains a YSR state, the Andreev reflections are more complicated. Particularly interesting is the second order process that connects the YSR state back to itself, which is forbidden due to the spin polarization of the YSR state. This will be discussed in detail in Chapter 5.

2.5.3 The Josephson effect

The two Josephson equations Brian David Josephson predicted in 1962 that current can flow through a tunnel junction consisting of two superconductors without any voltage applied [101], called the Josephson effect. A set of two equations describes the Josephson effect. The first Josephson equation

$$I(\phi) = I_c \sin\phi \qquad (2.66)$$

describes the DC Josephson effect, which means that a direct current (DC) flows if there is phase difference between the two superconductors without needing a bias voltage. The maximum current without dissipation is called the critical current I_c. The second Josephson equation

$$\frac{\partial \phi}{\partial t} = \frac{2eV}{\hbar} \qquad (2.67)$$

yields the AC Josephson effect, which describes that if a finite bias voltage is applied across the junction, the phase will rotate with time, resulting in an alternating current (AC) with frequency $\nu = \frac{2eV}{\hbar}$.

The critical current I_c The critical current can be written in terms of the retarded anomalous Green's functions of the two electrodes $F_{s,t}$ [69, 90]:

$$I_c = \frac{8et^2}{\hbar} \int \frac{d\omega}{2\pi} f(\omega) \text{Im}[F_s(\omega) F_t(\omega)], \qquad (2.68)$$

where $f(\omega)$ is the Fermi distribution function and t is the hopping between the two electrodes.

In the simple case when the two electrodes are both clean BCS superconductors with order

parameters $\Delta_{1,2}$, Vinay Ambegaokar and Alexis Baratoff showed in 1963 that the critical current can be written as [102]

$$I_c = \frac{\Delta_1(T)}{eR_N} K\left(\sqrt{1 - \frac{\Delta_1^2(T)}{\Delta_2^2(T)}}\right), \tag{2.69}$$

where $\Delta_1 \leq \Delta_2$, R_N is the normal state resistance and K stands for the complete elliptic integral of the first kind. This is the so-called Ambegaokar-Baratoff formula. Since $K(0) = \frac{\pi}{2}$, for $\Delta_1 = \Delta_2 = \Delta$, the formula further simplifies to

$$I_c = \frac{\pi\Delta(T)}{2eR_N} = \frac{e\Delta}{2\hbar}\tau. \tag{2.70}$$

Notice that the order parameters are generally temperature dependent. The critical current vanishes when $T \geq T_c$ where $\Delta(T) = 0$ as expected. In this thesis, we always work in the low temperature limit where $\Delta = \Delta(0)$.

The energy phase relation An alternative approach to calculate the critical current is through the energy phase relation $E(\phi)$, which is the dependency of the energy of the system as a function of the superconducting phase difference across the junction.

The current phase relation (recall Eq. 2.66) at the zero temperature limit can be calculated from $E(\phi)$ through [103]

$$I(\phi) = \begin{cases} \frac{2e}{\hbar}\frac{\partial E(\phi)}{\partial \phi} & \text{(spin degenerate)}, \\ \frac{e}{\hbar}\frac{\partial E(\phi)}{\partial \phi} & \text{(spin non-degenerate)}. \end{cases} \tag{2.71}$$

After the current phase relation is known, the critical current is directly obtained through Eq. 2.66. The factor of two difference in Eq. 2.71 is important for comparing the Josephson current through YSR states (spin non-degenerate) and that in a clean superconducting junction (spin degenerate). Alternatively, we can take the factor of two in the spin degenerate situation as an additional prefactor in front of $E(\phi)$ and use the spin non-degenerate formula always (which we adopt in Chapter 6).

Generally, $E(\phi)$ may contain high order harmonics (see Eq. 2.78). At low transmission, only the first harmonic term exists [98]

$$E(\phi) = C - E_J \cos(\phi), \tag{2.72}$$

where E_J is the Josephson coupling energy and C is a constant shift. Inserting the above equation in Eqs. 2.71 and 2.66, E_J relates to I_c in the spin degenerate case (like in a BCS-BCS junction) by

$$E_J = \frac{\hbar}{2e}I_c. \tag{2.73}$$

The energy phase relation for a BCS-BCS junction As an example, consider the tunneling between two BCS superconductors with equal gaps. The energy-phase relation is given by [103–105]

$$E^{\text{BCS-BCS}}(\phi) = \pm\Delta\sqrt{1 - \tau\sin^2(\phi/2)}. \tag{2.74}$$

In the case of small transmission $\tau \ll 1$, the relation becomes harmonic

$$E^{\text{BCS-BCS}}(\phi) = \pm\frac{\Delta}{4}\tau\cos\phi, \tag{2.75}$$

which yields $I_c = \frac{e\Delta}{2\hbar}\tau$ using Eq. 2.71. This is consistent with the Ambegaokar-Baratoff formula (Eq. 2.70). In Chapter 6, we will investigate a more complicated situation which is the Josephson effect in the presence of the YSR states, which is spin non-degenerate.

The voltage biased Josephson current in the DCB regime Apart from E_J, another important energy scale for a Josephson junction is the charging energy defined in Eq. 2.56, and we recall it for Cooper pairs $E_c = 2e^2/C_J$.

Due to the commutation relation $[\phi, q] = 2ie$ between the phase ϕ and the charge q, they cannot be both exactly known at the same time. If $E_J \gg E_c$, ϕ is a good quantum number while q is not, and the Cooper pairs tunnel coherently. The opposite scenario (the so-called DCB regime) where $E_J \ll E_c$ means that q is a good quantum number, and the Cooper pairs tunnel sequentially at finite voltage $V = h\nu/(2e)$, emitting photons of corresponding energy to the environment. The second case is actually the situation for low temperature scanning tunneling microscopes (STM).

In the DCB regime, the Cooper pair current in a voltage-biased Josephson junction can be described using the $P(E)$ function [98]

$$\begin{aligned}
I(V) &= 2e\left(\overrightarrow{\Gamma}(V) - \overleftarrow{\Gamma}(V)\right), \\
&= \frac{\pi e E_J^2}{\hbar}[P(2eV) - P(-2eV)].
\end{aligned} \tag{2.76}$$

At high transmission, the above formula needs to be corrected to be [105]

$$I(V) = \frac{2\pi}{\hbar}\sum_{m=1}^{+\infty}|E_m|^2(2me)[P_m(2meV) - P_m(-2meV)], \tag{2.77}$$

where $P_m(E) = \frac{1}{2\pi\hbar}\int_{-\infty}^{+\infty}dt\exp\left(m^2 J(t) + \frac{iEt}{\hbar}\right)$ is the modified $P(E)$ function accounting for the transfer of m Cooper pairs. Notice that Eqs. 2.76 and 2.77 are valid in the spin degenerate case (recall Eq. 2.71), while in the spin non-degenerate case, there is an additional prefactor of $1/4$ on the right hand side. The coefficients E_m are the Fourier components of the energy phase

relation

$$E(\phi) = \sum_{m=-\infty}^{+\infty} E_m e^{im\phi}, \tag{2.78}$$

where ϕ is the phase difference between two electrodes.

In the case of low transmission ($\tau \ll 1$), only $m = \pm 1$ terms need to be considered, and thus $E(\phi) = (E_1 + E_{-1})\cos\phi + (E_1 - E_{-1})i\sin\phi$. Assuming that $E(\phi)$ and $E_{\pm 1}$ are all real, we have $E_1 = E_{-1}$ and

$$E_{\tau \ll 1}(\phi) = 2E_1 \cos\phi, \tag{2.79}$$

which yields $|E_1| = E_J/2$ after comparing with Eq. 2.72. With this, Eq. 2.77 reduces to Eq. 2.76. In this thesis, we only consider the low transmission scenario where Eq. 2.76 is sufficient.

Since the $P(E)$ function is sharp and asymmetric, the $I(V)$ feature of the Josephson effect exist near zero bias voltage and its shape is basically due to the asymmetry of the $P(E)$ function.

The switching current I_s According to Eq. 2.76, $I(V) \to 0$ for $V \to \pm\infty$ (because $P(E) \to 0$ for $E \to \pm\infty$) as well as $V \to 0$. Consequently, the Josephson current will have a maximum at the positive voltage side called the switching current I_s (see Fig. 2.16 d)) which is directly measurable experimentally. Since the $P(E)$ function is a global property of the junction regardless of the local properties, we have

$$I_s \propto E_J^2 \propto |E_1|^2 \propto I_c^2, \tag{2.80}$$

if we only consider the lowest order harmonic in Eq. 2.78.

In the case of a clean BCS-BCS junction where the Ambegaokar-Baratoff formula is valid (Eq. 2.70), we have

$$I_s \propto G_N^2 \Delta^2, \text{or } \sqrt{I_s} R_N \propto \Delta \tag{2.81}$$

where $R_N = 1/G_N$ is the normal state resistance. This means that the Josephson switching current scales with τ^2 and is quadratically proportional to the order parameter. The $\sqrt{I_s} R_N$ product is proportional to Δ independent of the conductance.

About the local order parameter It is tempting to extend the simple formula Eq. 2.81 and interpret Δ as the local order parameter discussed in Eq. 2.31, and propose using the Josephson measurement in STM (the so-called Josephson STM) as a measurement tool for the local order parameter [69, 106]. However, remember that Eq. 2.81 only holds for homogeneous BCS superconductors with equal gaps. Even in the homogeneous case where the tip and sample gaps are not equal, this already fails (recall Eq. 2.69). Moreover, when Δ varies locally, the idea that the Josephson current is directly related to the local order parameter also breaks down.

Experimentally, the suppression of I_s on magnetic impurities has been observed [106], which has been conventionally interpreted as a direct probe of the reduced local order parameter on

the impurity (c.f. Figs. 2.6 b) and c)) [69]. In Chapter 6, we will interpret this observation as the interference between two channels, where the local order parameter is largely irrelevant. In fact, the variation of the local order parameter has only minor influence on the $I_c R_N$ product in the measurement (contrary to the conclusion in Ref. [69]). A more detailed discussion see section 6.6.2.
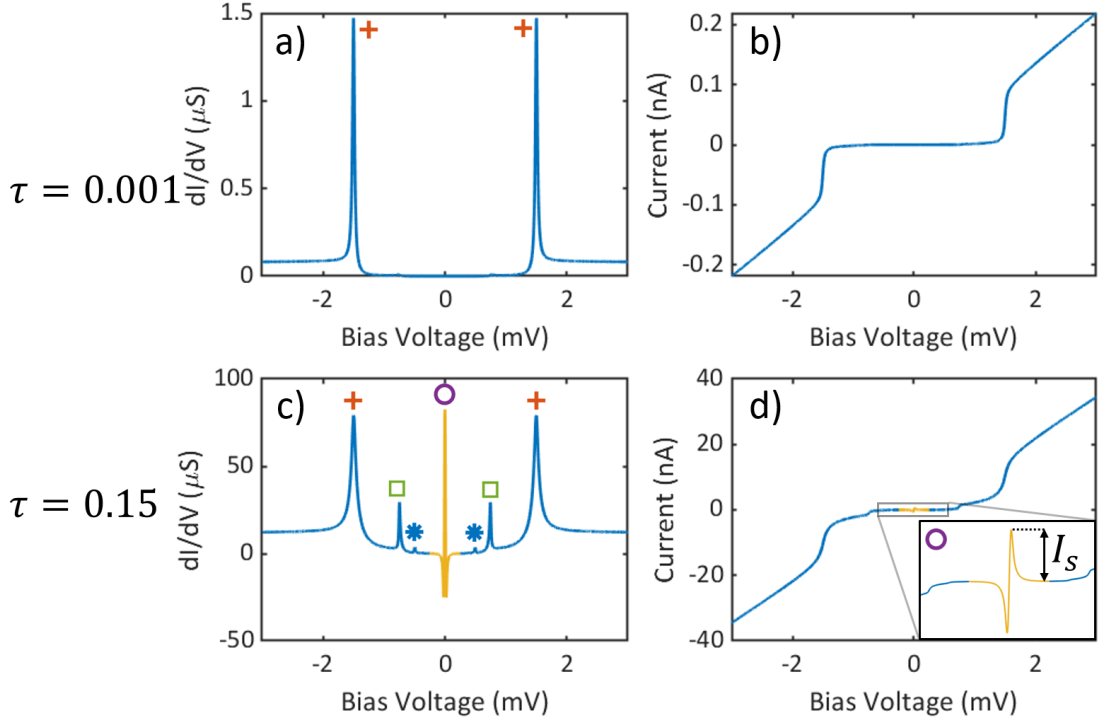
Figure 2.16 – **Simulations of tunneling measurements at different transmission.** a,b) $\tau = 0.001$ and c,d) $\tau = 0.15$. The labels on the peaks denote the tunneling processes using the same labels shown in Fig. 2.14. a) The dI/dV spectrum at low transmission shows only quasiparticle tunneling peaks. b) The $I(V)$ curve shows no current in the gap. c) The dI/dV spectrum at high transmission shows all three types of tunneling processes. d) In the $I(V)$ curve, the gap fills up more than that in b), and a zoom-in to the bias voltage close to zero shows the Josephson feature. The maximum of the current peak there is the switching current I_s.

2.5.4 The transmission dependence of various processes

In the last part of this section, we would like to connect the three tunneling processes (the quasiparticle tunneling, MARs and the Josephson effect) through the transmission. At low transmission $\tau \ll 1$, only the quasiparticle tunneling processes which are first order in τ can be seen in the dI/dV spectrum (Fig. 2.16 a)).

When the transmission increases, second order processes start to emerge, including the Josephson effect near zero bias and the Andreev reflections at $eV = \pm\Delta_{s,t}$ (the peaks labeled with ∘ and □ in Figs. 2.14 b,c) and Fig. 2.16 c)). Since they scale quadratically, they become

more pronounced with increasing transmission.

When τ increases further, higher order MAR processes become visible (for instance the peaks labeled with $*$ in Fig. 2.16 c)).

The above discussion is of experimental relevance for the STM, where the junction transmission can be controlled by changing the distance between the tip and the sample. With the tip approaching the sample surface, the transmission increases, revealing different tunneling phenomena. The experimental details of the STM will be discussed in the next chapter.

3 Experimental setup

The experiments in this thesis are done using a scanning tunneling microscope (STM) operating at a base temperature of $10\,$mK (the mK-STM) with the vanadium (100) surface and the vanadium tip. In this chapter, we will discuss the basic principles of an STM, some details of our STM, and the sample and tip preparation procedures.

3.1 Scanning tunneling microscopy and spectroscopy

The STM uses an atomically sharp tip to probe the sample of interest. The STM was first developed in 1981 by Gerd Binnig and Heinrich Rohrer [14], which later won them the Nobel prize in physics in 1986.

3.1.1 Microscopy

The central part of an STM is the tunnel junction consisting of the sample and the tip, both of which are conducting. They are separated by a very small distance in vacuum (on the order of Ångströms). In a voltage biased measurement, a bias voltage V is applied across the junction and the tunneling current I is measured. The tip positions (in x- y- and z-) are controlled electronically in a precise way using piezoelectric tubes. The structure of the STM unit of the mK-STM is shown in Fig. 3.3.

The tunneling current satisfies [107]

$$I \propto e^{-2kz} \text{ with } k = \frac{\sqrt{2m\phi}}{\hbar}, \tag{3.1}$$

where ϕ is the work function of the surface and z is the distance between the tip and the sample, showing that the tunneling current decays monotonously and exponentially with z.

To image the surface topography, an STM can scan the surface in two modes [107]: the constant current mode, where the tunneling current is kept constant at a setpoint value using a feedback

loop adjusting the vertical position of the tip z which is recorded, and the constant height mode, where the tip height is fixed while the change in the tunneling current is recorded. The first mode is much more common because the second mode works only for very flat surfaces. Since the tunneling current depends exponentially on the tip-sample distance and thus is very sensitive to it, keeping the current constant allows for the detection of surface features with extraordinary precision.

3.1.2 Spectroscopy

Another use of the STM is the so-called scanning tunneling spectroscopy (STS), where the tip is positioned somewhere and the voltage is swept recording the current or the dI/dV signal. The tunneling current in the low conductance regime can be written as [107]

$$I(V) = \frac{4\pi e|t|^2}{\hbar} \int_{-\infty}^{\infty} \rho_t(E_F - eV + \epsilon)\rho_s(E_F + \epsilon)[f(E_F - eV + \epsilon) - f(E_F + \epsilon)]d\epsilon, \quad (3.2)$$

where $f(E) = 1/(1 + e^{\frac{E-E_F}{k_B T}})$ is the Fermi distribution function, E_F is the Fermi energy, $\rho_{s,t}$ are the density of states of the sample and the tip and t is the tunnel hopping term. In the zero temperature limit,

$$I(V) = \frac{4\pi e|t|^2}{\hbar} \int_0^{eV} \rho_t(E_F - eV + \epsilon)\rho_s(E_F + \epsilon)d\epsilon. \quad (3.3)$$

If the tip has a constant density of states in the voltage range of interest,

$$\frac{dI}{dV} \propto \rho_s(E_F + eV), \quad (3.4)$$

which means that the dI/dV is proportional to the sample density of states. This makes the STM an important tool to measure the local density of states on the surface.

In a more general case, especially when the tunnel junction consists of superconductors, the spectra are more complicated due to the existence of the Nambu space (see section 2.5) and the tunneling current needs to be described in the Green's function formalism (see section 2.4.1). The experiments in this thesis mainly concern the tunneling between superconductors (the only exception being the Kondo measurements in Chapter 7 where both the tip and the sample are normal conducting and thus Eq. 3.4 applies), which justifies the detailed discussion of the Green's function formalism in Chapter 2.

3.1.3 Grid spectroscopy

The grid spectroscopy is a powerful extension of STS by combining it with the microscopy capability of the STM. Basically the area of interest is divided into a grid of points, say 100×100 points in an area of $10\,\text{nm} \times 10\,\text{nm}$. Then, the tip scans the surface in the constant current

mode (for example 4 mV at 100 pA setpoint current), recording the surface topography. When it reaches each measurement point (in this example every 0.1 nm), the feedback loop is turned off and a bias spectroscopy measurement is taken, after which the feedback is turned back on and the tip continues to move to the next measurement point. The spatial resolution of the spectroscopy measurement is achieved in this way.

3.2 The millikelvin scanning tunneling microscope

The STM used to acquire the experimental data in this thesis is the mK-STM operating at a base temperature of 10 mK with the capability to apply magnetic fields up to 14 T perpendicular and 0.5 T horizontal to the sample surface, which is located in the Precision Laboratory (PL) of the Max Planck Institute for Solid State Research in Stuttgart.

The construction of the mK-STM and the first measurements on the machine are described in details in the PhD-thesis by Maximilian Assig in 2011[53]. Over the subsequent years, the mK-STM continues to evolve technically especially in the aspect of the energy resolution, which can be seen in the PhD-thesis by Berthold Jäck [108], Matthias Eltschka [109] and Jacob Senkpiel [55]. Without the previous efforts on the technical improvements, the work presented in this thesis would not have been possible.

One milestone among the improvements is the movement of the mK-STM into the PL, an infrastructure that offers world leading acoustic, electromagnetic and seismic isolation required for sensitive STM measurements. The mK-STM sits on the floor of the second level inside a two-story box with 100 dB electromagnetic shielding (Fig. 3.1). The second floor is a 100 t fiberglass reinforced concrete slab floated by twelve air dampers ensuring an extremely low vibration level below 10 nm/s. The discussion of the PL and the benefits it offers to the mK-STM is detailed in the PhD thesis by Jacob Senkpiel [55].

The mK-STM integrates a ^{3}He $-$ ^{4}He dilution refrigerator (DR) to achieve mK temperatures, the mechanism of which will be covered in section 3.2.1. Since the operation of the DR requires continuous pumping which generates detrimental vibrations, the pumps are placed in a separate acoustically shielded room with all pumping lines damped by multiple vibration isolation stages (Fig. 3.1). Apart from mechanical noise, electrical noise is also a decisive factor for the performance, which will be discussed in sections 3.2.2 and 3.2.3.

3.2.1 Achieving millikelvin temperature

The aim for researching refrigeration in the early days was related to the food industry, for example to freeze meat for shipping from the British Dominions on other continents to the United Kingdom. For this purpose, a temperature not far below the freezing temperature of water is sufficient.

Scientifically, however, it is interesting to go lower in temperature and explore the physics
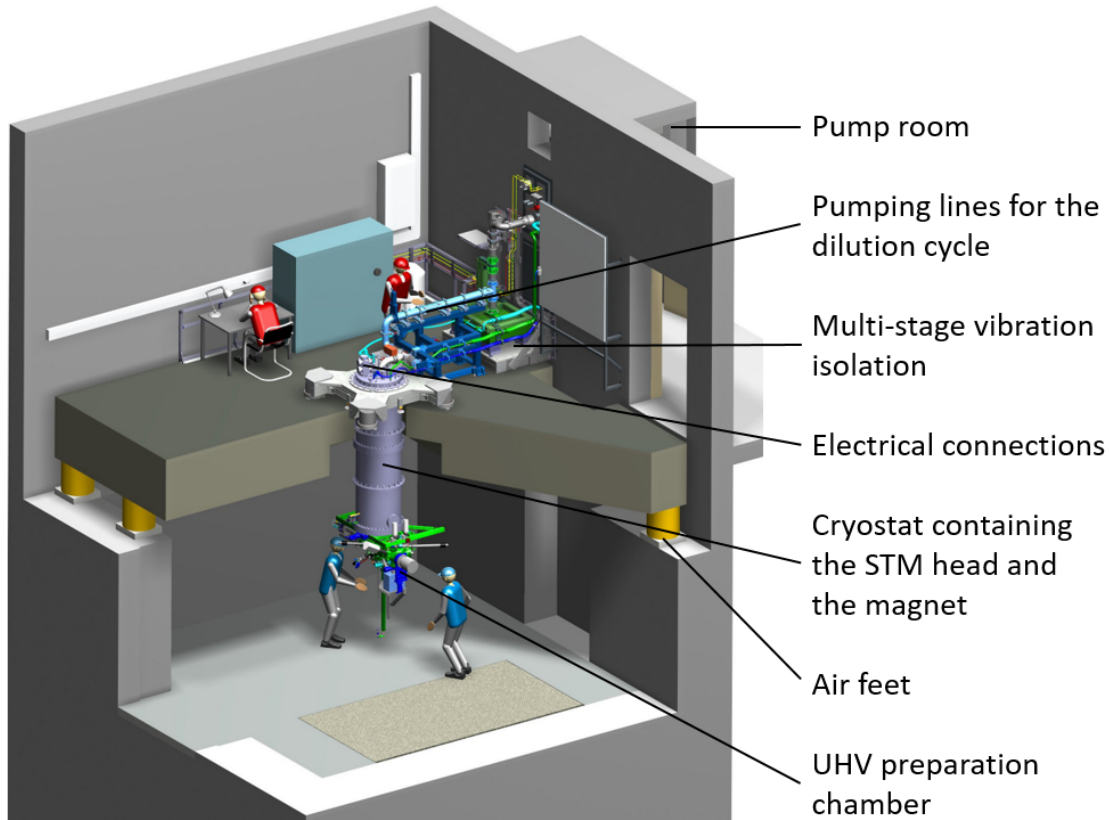
Figure 3.1 – **The mK-STM in the Precision Laboratory.** The mK-STM hangs from the second floor floated by air dampers as a whole. The ultra high vacuum (UHV) preparation chamber at the bottom is capable of surface preparation including sputtering, annealing, atomic/-molecular evaporation and cleaving. The sample is loaded from the bottom into the STM head in the cryostat. The pumping lines and the electrical connections are on the top. The superconducting magnet offers a maximum magnetic field of 14 T perpendicular and 0.5 T parallel to the sample surface. Adapted from [55].

there. Nitrogen was first liquefied ($T = 77\,\mathrm{K}$) in 1883 by two Polish scientists, Karol Olszewski and Zygmunt Wróblewski. In 1908, helium-4 was first liquefied at $T = 4.2\,\mathrm{K}$ by the Dutch scientist Heike Kamerlingh Onnes. He further pumped on a bath of helium-4 and reached $0.83\,\mathrm{K}$ in 1922, opening up the sub-Kelvin era to science [110].

To achieve lower temperature for a bulk material, one can pump on a helium-3 bath ($T = 0.3\,\mathrm{K}$, available since 1950), use $^{3}\mathrm{He} - {}^{4}\mathrm{He}$ dilution refrigeration ($T = 10\,\mathrm{mK}$, available since 1965), or use nuclear magnetic refrigeration ($\mu\mathrm{K}$ range, available since 1956) [110]. The main technology the mK-STM uses to achieve $T = 10\,\mathrm{mK}$ is the $^{3}\mathrm{He} - {}^{4}\mathrm{He}$ dilution, the mechanism of which will be detailed in the following part.
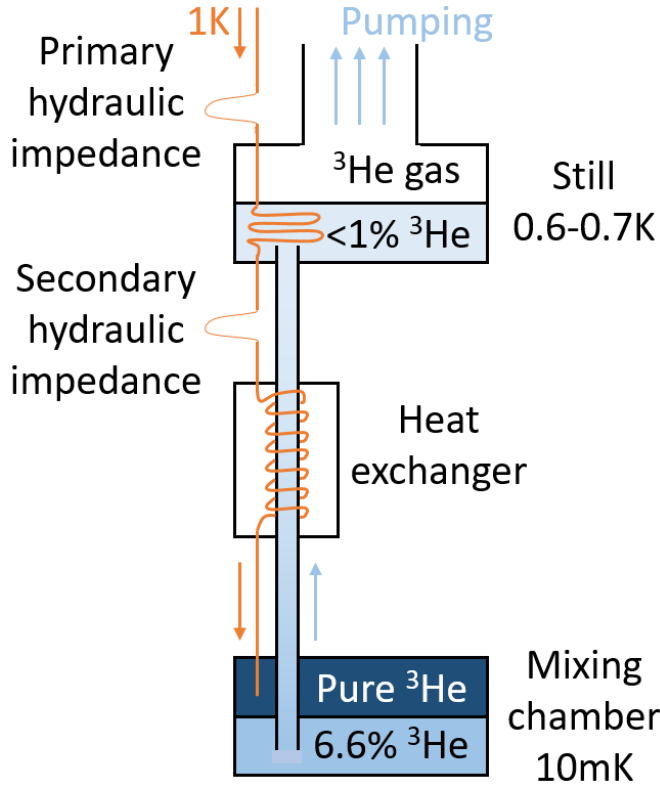
Figure 3.2 – **Schematics of a dilution refrigerator.** In the mixing chamber, the ^{3}He $-$ ^{4}He mixture separates into two phases, the dilute phase at the bottom and the concentrated phase on the top. Moving ^{3}He from the concentrated phase to the dilute phase generates the cooling effect. This is realized by the design of the still which functions as a distillation chamber to evaporate ^{3}He from the dilute phase. The ^{3}He pumped out is resupplied into the concentrated phase via the orange line through multiple thermalization stages for cooling down. For details see Ref. [110].

^{3}He $-$ ^{4}He dilution refrigerator

The schematics of a DR is shown in Fig. 3.2. The main idea is that [110] below 0.87 K, a ^{3}He $-$ ^{4}He mixture with the mole percentage of ^{3}He higher than 6.6% will separate into two phases, the dilute phase and the concentrated phase (with respect to the ^{3}He concentration). When the temperature approaches absolute zero, the dilute phase contains about 6.6% ^{3}He (the finite solubility), while the concentrated phase becomes pure ^{3}He.

Moving ^{3}He from the concentrated phase to the dilute phase will result in the heat of mixing and thus cooling, which happens in the mixing chamber. To achieve this ^{3}He flow direction, we need to pump ^{3}He out from the dilute phase, which is unfortunately the lower part of the liquid due to its higher density (since ^{3}He is lighter than ^{4}He).

Consequently, we need to expose the dilute part for pumping, which happens in the still chamber (Fig. 3.2). One consideration of the still chamber is that the cooling power $\dot{Q}$ is proportional to the ^{3}He flow rate $\dot{n}_3$ (in the unit of moles per second) [110]

$$\dot{Q} = 84\dot{n}_3 T^2 \ \text{[W]}. \tag{3.5}$$

Therefore, the temperature of the still is typically designed to be around $0.6 - 0.7$ K, which is high enough such that there is sufficient vapor pressure of ^{3}He for a reasonable pumping speed, but the vapor pressure of ^{4}He is still low such that the cycled gas is mainly ^{3}He, otherwise any

[4]He will burden the pumping system while not contributing to the cooling process.

For a continuous operation, [3]He pumped out from the still needs to be resupplied to the concentrated phase in the mixing chamber (through the orange line in Fig. 3.2). It will first be precooled in the 1K pot and liquefied through an impedance, then cooled to the still temperature and further cooled to the mK temperature by exchanging heat with the cold outcoming dilute phase of the mixture. Special heat exchangers are carefully designed for this purpose which are extremely important for the performance of a DR, because a major heat load on the mixing chamber comes from the incoming [3]He, which is an essential factor for the lowest temperature a DR can reach [110].

The [3]He circulation rate at $10\,\mathrm{mK}$ base temperature without still heating is around $80\,\mu\mathrm{mol/s}$ for the mK-STM, which gives a cooling power on the order of $1\,\mu\mathrm{W}$ at the base temperature according to Eq. 3.5, typical for a DR [110]. A cooling power on this order requires careful reduction of external heat loads by the inclusion of multiple precooling stages and radiation shutters, which will be discussed in the following part.

Cryostat structure

The cryostat and the STM unit of the mK-STM are shown in Fig. 3.3. The mK-STM contains an outer liquid nitrogen reservoir ($77\,\mathrm{K}$) to reduce the consumption of the liquid helium-4 in the inside reservoir ($4.2\,\mathrm{K}$). The DR is attached below the 1K-pot which is a small liquid helium container (the helium inside is supplied by the main helium reservoir through a needle valve capable of regulating the incoming flow) that is continuously pumped to reach $1\,\mathrm{K}$. The incoming mixture is precooled in the 1K pot which travels further to the DR as shown in Fig. 3.2. The STM head is connected to the mixing chamber allowing for the sample and the tip to be thermalized at $10\,\mathrm{mK}$.

As discussed before, the radiation shutters are important for ultra low temperature applications. Since we transfer the sample from the bottom (Fig. 3.1), we need to cover the holes by rotational shutters for the $77\,\mathrm{K}$ and $4.2\,\mathrm{K}$ stages and a linear shutter for the still temperature stage (Fig. 3.3).

Although the crystal temperature reaches approximately $10\,\mathrm{mK}$ as shown by the thermometers, the electronic temperature measured in experiments may depend on the electrical noise and thus differ. This will be discussed in the next section.

Varying temperature

The mK-STM has two main operation modes. With nearly all the mixture condensed inside the DR, the STM will reach the base temperature of $10\,\mathrm{mK}$. When almost all the mixture is taken out into the dumps (only a tiny amount is left inside the cycle to transfer heat between the 1K pot and the DR), the STM will be at around $1\,\mathrm{K}$.

feedthrough for wires going into the UHV space

liquid nitrogen reservoir

liquid helium reservoir

still pumping line

IVC flange

1K-Pot

still

outer vacuum shell

heat exchangers

mixing chamber

magnet system

link structure

STM unit

shutter feedthroughs

4.2K radiation shutter

77K radiation shutter

UHV flange to experimental chamber

contact plate for electrical connections

coarse-motion

scanning piezo (xyz)

tip

sample

bias contacts

guiding cone for sample transfer

Figure 3.3 – **The cryostat and the STM unit of the mK-STM.** Left: the cryostat of the mK-STM consisting of a liquid nitrogen reservoir on the outside, a liquid helium bath in the inside, and a DR insert in the center. The STM head is attached to the bottom of the DR, labeled by a green dashed box. The electrical connections travel from the STM head upwards through different thermalization stages to the top of the cryostat. The tip and sample are transferred from the bottom, and the openings for the transfer on the shields can be closed by shutters. Right: a zoom-in of the STM head showing the sample facing upwards and the tip facing downwards. The tip can be moved vertically over millimeters by the coarse-motion motor to approach the sample surface. Once in contact, its position (xyz) can be precisely controlled by the scanning piezo-actuators. Taken from [109].

The mixing chamber is equipped with a heater. Temperatures between 10 mK and around 500 mK can be achieved in a continuous manner by supplying current through the heater starting from the 10 mK operation mode. Temperatures around 0.6 K and 0.8 K can be reached by adding a small amount of mixture into the cycle from the 1K operation mode, while temperatures above 1K can be realized by heating up instead.

It is also possible to reach below 10 mK by stopping the incoming ^{3}He supply to the mixing chamber to reduce the heat load. However, this is a single shot operation because the ^{3}He in the mixing chamber will run dry at some point and the cooling stops. In the mK-STM, this operation can lower the temperature to around 6 mK to 7 mK.

3.2.2 Electronic circuit

The schematic of the electronic circuit of the mK-STM is shown in Fig. 3.4 a). The tip is connected to ground through a transimpedance amplifier where the tunneling current through the tip (both DC and AC up to the kilohertz regime) is converted to a voltage subsequently measured by a voltmeter integrated in a Nanonis SPM controller. The sample is biased by a voltage source in a Nanonis SPM controller. Since the phenomena that we are interested in (the superconducting gap, the YSR states and the Kondo peaks) occur in the voltage range of a few mV while the voltage output from a Nanonis SPM controller has the range of ±10 V, it is beneficial to divide the voltage by a factor of 100 such that the range reduces to ±100 mV and the resolution is greatly improved. This is especially important for measuring the Josephson effect which requires a resolution of a few µV. The filtering will be discussed in section 3.2.3.

To measure $I(V)$, the voltage is swept slowly in the range of interest and the current is recorded. To obtain the dI/dV, we can not only differentiate the $I(V)$ curve but also use the lock-in technique, which gives an improved signal to noise ratio.

For a lock-in measurement, we modulate the bias voltage V_0 by a small sinusoidal component with a certain reference frequency on top such that $V = V_0 + V_{ac} \sin \omega t$, and detect the response in the current at the same frequency. The current, expanded in the Taylor series, is

$$I(V_0 + V_{ac} \sin \omega t) \approx I(V_0) + \frac{dI}{dV} V_{ac} \sin \omega t + \frac{1}{2} \frac{d^2 I}{dV^2} V_{ac}^2 \sin^2 \omega t + \cdots, \qquad (3.6)$$

where the first harmonic term corresponds to dI/dV while the second harmonic is proportional to the second derivative of the current.

3.2.3 Energy resolution

In reality, both $I(V)$ and dI/dV are broadened by the voltage noise of various origins, and thus there is a limit of the sharpness of the spectroscopic features that can be detected by an STM, called the energy resolution. Reliably measuring the energy resolution of an STM at ultra low temperature, however, is non-trivial, because few processes offer extremely sharp features

in the spectrum.

Measuring the energy resolution
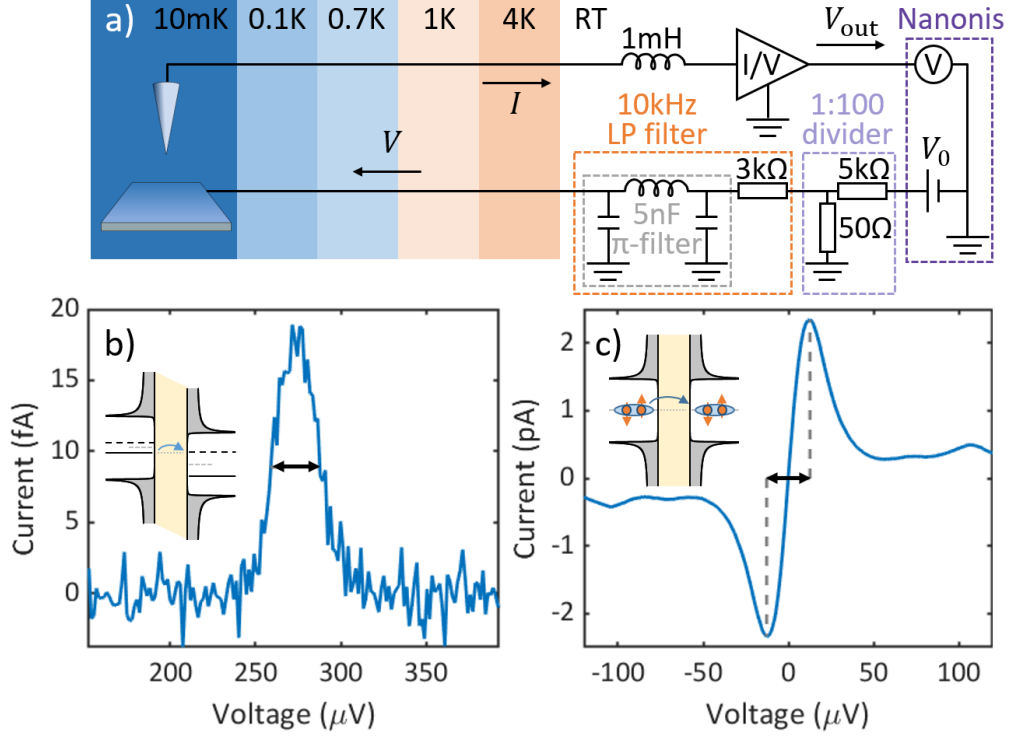
Figure 3.4 – **Electronic circuit and the energy resolution.** a) The electronic circuit of the mK-STM. The current line is filtered by an 1 mH inductor and the tunneling current I is converted to a voltage V_{out} by a transimpedance amplifier which is subsequently measured by a Nanonis SPM controller. The bias voltage V_0 supplied by a Nanonis SPM controller is first divided by a $1:100$ divider ($V \approx V_0/100$ but the exact ratio depends on the resistors) and then filtered by a 10 kHz low pass (LP) filter before going into the cryostat. b) The Shiba-Shiba tunneling process (the tunneling between two YSR states) at low conductance features a sharp peak in the current whose width (the black arrow) is a direct measurement of the energy resolution. The energy diagram is shown in the inset showing the tunneling between two discrete levels protected by the gap. c) The Josephson effect, the tunneling of Cooper pairs (see inset), offers an alternative to quantifying the energy resolution. The distance between the two peaks is a measure of the energy resolution (the black arrow).

One possibility is to measure the $I(V)$ curve of the Shiba-Shiba tunneling which is the tunneling between two YSR states. The YSR states are quasiparticle levels protected by the superconducting gap, and thus the Shiba-Shiba tunneling is the transition between two discrete levels (the inset of Fig. 3.4 b)). Usually the intrinsic width is negligible due to long lifetime of the YSR states, and thus the lineshape in the low conductance regime (where the tunnel broadening is negligible) directly reflects the $P(E)$ function and thus the energy resolution of the machine through the full width at half maximum (FWHM), shown in Fig. 3.4 b). At

10 mK in the mK-STM, a typical FWHM of the Shiba-Shiba current peak is around 27 μV. The Shiba-Shiba tunneling will be discussed in detail in Chapter 8.

Although Shiba-Shiba tunneling directly measures the energy resolution function (the broadening of a δ function like peak), the preparation of a Shiba-Shiba junction is non-trivial. Consequently, as an alternative, the Josephson effect is more often used to characterize the energy resolution because it only requires two clean superconductors. The reason why the Josephson effect can be used as a measure for the energy resolution is that the $I(V)$ curve of the Josephson measurement is the asymmetry of the $P(E)$ function as shown in Eq. 2.76 and thus reflects the energy resolution of the system. Usually, the distance between the positive and negative peaks in the voltage axis is a good quantitative indicator of the energy resolution (Fig. 3.4 c)). At 10 mK in the mK-STM, this value is usually around 24 μV independent of the superconducting material.

Noise sources

Part of the noise comes from inside the tunnel junction and is called the *internal noise.* One example is the capacitive noise in the $P(E)$ function, as discussed in section 2.4.2. To reduce the capacitive noise, we can increase the junction capacitance by using thicker tips [95].

Another category of noise is the *external noise*, which comes from outside of the tunnel junction. For example, if the voltage source contains noise resulting in an slight oscillation of the bias voltage near the setpoint (similar to a large lock-in modulation), the measurement will be broadened. Another possibility is that the cables may not be perfectly shielded and pick up radio-frequency signals from outside. In addition, a fluctuating ground or the presence of ground loops may also deteriorate the energy resolution.

Reducing the external noise

To reduce the external noise, several measures have been taken on the mK-STM. First, all wires are grounded on the same copper plate whenever possible. The preparation chamber and the pumping lines are electrically isolated from the cryostat, avoiding ground loops. Second, both the bias voltage line and the current line are shielded all the way to the STM junction. In addition, all electronic lines pass through low-pass filters before going inside the cryostat (Fig. 3.4 a)). The bias voltage line is filtered by a 10 kHz low pass (LP) filter consisting of a π-filter and a 3 kΩ resistor to lower the cutoff frequency. The filter for the current line, however, cannot contain capacitors due to the property of the amplifier in use, and thus a 1 mH inductor is used. Apart from the cabling and the filters, the infrastructure in the PL including the 100 dB electromagnetic shielding of the measurement box and the separate grounding for each box provides an excellent basis for a low noise environment.
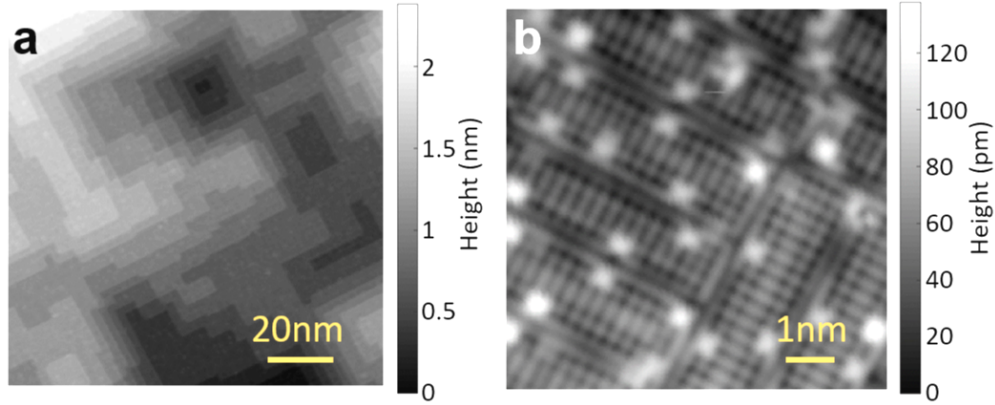
Figure 3.5 – **The V(100) surface visualized by the STM.** a) The V(100) surface imaged with 50 mV, 50 pA conditions revealing the atomic terraces. b) Atomically resolved (5 × 1) reconstructions under 4 mV, 1 nA imaging conditions. The bright spots are possible oxygen vacancies. Taken from [114].

3.3 Sample and tip preparation

The material used in this thesis is vanadium: V(100) as the sample and vanadium wire as the tip. In the following parts, we will discuss the basic procedure for sample and tip preparations.

3.3.1 V(100) sample preparation

The V(100) sample is a single crystal with > 99.99% purity. It is prepared by standard sputter-anneal cycles for metals, which involves multiple cycles of argon sputtering at around 1 keV and annealing at around 700°C.

The V(100) surface is very difficult to clean, free of foreign elements. This is because at different annealing temperatures, different impurities diffuse to the surface, from carbon at low temperatures (around $200-400$°C), oxygen at intermediate temperatures (around $400-800$°C which contains the annealing temperature we choose) to phosphorus and sulfur at high temperatures (approximately above 800°C) [111]. Therefore, after our preparation procedure, the surface is typically covered with a layer of oxygen resulting in (5 × 1) superstructure which comes from the segregation of oxygen from the bulk during annealing [111–113].

The resulting surface is typically like Fig. 3.5 a) and Fig. 3.6 a) featuring rectangular atomic terraces characteristic of a single crystal of (100) orientation. A zoom-in to the atomic features reveal the (5 × 1) reconstructions shown in Fig. 3.5 b).

On the surface, the most abundant impurities visible are the slight protrusions at 4 mV scanning voltage that may come from oxygen vacancies [115, 116]. This is because electronegative elements like oxygen or carbon usually deplete the density of states nearby therefore appearing dark in the STM topography and thus the vacancies show up as bright spots [117]. A typical

concentration of such impurities observed is around 4% of a monolayer (ML), although this largely depends on the sample preparation procedure.

Another kind of impurity that can also be abundant is carbon due to diffusion during the slow cooling process after annealing [116]. Unfortunately, carbon substitution for the oxygen is largely invisible in the STM because the contrast in the apparent height is small [115]. However, a closer look at Fig. 3.5 b) reveals other variations of the (5×1) reconstruction including the (4×1) and (6×1) reconstructions, which indicates a changing chemical environment suggesting the existence of a non-uniform carbon concentration [118].

Below $T_c = 5.4\,\text{K}$, vanadium becomes a type-II Bardeen-Cooper-Schrieffer (BCS) superconductor exhibiting an order parameter around $\Delta = 750 \pm 10\,\mu\text{eV}$. Here, $2\Delta/(k_B T_c)$ is around 3.22, close to but slightly smaller than the predicted value of 3.528 in the BCS theory, which may be due to the influence of the vanadium surface layer in the tunnel junction [119]. Better agreement has been observed via bulk sensitive methods for measuring the gap [120]. Apart from this, the above surface features (the surface reconstructions, the oxygen vacancies and carbon impurities) usually have little effect on the superconductivity because of the long coherence length, but there is a sparse distribution of intrinsic magnetic defects on the surface that generates YSR states.

To find the intrinsic impurities, spectroscopy measurements are done point by point (grid spectroscopy) in the area of interest. The current inside the gap reveals the YSR states: normally it should be zero for a clean gap at low conductance, and if an in-gap state exists, the current will be non-zero (Fig. 3.6 b)). A typical topography of a YSR impurity is shown in Fig. 3.6 d) marked by the yellow circle, while the other protrusions in the view are possible oxygen vacancies. We find a concentration of such YSR impurities to be around 0.02%-0.05% ML, which is possibly an overestimate due to the spatial extension of the YSR states and thus the inclusion of the sub-surface YSR states. The concentration is also expected to depend on the sample preparation procedures. Nevertheless, the YSR impurities are much less common than the oxygen vacancies, indicating that most of the oxygen vacancies (or the carbon atoms whose concentration should also be much higher) do not generate YSR states.

The intrinsic YSR impurities probably also do not originate from transition metal elements which should be even less common in the crystal. In addition, many intrinsic YSR impurities only contain one pair of YSR states inside the gap and transition metal ions usually exhibit high spins resulting in multiple pairs of YSR states. Instead, the intrinsic YSR impurities may originate from some combinations of simple elements like oxygen and carbon which features a spin, but the exact origin still calls for further research.

Despite their unclear origin, the intrinsic YSR impurities offer several advantages. First, many of them exhibit only one pair of YSR state inside the gap, simplifying the analysis of the spectra especially in the Shiba-Shiba tunneling case (see Chapter 8). In addition, the YSR energy spans the whole gap (Fig. 3.6 e)) (other properties as well, including the YSR asymmetry and intensity), making it possible to search for YSR states with desired properties.
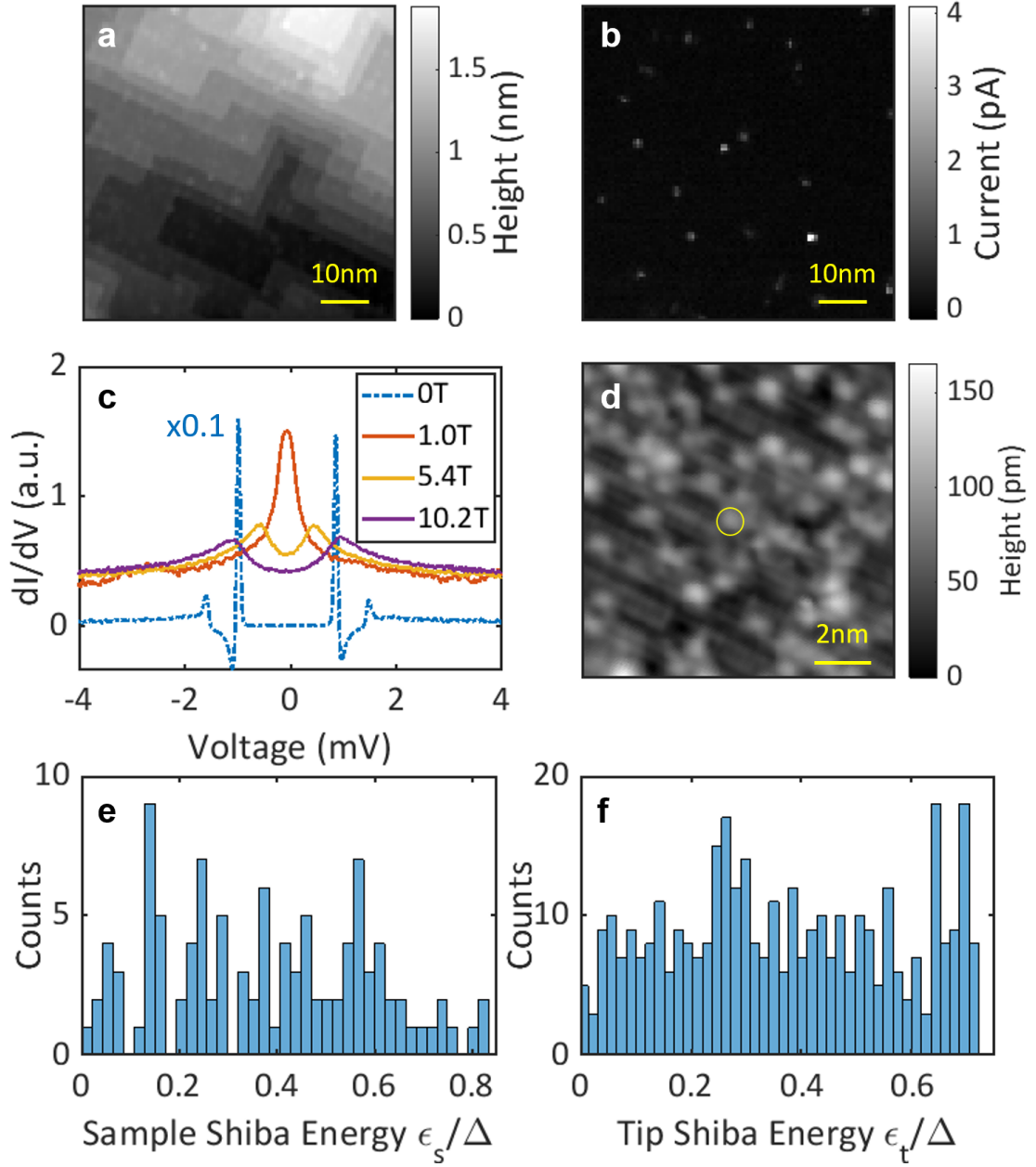
Figure 3.6 – **Intrinsic YSR impurities on the V(100) surface and on the vanadium tip.** a) The surface topography of V(100) imaged at 4 mV, 10 pA. b) The current at 1.42 mV just inside the gap ($2\Delta = 1.5$ meV) from a grid spectroscopy measurement in the same area as a), revealing the intrinsic YSR states as bright spots. c) The spectra of a YSR tip under the magnetic field, showing in-gap states at the zero field and split Kondo peaks at high fields. d) The atomically resolved topography of an intrinsic YSR impurity (labeled by the circle) on the surface. e),f) The histogram of the energy distribution of the intrinsic YSR impurities on the sample (e)) and the YSR tips (f)). Taken from [114].

3.3.2 Vanadium tip preparation

The tip is cut in air mechanically from polycrystalline vanadium wire of 99.8% purity, which is further cleaned in UHV by argon sputtering. The tip is then prepared *in situ* on the V(100) surface by field emission (42 V, $10 - 30\,\mu A$) to obtain a reasonably large superconducting gap. Standard tip shaping techniques like dipping and bias pulsing are used subsequently (still on the V(100) surface) to obtain the desired spectra and to achieve atomic resolution.

During tip shaping (moderate dipping and pulsing), sometimes the tip picks up a YSR state (see the 0 T spectrum in Fig. 3.6 c)), which we call a YSR tip. The tip YSR states usually only have one pair of YSR states inside the gap, and the Kondo measurements shown in Fig. 3.6 c) suggest that they are spin-½ impurities (for details see Chapter 7).

The energy distribution of the YSR state on the tip is shown in Fig. 3.6 f), similarly widespread as the intrinsic impurities on the sample (Fig. 3.6 e)), indicating a similar origin. Nevertheless, the exact origin of the YSR tip is also unknown, possibly coming from oxygen or carbon atoms picked up from the surface forming a special structure.

To facilitate the fabrication of a YSR tip, we have written a LabVIEW program to automate the process. Basically the tip is first dipped/pulsed at one spot on the surface and a spectrum is measured at a clean spot to check the existence of in-gap states. This process is automatically repeated until a YSR tip of desired properties (energy, asymmetry, intensity, number of YSR states and even stability) is successfully obtained. This is a random process but turns out to be efficient and highly reliable. This procedure makes the YSR tips more flexible than the intrinsic sample YSR impurities, and the YSR states on the tip can be more stable especially at high conductance. Therefore, for the experiments concerning only single YSR state, we can also use tip YSR state which may seem unconventional compared to the literature but is actually the same as if the YSR state is on the sample. Another feature of the YSR tip is the possibility to fabricate a tip with a YSR state tunable across the QPT during tip approach, shown in Chapters 4, 5, 6 and 7.

YSR-STM

A YSR tip has far reaching consequences more than just reversing the junction and measuring the YSR state on the tip rather than on the sample. With this technique, we can move the YSR state to any object of interest on the sample and probe the tunneling from the YSR state to the object. Consequently, the YSR tip, a novel tip functionalized with a sharp discrete level, opens many new possibilities, and we call the STM featuring a YSR tip the YSR-STM.

One application of the YSR-STM is Shiba-Shiba tunneling, where we move the YSR tip onto one YSR impurity on the surface and study the tunneling between the YSR states, which will be discussed in detail in Chapter 8. We will show that it allows for the determination of the YSR lifetimes, and by extension, the lifetime of other single levels such as the Majorana bound states if they are probed by the YSR tip (see Chapter 9 for more discussion).

4 Quantum phase transitions and the role of impurity-substrate coupling in Yu-Shiba-Rusinov states[1]

4.1 Introduction

As discussed in Chapter 2, the energy of a YSR state ϵ_{YSR} depends on the coupling between the impurity and the superconducting substrate such that ϵ_{YSR} varies from the gap edge Δ to zero and then back to the gap edge when the coupling increases continuously. The relevant parameter for the coupling in the Kondo impurity model is the exchange coupling J (Eq. 2.21 and Fig. 2.5 d)), and it is the impurity-substrate coupling Γ in the SIAM (Fig. 2.11 a)). While both descriptions are largely equivalent ($J \propto \Gamma$, recall the Schrieffer–Wolff transformation in Eq. 2.33), Γ has a more intuitive aspect as it is directly related to the wavefunction overlap and thus the hybridization or hopping between the impurity and the substrate. As a thought experiment, if we push the impurity towards the substrate from the equilibrium position, Γ will increase, while if we pull the impurity away, Γ will decrease. Consequently, we adopt the SIAM in our analysis.

Although such dependency of ϵ_{YSR} on Γ (or J) has been proposed theoretically already in the 1960s [1–3], tuning Γ continuously to examine such dependency experimentally turns out to be challenging. This has first been realized in asymmetric S-QD-N junctions [121–123] with a quantum dot (QD) sandwiched between a superconductor (S) and a normal metal (N) with the quantum dot strongly coupled to the superconductor, generating the YSR states. The coupling Γ can be tuned by backgating continuously.

One step further would be to realize that in atomic junctions using the STM, which usually provides cleaner superconducting gaps and spectroscopic features compared to quantum dot systems. However, tuning Γ is non-trivial because usually there is no local gating available in the STM, and thus it has only been shown fairly recently [21, 23, 25, 28, 35, 124]. The suggested mechanism is similar for different systems, that when approaching the STM tip to the impurity on the surface (and thus increasing the conductance), the atomic force exerted by the tip on the impurity changes continuously, approximated as the Lennard-Jones force

---

[1]This chapter is based on the publication #8 from the publication list.

[21]. The force is initially attractive and increases upon approaching, pulling the impurity away from the substrate, resulting in a decreasing Γ. When the tip sample distance decreases further, the force eventually becomes repulsive and pushes the impurity back towards the substrate, resulting in an increasing Γ. When the impurity is magnetic and the substrate is superconducting, changing Γ will result in a continuous evolution of ϵ_{YSR} visible in the tunneling spectra.

We have observed such moving YSR states in many of the intrinsic impurities on V(100) surface as well as the YSR functionalized vanadium tip (Fig. 4.2 (a) and Fig. 4.5 (a)). Both tip and sample are made of superconducting vanadium, and the order parameters are approximately the same $\Delta_t = \Delta_s = 750\,\mu eV$. Consequently, the junction is in the YSR-BCS tunneling scenario (see section 2.5.1). The experimental temperature is $10\,mK$, and thus the thermal processes at $eV = \pm(\Delta_t - \epsilon_s)$ are absent (assuming that ϵ_s is not too close to zero).

Apart from the movement of the YSR states upon tip approach, we also observe that the normal state transmission deviates from the simple exponential dependency on the tip sample distance (Fig. 4.3), also indicating a change of the impurity substrate coupling Γ. In this chapter, we will employ the SIAM in the mean field approximation to unify both observations on a quantitative level.

4.2   The SIAM in the mean field approximation

The SIAM can be fully solved numerically by the NRG theory (see section 2.3.3), but in order to get an analytic formula for fitting the experimental data, we adopt the mean field approximation [125] neglecting correlations, which is largely equivalent to the classical Shiba model [2, 71] (see Figs. 4.1 a,b) and section 2.3.1). It is usually sufficient unless Kondo related phenomena are involved in the spectra (discussion see last part of section 2.3.3), which will be investigated in Chapter 7.

We rewrite the Anderson Hamiltonian $H_{\text{imp}} = \epsilon_d n + U n_\uparrow n_\downarrow$ (Eq. 2.32) using the mean field approximation

$$
\begin{aligned}
H_{\text{imp}} &= \epsilon_d (n_\uparrow + n_\downarrow) + U(\langle n_\uparrow \rangle n_\downarrow + n_\uparrow \langle n_\downarrow \rangle) \\
&= (\epsilon_d + U \langle n_\uparrow \rangle) n_\downarrow + (\epsilon_d + U \langle n_\downarrow \rangle) n_\uparrow \\
&= (E_U + E_J) n_\downarrow + (E_U - E_J) n_\uparrow.
\end{aligned}
\tag{4.1}
$$

Here, E_J and E_U denote the level splitting and the level offset instead of the original ϵ_d and U in the SIAM, while Γ_s remains the same definition as the coupling strength in the SIAM (Fig. 4.1 c)) and Δ_s is the superconducting order parameter. Without losing generality, we assume
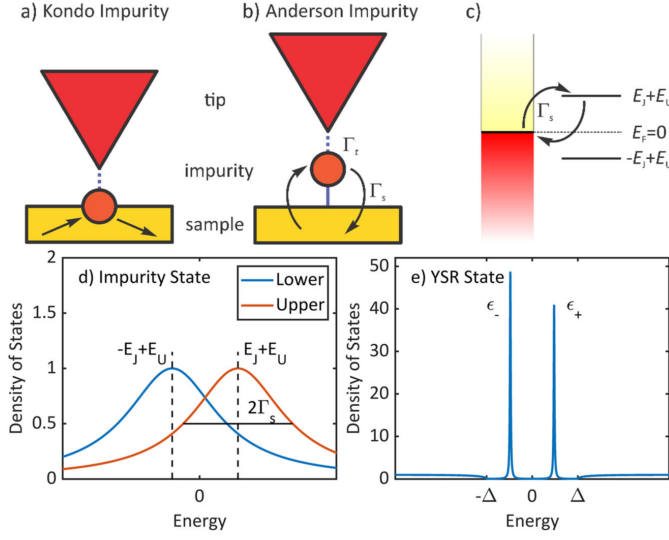
Figure 4.1 – **The SIAM in the mean field approximation.** a) The Kondo impurity model treats the interaction between the impurity and the substrate as a scattering process. b) In the SIAM, the hopping Γ_s couples the impurity to the substrate. c) The energy diagram of the SIAM in the mean field approximation showing impurity levels at $E_U \pm E_J$. d) The density of states of the SIAM without superconductivity showing the impurity levels broadening by Γ_s. e) The SIAM with superconductivity generates a pair of YSR states inside the gap. Taken from Ref. [28].

$E_J \geq 0$. The resulting Green's function at the impurity site in 4×4 Nambu space is [126]

$$g_{\text{SIAM}}^{\text{YSR}}(\omega) = \begin{pmatrix} g_{\uparrow\uparrow}(\omega) & 0 \\ 0 & g_{\downarrow\downarrow}(\omega) \end{pmatrix}, \tag{4.2}$$

with

$$g_{\sigma\sigma}(\omega) = \frac{1}{D_\sigma(\omega)} \begin{pmatrix} \omega\Gamma_s + (\omega + E_U - E_{J\sigma})\sqrt{\Delta_s^2 - \omega^2} & \Gamma_s\Delta_s \\ \Gamma_s\Delta_s & \omega\Gamma_s + (\omega - E_U - E_{J\sigma})\sqrt{\Delta_s^2 - \omega^2} \end{pmatrix},$$

$$D_\sigma(\omega) = 2\Gamma_s\omega(\omega - E_{J\sigma}) + [(\omega - E_{J\sigma})^2 - E_U^2 - \Gamma_s^2]\sqrt{\Delta_s^2 - \omega^2},$$

$$E_{J\uparrow} = E_J, E_{J\downarrow} = -E_J. \tag{4.3}$$

This Green's function is block diagonalized into two 2×2 matrices and it is in principle sufficient to study only $g_{\uparrow\uparrow}$, for example. Nevertheless, we will stay in the 4×4 space in the following discussion.

The total density of states at the impurity site is

$$\rho(\omega) = \rho_\uparrow(\omega) + \rho_\downarrow(\omega), \tag{4.4}$$

where $\rho_\sigma(\omega) = \frac{1}{\pi}\text{Im}(\frac{\omega\Gamma_s + (\omega + E_U - E_{J\sigma})\sqrt{\Delta_s^2 - \omega^2}}{D_\sigma(\omega)})$, $\omega \to \omega - i\eta_s$ and η_s is a small positive number.

Eq. 4.2 is slightly more complicated than Eq. 2.20 that it generates a pair of broad impurity peaks at $\omega = E_J + E_U$ and $\omega = -E_J + E_U$ (Fig. 4.1 d)) besides the YSR states (Fig. 4.1 e)).

To obtain the YSR energy, we further limit ourselves to $\Delta_s \ll E_J$. Since the YSR state is inside the gap, we want to find the pole of the Green's function satisfying $|\omega| \leq \Delta_s \ll E_J$. Therefore,

the YSR energy is the solution of the approximate equation $D_\sigma(\omega) \approx 2\Gamma_s\omega(\mp E_J) + [E_J^2 - E_U^2 - \Gamma_s^2]\sqrt{\Delta_s^2 - \omega^2} = 0$, which yields

$$\epsilon_\pm = \pm\Delta_s \frac{E_J^2 - \Gamma_s^2 - E_U^2}{\sqrt{\left(\Gamma_s^2 + (E_J - E_U)^2\right)\left(\Gamma_s^2 + (E_J + E_U)^2\right)}}. \tag{4.5}$$

In the following, we assume electron-hole symmetry ($E_U = 0$) for simplicity, and then the equation is further simplified to

$$\epsilon_\pm = \pm\Delta_s \frac{E_J^2 - \Gamma_s^2}{E_J^2 + \Gamma_s^2} = \pm\Delta_s \frac{1 - \tilde{\Gamma}_s^2}{1 + \tilde{\Gamma}_s^2}, \tag{4.6}$$

with the scaled coupling being $\tilde{\Gamma}_s = \frac{\Gamma_s}{E_J}$ similar to a Schrieffer–Wolff-like transformation. The result is the same as Eq. 2.21 for the $\beta = 0$ case, showing the similarity between the two mean field models.

It is clear that ϵ_{YSR} only depends on $\tilde{\Gamma}_s$. Nevertheless, since the YSR energy has two solutions (plus and minus sign), there are two possibilities to convert the YSR energy to the scaled coupling

$$\tilde{\Gamma}_s = \frac{\sqrt{1 - \epsilon_+/\Delta_s}}{\sqrt{1 + \epsilon_+/\Delta_s}}, \tilde{\Gamma}_s^{\text{alt}} = \frac{\sqrt{1 + \epsilon_+/\Delta_s}}{\sqrt{1 - \epsilon_+/\Delta_s}}. \tag{4.7}$$

In Figs. 4.2 b) and c), we show one example of converting the YSR energy extracted from the measured spectra to $\tilde{\Gamma}_s$. In one case, the scaled coupling increases with decreasing z while in another case, the scaled coupling decreases.

As a technical side note, since in the dI/dV spectra, the YSR-BCS tunneling peaks are at $eV = \pm(\epsilon + \Delta)$, we need to subtract Δ to get the YSR energy. If the YSR state is on the tip, we need to subtract the sample $\Delta_s = 750\,\mu\text{eV}$. If the YSR state is on the sample, we need to subtract the tip Δ_t, which can be calculated from the coherence peak positions at $eV = \pm(\Delta_s + \Delta_t)$ given that $\Delta_s = 750\,\mu\text{eV}$.

The conversion from ϵ_s to $\tilde{\Gamma}_s$ is based on the simple mean field model neglecting correlation effects, which may not hold in experiments *a priori*. To verify this and also to remove the ambiguity of the two branches, we need to add independent information about the dependency of the normal state transmission τ on the tip sample distance z.

4.2.1 Junction transmission τ in the SIAM

First, we need to write the transmission τ in terms of the SIAM parameters. The transmission is measured at voltages much larger than the superconducting gap and thus the influence of the spectral features inside the gap can be ignored. In that case, τ is energy independent
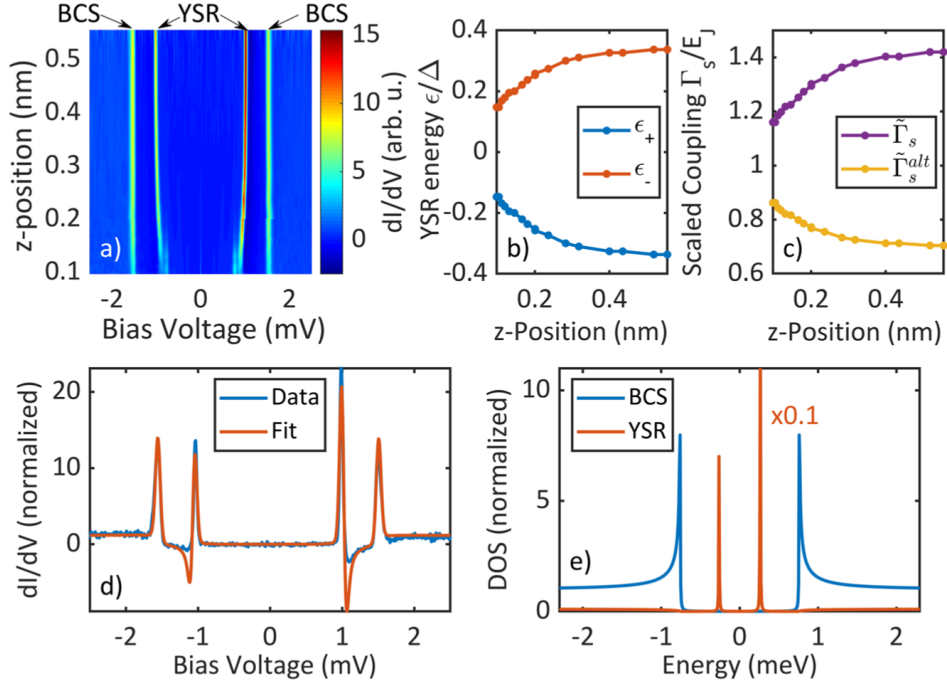
Figure 4.2 – **Properties of the dI/dV spectra during tip approach.** a) The color plot of a stack of dI/dV spectra with varying z (or transmission). The pair of bright peaks in the middle are the YSR-BCS tunneling peaks at $eV = \pm|\Delta_t + \epsilon_s|$, from which we extract the YSR energy. The pair of peaks outside are the coherence peaks at $eV = \pm|\Delta_t + \Delta_s|$. At small z, more peaks emerge which are Andreev reflections (discussed in Chapter 5). b) The YSR energy extracted from a). c) The scaled coupling $\tilde{\Gamma}_s$ calculated from the YSR energy via Eq. 4.7. There are two branches, one with decreasing $\tilde{\Gamma}_s$ when decreasing z and the other the opposite. d) A fit of the dI/dV spectrum at low conductance assuming two channels (one BCS and one YSR channel). The contribution of each channel is plotted in e). Taken from Ref. [28].

[91, 92]

$$\tau = \frac{4\pi^2 t_{ti}^2 n_i n_t}{|1 - t_{ti}^2 g_i g_t|^2}, \tag{4.8}$$

where t_{ti} is the hopping between the impurity and the other electrode, and $n_{i,t}, g_{i,t}$ are the density of states and the Green's function of the impurity and of the other electrode, respectively.

Here, g_i is the diagonal term in Eq. 4.2 in the limit $\Delta_s \ll |\omega| \ll E_J$ and since $E_U = 0$, $g_{i\sigma} = \frac{E_{J\sigma} + i\Gamma_s}{\Gamma_s^2 + E_{J\sigma}^2}$, and the density of states $n_i = \frac{1}{\pi}\text{Im}(g_i) = \frac{1}{\pi}\frac{\Gamma_s}{\Gamma_s^2 + E_J^2}$. For the tip electrode, we have $g_t = i\pi n_t$ with n_t being a number. Defining $\Gamma_t = \pi t_{ti}^2 n_t$ and considering $\Gamma_s \gg \Gamma_t$, we have

$$\tau_{\text{YSR}} = \frac{4\Gamma_s \Gamma_t}{(\Gamma_s + \Gamma_t)^2 + E_J^2}. \tag{4.9}$$

The more general formula for $E_U \neq 0$ is shown in Eq. 6.4. For a junction without the impurity,

$$\tau_{\mathrm{BCS}} = \frac{4\Gamma_s\Gamma_t}{(\Gamma_s + \Gamma_t)^2}. \tag{4.10}$$

4.3 Fitting the dI/dV spectra using two channels

In the measured dI/dV spectra shown in Fig. 4.2 (d) and Fig. 4.4 (a), the intensities of the coherence peaks at $eV = \pm|\Delta_s + \Delta_t|$ are significant, contrary to the theory prediction assuming only the YSR channel in the tunneling (c.f. Fig. 2.15). To explain the spectra, we need to assume a second independent channel through a clean superconducting gap, called the BCS channel, which gives rise to the coherence peaks. The relative contribution from the YSR channel is denoted by the parameter p, which can be obtained from fitting the quasiparticle tunneling spectrum at low transmission. In Fig. 4.2 d), $p = 22\%$ and the contributions from the two channels are plotted separately in Fig. 4.2 e).

Consequently, the total transmission is a weighted sum of the transmission of the two channels

$$\tau = p\overbrace{\frac{4\Gamma_s\Gamma_t}{(\Gamma_s + \Gamma_t)^2 + E_J^2}}^{\tau_{\mathrm{YSR}}} + (1-p)\overbrace{\frac{4\Gamma_s\Gamma_t}{(\Gamma_s + \Gamma_t)^2}}^{\tau_{\mathrm{BCS}}}, \tag{4.11}$$

$$\Gamma_t = \Gamma_{t0}\exp[-(z - z_0)/z_1], \tag{4.12}$$

where the tunnel coupling Γ_t depends exponentially on the tip sample distance z with Γ_{t0}, z_0 and z_1 being parameters. Since z_0 can be absorbed into Γ_{t0}, there are only two free parameters here (Γ_{t0} and z_1), which can be determined through the $\tau(z)$ measurement when the tip is far from the surface such that the atomic force is negligible where the YSR state does not move.

Similar as in the case for Γ_s, we also scale Γ_t with respect to E_J

$$\tilde{\Gamma}_t = \frac{\Gamma_t}{E_J}, \tilde{\Gamma}_{t0} = \frac{\Gamma_{t0}}{E_J}. \tag{4.13}$$

Consequently, $\tau(z)$ depends on $p, \tilde{\Gamma}_s, \tilde{\Gamma}_{t0}, z_1$ and z, and the only parameter besides z that depends on z is $\tilde{\Gamma}_s$ due to the varying atomic force on the impurity. Remember that $\tilde{\Gamma}_{t0}$ and z_1 can be fitted from the $\tau(z)$ curve at large tip sample distance and $\tilde{\Gamma}_s$ can be extracted from the YSR energy (Eq. 4.7), there is no free parameter left.

One important observation on Eq. 4.11 is that the transmission τ is roughly inversely proportional to Γ_s, so decreasing Γ_s will increase τ. This may be a bit counter-intuitive, but consider only the case of τ_{BCS} (Eq. 4.10), Γ_s needs to decrease to Γ_t to increase the transmission to one.
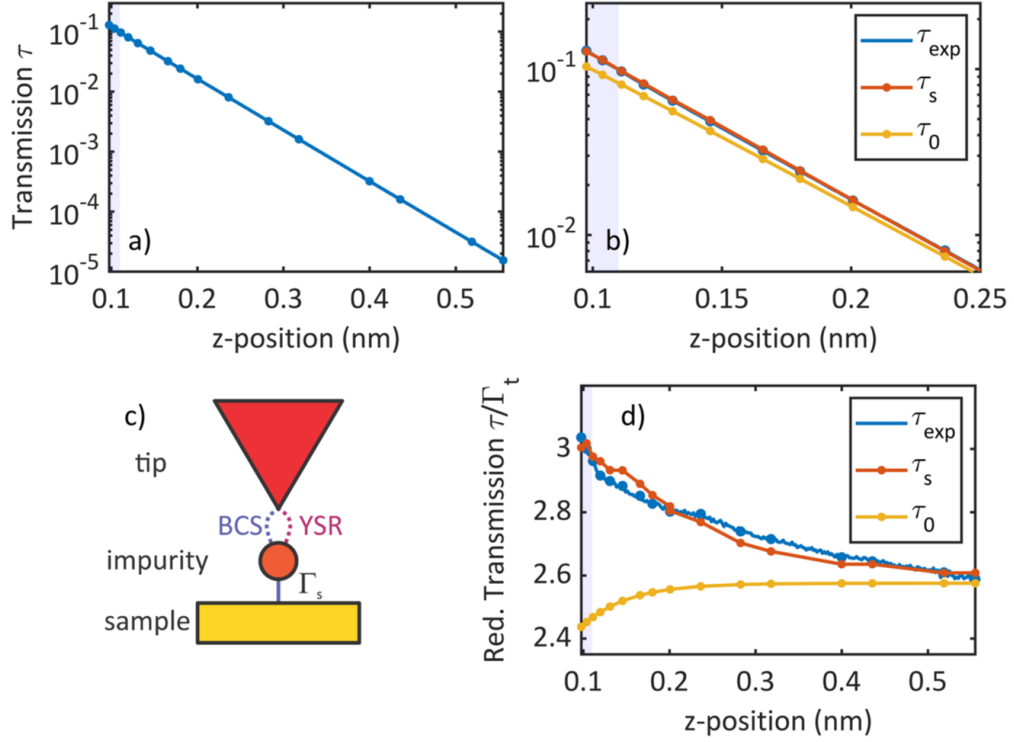
Figure 4.3 – **The dependence of the transmission τ on z.** Same YSR impurity as in Fig. 4.2. a) Measured normal state transmission τ_{exp} shows a general exponential dependency on z. b) A zoom-in to the high conductance regime reveals deviations from the expected τ_0 assuming a constant $\tilde{\Gamma}_s$. If we use the purple branch of the $\tilde{\Gamma}_s$ extracted from the YSR energy in Fig. 4.2 c), the calculated τ_s agrees with the experiment very well. c) The schematics of the two channel model. d) Eliminating the general exponential dependence of the transmission on z by dividing the transmission by $\tilde{\Gamma}_t$. The excellent agreement between τ_{exp} and τ_s is more obvious to see. Taken from Ref. [28].

4.4 Consistency between τ and ϵ_{YSR} through the SIAM

4.4.1 Review of the data analysis procedure

Before starting to show different examples, we would like to summarize the analysis procedure first for clarity. In the experiment, we measure the dependence of the YSR energy ϵ_{YSR} and the normal state transmission τ (at 4mV) on the tip sample distance z (z is a relative value).

For the analysis, we first convert ϵ_{YSR} to $\tilde{\Gamma}_s$ via Eq. 4.7. There will be two branches, one corresponding to increasing $\tilde{\Gamma}_s$ with tip approach while the other suggests decreasing $\tilde{\Gamma}_s$ with tip approach. To determine which branch is correct, we compare the experimental $\tau_{exp}(z)$ curve with the one assuming constant $\tilde{\Gamma}_s$ which is τ_0. If $\tau_{exp}(z) > \tau_0$, it means that $\tilde{\Gamma}_s$ decreases, and if $\tau_{exp}(z) < \tau_0$, $\tilde{\Gamma}_s$ increases, removing the ambiguity of the branch. Then, we plug in the $\tilde{\Gamma}_s$ extracted from the ϵ_{YSR} and calculate the $\tau_s(z)$ from Eq. 4.11, and compare it with τ_{exp}. In the following, we will show the quantitative agreement with marginal error.
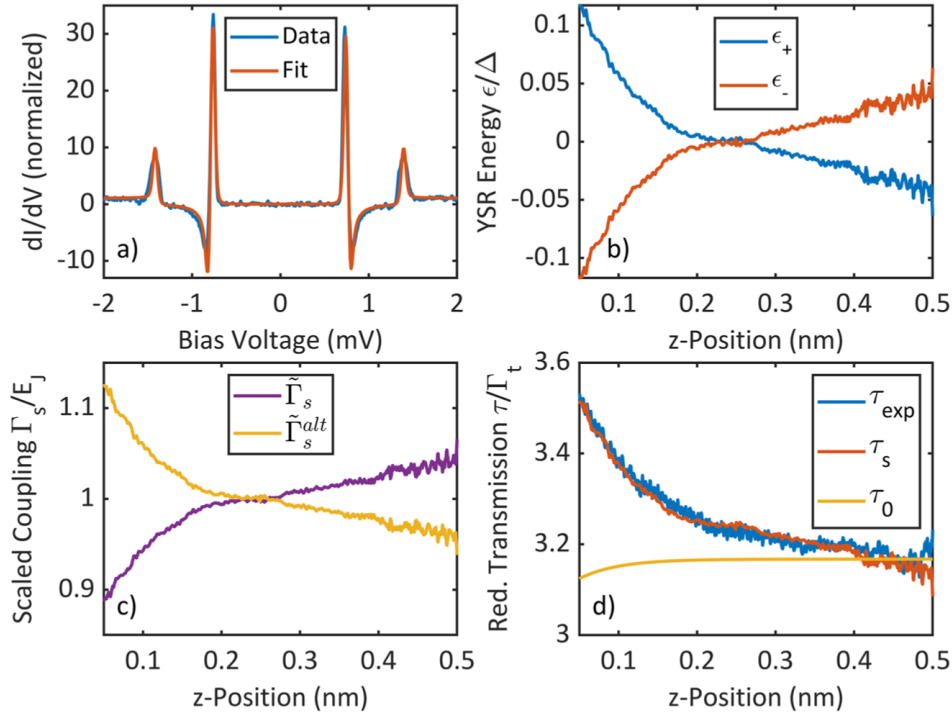
Figure 4.4 – **A YSR state moving across the QPT.** a) A fit of the dI/dV spectrum at low conductance. b) The evolution of the YSR energy moving across zero (the QPT). c) The two branches of the scaled coupling extracted from the YSR energy. d) The transmission divided by $\tilde{\Gamma}_t$ showing excellent agreement between the calculation τ_s using the purple branch of the $\tilde{\Gamma}_s$ in c) and the experiment τ_{exp}. Taken from Ref. [28].

Now we are ready to present three examples:

4.4.2 Decreasing Γ

Fig. 4.3 a) shows the $\tau(z)$ measurement for the same impurity as in Fig. 4.2. A closer look reveals that the measured τ is significantly higher than the expectation if $\tilde{\Gamma}_s$ is assumed constant (τ_0) (Fig. 4.3 b)). This means that $\tilde{\Gamma}_s$ is in the decreasing branch when z decreases, and the calculated transmission τ_s assuming this fits quantitatively well with the experiment.

To present the agreement in a more obvious way, we divide the transmission by $\tilde{\Gamma}_t$ to remove the exponential part (Fig. 4.3 d)). It can be seen that the error is very small. It means that the YSR state is in the strong scattering regime with the coupling decreasing with decreasing z resulting in a decrease in the YSR energy.

4.4.3 Decreasing Γ across the QPT

For another example (Fig. 4.4), the YSR state crosses the QPT (Fig. 4.4 b)). Here, the percentage of the YSR channel is $p = 39\%$. The calculated τ_s agrees again very well with the measured
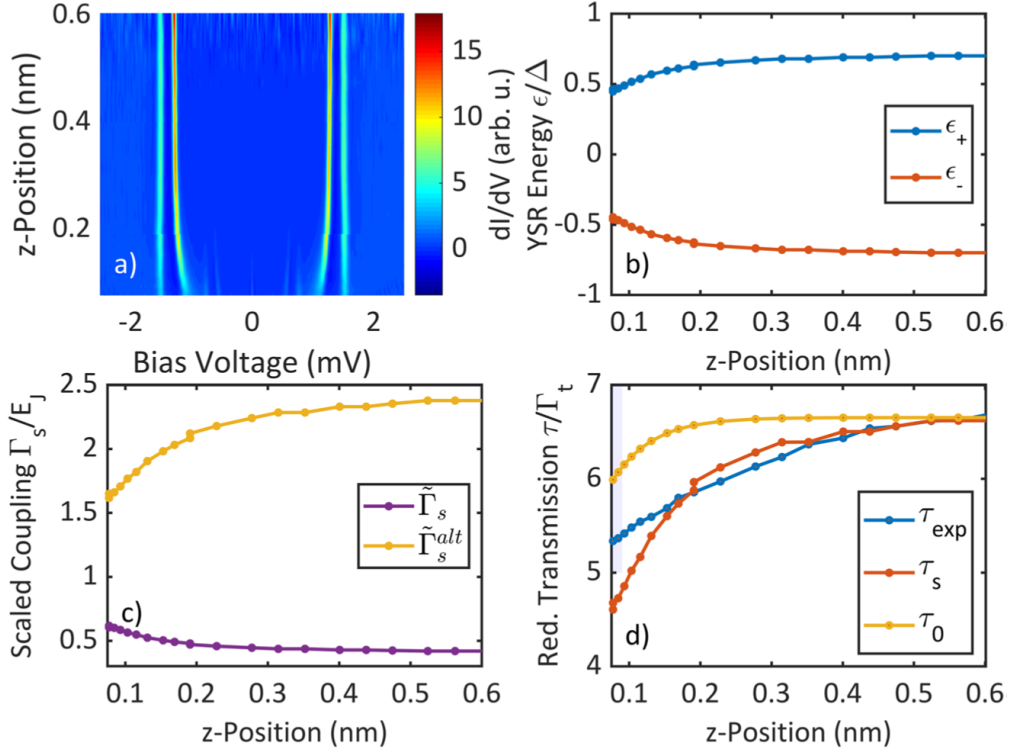
Figure 4.5 – **An example of increasing coupling upon tip approach.** a) The color plot of the dI/dV spectra during tip approach shows moving YSR states. b) The evolution of the YSR energy moving towards zero with decreasing z. c) The two branches of the scaled coupling extracted from the YSR energy. d) The transmission divided by $\tilde{\Gamma}_t$ showing good agreement between the calculation τ_s using the purple branch of the $\tilde{\Gamma}_s$ in c) and the experiment τ_{exp}. Unlike the examples before, here $\tilde{\Gamma}_s$ increases with decreasing z. Taken from Ref. [28].

transmission (Fig. 4.4 d)). It suggests that the impurity substrate coupling decreases when z decreases, moving across the QPT from the strong to the weak scattering regime.

4.4.4 Increasing Γ

The above two examples agree with the explanation in the introduction part of this chapter: with decreasing z, the attractive force increases, thereby lifting the impurity away from the surface, decreasing $\tilde{\Gamma}_s$. Nevertheless, we also see the other situation, where $\tilde{\Gamma}_s$ behaves the opposite way (Fig. 4.5). Since $\tau_{\text{exp}} < \tau_0$, $\tilde{\Gamma}_s$ increases. Indeed, assuming the increasing Γ branch, the calculated τ_s agrees well with the experiment (Fig. 4.5 d)). This means that the YSR state is in the weak scattering regime moving towards the QPT when the tip approaches. The origin of this behavior may be due to a change in the local density of states which can increase the coupling as well [23, 127].

Figure 4.6 – **The dependence of YSR energy on the scaled coupling.** The three datasets discussed in Figs. 4.2,4.3,4.4 and 4.5 are labeled by black wedges with the sharp end pointing to the direction of decreasing z. When Γ_s/E_J decreases starting from the strong scattering regime, the YSR energy moves across zero (the QPT) and then enters the weak scattering regime. Taken from Ref. [28].
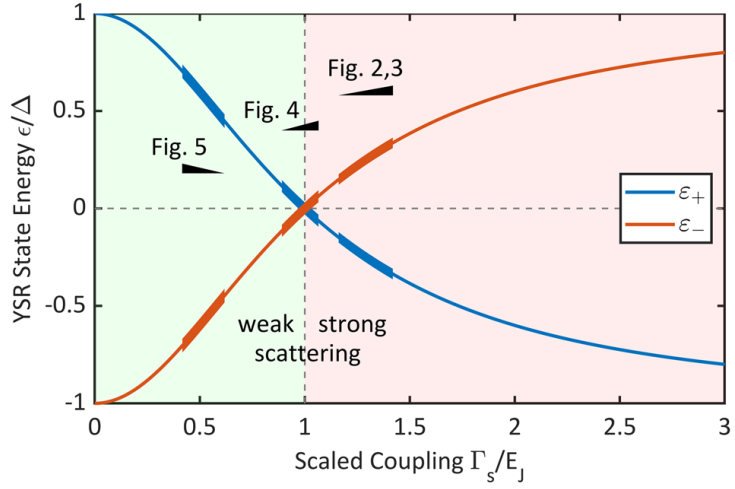
4.5 Conclusion

Here we have presented three examples of moving YSR states among the intrinsic YSR impurities on vanadium, summarized in Fig. 4.6. The YSR regimes and the behavior with decreasing z depends on the impurity.

With this analysis, we can determine on which side of the QPT the YSR state is. This is non-trivial because in the dI/dV spectrum, the YSR states always come in pairs, and the YSR asymmetry is also not a reliable indicator because it depends on the spatial distance to the impurity (recall Fig. 2.5 c)). Now, combining the YSR energy movement with the behavior of the normal state transmission, this determination is possible.

More importantly, the precise agreement with only marginal error of τ with parameters extracted from independent measurements of ϵ_{YSR} suggests that the whole mean field approximation which bridges the data analysis works well even on a quantitative level (and in both weak and strong scattering regimes). This is actually somewhat astonishing, because the mean field approximation neglects all electronic correlations, which is known to be essential for the Kondo effect, but somehow seems not relevant for YSR states in view of this nice agreement. Recalling the close resemblance between the full SIAM calculation and the mean field model on the properties of the YSR states (Figs. 2.5 and 2.11), it might be natural that the mean field model already captures most of the YSR physics.

Nevertheless, the Kondo correlations which the mean field approximation does not capture can in principle coexist with the YSR state. In Chapter 7, we will go beyond the mean field approach and solve the full SIAM via NRG to fit the corresponding Kondo spectra, and show the universal relation between Kondo and YSR physics. Before that, we stay in the mean field model in Chapter 5 and Chapter 6 and show the higher order tunneling processes as well as the Josephson effect related to the YSR states.

5 Interplay between Yu-Shiba-Rusinov states and multiple Andreev reflections[1]

5.1 Introduction

In the measurement of YSR-BCS tunneling at high transmission, we have observed multiple Andreev reflection (MAR) peaks (recall the extra peaks at small tip-sample distance in Figs. 4.2 a) and 4.5 a)). We have discussed the MARs between two BCS superconductors in section 2.5.2, and since a YSR state is hosted on a superconductor, we expect those processes to remain. The question is, what is the interplay between YSR states and MARs, what new processes will we observe due to the presence of YSR states, and what properties of the YSR state will it reveal.

5.2 Energy diagrams of the tunneling processes

From the energy diagrams, it is straightforward to write down the bias threshold for the tunneling processes of different orders including the YSR states (Fig. 5.1). The direct quasiparticle tunneling happens at $eV = \pm(\Delta_s + \Delta_t)$ and $eV = \pm(\epsilon_s + \Delta_t)$ (Fig. 5.1 a)). The conventional MARs between clean superconductors are at $eV = \pm\frac{\Delta_{s,t}}{n}$ and $eV = \pm\frac{\Delta_s + \Delta_t}{2n+1}$ for integer $n \geq 1$ (the lowest order is shown in Fig. 5.1 b)). The MARs connecting the YSR state to the continuum of the superconductor are shown in Fig. 5.1 c), at $eV = \pm\frac{\Delta_s + \epsilon_s}{2n}$ and $eV = \pm\frac{\Delta_t + \epsilon_s}{2n+1}$ for integer $n \geq 1$.

One exotic family of MARs related to the YSR states are the ones that connect a YSR state back to itself, at $eV = \pm\frac{\epsilon_s}{n}$ for integer $n \geq 1$ (for the lowest order process at $eV = \pm\epsilon_s$ see Fig. 5.1 d)). This requires that a YSR state has both spin species (consider the second order process at $eV = \pm\epsilon_s$ shown in Fig. 5.1 d) which basically transfers a Cooper pair through the junction from a YSR state, requiring it to accommodate both spin up and spin down electron at the same time). Since a YSR state is spin non-degenerate, this family of MARs is strictly forbidden.

---

[1]This chapter is based on the publications #9 and #6 from the publication list as well as some unpublished experimental data.
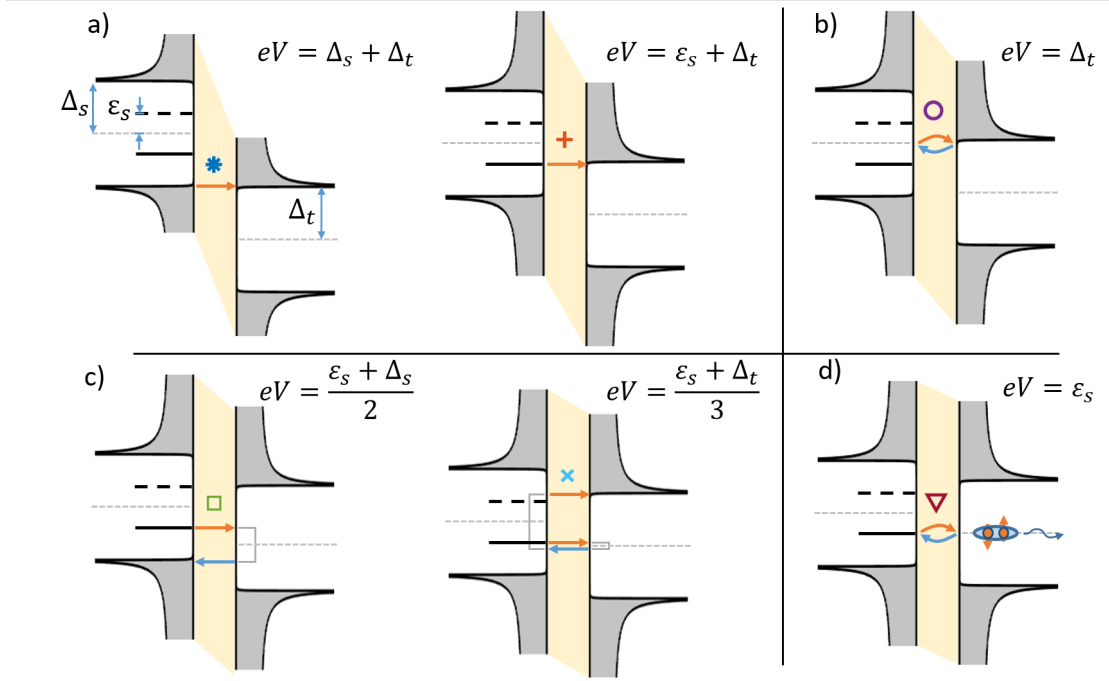
Figure 5.1 – **Tunneling processes between a YSR state and a clean superconductor.** a) Quasiparticle tunneling. Left: tunneling between gap edges resulting in the coherence peaks at $eV = \pm|\Delta_s + \Delta_t|$. Right: direct YSR-BCS tunneling at $eV = \pm|\epsilon_s + \Delta_t|$. b) Conventional Andreev reflection processes between superconductors. Only the second order process is shown here. For more, see Fig. 2.14. c) MARs involving YSR states, connecting the YSR state to the BCS continuum. Left: the second order process (with one reflection) at $eV = \frac{\epsilon_s + \Delta_s}{2}$. It connects the YSR state with the continuum of the same electrode. Right: third order process (two reflections) at $eV = \frac{\epsilon_s + \Delta_t}{3}$, connecting the YSR state with the continuum of the other electrode. d) A family of MARs that connects the YSR state with itself, which is forbidden due to spin non-degeneracy of the YSR state. Here, only the second order process at $eV = \pm\epsilon_s$ is shown. Taken from Ref. [100].

5.3 Simulating MARs in the presence of the YSR states

Tunneling spectra at arbitrary transmission can be calculated using the Green's function theory within the mean field approximation, which has been implemented in the SIAM framework by our collaborators in Madrid (J. C. Cuevas group) [126]. A calculation at relatively high conductance is shown in Fig. 5.2 with the SIAM parameters $\Delta_s = \Delta_t = \Delta, \Gamma_s = 100\Delta, \Gamma_t = \Delta, E_U = 0, k_{\rm B}T = 0.01\Delta$ and the broadening parameter for the Green's functions $\eta_t = 0.001\Delta, \eta_s = 0.01\Delta$. The YSR state moves across the QPT at $E_J = 100\Delta = \Gamma_s$ as expected from Eq. 4.5.

Here, the most prominent spectral feature is the direct quasiparticle tunneling peak at $eV = \Delta + \epsilon_s$, which touches Δ when crossing the QPT. The thermal quasiparticle tunneling peak at $eV = \Delta - \epsilon_s$ is suppressed due to low temperature. Then there are peaks at $eV = \Delta, 2\Delta/3, \Delta/2$
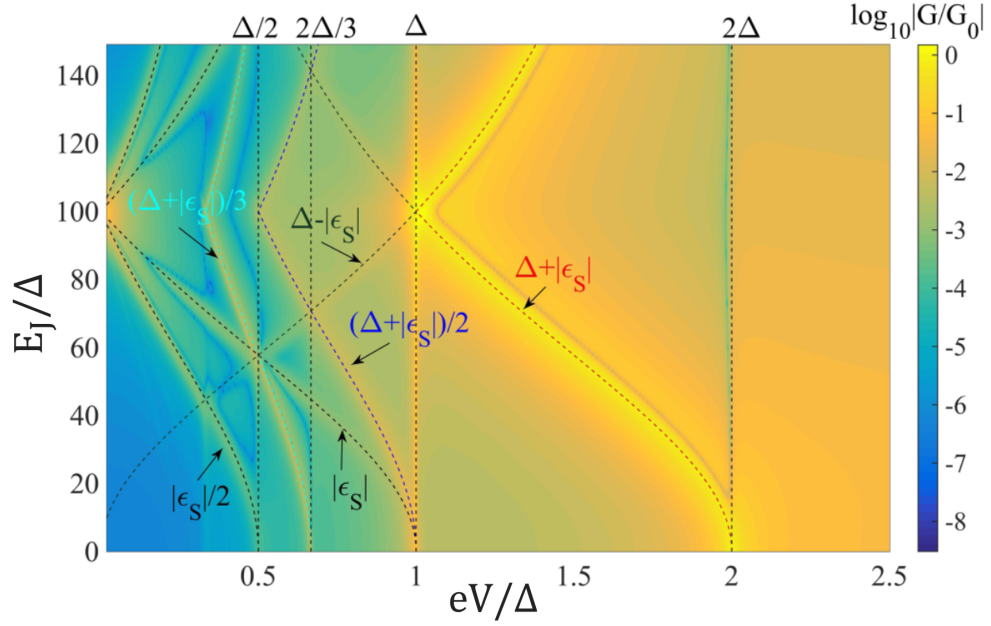
Figure 5.2 – **Simulation of the YSR-MARs processes.** The exchange energy E_J is swept moving the YSR state across the QPT. The processes at ϵ_s and $\epsilon_s/2$ are artifacts due to remnant quasiparticles. See text for calculation parameters. Adapted from Ref. [126].

from the conventional MARs between superconductors. The YSR-MARs are also seen at expected positions $eV = (\Delta + \epsilon_s)/2$ and $eV = (\Delta + \epsilon_s)/3$.

The last group of peaks in the calculation is located at $eV = \epsilon_s$ and $\epsilon_s/2$, which crosses zero energy along with the QPT. These are the forbidden family of MARs discussed in Fig. 5.1 d). If the process connects the sharp YSR state with itself (as in Fig. 5.1 d)), it should have a significant negative differential conductance characteristic of the tunneling between two resonance levels (similar to the Shiba-Shiba tunneling process which will be discussed later in Chapter 8). However, the peaks do not exhibit such a feature, and therefore the origin is instead mainly the tunneling between the YSR state and the continuous residual quasiparticle background in the gap induced by a finite η parameter. The process at $eV = \epsilon_s$ is the direct quasiparticle tunneling between the YSR state and the residual in-gap DOS of the other electrode, while the process at $eV = \epsilon_s/2$ comes from the contribution of a second-order Andreev reflection connecting the YSR state and the quasiparticle background of the same electrode.

The conclusion is thus, that the corresponding peaks originating from the forbidden family of MARs with expected behavior are indeed not reproduced in the calculation, but care has to be taken when interpreting the experimental data because the peaks originating from an imperfect gap happen to be at the same energy positions. This is especially important when the superconducting gap is not clean enough (for example in quantum dots where the gap is usually quite soft or in the STM where the tip not perfect) [106].
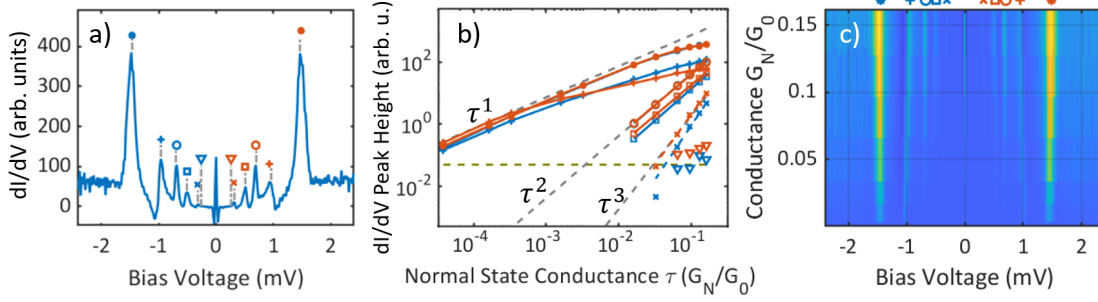
Figure 5.3 – **High conductance** dI/dV **spectra showing YSR-MARs.** All peaks are marked with labels consistent with those in Fig. 5.1 showing the corresponding tunneling process of each peak. a) The dI/dV spectrum measured at the transmission $\tau = 0.16$ showing multiple peak features inside the gap. The position of the forbidden tunneling at $eV = \pm\epsilon_s$ is marked with $\triangledown$, where indeed no peak is seen. The unlabeled peak at zero voltage is the Josephson effect. b) The transmission dependence of the peak heights shown in a), with consistent labels. Red (blue) points are the peaks at positive (negative) bias voltages. All peaks behave as expected, except for the signal at $eV = \pm\epsilon_s$, which should be τ^2 dependence if it exists, confirming the absence of such a process. c) The color plot of the tunneling spectra from low to high conductance, showing that the YSR energy does not move significantly during tip approach in this case. Taken from Ref. [100].

To tell these apart experimentally, the scaling of the peaks with respect to the transmission might provide some insight. For the peak at $eV = \epsilon_s$, if it is the forbidden Andreev process, it will scale $\propto \tau^2$, while if it is the quasiparticle tunneling to the remnant in-gap DOS, it will scale linearly with τ.

5.4 Measuring MARs on a YSR state

5.4.1 A non-moving YSR state

Now with our vanadium-vanadium junction and one intrinsic YSR impurity either on the tip or on the sample, we have observed the MARs related to the YSR states at high transmission. One example for a YSR state on the sample surface is shown in Fig. 5.3 where the YSR energy does not change significantly with tip approach. The corresponding tunneling processes for a peak is determined in the following way (in the case of a sample YSR state, for example). First, from the dI/dV spectrum measured at a low transmission where only quasiparticle peaks at $eV = \pm(\Delta_s + \Delta_t)$ and $eV = \pm(\epsilon_s + \Delta_t)$ are visible, we extract Δ_t and ϵ_s given that $\Delta_s \approx 750\,\mu eV$. Then we go to higher transmission and identify the lowest order Andreev reflections at $eV = \pm\Delta_{s,t}$ and correct the estimations above. With ϵ_s and $\Delta_{s,t}$ known, the positions of all MARs can be derived.

We have, therefore, attributed all peaks to the corresponding tunneling processes in Fig. 5.3 a). The labels are the same as in Fig. 5.1. The only family missing is the forbidden one (marked
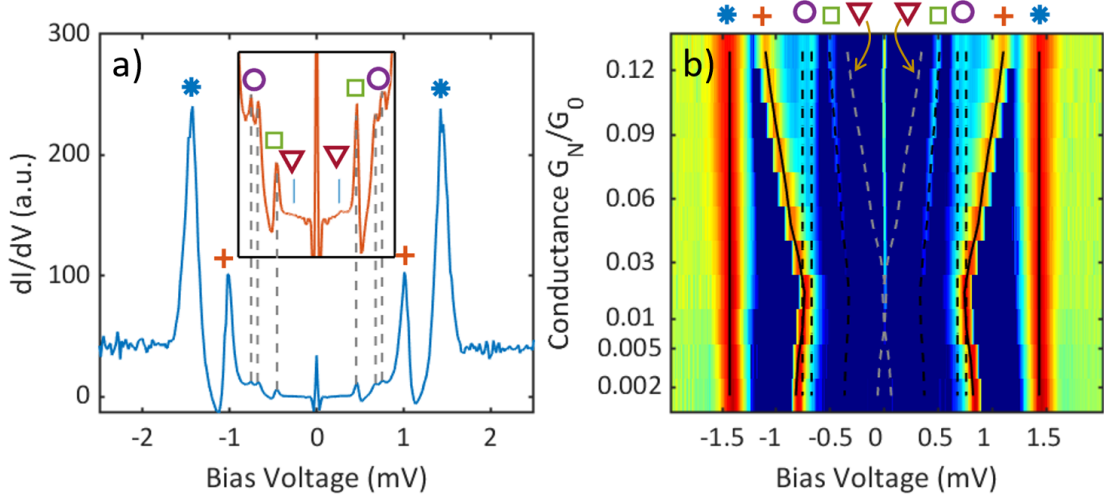
Figure 5.4 – **YSR-MARs across the quantum phase transition.** The peaks are labeled consistently with Figs. 5.1 and 5.3. a) The dI/dV spectrum at $\tau = 0.10$ of a YSR impurity on the tip that moves across the QPT during tip approach. The forbidden second order Andreev process at $eV = \pm\epsilon_t$ marked with $\triangledown$ is again absent. b) The color plot of the dI/dV spectra at different conductance normalized by the conductance. The color scaling is logarithmic to reveal small peak features and the expected positions of the peaks are drawn with solid lines (quasiparticle tunneling) and dashed lines (second order Andreev processes). The YSR state crosses the QPT, making the peaks at $eV = \pm(\Delta_s + \epsilon_t)$ (marked with + signs) reflect at $eV = \pm\Delta_s$. It nicely shows that all peaks move as expected and the forbidden process is clearly absent.

with $\triangledown$), as expected. Also notice that, the pair of peaks of the MARs involving the YSR states can generally be asymmetric in height if the YSR states are electron-hole asymmetric.

Usually a full conductance dependence measurement is beneficial (Fig. 5.3 c)), especially if the YSR state moves during tip approach, which will be discussed in the next section. Another advantage is that the scaling of the peak height can be determined, verifying the attribution of the processes. The conductance dependence of the corresponding peaks are plotted in Fig. 5.3 b) (with consistent markers). The quasiparticle tunneling peaks scale linearly first and then sublinearly due to higher order processes with the conductance. The second order Andreev peaks at $eV = \pm\Delta, \pm\frac{\epsilon_s + \Delta_s}{2}$ scale quadratically and the third order peaks at $eV = \pm\frac{\epsilon_s + \Delta_t}{3}$ scale proportional to τ^3. We also plot the dI/dV signal at $eV = \pm\epsilon_s$ even if there is no peak there, and the resulting conductance scaling clearly deviates from the expected τ^2 dependency. Additionally, noting that the peak height is close to noise level, we conclude the absence of the forbidden family experimentally.

5.4.2 A YSR state across the QPT

From Chapter 4 we know that some intrinsic YSR impurities are pulled away from the superconducting host during tip approach by the atomic force, resulting in changing YSR energies.

Here, we show one example of a tip YSR state moving across the QPT and the MARs along with it (Fig. 5.4). This closely resembles the theoretical calculation in Fig. 5.2.

In the case of moving YSR states during tip approach, a full conductance dependence measurement is desirable (Fig. 5.4 b)). In this way, the evolution of the quasiparticle peaks is traced to high transmission, making it possible to extract the YSR energy at arbitrary transmission. Nevertheless, it is also possible to analyze just a single spectrum without this additional information (only in the case of single YSR state though) knowing that the quasiparticle peaks at $\Delta_s + \Delta_t > \epsilon_t + \Delta_s$ are always the outermost peaks and the MARs peaks are all at lower bias voltages.

The corresponding MAR processes in Fig. 5.4 are thus identified and labeled by consistent markers in Fig. 5.1. Here, the second order Andreev reflection peaks at $eV = \pm\Delta_{t,s}$ are split slightly (see the peaks labeled by ∘ in Fig. 5.4) because Δ_t is slightly smaller than Δ_s in this case. Clearly, the peaks for processes not involving the YSR state do not move, but those that depend on the YSR energy move in the expected way quantitatively. This confirms the predictions of the positions of the MARs in Fig. 5.1 experimentally.

Notice that the forbidden transition at $eV = \epsilon_t$ (peak positions marked with ▽) is also absent, even viewed in the logarithmic colorplot in Fig. 5.4 b) intended to reveal minor features.

5.5 Conclusion

In this Chapter we have summarized the tunneling processes that occur in a YSR-BCS junction at high transmission, and discussed the peak attributions and properties. The MARs that connect a YSR state to itself (at $eV = \frac{\epsilon_s}{n}$) are predicted to be strictly forbidden theoretically due to spin non-degeneracy, which we have confirmed in the experiments.

Some previous experiments [106] nevertheless observed the peaks at $eV = \epsilon_s$. As discussed before, these peaks are due to the tunneling to remnant quasiparticles in the gap, which reduce if the gap is cleaner. The processes can be distinguished by checking the scaling with respect to the transmission. In our experiment, the absence of the peaks not only shows that the gap is clean but also confirms the spin non-degeneracy of the in-gap state observed, which is expected in theory but is *a priori* not clear experimentally. This is a necessary piece of information to use the YSR tip as a spin polarized probe. In addition, the systematic account of all possible tunneling processes involving the YSR state at arbitrary transmission via energy diagrams and the Green's function simulations in this chapter provides the foundation for further understanding the tunneling phenomena in the presence of YSR states. In the next chapter, we will focus on the interplay between the YSR state and another phenomenon that happens at relatively high transmission, which is the Josephson effect.

6 Supercurrent reversal through a quantum phase transition of a single Yu-Shiba-Rusinov state[1]

6.1 Introduction

We have seen examples of YSR states moving across the quantum phase transition (QPT) during tip approach in Chapters 4 and 5, the schematics of which is shown in Fig. 6.1 a). There, the changing YSR energy merely reflects the varying impurity substrate coupling, and it is not clear what happens at the zero energy crossing that qualifies it as a QPT. In theory, the ground state exchanges with the excited state at the QPT resulting in an abrupt change of the ground state between the free spin and screened spin regime (Figs. 6.1 b) and c), for details see section 2.3.3), but in the experiment, we always measure the transition between the ground state and the excited state in the quasiparticle spectrum, which renders such measurements insensitive to the nature of the ground state. Indeed, we need the somewhat advanced analysis from Chapter 4 to determine which side of the QPT a YSR state is at from quasiparticle tunneling spectra.

The question is thus, whether there is a tool to reveal the YSR ground state. Since the YSR ground state comprises not only the impurity spin but also the whole Cooper pair condensate coupled to it, the Josephson effect is a promising candidate to provide further information since it describes direct tunneling between Cooper pair condensates.

It has been demonstrated in Josephson junctions sandwiching quantum dots [129, 130] or ferromagnetic layers [131, 132] that the direction of the supercurrent reverses when unpaired spins exist in the Josephson junction due to a π shift in the phase. However, in the case of a single YSR impurity which is strongly coupled to the superconductor, a similar $0 - \pi$ transition was predicted theoretically [69] but remains elusive experimentally. In this chapter, we will demonstrate the supercurrent reversal when a single YSR impurity on the tip moves through the QPT at 10 mK. Both the sample and the tip are superconducting vanadium.

---

[1]This chapter is based on the publication #5 from the publication list.
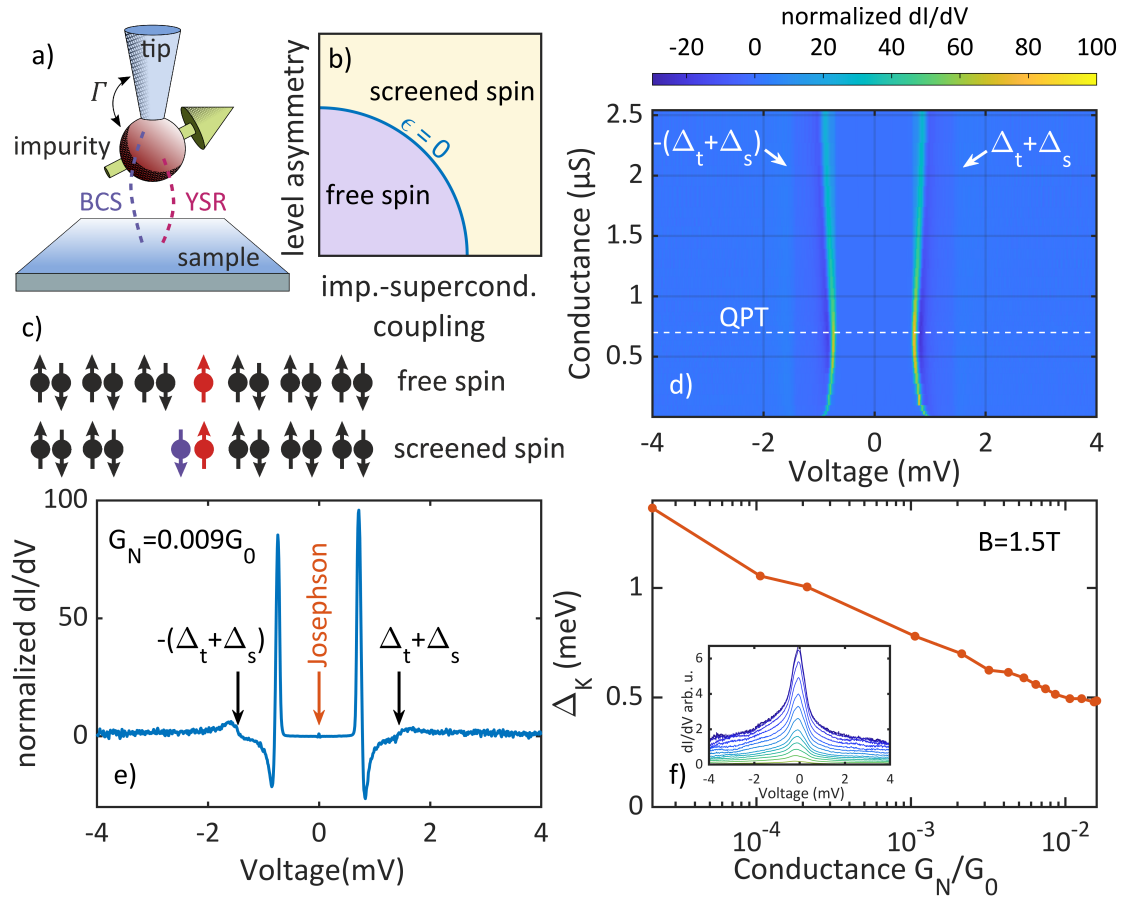
Figure 6.1 – **The YSR state moving across the QPT.** a) The schematics of the tunnel junction with a YSR impurity on the tip. There are two transport channels denoted by the dashed lines. b) The phase diagram of the YSR state with different level asymmetry E_U and impurity superconductor coupling Γ assuming constant E_J (recall Eq. 4.5). c) There is one unpaired spin in the free spin state while the impurity spin is paired in the screened spin state, suggesting a different parity. d) The conductance dependence of the dI/dV spectra showing the QPT where the YSR-BCS tunneling peaks at $\pm(\epsilon_t + \Delta_s)$ touches $\pm\Delta_s$. e) The dI/dV spectrum at the transmission $\tau = 0.009$ showing strong YSR-BCS tunneling peaks and strongly reduced coherence peaks. The Josephson effect manifests itself at zero voltage. f) The Kondo spectra measured at $B = 1.5$T when the superconductivity is quenched (inset). The width of the Kondo peaks decreases with increasing conductance, indicating a decreasing Kondo temperature T_K and therefore a decreasing coupling Γ. Taken from Ref. [128].

6.2 YSR phenomena across the QPT

6.2.1 Quasiparticle tunneling

Some intrinsic YSR impurities show varying YSR energies during tip approach due to the atomic forces in the junction that modify the impurity substrate coupling (see Chapter 4). Among those, some YSR states move across the QPT (Fig. 6.1 d)). Since the YSR tip usually provides more flexibility in producing such features (see section 3.3.2), the following measurements are based on one such an impurity on the tip (Fig. 6.1 a)).

A dI/dV spectrum measured at $\tau = 0.009$ is shown in Fig. 6.1 e) and more spectra at different conductance are shown as a colormap in Fig. 6.1 d), where the most intense pair of peaks is the quasiparticle tunneling process between the YSR state and the superconducting gap edge at $eV = \pm(\epsilon_t + \Delta_s)$, i.e. the sum of the YSR energy ϵ_t and the gap parameter Δ_s. The thermal processes at $eV = \pm(\Delta_s - \epsilon_t)$ are absent at 10 mK (except when the YSR state is very close to the QPT). These peaks are reflected at $eV = \pm\Delta_s$ when the YSR energy crosses zero signaling the QPT (Fig. 6.1 d)). The coherence peaks at $eV = \pm(\Delta_t + \Delta_s)$ are present but largely suppressed, indicating a small yet existent BCS channel besides the YSR channel (see discussion in section 4.3). Later we will see that this second channel is essential for the interpretation of the Josephson measurements.

From Fig. 6.1 d) we can extract the YSR energies ϵ_t as a function of conductance (the red curve in Fig. 6.2 b)) using $\Delta_s = 750\,\mu\text{eV}$. However, the uncertainty in Δ_s still allows for an arbitrary small shift of the YSR energy (on the order of μeV). We can fix the shift by converting the YSR energy to Γ (the coupling between the impurity and the superconducting host, which is the tip now) using Eq. 4.5 with a small shift as a parameter to make the resulting Γ a smooth function of G_N without kinks. This will result in a small gap in the YSR energy when it crosses the QPT (Fig. 6.2 b)), which can be confirmed independently by the position of the thermal peaks close to the QPT. Such a gap is expected in a self-consistent calculation (Fig. 2.6 a)).

It is still ambiguous whether Γ increases or decreases when the YSR state goes through the QPT. To clarify this, we apply a $B = 1.5\,\text{T}$ magnetic field to quench the superconductivity in both the tip and the sample, revealing the Kondo effect in the dI/dV spectrum (inset Fig. 6.1 f)). The Kondo peak width, which is proportional to the Kondo temperature T_K, decreases with increasing conductance, suggesting decreasing Γ with increasing conductance. This indicates that the ground state changes from the screened spin regime at low conductance to the free spin regime at high conductance. Now, we will see how this ground state change will affect the Josephson effect.

6.2.2 The Josephson effect

The Josephson effect is located near zero bias voltage, and it is beneficial to look at the current curve rather than the dI/dV spectrum because the current can be directly modeled and fitted
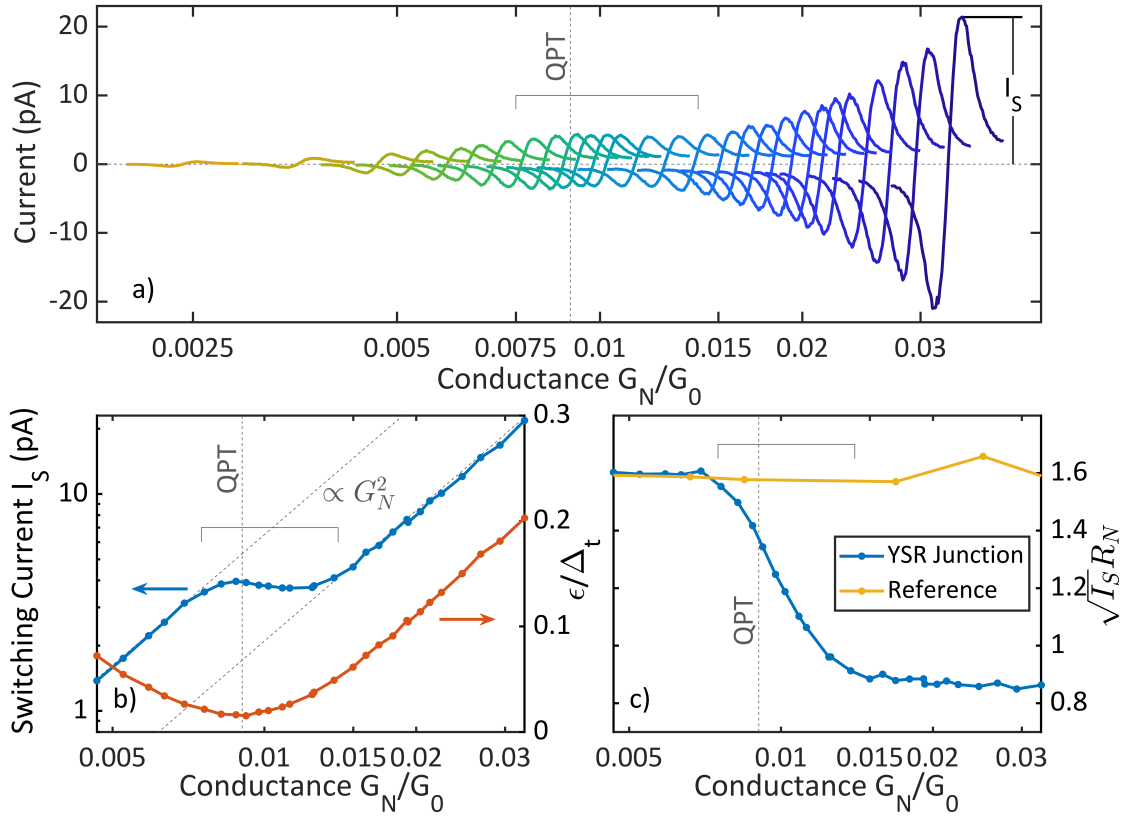
Figure 6.2 – **The Josephson effect through the QPT.** a) The $I(V)$ curves within $\pm 60\,\mu eV$ measured at different normal state conductance, showing the Josephson effect. The Josephson switching current I_s is defined as the height of the peak. b) The YSR energy (the red curve) and the switching current (the blue curve) as a function of the normal state conductance. The position of the QPT where the YSR energy crosses zero is labeled. The gray dotted lines show the quadratic dependence on the conductance. The switching current obeys G_N^2 scaling at low and high conductance as expected, but it exhibits a significant step near the QPT. c) The dependence of $\sqrt{I_s}R_N$ on the conductance for the data in b) (the blue curve) as well as one from a clean junction without the YSR state (the yellow curve), eliminating the background $\propto G_N^2$ dependence in I_s. R_N is the renormalized normal state resistance taking the Kondo anomaly into consideration (details see text). Taken from Ref. [128].

by the asymmetry of the $P(E)$ function (see section 2.5.3). The Josephson current curves during the YSR measurements are shown in Fig. 6.2 a). We extract the peak height I_s (the switching current) and plot it against the normal state conductance along with the evolution of the YSR energy in Fig. 6.2 b). Generally, I_s scales with G_N^2 at low and high conductance, as expected from Eq. 2.81. However, at the QPT, there is a significant step.

To better illustrate the change, we plot $\sqrt{I_s}R_N = \sqrt{I_s}/G_N$ as a function of the conductance which eliminates the underlying G_N^2 dependence (Fig. 6.2 c), blue curve), where a nearly 50% step around the QPT is clearly observed. As a comparison, the same quantity for a clean superconducting junction without a YSR state is plotted as the yellow curve in Fig. 6.2 c), being largely independent on the conductance as expected. We will show that such a reduction in the Josephson current across the QPT is due to the interference between the BCS and the YSR transport channels with the YSR channel showing a $0 - \pi$ transition.

As a side note, R_N is renormalized in the YSR case to account for the enhancement of the density of states at the Fermi energy from the Kondo effect (recall the inset of Fig. 6.1 f)). This only affects the absolute scaling of $\sqrt{I_s}R_N$ and thus the comparison with the reference measurement, while the step behavior at the QPT is robust irrespective of this scaling. This will be discussed in more detail in section 6.4.

6.3 Modeling the Josephson effect in the SIAM

6.3.1 The Green's function of a YSR impurity coupled to two electrodes

Since the Josephson effect describes Cooper pair transport between two electrodes, we need to include another electrode and allow for an arbitrary phase difference between the order parameters in the two electrodes. Consequently, the SIAM Hamiltonian from Eq. 2.35 is modified to the situation where the impurity is coupled to the sample and the tip via hopping terms t_s and t_t, with both the tip and sample being BCS superconductors. We further define $\Gamma_j = \pi v_{0j} t_j^2$ as the coupling strength, with $j = t, s$ and v_0 as the normal state density of states near the Fermi energy, which is assumed to be constant.

Another aspect is that the Josephson effect depends on the phase difference between the electrodes, which can be absorbed into the complex phase of the order parameters. With this in mind and using the mean field approximation (Eq. 4.1), the resulting Green's function can be written as [128]

$$g_{\substack{\text{YSR, SIAM} \\ \text{2 electrodes}}}(\omega) = \begin{pmatrix} g_{\uparrow\uparrow}(\omega) & 0 \\ 0 & g_{\downarrow\downarrow}(\omega) \end{pmatrix}, \tag{6.1}$$

with

$$g_{\sigma\sigma}(\omega) = \frac{1}{D_\sigma(\omega)}$$
$$\times \begin{pmatrix} \omega(\Gamma_s + \Gamma_t) + (\omega + E_U - E_{J\sigma})\sqrt{\Delta^2 - \omega^2} & \Gamma_s \Delta e^{i\phi_s} + \Gamma_t \Delta e^{i\phi_t} \\ \Gamma_s \Delta e^{-i\phi_s} + \Gamma_t \Delta e^{-i\phi_t} & \omega(\Gamma_s + \Gamma_t) + (\omega - E_U - E_{J\sigma})\sqrt{\Delta^2 - \omega^2} \end{pmatrix},$$

$$D_\sigma(\omega) = 2(\Gamma_s + \Gamma_t)\omega(\omega - E_{J\sigma}) + [(\omega - E_{J\sigma})^2 - E_U^2 - (\Gamma_s + \Gamma_t)^2]\sqrt{\Delta^2 - \omega^2}$$
$$+ \frac{4\Delta^2}{\sqrt{\Delta^2 - \omega^2}}\Gamma_s\Gamma_t \sin^2(\phi/2), \tag{6.2}$$

where $E_{J\uparrow} = E_J$, $E_{J\downarrow} = -E_J$ and $\phi = \phi_t - \phi_s$ is the superconducting phase difference across the junction. The tip and sample superconducting gaps are assumed to be equal $\Delta_{s,t} = \Delta$. The phase-dependent YSR energy is given by

$$E^{\text{YSR}}(\phi) = \pm\Delta \frac{(\Gamma_s + \Gamma_t)^2 + E_U^2 - E_J^2 - 4\Gamma_s\Gamma_t \sin^2(\phi/2)}{\sqrt{\left((\Gamma_s + \Gamma_t)^2 + (E_J - E_U)^2\right)\left((\Gamma_s + \Gamma_t)^2 + (E_J + E_U)^2\right)}}, \tag{6.3}$$

which is plotted as the blue curves in Fig. 6.3 a). It reduces to Eq. 4.5 in the case of coupling to only a single electrode (i.e. when $\Gamma_t = 0$ or $\Gamma_s = 0$), where the quantum phase transition happens at $\Gamma^2 + E_U^2 - E_J^2 = 0$, which represents a circle shown in Fig. 6.1 b).

The transmission through the YSR channel is

$$\tau_{\text{YSR}} = \frac{2\Gamma_s\Gamma_t}{(\Gamma_s + \Gamma_t)^2 + (E_U - E_J)^2} + \frac{2\Gamma_s\Gamma_t}{(\Gamma_s + \Gamma_t)^2 + (E_U + E_J)^2}, \tag{6.4}$$

which reduces to Eq. 4.9 for $E_U = 0$.

6.3.2 The energy phase relations

For the BCS channel (the tunneling between two BCS superconductors), the energy-phase relation is given by Eq. 2.74. At low transmission, it becomes harmonic (Eq. 2.75) and the amplitude of its first harmonic (Eq. 2.79) is

$$E_1^{\text{BCS}} = \frac{\Delta}{8}\tau_{\text{BCS}}, \tag{6.5}$$

in which τ_{BCS} is the transmission of the BCS channel.

For the YSR channel, from the energy phase relation in Eq. 6.3 we can calculate the amplitude of its first harmonic

$$E_1^{\text{YSR}} = \frac{\text{sgn}[(\Gamma_s + \Gamma_t)^2 + E_U^2 - E_J^2]\Delta\Gamma_s\Gamma_t}{\sqrt{\left((\Gamma_s + \Gamma_t)^2 + (E_J - E_U)^2\right)\left((\Gamma_s + \Gamma_t)^2 + (E_J + E_U)^2\right)}}, \tag{6.6}$$
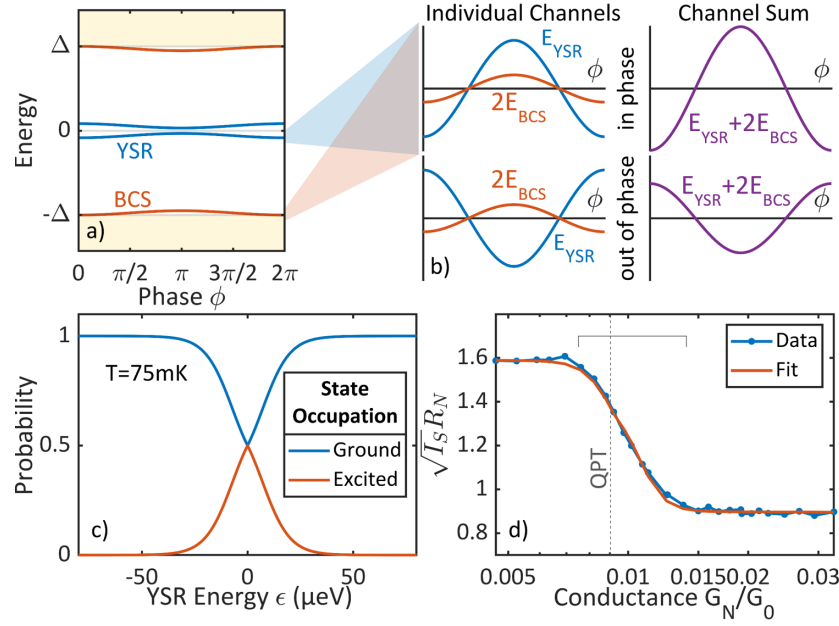
Figure 6.3 – **Supercurrent reversal.** a) The energy phase relations of the BCS channel and the YSR channel. The absolute offset is not relevant for the calculation of the supercurrent but the oscillation is. b) The oscillating part of the energy phase relations in a). When the two channels are in phase, the total amplitude is larger (upper two plots), while if the two channels are out of phase, the total amplitude is smaller (lower two plots). Here, the phase of the BCS channel is constant while the phase of the YSR channel reverses across the QPT (the $0-\pi$ transition). The extra factor of two for E_{BCS} comes from the spin degeneracy. c) The probability for a thermal excitation of the system at $T = 75\,\mathrm{mK}$ for YSR states close to zero energy. d) The fit of the $\sqrt{I_s}R_N$ considering the interference between two channels at a finite temperature showing excellent agreement. Taken from Ref. [128].

in which sgn is the sign function. If the YSR energy is far from the QPT, the YSR energy phase relation (Eq. 6.3) only contains the first harmonic term. However, close to the QPT, the energy phase relation crosses zero and the lower branch has to be taken, resulting in higher order harmonics. This is only important near the QPT at relatively high transmission where the energy phase relation has significant amplitude. At low transmission which our experiment satisfies (τ smaller than 0.05, see Fig. 6.2 b)), the first harmonic dominates, and thus we limit ourselves to the first harmonic in the following.

If $E_U = 0$, the above equation can be further simplified as

$$
\begin{aligned}
E_1^{\mathrm{YSR}} &= \mathrm{sgn}[(\Gamma_s + \Gamma_t)^2 - E_J^2] \frac{\Delta \Gamma_s \Gamma_t}{(\Gamma_s + \Gamma_t)^2 + E_J^2} \\
&= \mathrm{sgn}[(\Gamma_s + \Gamma_t)^2 - E_J^2] \frac{\Delta}{4} \tau_{\mathrm{YSR}} \\
&= \begin{cases} \frac{\Delta}{4} \tau_{\mathrm{YSR}} & \text{if } \Gamma_s + \Gamma_t > E_J \text{ (screened spin)}, \\ -\frac{\Delta}{4} \tau_{\mathrm{YSR}} & \text{if } \Gamma_s + \Gamma_t < E_J \text{ (free spin)}. \end{cases}
\end{aligned}
$$

(6.7)

This means that across the QPT, the phase changes sign for a YSR channel, with the sign being the same as the BCS channel in the screened regime (0-phase) while the sign being negative in the free-spin regime (π-phase). The negative sign acquired across the QPT means that the supercurrent reverses. Nevertheless, if there is only the YSR channel, we will not be able to see any change in the Josephson measurement because we can only measure the amplitude, not the sign (recall Eq. 2.77). In the next section, we will see that the step in $\sqrt{I_s}R_N$ emerges when the two channels are allowed to combine and interfere.

6.4 Quantum interference between two channels

The total energy phase relation is the coherent superposition of the two channels $E(\phi) = 2E^{\mathrm{BCS}}(\phi) + E^{\mathrm{YSR}}(\phi)$. The extra factor of two in front of E^{BCS} comes from the spin degeneracy of the BCS channel (recall Eq. 2.71). At low transmission as discussed previously, the energy phase relation can be represented by the first harmonic proportional to $\cos\phi$ whose coefficient is

$$E_1 = 2E_1^{\mathrm{BCS}} + E_1^{\mathrm{YSR}}. \tag{6.8}$$

Notice that close to the QPT, higher harmonics may also contribute at low transmission which may result in corrections, but here we ignore this effect. Such superpositions are shown in Fig. 6.3 b). When the signs of E_1^{BCS} and E_1^{YSR} are the same, the superposition is constructive, resulting in a larger E_1^2 (the upper two plots of Fig. 6.3 b)), while when they are opposite, the superposition is destructive, resulting in a smaller E_1^2 (the lower two plots of Fig. 6.3 b)). Consider for a moment again $E_U = 0$, where Eq. 6.8 becomes

$$E_1 = \begin{cases} \frac{\Delta}{4}(\tau_{\mathrm{BCS}} + \tau_{\mathrm{YSR}}) = \frac{\Delta}{4}\tau & \text{if } \Gamma_s + \Gamma_t > E_J \text{ (screened)}, \\ \frac{\Delta}{4}(\tau_{\mathrm{BCS}} - \tau_{\mathrm{YSR}}) = \frac{\Delta}{4}\tau(2x-1) & \text{if } \Gamma_s + \Gamma_t < E_J \text{ (free-spin)}, \end{cases} \tag{6.9}$$

where $\tau = \tau_{\mathrm{BCS}} + \tau_{\mathrm{YSR}}$ is the total transmission and $x = \tau_{\mathrm{BCS}}/\tau$ is the percentage of the BCS channel contribution in the total transmission.

Since the switching current is proportional to E_1^2 (Eq. 2.80),

$$\sqrt{I_s}R_N \propto \frac{|E_1|}{\tau} = \begin{cases} \frac{\Delta}{4} & \text{if } \Gamma_s + \Gamma_t > E_J \text{ (screened)}, \\ \frac{\Delta}{4}|2x-1| & \text{if } \Gamma_s + \Gamma_t < E_J \text{ (free-spin)}. \end{cases} \tag{6.10}$$

This means that in the screened regime (the low conductance side in Fig. 6.2 c)), the Josephson current adds up, recovering the clean BCS limit irrespective of the parameters of the YSR state.

However, if we directly plot the experimental $\sqrt{I_s}R_N = \sqrt{I_s}/G_N$ value, the reference measurement and the YSR measurement does not match at both low and high conductance. The reason is that we measure the normal state conductance G_N (which is the conductance without superconductivity) from the differential conductance at 4mV well outside the superconducting gaps, while for the quantity $\sqrt{I_s}R_N$ we need the G_N at the Fermi level. It is reasonable to

assume a constant G_N without the magnetic impurity, but the Kondo effect in the presence of such an impurity (see Fig. 6.1 f)) enhances the conductance at the Fermi level and thus the conductance at 4mV would result in an underestimation of the conductance.

Although this is qualitatively clear, it is not straightforward to quantify this behavior because in the superconducting state, the Kondo peak is usually masked by the superconducting gap making it not possible to estimate the peak height. In addition, it is not clear theoretically which conductance to use exactly when the normal state density of states varies on the order of the superconducting gap, whether to use G_N at the Fermi level or some sort of average in the gap. Here, we just take a phenomenological approach and scale the YSR measurement (the blue curve in Fig. 6.2 c)) to the reference measurement (the yellow curve in Fig. 6.2 c)) in the low conductance side (screened regime) according to Eq. 6.10 and the required renormalization is $R_N = 1/(2.05 G_N)$ for the YSR case, agreeing qualitatively with the enhancement of the conductance due to the presence of the Kondo effect. Notice that this scaling factor depends on the specific impurity because the Kondo peak height and peak shape is different. Nevertheless, the main observation in this chapter (the step in the $\sqrt{I_s} R_N$) is independent of this scaling.

In the free-spin regime (the high conductance side in Fig. 6.2 c)), the interference is destructive and the relative reduction is a direct measure of the relative channel transmissions. In the case shown in Fig. 6.2 c), $x = 21.6\%$, meaning that the YSR channel contributes 78.4% while the BCS channel contributes 21.6%.

6.5 Finite temperature effect and fitting the data

One detail is that in the experiment data, the step is rounded, suggesting a temperature broadening. Therefore, the thermal excitation of the YSR state near the QPT needs to be considered, and the final coefficient E_1 is

$$E_1^2 = (1-p)|2E_1^{\text{BCS}} + E_1^{\text{YSR}}|^2 + p|2E_1^{\text{BCS}} - E_1^{\text{YSR}}|^2, \tag{6.11}$$

with $p = 2/(3 + \exp(|\epsilon|/k_B T))$ (plotted in Fig. 6.3 c)).

To calculate the Josephson current, we plug Eq. 6.11 into Eq. 2.77 limiting ourselves to $m = 1$. With this, we can fit the experimental data (the blue curve in Fig. 6.2 c)) and the agreement is excellent (Fig. 6.3 d)). The effective temperature in the fit is $T_{\text{eff}} = 75$ mK.

6.6 Origin of the supercurrent reversal

6.6.1 The $0 - \pi$ transition in the YSR states

Now that we have identified the $0 - \pi$ transition of the YSR channel and reached quantitative consistency between the theory and the experiment, we would like to demonstrate that such a

Figure 6.4 – **Schematics of the sign change of the Cooper pair tunneling.** The Cooper pair tunneling involves the continuum in the sample and the excited YSR state in the tip as intermediate states. The tunneling order is labeled with numbers on the red arrows. a) In the free-spin regime, the presence of an unpaired spin in the YSR ground state results in an exchange of the Fermionic operators (schematically the reordering of the electron spins in the Cooper pair before and after tunneling) which causes a π shift in the phase. b) In the screened regime, the system recovers the clean junction case where the order is preserved, resulting in a 0 phase shift. Taken from Ref. [128].
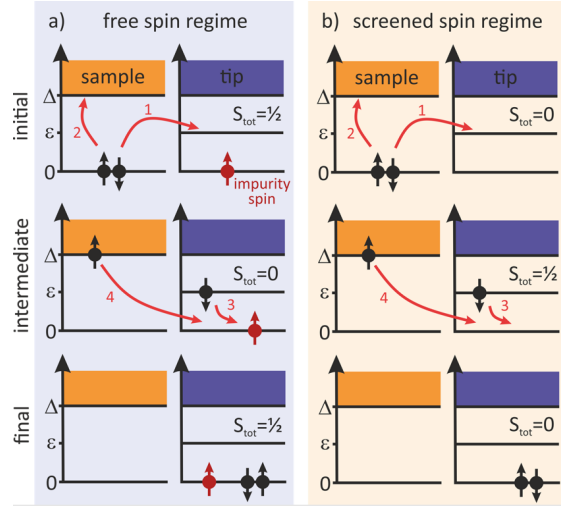
transition directly reflects the YSR ground state (Fig. 6.4). We limit our discussion here to a spin-½ impurity.

In the free-spin regime, the YSR ground state has one unpaired spin (Fig. 6.4 a)). A Cooper pair in the sample splits into two quasiparticles, with one going to the continuum of the same electrode and the other tunneling to excite the tip YSR state. Then, the two quasiparticles in the tip combine to form a Cooper pair, and the quasiparticle in the continuum of the sample tunnels subsequently to recover the original impurity spin. The two fermions in a Cooper pair transferring across the junction swap, resulting in a negative sign and thus a π phase shift [129, 130, 133]. This is consistent with the measurement shown in Fig. 6.2 c) that $\sqrt{I_s}R_N$ reduces due to the destructive interference at the high conductance which is the free-spin regime.

In the screened regime, the YSR ground state is non-magnetic (Fig. 6.4 b)). The transfer of a Cooper pair is similar to the clean junction case without a YSR state, and thus it is in the 0 phase and $\sqrt{I_s}R_N$ is largely unchanged.

6.6.2 About the local order parameter

In section 2.5.3, we have already discussed the common notion that $\sqrt{I_s}R_N$ (or something similar, for example the zero bias dI/dV conductance instead of I_s) measures the local order parameter, or the superfluid density according to Eq. 2.81 ($\sqrt{I_s}R_N \propto I_c R_N \propto \Delta$). In the presence of a YSR state moving across the QPT, a self-consistent calculation shows that the local order parameter on the impurity changes sign (which cannot be measured in the STM if there is no reference channel) as well as amplitude (measurable in the STM) at the QPT (Fig. 2.6 c)). It is therefore tempting to interpret the result shown in this chapter as a direct measurement of the amplitude of the local order parameter, which has been the interpretation of the Josephson measurement on the YSR impurity before [106]. Nevertheless, this is generally

not true which we are going to show in the following.

Remember that Eq. 2.81 is a simple extension of the Ambegaokar-Baratoff formula which only holds in the clean BCS junction without any impurity. Although previous theoretical work [69] suggested that the I_c is approximately proportional to the local order parameter in the presence of a YSR state, this approximation only works if the tip gap is much larger than the sample gap (which is not our case where the two gaps are equal), and it deviates especially on the impurity site which we are interested in.

Since the variation of the local order parameter is a result of the self-consistent treatment, to clarify this longstanding issue, we calculate the critical current directly under the self-consistency condition rather than simply believing that $I_c \propto \Delta$. Our collaborators in Sweden (A. M. Black-Schaffer group) have thus extended the self-consistent calculation to two electrodes (with the YSR impurity sitting at the center of a 2D square lattice coupled to a 1D chain as the other electrode via tunnel coupling) and directly calculated the critical current I_c from the energy phase relation. The result is shown in Fig. 6.5, while for the details of the calculation see Ref. [128]. The calculations of the local order parameter as well as the YSR energy in Figs. 6.5 a)-c) are consistent with our previous calculation with one electrode (Fig. 2.6).

One important result is that although the critical current I_c changes sign at the QPT, there is no significant jump in its amplitude in both self-consistent and non-selfconsistent calculations (Fig. 6.5 d)). This means that the step in the $\sqrt{I_s}R_N$ at the QPT cannot be explained by a single YSR channel model even taking into account the self-consistency condition and the reversal of the local order parameter. Therefore, we need a reference channel to reflect the $0-\pi$ transition in the YSR channel. In addition, the involvement of the self-consistency condition only results in minor changes in measurable quantities (the drastic change in the local order parameter is not directly measurable), indicating that our theoretical treatment based on a non-selfconsistent calculation is justified and sufficient.

One general remark is that I_c is not simply proportional to the local order parameter $\Delta(0)$ ($\Delta(0)$ does show a significant jump in the amplitude at the QPT while I_c does not). Consequently, special care needs to be taken when interpreting the local Josephson measurements (the Josephson STM) as the spatially resolved local order parameter.

6.7 Conclusion

In this chapter, we discussed the observation of the reduction of the Josephson current I_s when a YSR state passes through the QPT from the screened regime to the free-spin regime. We model this as the quantum interference between two channels, one being the YSR channel and the other being the BCS reference channel. The phase of the reference channel is constant, while the YSR channel acquires a π phase in the free-spin regime (0 phase in the screened regime), resulting in a destructive interference between the two channels and thus a reduction of $\sqrt{I_s}R_N$ in the free-spin regime. The underlying physics is that the presence of an
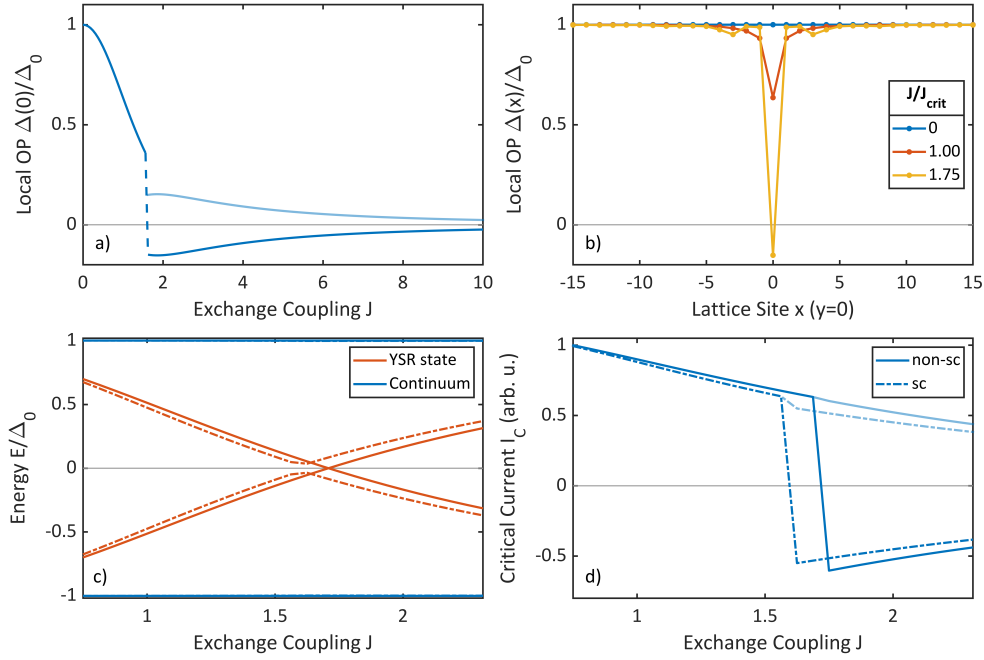
Figure 6.5 – **Self-consistent calculation vs. non-selfconsistent calculation.** a) The evolution of the local order parameter at the impurity site $\Delta(0)$ with respect to the exchange coupling J. The absolute value is plotted in light blue showing a significant jump in the amplitude at the QPT. b) The spatial variation of the local order parameter near the impurity at site 0 at different J. At $J = 0$, $\Delta(0)$ recovers the bulk value Δ_0, while for $J > J_{\text{critical}}$ (the yellow curve) beyond the QPT, $\Delta(0)$ changes sign at the impurity site. c) The YSR energy as a function of J. There is only a slight difference between self-consistent (dash-dotted lines) and non-selfconsistent (solid lines) calculations. d) The Josephson critical current I_c as a function of J, showing also only a slight correction when involving the self-consistent condition. There is no significant jump in the amplitude (with the absolute value plotted in light blue) in both cases. Taken from Ref. [128].

unpaired impurity spin in the YSR ground state in the free-spin regime causes an exchange of Fermionic operators in the Cooper pair transport, resulting in a sign change or a π phase shift. Consequently, the $\sqrt{I_s}R_N$ probes the parity change of the YSR ground state across the QPT, confirming that it is indeed a quantum phase transition. In addition, this quantum interference between two channels introduces some rudimentary phase sensitivity to the STM. It is similar to a superconducting quantum interference device (SQUID), although it has atomic sizes and the phase is controlled by the quantum properties of the YSR impurity rather than the magnetic flux. Also, the possibility to tune the YSR state continuously across the QPT and thus switching the junction between 0 and π might provide opportunities for quantum sensing and quantum computing applications.

7 Experimental connection between the Kondo effect and Yu-Shiba-Rusinov states through NRG theory[1]

So far, we have seen that the mean field (MF) approximation works very well in reproducing various YSR phenomena from the YSR energy and the junction transmission (Chapter 4) to the YSR related MARs (Chapter 5) and the Josephson effect (Chapter 6). These quantitative agreements are important results which are not naturally expected since it is *a priori* not clear that the completely ignored correlation effects in the MF approximation are not important in the YSR states. This result therefore supports the use of the MF approach and the correlation effects seem to be not important for YSR related phenomena because of the presence of the superconducting gap.

Nevertheless, the mean field approach is known to fail in reproducing the Kondo effect, where the electronic correlations are essential. Both the Kondo effect and the YSR state involve the coupling of a magnetic impurity to the surface, the only difference being the existence of superconductivity in the YSR case. This raises two questions: what is the relation between the Kondo effect and the YSR physics, and whether the correlation effects still exist in the YSR case. In the following two sections, we will discuss these two issues with the help of the numerical renormalization group (NRG) technique using the SIAM (for theoretical details see section 2.3.3). The NRG simulations are done using the "NRG Ljubljana" code [85].

7.1 Relation between YSR and Kondo phenomena

7.1.1 Introduction

The relation between the Kondo effect and the YSR state has been studied extensively both theoretically [10, 11, 81, 88, 134] and experimentally [20, 44, 45]. It has been shown theoretically through the NRG theory that the YSR energy ϵ/Δ depends on the Kondo temperature $k_B T_K/\Delta$ irrespective of the details of the SIAM parameters, and the QPT happens around $k_B T_K/\Delta = 0.2 \sim 0.3$ [81, 88]. Notice that unlike the discussion in Chapter 2, in this chapter, T_K is in the unit of temperature and $k_B T_K$ is the corresponding energy.

---

[1]This chapter concerns the publications #1 and #2 from the publication list.

In experiments, however, the $k_B T_K / \Delta$ at the QPT deviates significantly, from around 1.2 in Refs. [44, 135], around 0.7 in Ref. [46] to around 0.6 in Ref. [123]. There are several reasons for these discrepancies. First, a real system is usually more complicated that a simple spin-½ impurity considered in the theoretical calculations. Sometimes multiple impurities are involved [45] and in other cases the magnetic anisotropy is non-zero in a high spin system [20, 26], which complicates the situation. A pure spin-½ impurity is not common since the transition metal atoms widely used as magnetic atoms or magnetic centers in molecules usually exhibit high spin configurations.

Another difficulty is the experimental extraction of the Kondo temperature T_K and the existence of multiple definitions of T_K, discussed in section 2.3.2. As a rough estimation, the half-width at half-maximum (HWHM) of a Kondo peak at zero temperature limit corresponds to the $k_B T_K$, and a slightly more elaborate approach is to fit the Kondo peak to either the Fano or the Frota function (for details see section 2.3.2). These fitting functions are purely phenomenological and cannot predict the evolution of the Kondo peak in the magnetic field nor at an elevated temperature, let alone including superconductivity. Consequently, a proper microscopic theory that provides a consistent picture is urgently called for. For this, the NRG theory with the SIAM presents itself as a better solution. The details about the SIAM and the NRG theory have already been introduced in section 2.3.3.

Here, the intrinsic YSR impurities that we study on vanadium are the ones with only one pair of YSR state inside the gap, indicating a spin-½ behavior, which is also suggested in the Kondo spectra as shown by the good agreement with the spin-½ SIAM in the following. This simple system is thus a model platform to study the connection between the YSR states and the Kondo effects.

In this section, with two examples of YSR states (one continuously tunable through the QPT and the other having a constant YSR energy), we are able to relate the Kondo and YSR effects quantitatively experimentally. We fit the Kondo spectra in various magnetic fields finding consistent parameters, demonstrating the predictive power of the NRG theory. The asymmetry of the Kondo peak is captured by the asymmetry in the SIAM naturally, which offers an alternative interpretation to the Fano mechanism.

7.1.2 Kondo and YSR measurements on an impurity moving across the QPT

The YSR impurity shown in Figs. 7.1-7.5 is the same as the one in Chapter 6, which is a magnetic impurity on the tip that moves across the QPT during tip approach from the screened regime to the free-spin regime. For convenience, we reproduce the YSR measurements at zero magnetic field in Fig. 6.1 d) here as Fig. 7.1 c).

We have shown in Chapter 4 that the mechanism of the moving YSR state can be quantitatively captured by a changing Γ in the SIAM. Consequently, the example presented here is an intriguing model system where Γ changes continuously causing the YSR state to move across
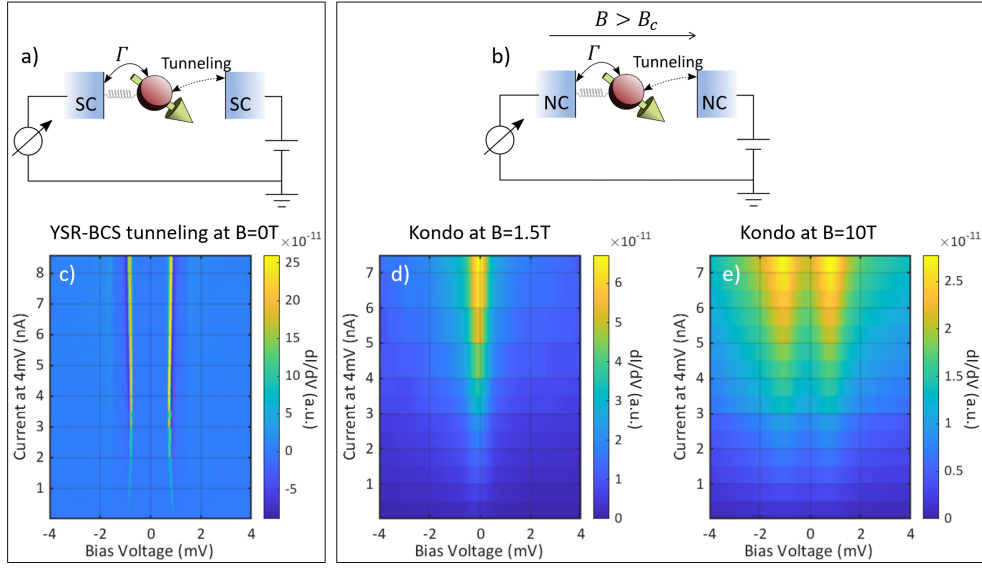
Figure 7.1 – **Spectra of a YSR impurity moving across the QPT.** a) Schematics of the experiment at $B = 0$ T. b) Schematics of the experiment in an external magnetic field higher than the critical field, quenching the superconductivity in both the tip and the sample. c) The tunneling between the YSR state on the tip and the superconducting sample at zero field, showing the QPT upon tip approach (where the peaks at $\pm(\epsilon + \Delta)$ touches $\pm\Delta$). d) The Kondo peak measured at $B = 1.5$ T. e) The split Kondo peaks measured at $B = 10$ T.

the QPT, which offers a unique opportunity to trace the Kondo effect along with it.

To reveal the Kondo effect which is masked by the superconducting gap at zero field, we apply an external magnetic field $B > 1$ T perpendicular to the surface, which quenches the superconductivity in both the tip and the sample (Fig. 7.1 b)). Basically we measure the Kondo spectra as a function of the conductance at various magnetic fields ranging from 0 T to 10 T, and those measured at 1.5 T and 10 T are plotted in Figs. 7.1 d) and e), respectively. At 1.5 T, the Kondo peak is located at zero bias, which clearly splits at $B = 10$ T. In the following, we will fit the Kondo data using the NRG theory within the SIAM.

7.1.3 Solving the SIAM using NRG theory

In section 2.3.3, we have discussed the SIAM and its numerical solution through NRG theory, and now we expand a bit on that. Recall that in the SIAM, the impurity levels at ϵ_d and $\epsilon_d + U$ couple to the continuum through Γ (Figs. 7.2 a) and b)). If the continuum is a simple metal, the Kondo effect appears in the spectrum. If the continuum is a superconductor, a pair of YSR states emerges inside the superconducting gap. For convenience, we define $\delta = \epsilon_d + U/2$, so that if $\delta = 0$, the two impurity levels are symmetric around zero, resulting in electron-hole symmetry and symmetric spectral functions around zero voltage. Therefore, the parameters of the SIAM are (δ, U, Γ) plus the superconducting gap Δ in the superconducting case. Here,

Figure 7.2 – **The single impurity Anderson model (SIAM).** a) The SIAM with a normal metal generating the Kondo effect. b) The SIAM with a superconductor generating the YSR state. c,d) Symmetric SIAM ($\delta = 0$). c) The YSR energy as a function of Γ for different U. d) The dependency of the YSR energy on $k_B T_K/\Delta$ being a universal function independent of U.
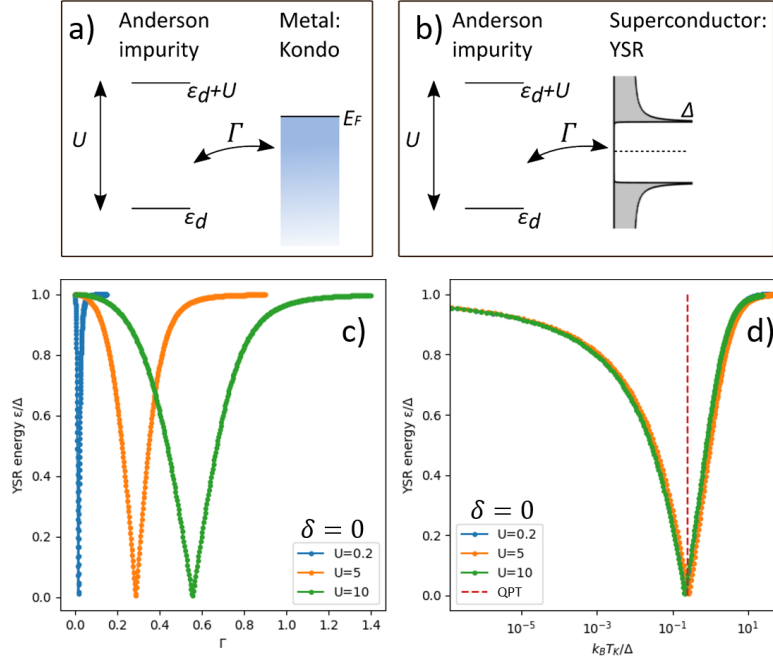
all parameters are in the unit of the band width D which is set to one. For the existence of the Kondo effect and the YSR states, the parameters satisfy $U \gg \pi\Gamma$ and $|\delta| < U/2$.

In the symmetric case ($\delta = 0$), the YSR energy $\epsilon_{\mathrm{YSR}}/\Delta$ crosses zero (the QPT) when increasing Γ, shown in Fig. 7.2 c). With different U, the behavior is similar but the shape and the QPT position change. However, if we use the definition of the Kondo temperature T_K in Eq. 2.33 and convert Γ to the ratio $k_B T_K/\Delta$ as the new x-axis, all curves lie on top of each other, indicating that the low energy physics including the YSR states only depends on the Kondo temperature, making the choice of U irrelevant (Fig. 7.2 d)). Therefore, we choose $U = 10 \gg D = 1$ in the following such that the Kondo temperature has an analytical formula and the Hubbard satellite peaks are not visible near the superconducting gap.

Now we can discuss the role of δ. Similar as U, changing δ will shift the dependency of the YSR energy on Γ (Fig. 7.3 a)), but $\epsilon_{\mathrm{YSR}}/\Delta$ depends on $k_B T_K/\Delta$ universally regardless of δ (and U), see Fig. 7.3 b). The QPT happens at around $k_B T_K/\Delta = 0.22$, consistent with literature values (see section 2.3.3).

Nevertheless, this does not make δ yet another redundant parameter. The asymmetry of the simulated Kondo peak (Fig. 7.3 c)) and the YSR states (Fig. 7.3 d)) depends critically on δ. Changing the sign of δ will exchange the electron and hole components resulting in the flipping of the energy axis, but will not influence T_K and ϵ_{YSR}.
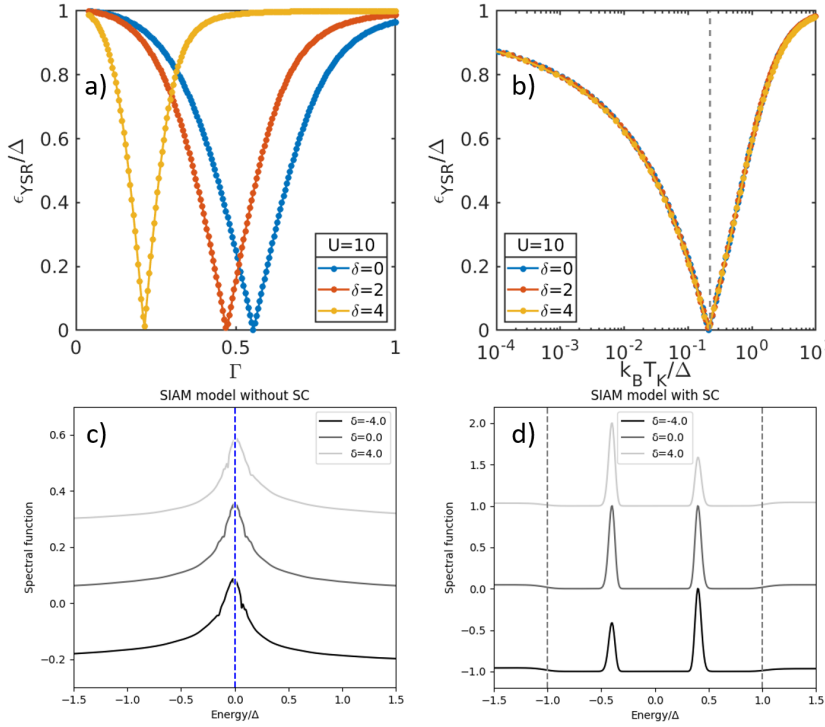
Figure 7.3 – **Asymmetric SIAM.** a,b) The SIAM with $U = 10$. a) The YSR energy as a function of Γ with different δ as a parameter. b) The YSR energy as a function of $k_B T_K/\Delta$, showing the same universal curve as in Fig. 7.2 d). c) The asymmetry of the Kondo spectrum depends on δ. d) Simulated spectra with superconductivity (SC) showing asymmetric YSR states for non-zero δ.

7.1.4 Fitting the Kondo measurements using NRG theory

Usually, the asymmetry of the Kondo effect is considered to originate from interfering tunneling pathways through the sharp resonance and through the delocalized band electrons [76] resulting in the Fano lineshape. Here, we have seen in the Josephson effect and the quasiparticle tunneling at zero field that the tunneling to the continuum (the BCS channel) is much smaller compared to the YSR channel (details see Chapter 6), and thus the Kondo peak preserves its original shape. We can actually fit the Kondo peaks at all conductances at different magnetic fields ($B = 1.5$ T and $B = 10$ T shown in Fig. 7.4) using only the SIAM model, and the fit works very well recovering even details of the spectra. This excellent agreement is another reason why we interpret the slight asymmetry observed here as the intrinsic asymmetry in the SIAM.

Let us take a closer look at the fit. To obtain the best fit for the Kondo asymmetry at 1.5 T, we find $\delta = -4$, which turns out to work quite well for reproducing the asymmetric heights of the split peaks at 10 T. Then, the peaks are fitted with Γ being the only free parameter (for the magnetic field, we assume a g-factor of 2, which reproduces the splitting at high fields). The fit not only captures the evolution of the Kondo peak width with respect to the normal state transmission $\tau = G_N/G_0$ but also the shape as well as the details of the split peaks at $B = 10$ T. Notice that the voltage range of the spectra at $B = 10$ T is sufficiently larger than that at $B = 0$ T, and the broader bumps deviating from the fit may be due to non-flat density of states or some other nearby impurities.
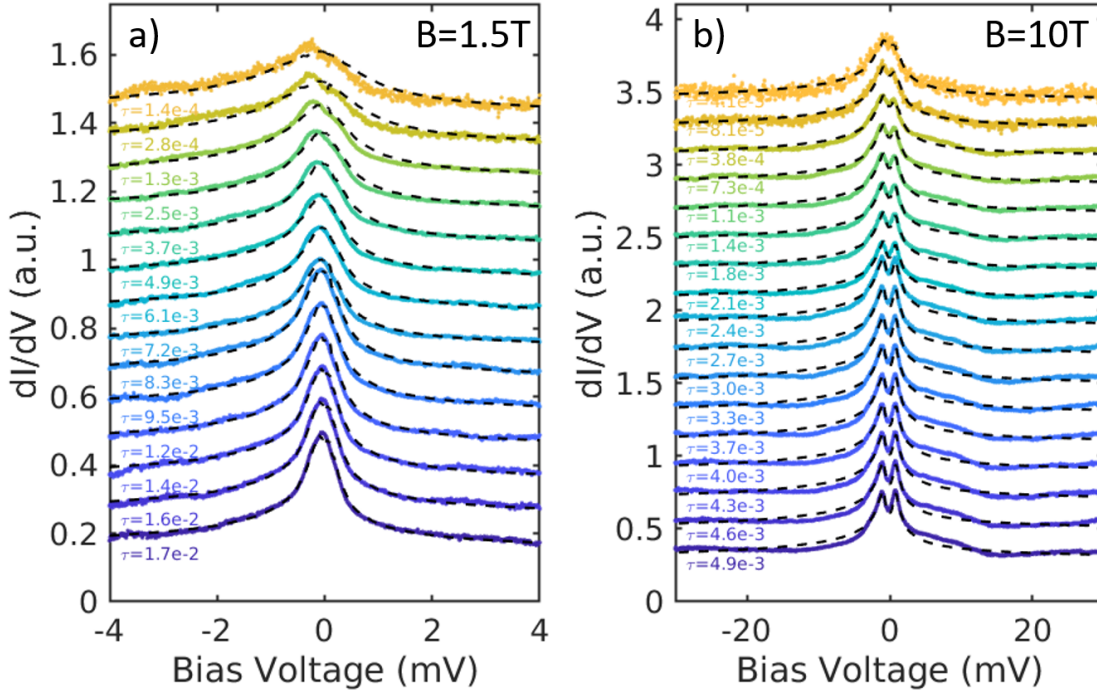
Figure 7.4 – **Fitting the Kondo spectra using the NRG theory.** We set $U = 10$ and $\delta = -4$, letting Γ as the only free parameter in the SIAM and fit the Kondo spectra at different transmission τ at $B = 1.5\,\mathrm{T}$ (panel a)) and $B = 10\,\mathrm{T}$ (panel b)).

From the fit, we can extract the change of Γ with respect to τ (Fig. 7.5 a)). Such dependence at different magnetic fields is very similar, indicating a consistent picture. One observation here is that Γ decreases with increasing τ, indicating that the impurity moves from the screen regime to the free-spin regime during tip approach, consistent with the simple analysis from the Kondo peak width in Fig. 6.1 f). We can further convert Γ to the corresponding Kondo temperature T_K using Eq. 2.33 in the following.

7.1.5 The dependence of the YSR energy on the Kondo temperature

The evolution of the YSR energy on τ can be straightforwardly extracted from the spectra in Fig. 7.1 c) (details see Chapter 6), shown in Fig. 7.5 b). Since we know that Γ decreases with increasing τ, there is no ambiguity in the two YSR branches.

We have seen that the dependence of Γ on τ does not change even in very different magnetic fields (Fig. 7.5 a)), and thus it is reasonable to further assume that such field independence largely preserves to the zero field scenario. This is sensible because we measure τ from the differential conductance at $4\,\mathrm{mV}$, which is well outside of the superconducting gap and the main Kondo resonance. Consequently, the opening of the superconducting gap at $0\,\mathrm{T}$ should not influence the measurement of τ.
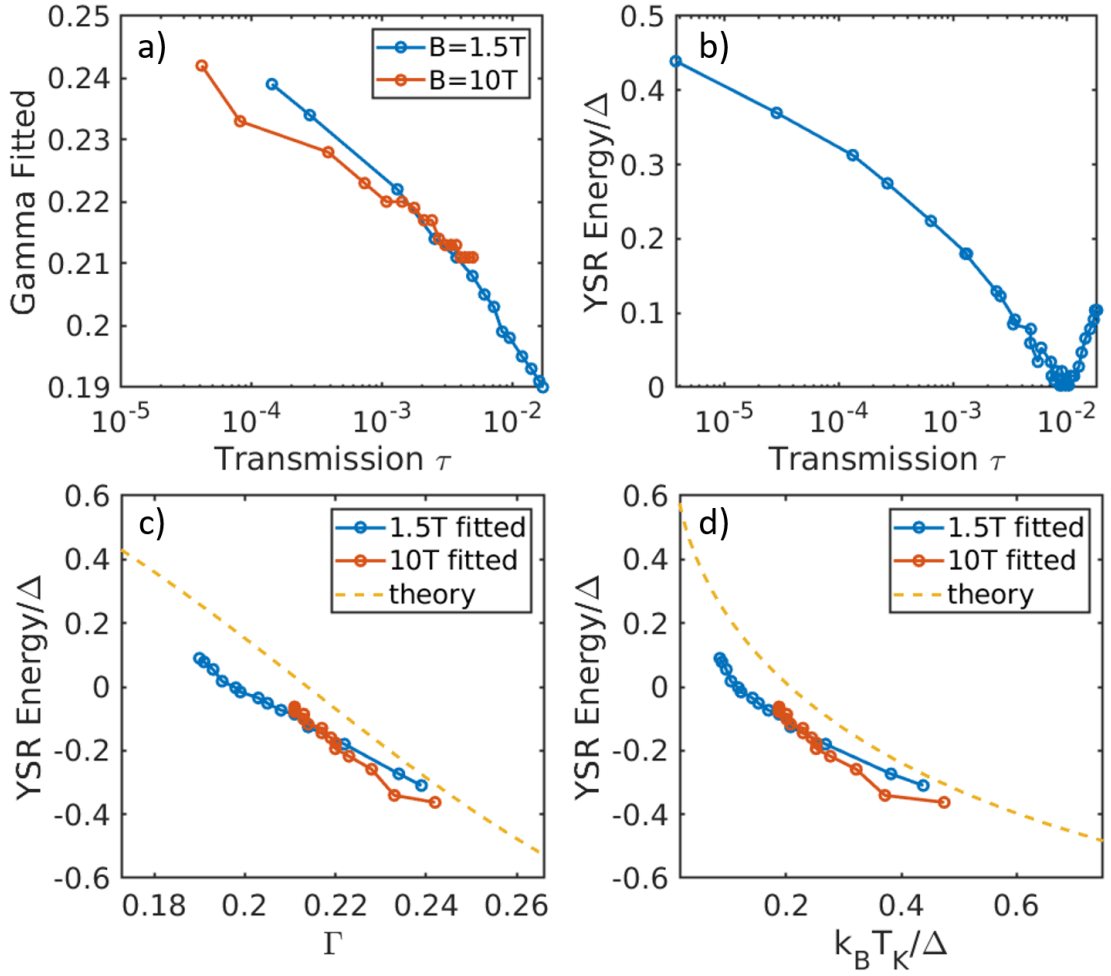
Figure 7.5 – **The relation between the YSR energy and the Kondo temperature.** a) The fitted Γ (in the unit of D which has been set to 1) from the Kondo measurements in Fig. 7.4. b) The YSR energies from the zero field measurement in Fig. 7.1 c). c) The dependence of the YSR energy on Γ. d) The comparison of the experimental data of the YSR energy as a function of the Kondo temperature with the theoretical scaling.
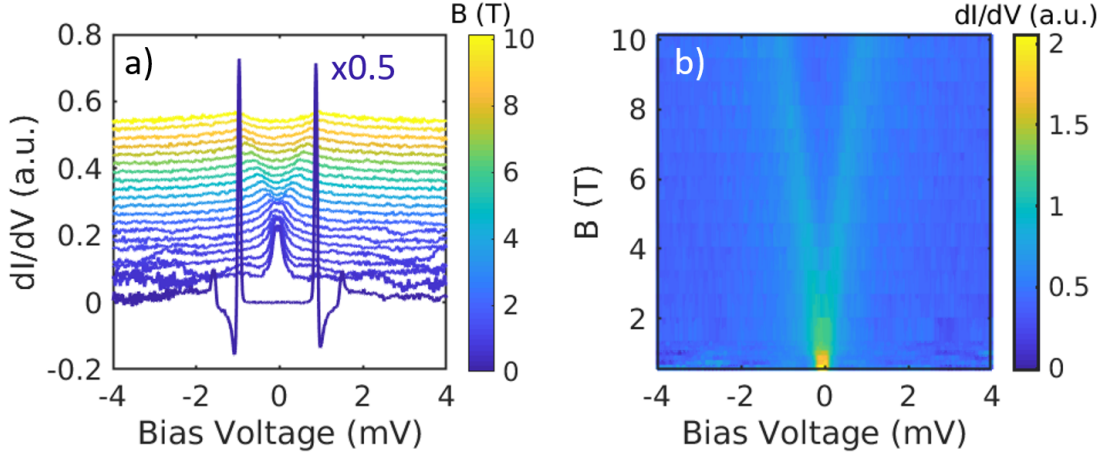
Figure 7.6 – **Magnetic field dependent** dI/dV **spectra measured on a tip YSR impurity with a constant energy.** The dI/dV spectra at various magnetic fields from 0 to 10.2 T are plotted as a) a cascade plot and b) a color plot, both showing the emergence of a Kondo peak when the superconductivity is quenched which splits into two peaks at higher magnetic fields. In a), the spectra are offset and the YSR spectrum at 0 T is reduced by 50% in height for clarity. In b), only the spectra in non-zero field are plotted.

Now we combine Figs. 7.5 a) and b) and plot the normalized YSR energy versus the coupling Γ (Fig. 7.5 c)). The theory curve is shown as a dashed line for reference. The general trend as well as the absolute value for Γ fits the theoretical prediction quite well. Notice that the deviation in Γ is only a few percent.

We further convert Γ to T_K and plot the standard plot of ϵ_{YSR}/Δ as a function of $k_B T_K/\Delta$ in Fig. 7.5 d). The general shape of the curve closely resembles the theoretical prediction. Nevertheless, the QPT point moves to lower Kondo temperature, to around $k_B T_K/\Delta = 0.1$. We will discuss possible origins of this deviation later, but first, we will present another example where the agreement is better.

7.1.6 Another example of a non-moving YSR state

For a YSR state that changes energy during tip approach, to compare the YSR and the Kondo measurements, we have to assume that the atomic force is independent of the magnetic field. Although this is reasonable because for the Lennard-Jones force it is indeed the case, there may be corrections to it. Therefore, it is beneficial to investigate another example where the YSR energy is independent of the transmission (the relative change of the YSR energy is < 4% between $\tau \approx 3 \times 10^{-5}$ to 3×10^{-3}). The YSR impurity is on the tip also, and the measurements presented below are all measured around $\tau = 2.7 \times 10^{-4}$. Consequently, the procedure is simpler than before in the sense that we only need to stay at a constant τ and measure the dI/dV spectra at different magnetic fields.

The experimental data is collected in Fig. 7.6. The spectrum at 0T is a typical YSR-BCS
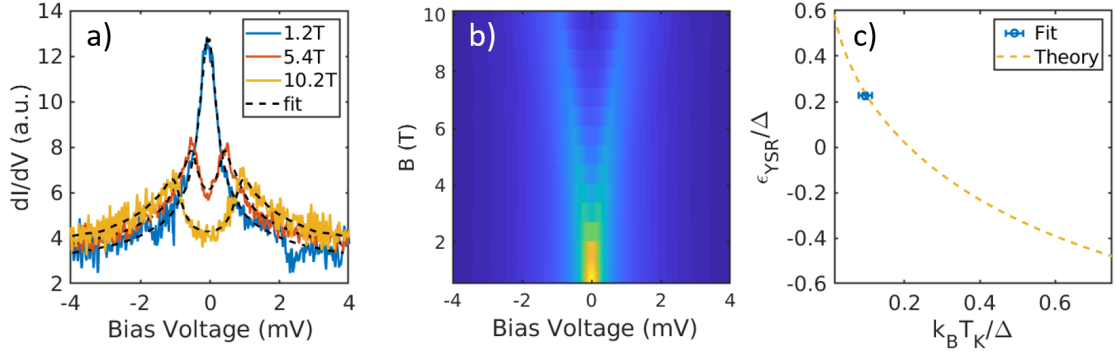
Figure 7.7 – **Fits using the SIAM and the NRG theory.** a) The spectra in different magnetic fields are fitted independently. b) Using the average Γ from the fits in different fields, the evolution of the Kondo spectra in the magnetic field is simulated, agreeing quantitatively with the measurements shown in Fig. 7.6 b). c) The normalized YSR energy as a function of $k_B T_K/\Delta$ agreeing with well the theoretically prediction.

spectrum with a pair of sharp YSR peaks inside the gap region, from which we extract the YSR energy $\epsilon_{YSR} = 0.219\Delta$. Above around 1T, the superconducting gap on both the tip and sample quenches completely and the spectrum features a Kondo peak split by the magnetic field. Between 0T and 1T, the superconducting gap is not fully closed yet the Kondo peak already emerges, which will not be discussed here.

Notice that in this example, the YSR peaks as well as the Kondo features are symmetric with respect to zero bias voltage, indicating the symmetric case ($\delta = 0$) in the SIAM, which further simplifies the analysis. For the fitting, we fix $U = 10, \delta = 0, g = 2$ and let Γ be the only free parameter. We fit the Kondo spectra in different magnetic fields independently (allowing different Γ for each magnetic field) in order to give an error estimation in the horizontal direction in Fig. 7.7 c). It turns out that the fitted Γ is similar for different fields being $\Gamma = 0.50 \pm 0.01$, and the fit works excellent, shown in Fig. 7.7 a). Using the mean value of all fitted Γ as an estimate of the final Γ, the simulation in different magnetic fields (Fig. 7.7 b)) is very close to the measured data (Fig. 7.6 b)), further indicating the consistency.

As usual, we convert Γ to T_K and plot the YSR energy as a function of $k_B T_K/\Delta$ in Fig. 7.7 c). Since there is only one YSR energy, there is only one data point for the measurement. Nevertheless, it lies right on top of the theory curve. Notice that there is no scaling in the analysis and everything is modelled consistently within the SIAM using the NRG theory, this agreement is a strong evidence to support the NRG theory quantitatively and to indicate again that the tip YSR impurity studied is a spin-½ impurity (because of the agreement with the spin-½ SIAM model).

7.1.7 Discussion

We have presented two examples of tip YSR states, with the first (with a moving YSR state) showing some deviation from the theory (though smaller compared to other reported values) while the other shows excellent agreement. There are two main differences. The second example is electron-hole symmetric while the first one is not. However, this should not result in deviations because we find that the result is not sensitive to the choice of δ for the first case.

Another difference is that the first example is the one that features a moving YSR state. The deviation from theory may thus originate from a different force on the impurity due to the presence of superconductivity. Although the main Lennard-Jones force which pulls the impurity up does not depend on a magnetic field, the magnetic impurity may feel an additional force if the junction is superconducting. Further research is necessary to quantify this effect, but given that the actual change in Γ needed is only a few percent, this is a plausible assumption. Another possibility is the existence of nearby impurities that interacts and complicates the system.

7.1.8 Conclusion

The data shown above sheds more light on the relation between the Kondo and the YSR phenomena. First, the spin-½ impurity shows a simple Kondo peak with small asymmetry thanks to the suppression of the tunneling channel to the continuum, allowing for the description of the spectrum completely within the simple SIAM. Second, since everything in this analysis is defined consistently in the SIAM, there is no ambiguity on the definition of the Kondo temperature compared to the determination of the Kondo temperature by fitting phenomenological functions. The fit to the microscopic SIAM model is precise and the evolution in the magnetic field is reproduced quantitatively. Third, the impurity is tuned continuously through the QPT, offering a unique opportunity to trace the evolution of the universal scaling with fine details. In addition, at 10 mK experimental temperature, thermal broadening effect can be ignored.

Consequently, we have presented a model experimental system for verifying the NRG theory by comparing the YSR and Kondo phenomena. Agreements are observed, but the deviation in the moving YSR case calls for further investigation. In the next section, we will show that the Kondo effect not only relates to the YSR states, but also influences the current in the superconducting state.

7.2 Remaining correlation effects in the superconducting state

7.2.1 Introduction

Up till now, we have seen that the Kondo and the YSR physics are related by the universal scaling shown in Figs. 7.5 d) and 7.7 c). However, this only means that both phenomena can be described in the same parameter space in the SIAM and it does not answer the question

whether correlation effects still exist in the superconducting case and how important they are. From the quantitative agreement between various aspects of the YSR observations and the mean field model without correlations shown in Chapters 4, 5 and 6, it is tempting to think that the correlation effects are not important for YSR physics.

Additionally, for the YSR state to occur inside the gap, the Kondo temperature (and consequently the peak width) will need to be on the same order of the superconducting gap, which will be masked by the superconducting gap and thus will be largely invisible in the presence of YSR states. As a side note, the co-existence of the YSR state on top of a large Kondo peak commonly seen in the literature usually comes from an additional broad Kondo peak irrelevant to the YSR state and the related narrow one is only revealed via fitting double peaks [26, 44, 46, 135], which is not the case in our experiments. Hence, the question becomes more pressing: if the Kondo peak becomes shadowed by the gap and there is not much visible in the density of states, how do we know the existence of the correlation effects in the presence of YSR states?

To shed light on this, we compare the difference between the mean field calculations and the NRG simulations (Fig. 7.8), which reflects the correlation effects. In the following, we will look at the $I(V)$ curves rather than the conventional dI/dV measurement and propose the offset current I_{off} (the difference between the measured tunneling current and the current from an ohmic junction at the same transmission which is discussed in more detail later) as an indicator of the remaining correlation effects and confirm the existence of I_{off} experimentally.

7.2.2 The offset current and correlation effects

The NRG simulations are done with the SIAM parameters $U = 10$, $\delta = 0$ (and $\Delta_{SC} = 760 \times 10^{-6}$ in case of the YSR calculations which corresponds to the experimental gap) with different Γ and the mean field calculations are conducted using Eq. 2.20 matching the YSR energy to the corresponding NRG calculation (Fig. 7.8). In the NRG simulations of the YSR states, the coupling at the QPT is around $\Gamma_c = 0.555$.

If $\Gamma \rightarrow 0$, the Kondo peak vanishes and the YSR state merges into the continuum (Fig. 7.8 a)). The simulated $I(V)$ curve in the Kondo situation is a straight line similar to an ohmic junction, while those in the mean field case and the NRG case for the YSR-BCS tunneling overlap, both showing a gap within $\pm 2\Delta_{SC}$.

We define the difference between the measured current and the current from an ohmic junction assuming the same transmission (the differential conductance well outside of the gap) as the offset current I_{off}, labeled in Fig. 7.8 g). Experimentally, I_{off} is measured around $V = 4\,\text{mV}$ which is much larger than the gap. Now going back to Fig. 7.8 e), the offset current is nearly zero for all situations.

Now we increase Γ to 0.45 which has not reached the QPT. The Kondo peak is narrower than the superconducting gap, and in the presence of superconductivity, there is only a tail of the
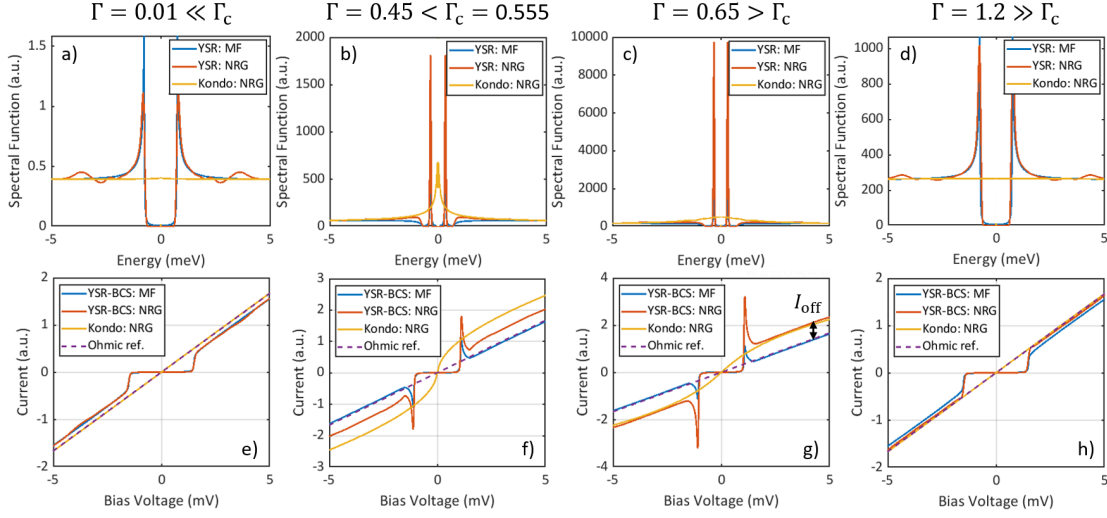
Figure 7.8 – **Simulations of the density of states and the $I(V)$ curves with the mean field theory (MF) and the NRG theory.** The SIAM parameters for the NRG calculations are $U = 10$, $\delta = 0$ and $\Delta_{SC} = 760 \times 10^{-6}$, all in the unit of $D = 1$. a)-d) The density of states (DOS). e)-h) The $I(V)$ curves, where the probing electrode is a metal with a constant DOS in the Kondo case and a BCS superconductor with the same gap in the YSR cases. The offset current I_{off} is defined in g) as the difference between the $I(V)$ and the ohmic reference assuming the same differential conductance at a high bias voltage. a),e) $\Gamma = 0.01$ which is close to zero and d),h) $\Gamma = 1.2$ which is far across the QPT (the QPT is at $\Gamma = \Gamma_c = 0.555$ here), both featuring the YSR state merging into the coherence peaks recovering the clean BCS limit. The NRG calculations are nearly the same as the MF ones, and there is no offset current. b),f) $\Gamma = 0.45$ before the QPT (the free-spin regime) and c),g) $\Gamma = 0.65$ after the QPT (the screened-spin regime) showing YSR states inside the gap as well as a significant offset current in both the superconducting case and the Kondo case in the NRG simulation but not in the MF case.

Kondo peak visible at the gap edge that differs from mean field theory (Fig. 7.8 b)). However, in the $I(V)$ (Fig. 7.8 f)), the difference is much more obvious, especially in the offset current. For both NRG calculations (Kondo and YSR), the offset current is significant, while for the mean field calculation, the offset current remains zero.

We further increase Γ to 0.65 beyond the QPT. The YSR energy is comparable to the previous case, but the Kondo peak in the normal conducting case is much wider (Fig. 7.8 c)). The difference between the NRG and the mean field calculation in the YSR density of states is still not obvious, which only shows up near the gap edge. However, the $I(V)$ shows a similar behavior that the mean field calculation yields no offset current, while the NRG simulations result in a sizable offset current.

If Γ increases further far across the QPT ($\Gamma = 1.2$ shown in Figs. 7.8 d),h)), the Kondo peak is much wider than the superconducting gap and the spectrum effectively recovers the BCS limit. The offset current in both mean field and NRG simulations returns to zero (Fig. 7.8 h)).
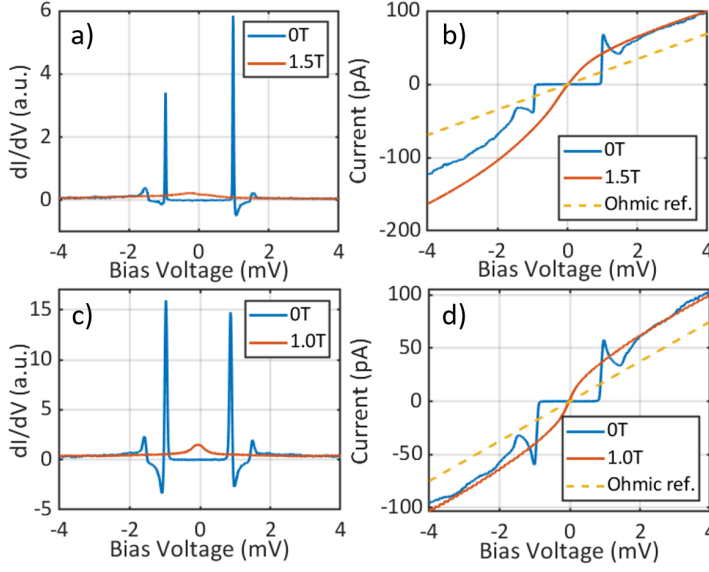
Figure 7.9 – **The dI/dV and $I(V)$ curves of two examples showing significant offset current.** a),b) The impurity shown in Fig. 7.1 and c),d) the impurity shown in Fig. 7.6. In both cases, the dI/dV spectrum does not show signs of the remnant Kondo peak in the superconducting case, but the offset current clearly confirms the existence of Kondo correlations.

The offset current in the Kondo case is straightforward to understand. It basically reflects the enhanced density of states near the Fermi energy. When the superconductivity is introduced, a gap opens, but the spectral weight of the original Kondo peak gets redistributed near the gap edges, still contributing to an offset current as a first approximation. However, the offset current may be different between the Kondo case and the YSR case depending on the side of the QPT, which may be due to incomplete screening in the free spin regime calling for further understanding.

To summarize, in the mean field description, the offset current is always zero, while in the NRG simulations, the offset current is sizable if the YSR state is seen clearly inside the gap. Since the main difference between the NRG and the mean field theory is the inclusion of the correlation effects, the offset current is an indicator that there are still correlation effects in the superconducting state.

7.2.3 Measuring the offset current

In experiments, we do observe the offset current in the presence of a YSR state. For the case of the moving YSR state shown earlier in this chapter (Fig. 7.1), the Kondo and the YSR measurements at the same transmission are plotted in Figs. 7.9 a) and b). Indeed, in the dI/dV spectrum at 0 T, there is no obvious sign of the Kondo effect due to the opening of the superconducting gap, but in the $I(V)$ curve, the offset current is obvious. In this case, the offset current is also asymmetric, like the YSR state and the Kondo peak.

For the case of the non-moving YSR state shown in Fig. 7.6, the spectra are plotted in Figs. 7.9 c) and d). In the $I(V)$ curve, the offset current is significant and symmetric (consistent with the symmetry of the Kondo peak and the YSR states).

Notice that the offset current also depends on the relative channel transmission through the YSR channel (for the discussion of the two channels see Chapters 4 and 6). If the BCS channel dominates, the offset current as well as the intensity of the YSR-BCS tunneling peaks in the spectrum will be suppressed.

7.2.4 Conclusions

In this section, we have presented the offset current as a signature of remnant Kondo correlations in the presence of superconductivity. Even if the superconducting gap masks the Kondo peak in the dI/dV spectra, the offset current still serves as an indication of the existence of the Kondo correlations.

The observation of the offset current also justifies the renormalization of the conductance for the Josephson effect in the presence of the YSR state in Chapter 6. Because the offset current basically reflects an enhancement of the density of states near the Fermi energy, its existence suggests that the normal state density of states seen by the Josephson effect is enhanced by the Kondo peak regardless of the competition between the Kondo effect and the superconductivity discussed in Ref. [44].

8 Tunneling processes between Yu-Shiba-Rusinov states[1]

8.1 Introduction

In the previous chapters we have dealt with only one YSR state in the junction, and the tunneling happens between the YSR state and a clean BCS superconductor. The YSR state is a discrete level inside the superconducting gap, featuring a pair of sharp peaks in the dI/dV spectrum. Nevertheless, a YSR level is much more than a sharp density of states. A single energy level is the fundamental building block of the electronic structure and carries coherence as well as possible entanglement when protected by a gap, as in the case of a YSR state. The lifetime of such a state is greatly enhanced due to the presence of the gap, and is interesting as a model quantum system. In addition, the level is spin-nondegenerate for the YSR case, further indicating the presence of the spin information. Unfortunately, these intriguing properties are not accessible in the YSR-BCS junction because of the tunneling to the continuum which relaxes quickly and is spin degenerate.

Therefore, it is compelling to build a junction with one YSR state on each electrode and realize the tunneling between two YSR states, which we call *Shiba-Shiba tunneling*. The advantage is that it is the elementary tunneling process between single levels which indicates a coherent transport and a long lifetime. Nevertheless, it has been challenging to introduce a YSR impurity onto the tip reliably, especially one with a single pair of YSR states inside the gap. Now in this thesis, we have demonstrated the possibility to fabricate such tips with desirable properties controllably, paving the way for the realization of a Shiba-Shiba junction.

In the next two sections, we will move such YSR tips onto the intrinsic YSR states on the sample, and demonstrate the basic transport properties of Shiba-Shiba tunneling and the essential role of the spin in the tunneling process.

---

[1]This chapter is based on the publications #6 and #7 from the publication list.

Figure 8.1 – **Shiba-Shiba tunneling.** a) Schematics of the experiment. b) Topography of the surface. c) The in-gap current revealing the intrinsic YSR states in the same area in b). d) The dI/dV spectra of different impurity configurations at 10 mK, where no thermal process is visible. Shiba-Shiba tunneling features a pair of peaks in the shaded area with significant negative differential conductance (yellow curve). Taken from Ref. [114].
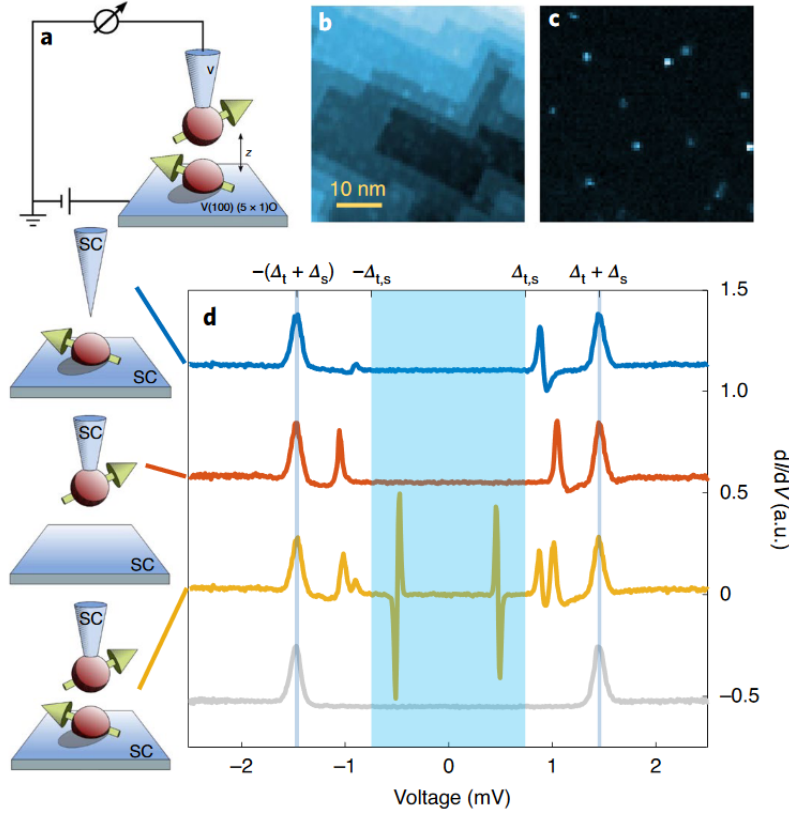
8.2 Shiba-Shiba tunneling

8.2.1 Quasiparticle tunneling involving YSR states

The schematics of the Shiba-Shiba tunneling junction is shown in Fig. 8.1 a), where both tip and sample are vanadium being superconducting with one magnetic impurity on the sample and one on the apex of the tip generating YSR states. To search for intrinsic YSR states on the sample, spectroscopy measurements are done in a grid manner. The current signal just inside the superconducting gap is plotted in Fig. 8.1 c) showing the YSR states as bright spots, and the surface topography in the same area is presented in Fig. 8.1 b) showing atomic terraces.

With tip and sample YSR states as building blocks, there are four possible combinations and respective quasiparticle tunneling spectra at low conductance at 10 mK are plotted in Fig. 8.1 d). If both the tip and sample are clean without a YSR state, the tunneling spectrum will be the gray curve in Fig. 8.1 d), with two coherence peaks at the edge of the gap at $eV = \pm|\Delta_s + \Delta_t|$. If there is one YSR state in the junction (either on the tip or on the sample), the spectra will be similar to the blue and red curves in Fig. 8.1 d), featuring one pair of YSR-BCS tunneling peaks inside the gap at $eV = \pm|\epsilon_{s,t} + \Delta_{t,s}|$.

Now if the YSR tip shown in the red curve is moved to form a tunnel junction with the sample YSR impurity shown in the blue curve, the resulting junction is a Shiba-Shiba junction featuring
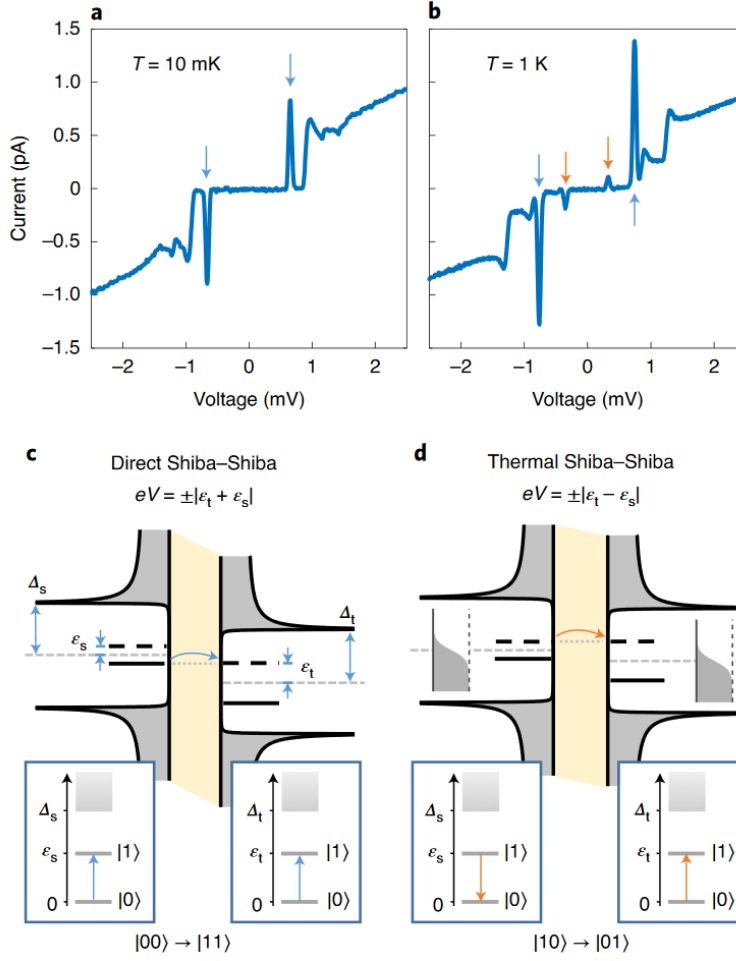
Figure 8.2 – **Direct and thermal Shiba-Shiba tunneling.** a) At 10 mK, only the direct Shiba-Shiba peaks at $eV = \pm|\epsilon_s + \epsilon_t|$ (blue arrows) are observed. b) At higher temperature (1 K), the thermal peaks at $\pm|\epsilon_s - \epsilon_t|$ (orange arrows) are also observed besides the direct peaks. c) The energy diagram for the direct Shiba-Shiba tunneling process, where both YSR states are excited during tunneling in the many-body picture. d) The energy diagram of the thermal Shiba-Shiba tunneling process, where the excitation transfers from one YSR state to another YSR state. Taken from Ref. [114].

the yellow curve in Fig. 8.1 d). It inherits the coherence peaks and the YSR-BCS tunneling peaks at the same positions, but there is a pair of new features inside the shaded area where usually no dI/dV signal is expected at low conductance and low temperature due to the opening of a superconducting gap. This pair of peaks is very sharp with a significant negative differential conductance, indicating the involvement of sharp levels in the tunneling process. These features are attributed to the tunneling between the YSR states, called *Shiba-Shiba tunneling*.

It is actually more intuitive to look at the current voltage characteristics (the $I(V)$ curve) in Figs. 8.2 a) and b) rather than the dI/dV spectrum. At 10 mK, there is only one pair of peaks in the current at $eV = \pm|\epsilon_s + \epsilon_t|$, which we call *direct Shiba-Shiba tunneling*. At higher temperature (1 K), one additional pair of peaks of suppressed intensity emerges at lower bias voltages $eV = \pm|\epsilon_s - \epsilon_t|$, which is called *thermal Shiba-Shiba tunneling*. Here, we let $\epsilon_{s,t} \geq 0$.

8.2.2 Direct and thermal Shiba-Shiba tunneling

The energy diagram of the direct Shiba-Shiba tunneling process is shown in Fig. 8.2 c), where a quasiparticle transfers from the filled level of one electrode to the unfilled level of the counter-electrode, at the sum of the YSR energies as the bias voltage. The many-body picture reflects the underlying physics better that a YSR state consists of a ground state ($|0\rangle$) and an excited state ($|1\rangle$) separated by the YSR energy (insets of Fig. 8.2 c)). Both taking one quasiparticle away from the YSR impurity and adding one quasiparticle to the YSR impurity excite the YSR state. Therefore, in the direct Shiba-Shiba tunneling process, the transport of one quasiparticle excites both the tip and sample YSR states, resulting in a transition from $|00\rangle$ to $|11\rangle$.

As for the thermal Shiba-Shiba tunneling process shown in Fig. 8.2 d), a quasiparticle transfers between two electron-like (or two hole-like) levels at the bias voltage $eV = \pm|\epsilon_s - \epsilon_t|$. Since there is no quasiparticle to tunnel from the level above the Fermi surface (also there is no space for a quasiparticle to tunnel into the level below the Fermi surface) unless there is thermal excitation, this Shiba-Shiba process is thus called thermal Shiba-Shiba tunneling and is suppressed by the Boltzmann factor. In the many body picture, it swaps the excitation from $|10\rangle$ to $|01\rangle$.

One feature is that the spectroscopic peaks are well separated since $|\epsilon_s - \epsilon_t| \leq |\epsilon_s + \epsilon_t| \leq |\epsilon_{s,t} + \Delta_{t,s}| \leq |\Delta_{s,t} + \Delta_{t,s}|$, allowing for addressing different processes individually in a single spectrum measured.

The thermal processes will be covered in more detail in the second part of this chapter (section 8.3) about the role of the spin in Shiba-Shiba tunneling. For now, we focus only on the direct processes at 10 mK.

8.2.3 Relaxation channels for YSR states

To support a continuous tunneling current, the YSR states need to relax to the ground state after being excited during the tunneling process. There are two possibilities. One is that the YSR states relax through the intrinsic channels ($\Gamma_{s,t}$ in Fig. 8.3 a)) within the respective electrodes. Since there is no charge transfer through the junction, it is the intrinsic property of the YSR states and is independent of the transmission τ.

Another possible relaxation pathway occurs as quasiparticles transfer across the junction, shown as the process one and two in Fig. 8.3 a). These processes depend on the tunnel coupling and are thus not important at the low conductance limit. Also, the existence of such processes depends on the YSR energies. Process one only exists when $2\epsilon_s + \epsilon_t \geq \Delta_t$, while process two only occurs when $2\epsilon_t + \epsilon_s \geq \Delta_s$. This is summarized in Fig. 8.3 b). Both processes can occur at the same time if the system is in the orange regime shown in Fig. 8.3 b). If both YSR energies are small, the Shiba-Shiba system is in the blue regime where the relaxation channels are reduced to the minimum which are the intrinsic ones.
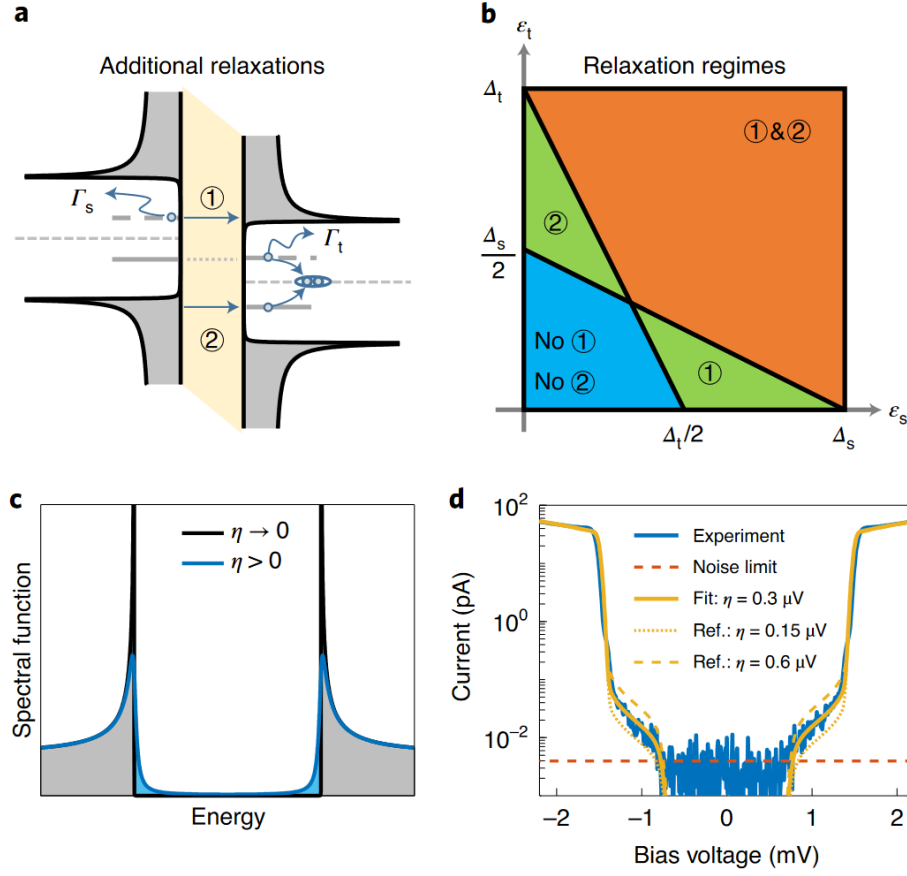
Figure 8.3 – **Relaxation processes.** a) Possible relaxation processes including the intrinsic ones ($\Gamma_{s,t}$) and the ones across the junction (process one and two). b) The existence of process one and two depends on the YSR energies. In the blue regime, the intrinsic channels are the only relaxation mechanisms. c) The Dynes' parameter η phenomenologically represents the quasiparticle background inside the gap. d) A fit of the clean BCS-BCS tunneling $I(V)$ curve yields $\eta = 0.3\,\mu$eV, confirming the existence of a small but finite background as the intrinsic relaxation pathway. Taken from Ref. [114].

At 10 mK, the thermal relaxation to the continuum is nearly zero (the Boltzmann factor for the vanadium superconducting gap of 750 μeV is around 10^{-383}), and thus ideally, the intrinsic lifetime of the YSR states is expected to be nearly infinite. The non-zero Shiba-Shiba current measured, however, shows that this cannot be true and there must be other intrinsic relaxation mechanisms even close to zero temperature as in our case.

One possibility is the existence of a finite quasiparticle background in the superconducting gap that provides the relaxation pathways without the need of thermal energy. Phenomenologically, the small but finite Dynes' paramater η in the Green's function (recall Fig. 2.2) accounts for such a background. If $\eta > 0$, the quasiparticle density of states inside the gap is no longer zero (Fig. 8.3 c)). In addition, in a simple Green's function description, the YSR state is a Lorentzian peak with the width η (see Eq. 2.25).
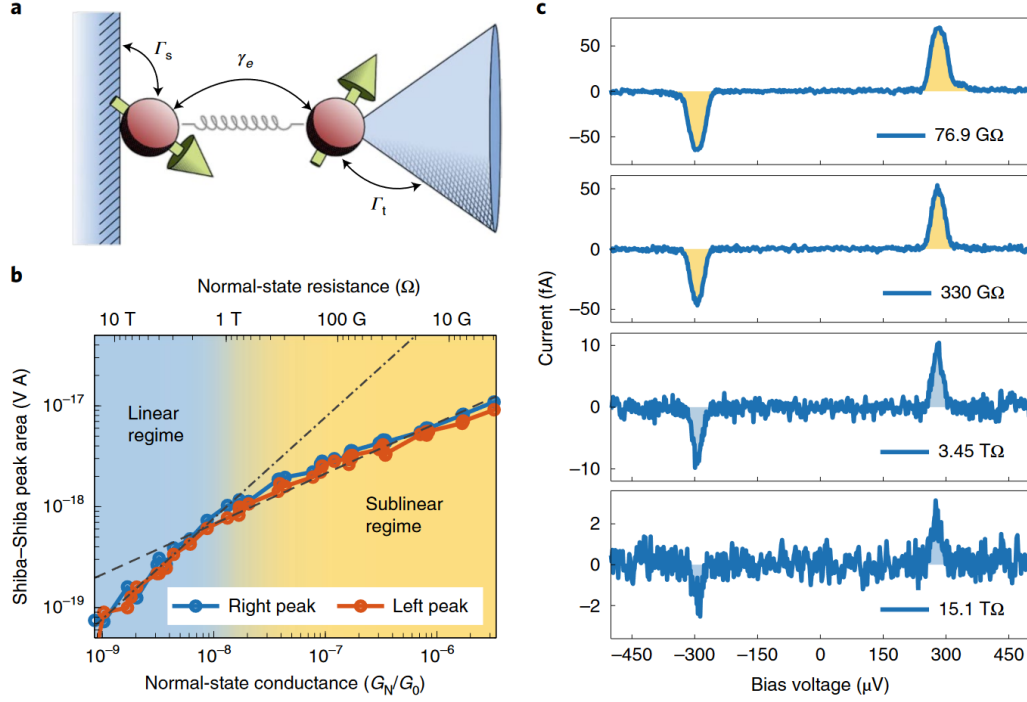
Figure 8.4 – **Tunneling dynamics.** a) The diagram of the charge transport showing the intrinsic relaxations $\Gamma_{s,t}$ and the tunnel coupling γ_e. b) The Shiba-Shiba current peak area as a function of the conductance, showing the linear to sublinear transition. The dash-dot (dashed) line indicates linear (square root) behavior. c) The Shiba-Shiba current curves at different normal state conductance/resistance. Taken from Ref. [114].

To quantify this effect, we measured the $I(V)$ characteristic of the same junction without any YSR states (the case of the gray curve in Fig. 8.1 d)). The current plotted in the logarithmic plot to reveal tiny signals is shown in Fig. 8.3 d). It can be seen that the current within the gap region $|eV| \le (\Delta_s + \Delta_t)$ is non-zero, while the signal within $|eV| \le \Delta_{s,t}$ is basically zero below the detection limit. This agrees quantitatively with the description of the Dynes' parameter and a fit yields around $\eta = 0.3\,\mu\text{eV}$ (the yellow solid line in Fig. 8.3 d)). This fit is quite sensitive because doubling or reducing η by half results in significant changes in the curve (yellow dashed and dotted lines in Fig. 8.3 d)).

8.2.4 Conductance dependence of Shiba-Shiba tunneling

Now we show one example of Shiba-Shiba tunneling in the blue regime at 10 mK, where the only relaxation possible is through the intrinsic channels $\Gamma_{s,t}$ (Fig. 8.4 a)). The intrinsic relaxations are the properties of the impurities independent of the tip sample distance, but we can control the tunnel coupling γ_e precisely by changing the tip height (and thereby changing the conductance).

We measure the Shiba-Shiba current peak at different conductance spanning several orders of magnitude (Fig. 8.4 c)), and summarize the area enclosed by the peak (the shadings in Fig. 8.4 c)) as a function of the normal state conductance in Fig. 8.4 b).

At low conductance, the Shiba-Shiba peak area scales linearly with the conductance, as expected for a normal quasiparticle tunneling process. However, at higher conductance, the scaling becomes sublinear. This is because at low conductance, the bottleneck of the tunneling current is the tunnel coupling γ_e, while at high conductance, the intrinsic relaxation rate limits the tunneling current reducing it below the linear dependency.

The above understanding is further supported theoretically by solving the master equations for the dynamics presented in Ref. [114] which is done by our collaborators in Ulm (J. Ankerhold group). The Shiba-Shiba peak in the blue regime in Fig. 8.3 b) can be described by a Lorentzian function

$$I_0(\nu) = \frac{e}{\hbar} \frac{2\Gamma_s \Gamma_t}{\Gamma_s + \Gamma_t} \frac{|\gamma_e|^2}{|\gamma_e|^2 \frac{(\Gamma_s + \Gamma_t)^2}{\Gamma_s \Gamma_t} + \frac{(\Gamma_s + \Gamma_t)^2}{4} + (e\nu)^2}, \tag{8.1}$$

where $\Gamma_{s,t}$ are the intrinsic lifetime of the sample and the tip YSR states in the unit of the energy, ν is the voltage detuning from the resonance $e\nu = eV \pm |\epsilon_s + \epsilon_t|$ and $|\gamma_e|^2 \propto G_N$.

The $P(E)$ function discussed in section 2.4.2 will further broaden the peak experimentally. However, the area of the peak is conserved

$$\begin{aligned}
A &= \int_{-\infty}^{\infty} I_0(\nu) d\nu \\
&= \frac{4\pi}{\hbar} \frac{(\Gamma_s \Gamma_t)^{3/2}}{(\Gamma_s + \Gamma_t)^2} \frac{|\gamma_e|^2}{\sqrt{4|\gamma_e|^2 + \Gamma_s \Gamma_t}}.
\end{aligned} \tag{8.2}$$

At low conductance where $4|\gamma_e|^2 \ll \Gamma_s \Gamma_t$, the peak area $A \propto |\gamma_e|^2 \propto G_N$ grows linearly with the conductance. At high conductance, $4|\gamma_e|^2 \gg \Gamma_s \Gamma_t$, and thus $A \propto |\gamma_e| \propto \sqrt{G_N}$ scales sublinearly. Such a square root dependence is indeed observed in the experiment (Fig. 8.4 b) dashed line.)

8.2.5 Measuring the lifetime

At the transition between the two regimes, $4|\gamma_e|^2 = \Gamma_s \Gamma_t$. The area thus becomes

$$A_{\text{trans}} = \frac{\pi}{\sqrt{2}\hbar} \left(\frac{\Gamma_s \Gamma_t}{\Gamma_s + \Gamma_t} \right)^2 = \frac{\pi}{\sqrt{2}\hbar} \Gamma_{\text{tot}}^2, \tag{8.3}$$

where Γ_{tot} is the combined lifetime broadening satisfying $\frac{1}{\Gamma_{\text{tot}}} = \frac{1}{\Gamma_s} + \frac{1}{\Gamma_t}$. If the tip and sample YSR states have the same lifetime $\Gamma_s = \Gamma_t = \Gamma$, Eq. 8.3 further reduces to

$$A_{\text{trans}} = \frac{\pi}{4\sqrt{2}\hbar} \Gamma^2. \tag{8.4}$$
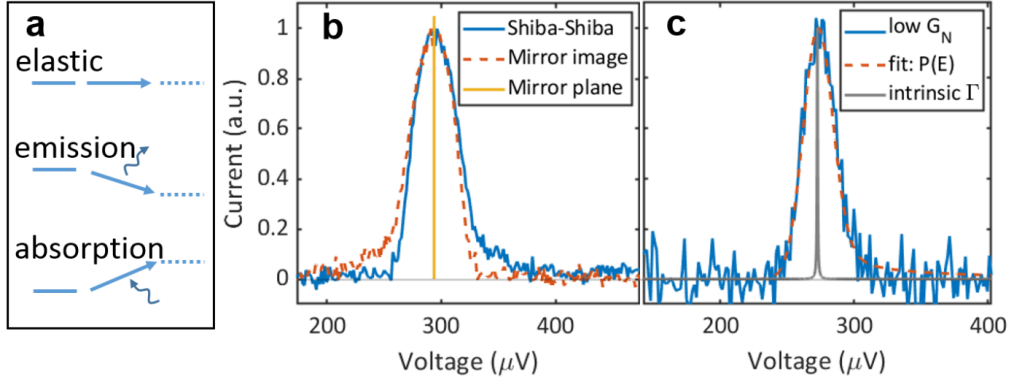
Figure 8.5 – **Broadening of the Shiba-Shiba peak from the interaction with the environment.** a) The elastic and inelastic tunneling processes involving photon exchange with the environment, which is captured by the $P(E)$ function. b) A typical Shiba-Shiba peak in the current with its mirror image with respect to the center position showing the asymmetry in the lineshape. c) A fit of the peak at low conductance to the $P(E)$ function using an ohmic impedance model with $T = 11\,\mathrm{mK}$ and $C = 5.2\,\mathrm{fF}$. The original Lorentzian lineshape from the intrinsic lifetime is plotted as the gray solid curve for comparison, showing that the broadening mainly comes from the $P(E)$ function. Taken from Ref. [114].

We treat Γ in the above equation as an effective combined lifetime, and, therefore, the peak area at the linear to sublinear transition is a direct measurement of the YSR lifetime. In the case of the data shown in Fig. 8.4 b), $A_{\mathrm{trans}} = 1 \times 10^{-18}\,\mathrm{V \cdot A}$ corresponding to $\Gamma = 0.1\,\mu\mathrm{eV}$, which translates to a lifetime of $\tau = h/\Gamma = 41\,\mathrm{ns}$.

In Fig. 8.3 d), we have shown the existence of a quasiparticle background inside the gap on the order of $\eta = 0.3\,\mu\mathrm{eV}$ which is the possible mechanism of the intrinsic relaxation processes. Γ extracted here is on the same order of magnitude as η, indicating that the relaxation through the quasiparticle background is reasonable.

8.2.6 The peak lineshape as a direct measurement of the $P(E)$ function

Assuming $\Gamma_s = \Gamma_t = \Gamma$, Eq. 8.1 simplifies to

$$I_0(v) = \frac{e}{\hbar}\Gamma \frac{|\gamma_e|^2}{4|\gamma_e|^2 + \Gamma^2 + (ev)^2},$$
(8.5)

which is a Lorentzian function with the full width at half maximum (FWHM) of $2\sqrt{4|\gamma_e|^2 + \Gamma^2}$. In the linear regime, the FWHM is 2Γ.

If we directly insert the intrinsic lifetime extracted before into Eq. 8.5 in the linear regime, we will see an extremely sharp Lorentzian peak (FWHM around $0.2\,\mu\mathrm{eV}$), but the measured Shiba-Shiba peak is not only much broader (FWHM around $27\,\mu\mathrm{eV}$) but also not a symmetric Lorentzian shape (Fig. 8.5 b)).

The reason is that the broadening from the $P(E)$ function discussed in section 2.4.2 dominates the lineshape at low conductance. In fact, we can fit the curve with the $P(E)$ function using reasonable parameters (Fig. 8.5 c)). The asymmetry of the Shiba-Shiba peak reflects the asymmetry of the $P(E)$ function due to different probabilities for photon emission and absorption (c.f. Eq. 2.63). Indeed, the intrinsic linewidth is much smaller than the $P(E)$ contribution, indicating that the Shiba-Shiba peak at low conductance is a direct measurement of the $P(E)$ function. Since the $P(E)$ function is independent of the microscopic detail of the junction, the lineshape of the Shiba-Shiba peak at low conductance is largely universal on different impurities.

With increasing conductance, the γ_e broadening in Eq. 8.5 becomes more important and broadens the Shiba-Shiba peak on top of the $P(E)$ function.

8.2.7   Conclusion

In this section, we have shown the basic Shiba-Shiba tunneling processes including the direct Shiba-Shiba tunneling and the thermal Shiba-Shiba tunneling, both featuring sharp peaks in the current indicating the transport between single levels. The direct Shiba-Shiba peaks scale linearly with the conductance at low conductance while they evolve sublinearly at high conductance. The peak area at the transition between the linear and the sublinear regime is a direct measurement of the YSR lifetime, and in this case we identify the lifetime to be around 41 ns, which is quite long given that no optimization on the quasiparticle background has been done in our system.

8.3   The role of spin in the Shiba-Shiba tunneling processes

In the previous section, we have utilized the charge degree of freedom of the YSR states in Shiba-Shiba tunneling, basically the fact that a YSR state is a single quasiparticle level with an intrinsic lifetime. However, a YSR state is more than a discrete level. It is a spin non-degenerate level which can be spin polarized in the presence of a magnetic field or if there is a finite magnetic anisotropy. Therefore, in this section, we will discuss the role of the spin in the Shiba-Shiba tunneling process in the linear regime.

8.3.1   The thermal-direct ratio for the YSR-BCS tunneling

We first take one step back and discuss the case where there is only one YSR state in the junction tunneling to another clean BCS superconductor. At finite temperature, there will also be an additional pair of thermal peaks in the dI/dV spectrum (recall Fig. 2.15). The ratio between the thermal peaks and the direct peaks in the linear regime is the Boltzmann factor (Eq. 2.65). In Fig. 8.6, we present the measurement of this ratio at 1 K temperature for various tip or sample YSR states in a wide energy range, which all lie on top of the prediction from

Figure 8.6 – **The thermal-direct ratio for the YSR-BCS tunneling.** The ratio between the thermal and direct YSR-BCS tunneling peaks in the dI/dV spectra for various tip or sample YSR states on vanadium measured at 1 K. All data points agree with the prediction from the Boltzmann factor with small uncertainty. Taken from Ref. [100].
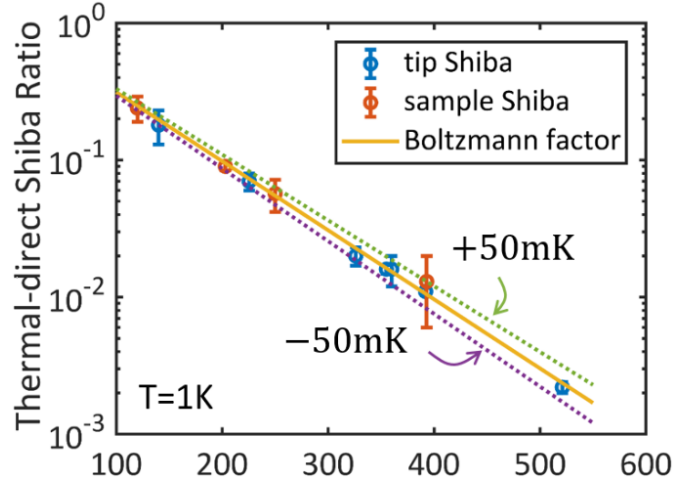
the Boltzmann factor (Eq. 2.65) within marginal uncertainty. This confirms the validity of the Green's function model and the presence of only one pair of YSR states inside the gap. In the presence of multiple pairs of YSR states, the dynamics is more complex, resulting in a deviation from the Boltzmann factor observed in Ref. [19].

8.3.2 Direct and thermal Shiba-Shiba tunneling in more detail

Now we go back to the case of Shiba-Shiba tunneling. In Fig. 8.2, we have discussed the energy diagram and the experimental observation of the direct and thermal Shiba-Shiba tunneling processes. Here in Fig. 8.7, we further distinguish the corresponding peaks.

The direct Shiba-Shiba tunneling happens when the bias voltage aligns the electron-like part of one YSR state with the hole-like part of the other YSR state (Fig. 8.7 b)), generating a pair of peaks at $eV = \pm|\epsilon_s + \epsilon_t|$ (Fig. 8.7 d),e)). We label the peak at positive bias voltage d^+ and the peak at negative voltage d^-. The height of the two peaks are usually not the same due to the electron-hole asymmetry of the YSR states.

The thermal Shiba-Shiba peaks are located at $eV = \pm|\epsilon_s - \epsilon_t|$ (Fig. 8.7 e)). They originate from the tunneling between either two electron-like parts or two hole-like parts of the two YSR states (Fig. 8.7 c)). The two peaks at the positive and negative bias voltages are labeled as t^+ and t^-, respectively.

8.3.3 Green's function theory for Shiba-Shiba tunneling

Beyond the intuitive picture above, simulations using the Green's function theory can offer deeper understanding. For simplicity, we restrict ourselves to 2×2 Nambu space for the moment. To calculate the Shiba-Shiba tunneling current in the linear regime, we need the density of states of the tip and the sample, both of which are the YSR density of states from Eq.
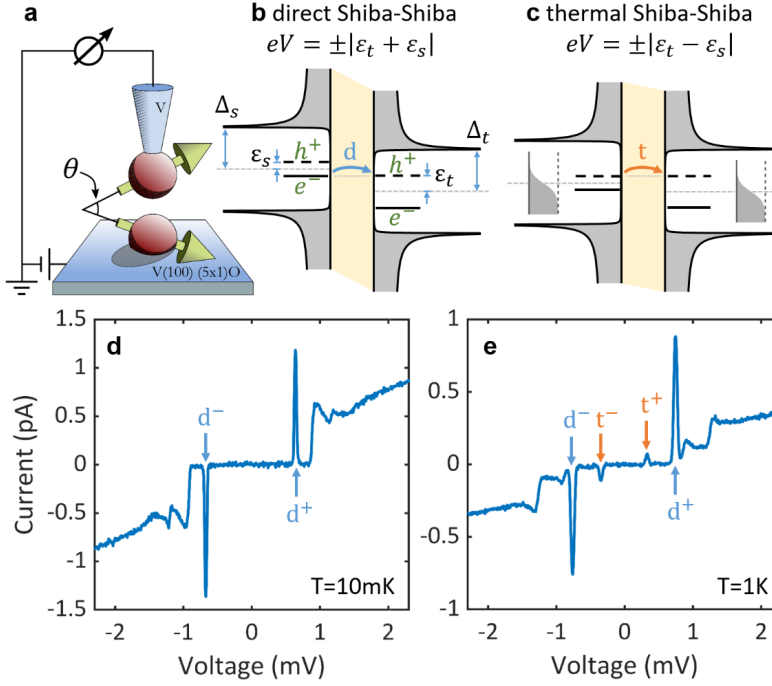
Figure 8.7 – **Direct and thermal Shiba-Shiba tunneling.** a) The relative angle between the YSR spins is labeled as θ. b) and c) are the energy diagrams for the direct and thermal Shiba-Shiba tunneling. d) and e) are the $I(V)$ curves measured at $10\,\mathrm{mK}$ and $1\,\mathrm{K}$, showing the direct peaks ($d^{-,+}$) and the thermal peaks ($t^{-,+}$) at negative ($-$) and positive ($+$) voltage. Taken from Ref. [100].

2.25

$$\rho_{t,s}^{\mathrm{YSR},11}(\omega) = \frac{1}{\pi} \frac{u_{t,s}^2 \eta_{t,s}}{(\omega - \epsilon_{t,s})^2 + \eta_{t,s}^2},$$

$$\rho_{t,s}^{\mathrm{YSR},22}(\omega) = \frac{1}{\pi} \frac{v_{t,s}^2 \eta_{t,s}}{(\omega - \epsilon_{t,s})^2 + \eta_{t,s}^2}, \tag{8.6}$$

where t labels the tip and s denotes the sample.

Inserting Eq. 8.6 into Eq. 2.48, we have the expression for the current

$$I = \frac{4e|t|^2 \eta_t \eta_s}{h} \int_{-\infty}^{+\infty} d\omega \left(u_t^2 u_s^2 \frac{1}{(\omega - \omega_0 - \epsilon_t)^2 + \eta_t^2} \frac{1}{(\omega - \epsilon_s)^2 + \eta_s^2} \left(f(\omega - \omega_0) - f(\omega) \right) \right.$$

$$\left. + v_t^2 v_s^2 \frac{1}{(\omega - \epsilon_t)^2 + \eta_t^2} \frac{1}{(\omega - \omega_0 - \epsilon_s)^2 + \eta_s^2} \left(f(\omega - \omega_0) - f(\omega) \right) \right), \tag{8.7}$$

which is a convolution of two Lorentzian functions and the Fermi function $f(\omega)$ in which $\omega_0 = eV$ where V is the bias voltage.

In the integral in Eq. (8.7), the first term only contributes near $\omega = \epsilon_s, \omega_0 = \epsilon_s - \epsilon_t$ within the range on the order of $\eta_{s,t}$ (approximately within the width of the Lorentzian peaks). The second term only contributes near $\omega = \epsilon_t, \omega_0 = \epsilon_t - \epsilon_s$ within the range on the order of $\eta_{s,t}$. Assuming further $\eta_{t,s} \ll k_B T$ which is generally true even down to $10\,\mathrm{mK}$ (see Section 8.2.5), the Fermi function can be treated as a constant and taken out of the integral. Given the

convolution of two Lorentzian functions

$$\int_{-\infty}^{+\infty} dx \frac{1}{(x-a_1)^2 + g_1^2} \frac{1}{(x-a_2)^2 + g_2^2} = \frac{\pi}{g_1 g_2} \frac{g_1 + g_2}{(a_1 - a_2)^2 + (g_1 + g_2)^2}, \tag{8.8}$$

we arrive at the final formulae for the current

$$I = I_1 + I_2, \tag{8.9}$$

$$I_1 = \frac{4\pi e |t|^2}{h} u_t^2 u_s^2 \left(f(\epsilon_t) - f(\epsilon_s) \right) \frac{\eta_t + \eta_s}{(\omega_0 - (\epsilon_s - \epsilon_t))^2 + (\eta_t + \eta_s)^2}, \tag{8.10}$$

$$I_2 = \frac{4\pi e |t|^2}{h} v_t^2 v_s^2 \left(f(\epsilon_s) - f(\epsilon_t) \right) \frac{\eta_t + \eta_s}{(\omega_0 - (\epsilon_t - \epsilon_s))^2 + (\eta_t + \eta_s)^2}. \tag{8.11}$$

Eqs. 8.10 and 8.11 show that the intrinsic lineshape for the Shiba-Shiba tunneling peaks are Lorentzians (both direct and thermal peaks) having the width of the sum of the two YSR widths, agreeing with the independent theory discussed previously (Eq. 8.1 in the linear regime). Also, since I_1 and I_2 occur at opposite bias voltages, the Shiba-Shiba peaks inherit the asymmetry from the YSR states through the coherent factors u and v.

If $\epsilon_t \epsilon_s < 0$, $|f(\epsilon_t) - f(\epsilon_s)|$ approaches one when $T \to 0$ and thus I represents the direct Shiba-Shiba tunneling peaks at $eV = \pm(|\epsilon_t| + |\epsilon_s|)$. If $\epsilon_t \epsilon_s > 0$, $|f(\epsilon_t) - f(\epsilon_s)|$ approaches zero when $T \to 0$ and thus I in this case represents the thermal Shiba-Shiba tunneling peaks at $eV = \pm(|\epsilon_t| - |\epsilon_s|)$.

Therefore, one observation is that in the 2×2 formalism, the direct and thermal Shiba-Shiba processes never coexist. The reason is that in 2×2 Nambu space, the spins are by definition either parallel or anti-parallel, where only one Shiba-Shiba process is possible due to spin selection, which will be discussed in the following part in more detail. To properly account for arbitrary relative angle θ, we need to expand to 4×4 Nambu space where a superposition of spin up and spin down is allowed.

8.3.4 The role of spins in Shiba-Shiba tunneling

The YSR states are spin non-degenerate, as shown in Chapter 5. However, the spins on the two impurities do not necessarily point to the same direction. The angle between the YSR spins is denoted as θ shown in Fig. 8.7 a).

A YSR state is a Bogoliubov quasiparticle consisting of electron and hole parts (Eq. 2.23). From the definition of the 2×2 Nambu space in Eq. 2.12, the electron part and the hole part always have opposite spins, which is shown in Figs. 8.8 a)-d). This is experimentally demonstrated in Ref. [136].

If the YSR spins are parallel ($\theta = 0°$) which means that the filled levels have parallel spins (which
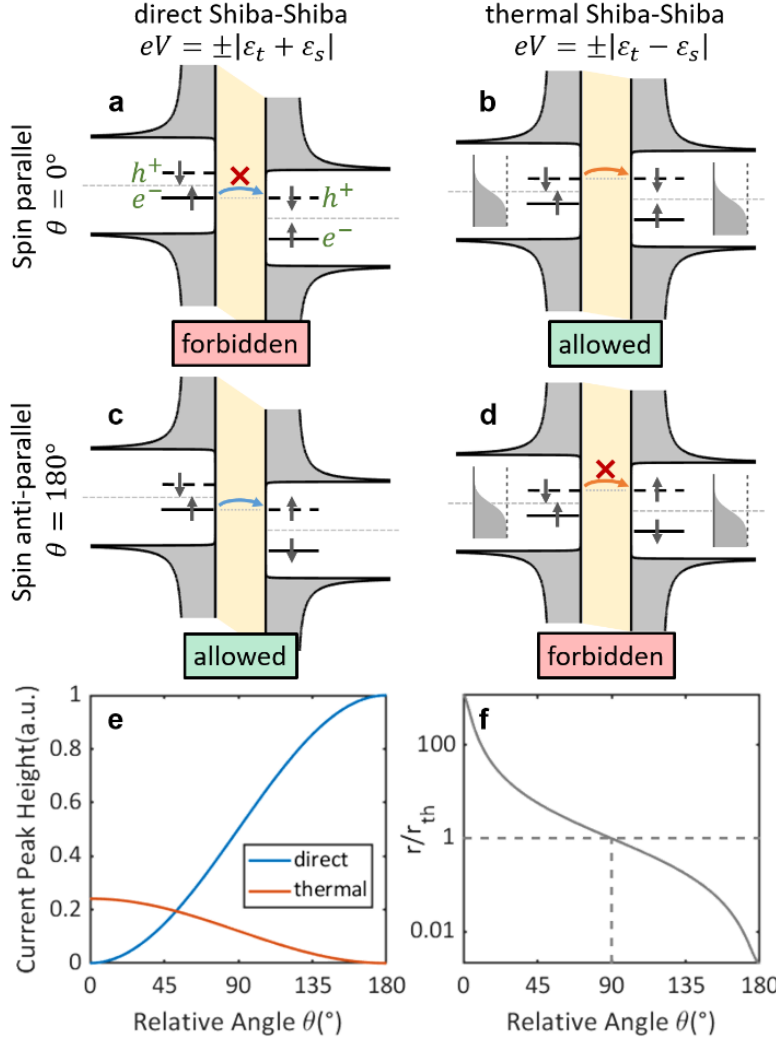
Figure 8.8 – **Theory about the dependence of the thermal and direct Shiba-Shiba tunneling on the relative spin angle θ.** For $\theta = 0°$, the direct Shiba-Shiba tunneling is forbidden (a)) but the thermal Shiba-Shiba tunneling is allowed (b)). For $\theta = 180°$, the direct Shiba-Shiba tunneling is allowed (c)) but the thermal Shiba-Shiba tunneling is forbidden (d)). e) A simulation of the thermal and direct Shiba-Shiba current peak height as a function of θ, agreeing with a)-d). f) The universal dependence of r/r_{th} on θ. Taken from Ref. [100].

ensures that the unfilled levels also have parallel spins), the direct Shiba-Shiba tunneling is forbidden (Fig. 8.8 a)) due to spin conservation in the tunneling process while the thermal Shiba-Shiba tunneling is allowed (Fig. 8.8 b)). On the contrary, if the spins are anti-parallel ($\theta = 180°$) which means that the corresponding levels have opposite spins, the direct Shiba-Shiba tunneling is allowed while the thermal Shiba-Shiba tunneling is forbidden.

As a side note, there are two scenarios for $\theta = 0°$: either the impurity spins are parallel and both YSR states are on the same side of the QPT, or the impurity spins are anti-parallel with the YSR states on the opposite side of the QPT. The reason is that the filled and unfilled levels of a YSR state switches spin direction at the QPT in the mean field model. Both scenarios correspond to $\epsilon_t \epsilon_s > 0$ in the 2×2 formalism. There are also two scenarios for $\theta = 180°$, that the impurity spins are parallel (anti-parallel) and the YSR states are on the opposite (same) side of the QPT, both of which yield $\epsilon_t \epsilon_s < 0$ in the 2×2 formalism.

109

The ratio r between the thermal and the direct Shiba-Shiba peaks is defined by

$$r \stackrel{\text{def}}{=\!=} \sqrt{\frac{p_{t^+} p_{t^-}}{p_{d^+} p_{d^-}}},\tag{8.12}$$

where p_i with $i = d^\pm, t^\pm$ is the intensity of the corresponding Shiba-Shiba current peak. Here, we can use either the peak height or the peak area in the $I(V)$ (the peak height in the dI/dV also works) because the thermal and direct processes share the same lineshape. In 2×2 Nambu space, the ratio r is either zero or infinity (θ equals $180°$ or $0°$). However, if we add up $\theta = 0°$ and $\theta = 180°$ situations, the averaged ratio can be directly calculated from Eqs. 8.10 and 8.11 (assuming $\epsilon_{s,t} > 0$ in the following)

$$\begin{aligned} r &= \left| \frac{f(\epsilon_s) - f(\epsilon_t)}{f(\epsilon_s) - f(-\epsilon_t)} \right| = \left| \frac{e^{-\epsilon_s/k_{\mathrm{B}}T} - e^{-\epsilon_t/k_{\mathrm{B}}T}}{1 - e^{-\epsilon_s/k_{\mathrm{B}}T} e^{-\epsilon_t/k_{\mathrm{B}}T}} \right| \\ &\cong \left| e^{-\epsilon_{\mathrm{s}}/k_{\mathrm{B}}T} - e^{-\epsilon_{\mathrm{t}}/k_{\mathrm{B}}T} \right| \stackrel{\text{def}}{=\!=} r_{\mathrm{th}}, \end{aligned}\tag{8.13}$$

which is independent of the YSR asymmetries (i.e. coherence factors u and v drop out). This is the reason behind the construction of the definition of r in Eq. 8.12. As it turns out later, r_{th} is not only the spin averaged ratio for the 2×2 case but also for the 4×4 case.

We can further extend the discussion above to an arbitrary angle θ using a 4×4 Green's function formalism in the tunneling regime [100]. Such a simulation yields the evolution of the direct and the thermal Shiba-Shiba peaks as a function of the relative angle θ (shown in Fig. 8.8 e)).

We further show that the ratio r has the following analytical form

$$r = \cot^2\left(\frac{\theta}{2}\right) \left| e^{-\epsilon_{\mathrm{s}}/k_{\mathrm{B}}T} - e^{-\epsilon_{\mathrm{t}}/k_{\mathrm{B}}T} \right| = \cot^2\left(\frac{\theta}{2}\right) r_{\mathrm{th}},\tag{8.14}$$

which only depends on the YSR energies and the angle between the YSR spins but not on the other details of the YSR state like the asymmetry and the absolute intensity. The quantity $\frac{r}{r_{\mathrm{th}}}$ further only depends on the angle irrespective of all other parameters. This universal behavior is plotted in Fig. 8.8 f). At $\theta = 90°$, $\frac{r}{r_{\mathrm{th}}} = 1$, which is also the spin averaged case.

r_{th} is the difference between the Boltzmann factors of the tip and sample YSR states which is experimentally accessible. It can be obtained not only via calculating from the YSR energy extracted from the spectra and the temperature reading in the experiment, but also via measuring the thermal-direct ratio of the YSR-BCS tunneling as discussed before (recall Fig. 8.6). The ratio r is also directly measurable in the experiment from the $I(V)$ curve (see Fig. 8.7 e)). Consequently, theoretically we can extract the relative spin angle from one Shiba-Shiba measurement.
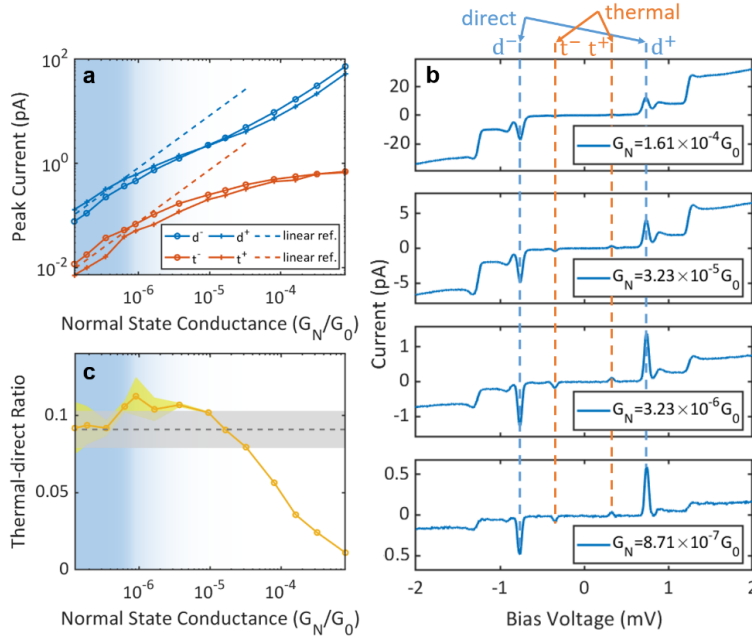
Figure 8.9 – **Conductance dependence of the Shiba-Shiba tunneling processes.** a) The Shiba-Shiba peak current as a function of conductance, showing the linear regime at low conductance. b) The current curves at selected conductances. c) The ratio r as a function of conductance, with only the value at the low conductance limit valid for further analysis. Taken from Ref. [100].

8.3.5 Conductance dependence of the direct and the thermal Shiba-Shiba processes

The prerequisite of Eq. 8.14 is the low conductance limit where the Shiba-Shiba tunneling is in the linear regime (c.f. Fig. 8.4). Therefore, it is necessary to investigate the conductance dependence of the spectra experimentally to confirm the applicability of the formula. In Fig. 8.9 a), the evolution of the direct and the thermal Shiba-Shiba peaks is plotted, showing the linear regime only below a transmission of 10^{-6}. The direct Shiba-Shiba tunneling behaves differently at high conductance than that shown in Fig. 8.4 (that it recovers from the sublinear dependence) because here the system is in the orange regime shown in Fig. 8.3 b) where the additional relaxation processes across the junction become important at high conductance. The current curves at selected conductances are shown in Fig. 8.9 b).

From Fig. 8.9 a), we can extract the ratio r according to Eq. 8.12 and plot it in Fig. 8.9 c). The ratio varies significantly at different conductances, showing the importance to extract r only in the low conductance limit, indicated by the shaded blue area. The uncertainty of r (the gray shading) not only comes from the noise of the low conductance measurements but also the determination of the linear regime.

8.3.6 Freely rotating spins down to milikelvin temperatures

Fig. 8.10 a) shows the ratio r as a function of r_{th} for a collection of Shiba-Shiba systems with different tip and sample YSR states (some of them shown in Fig. 8.6) at 1 K. Surprisingly, all data points lie on the identity line within marginal error, indicating $\theta = 90°$ according to Eq. 8.14. Nevertheless, it is unlikely that a random intrinsic YSR impurity on the vanadium surface
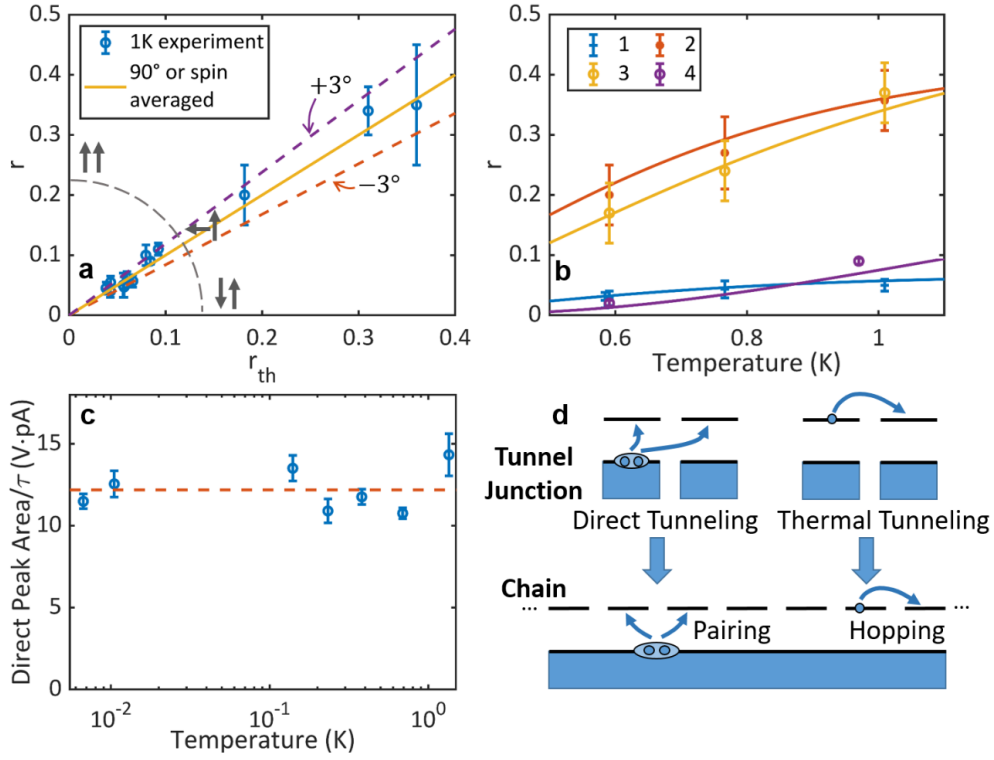
Figure 8.10 – **Temperature dependence measurements.** a) At 1 K, all measured Shiba-Shiba cases show $r = r_{th}$, indicating a freely rotating spin. b) The ratio r as a function of temperature above 0.6 K, showing nice agreement between the measurement (points) and the expectation from the Boltzmann factor (curves). c) The direct Shiba-Shiba peak area as a function of the temperature, which remains nearly constant, suggesting a freely rotating spin down to 7 mK. d) The analogy between the direct (thermal) Shiba-Shiba tunneling and the pairing (hopping) term in the chain scenario. Taken from Ref. [100].

exhibits a spin always 90° relative to the spin of a random tip YSR impurity. Since we know that the YSR state is spin non-degenerate, a natural explanation would be that the spin rotates freely and the measurement is the time average which gives $r = r_{th}$.

It may be that the temperature of 1 K is still too high for a magnetic object to stay in its preferred spin orientation. Therefore, we cool down the system to around 0.6 K and trace the ratio r as a function of temperature (Fig. 8.10 b)). The measurements (points with error bars) and the expectation from the temperature dependence of the Boltzmann factor assuming $r = r_{th}$ (curves) agree quite well, indicating that the spin is still freely rotating down to 0.6 K.

When the temperature is further lowered below 0.6 K, the thermal Shiba-Shiba peaks are suppressed exponentially due to the Bolzmann factor and become difficult to detect. Also, the YSR lifetime enhances resulting in the movement of the linear regime to lower conductance, hindering the extraction of the ratio r. However, recall that in Fig. 8.8 e), the direct Shiba-Shiba peak also depends critically on the relative angle, and thus we can trace the area of the direct

Shiba-Shiba peak down to 7mK plotted in Fig. 8.10 c). Here, we need to use the peak area in the current unlike in the case of r, because the $P(E)$ broadening which depends on the temperature will change the peak width but conserve the area. It can be seen that there is no obvious change in the direct Shiba-Shiba peak area, indicating a freely rotating spin down to 7mK.

The above observations indicate a spin isotropic scenario (the anisotropy energy, if non-zero at all, is at most the thermal energy of 7mK). Given the discussions in Chapter 7 that the tip YSR states are possibly spin-½, the results above are not surprising because a spin-½ system is automatically isotropic without a preferred quantization axis. This, however, requires further theoretical investigation because the discussions about the angle θ in Fig. 8.8 is based on a mean field model that breaks the spin symmetry and generates an artificial polarization. Consequently, the picture of rotating spin is an intuitive view, but the observation of $r = r_{th}$ actually reflects the intrinsic spin symmetry of a spin-½ impurity.

8.3.7 Conclusion

In this section, we have discussed the important role of the spin in Shiba-Shiba tunneling. The ratio r between the thermal and direct Shiba-Shiba tunneling is a measurement of the relative angle of the spins. We have demonstrated that the Shiba-Shiba systems constructed from the spin-½ impurities on vanadium exhibit a ratio r which equals the difference of YSR Boltzmann factors r_{th}, indicating a freely rotating spin in the mean field picture. The spin is freely rotating down to 7mK, suggesting the absence of a preferred quantization axis.

The direct and thermal Shiba-Shiba tunneling processes actually resemble the pairing and the hopping terms in the case of a magnetic chain on the superconductor (Fig. 8.10 d)). For the direct Shiba-Shiba tunneling and the pairing term, a Cooper pair splits, exciting two nearby YSR states. For the thermal Shiba-Shiba process and the hopping term, one excitation transfers to the adjacent site. Since coexistence of the pairing and the hopping terms is essential for generating the topological edge states, our discussion on the direct and thermal Shiba-Shiba processes offers some insight on the role of spins in the chain situation as well.

9 Conclusions & outlook

9.1 Conclusion

The central topic of this thesis is magnetic impurities on superconductors, which generate the YSR states inside the superconducting gap. The presence of YSR states not only changes the quasiparticle spectra and the normal state transmission, but also creates new families of multiple Andreev reflections and modifies the Josephson transport. These phenomena are successfully reproduced quantitatively in the mean field SIAM without considering correlation effects, suggesting a possible secondary role of correlations in the YSR states. Importantly, the $0 - \pi$ transition observed in the Josephson current confirms the change of the ground state condensate when increasing impurity substrate coupling, justifying the QPT. The YSR states are connected with the Kondo effect through fully correlated theories under the SIAM unifying the two quantum impurity problems and the offset current reveals the remaining correlation effects even in the presence of superconductivity.

As a technical advance, the capability of introducing the YSR states onto the STM tip provides a new category of tips functionalized with sharp discrete levels (the YSR-STM) with a prospect of coherence and entanglement with long lifetime offered by the protected quantum levels. The YSR tips are a more flexible alternative to the sample YSR states, and it is even possible to make YSR tips featuring YSR states tunable through the QPT during tip approach, realizing the $0 - \pi$ transition and some rudimentary phase sensitivity across the QPT. Moreover, the YSR tips can be moved around to study the object of interest locally. In this thesis, a first application called Shiba-Shiba tunneling, where the tunneling between tip and sample YSR states, is presented demonstrating the possibility of the lifetime extraction and the essential role of the spin in the tunneling process.

9.2 Outlook

Looking ahead, several intriguing questions remain in the context of Shiba-Shiba tunneling. Time resolved techniques can shed further light on the dynamics of the Shiba-Shiba system.

Figure 9.1 – **Higher order Shiba-Shiba tunneling processes in the blue regime.** At low conductance, Shiba-Shiba tunneling features a peak in the current with the shape of the standard $P(E)$ function. With increasing conductance, side resonance peaks emerge near the elastic one, especially on the high energy side. This possibly originates from higher order interactions with the environment due to long YSR lifetime.
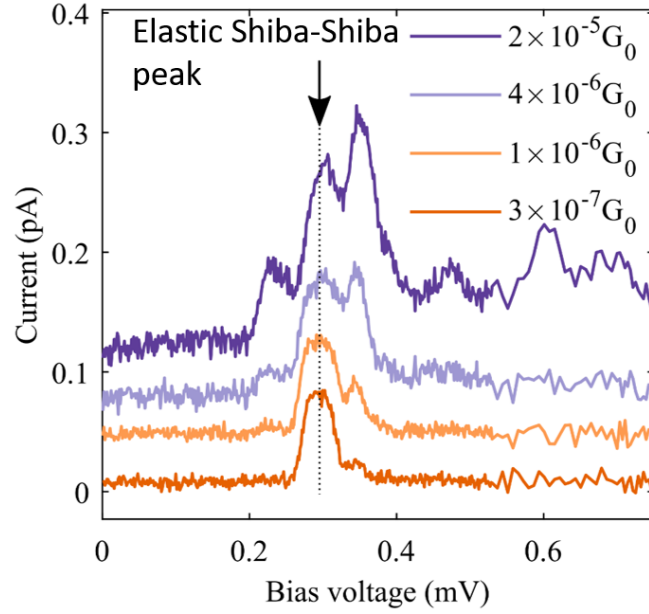
Further, the YSR-STM can be applied to various systems featuring discrete levels on the surface including the Majorana bound states. These possibilities of extending this thesis are presented in the following.

9.2.1 Shiba-Shiba tunneling at high conductance

In the first part of Chapter 8 about the lifetime extraction, we focus on the blue regime (recall the relaxation regimes in Fig. 8.3 b)) and the relatively low conductance range (just beyond the linear-sublinear transition). In the second part of Chapter 8 about the spin dependent tunneling and the ratio between the thermal and direct processes, we focus on the linear regime while the discussion is independent of the relaxation regimes.

Consequently, the relatively high conductance range has not yet been discussed. At higher conductance, we observe possible higher order $P(E)$ contributions in the blue regime and the beyond-sublinear scaling in the orange/green regime. If the conductance is increased even further, MARs involving both YSR states emerge. All of these require further analysis and theoretical understanding.

Higher order $P(E)$ contributions (the blue regime) In the blue regime, the additional relaxation channel across the junction is absent, therefore Shiba-Shiba tunneling is very similar to the tunneling process between isolated single levels. At low conductance (Fig. 8.5), the Shiba-Shiba peak is a direct measurement of the $P(E)$ function. At higher conductance (starting from the sublinear regime), the quasiparticle starts to tunnel back and forth between the YSR levels in the junction coherently due to the long lifetime. Such behavior cannot be modeled by the $P(E)$ function shown in section 2.4.2 because the assumed sequential tunneling no longer

holds here. As a consequence, the probability of interacting with multiple photons increases, resulting in multiple side peaks especially on the high voltage side which is the photon emission side (Fig. 9.1). This phenomenon has also been observed in the tunneling between single levels in double quantum dots [137]. Nevertheless, a quantitative understanding is still elusive, especially regarding the comparison between the side resonance energies from the Josephson effect [99] and the Shiba-Shiba tunneling. In addition, the temperature dependence of the spectra is also interesting.

Beyond-sublinear scaling (the orange and green regime) In Fig. 8.4 b), we have shown the linear to sublinear transition of the Shiba-Shiba tunneling peak in the blue regime. In the orange and green regime, however, the dependence of the peak area as a function of conductance deviates from this behavior at high conductance featuring a beyond-sublinear scaling (see Fig. 8.9 a)), which is due to the presence of the additional relaxation channels. A recent publication [138] confirms the existence of the relaxation regimes experimentally using double quantum dots, offering a theory considering the additional relaxation channels. Therefore, it is interesting to understand the conductance dependence in different regimes quantitatively.

Shiba-Shiba tunneling with MARs In a recent publication [139], the theoretical foundation of the MARs including both tip and sample YSR states was laid. Apart from the YSR-MARs introduced in Chapter 5, the involvement of two YSR states introduces a new family of MARs between the two YSR states at $eV = \pm(\epsilon_s + \epsilon_t)/(2n+1)$ where $\epsilon_{s,t}$ are the energies for the sample and the tip YSR states and $n \geq 1$ is an integer. At high conductance, the energies for these processes shift due to the hybridization of the tip and sample YSR states. It would thus be interesting to verify this experimentally.

9.2.2 Absolute spin polarization in the YSR-STM and Shiba-Shiba tunneling

In section 8.3, we have shown theoretically that the ratio between the thermal and direct Shiba-Shiba tunneling is a sensitive probe of the relative spin orientations, but due to the isotropic nature of the spin-½ impurity, we only observe an averaging effect without absolute spin polarization. It would thus be desirable, to demonstrate the spin selective tunneling with absolute spin polarization, either by the application of the magnetic field or by introducing sizable magnetic anisotropy in the system to fix the quantization axis.

External magnetic field To polarize a YSR state, the magnetic field should be smaller than the critical field of the superconductor B_c but should offer a Zeemann energy much larger than the thermal energy $k_B T$. This is possible for the tip YSR state due to the geometrical enhancement of the critical field in the tip [140] and we do observe the Zeeman splitting of the tip YSR states. However, using the magnetic field to polarize the intrinsic YSR states on the V(100) sample is

Figure 9.2 – **The Shiba-Shiba junction in the radiation of microwaves.** In the many-body picture, a YSR state is a two level system, and the Shiba-Shiba junction is a coupled quantum system of two two level systems with the coupling tunable by the bias voltage and the tip sample distance, which is in principle a double qubit. The microwave might be thus used to excite, drive and manipulate (initialize and write) the system and the state might be read out by the tunneling current. The microwave can be applied in a variety of ways to the system, including continuous driving and pulse manipulation.
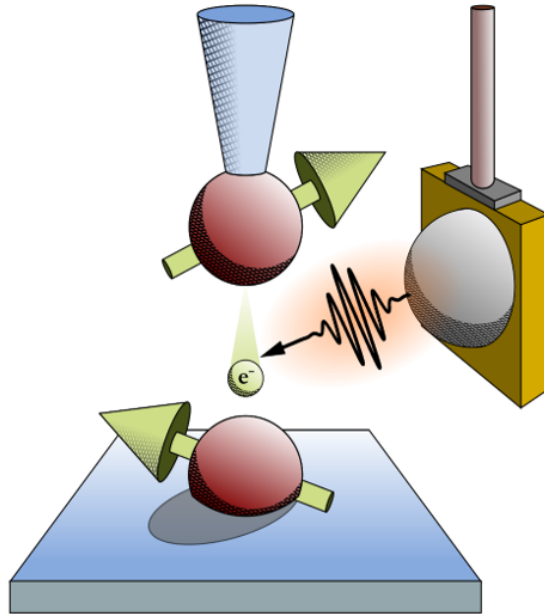
difficult, because vanadium is a type-II superconductor with a low critical magnetic field, and the phenomena observed in the magnetic field is complicated, possibly related to vortices. Therefore, to achieve spin polarization in the YSR-STM, applying a magnetic field is viable [141], but for the observation of the spin selection in the Shiba-Shiba tunneling, other systems with higher critical fields like 2D or thin film superconductors are desired.

Magnetic anisotropy One step further on the development of the YSR-STM is to use YSR impurities with sufficient anisotropy to fix the spin direction, for example using some small magnetic molecules like metallocene molecules. If both the tip and sample YSR states can acquire fixed quantization axis, the Shiba-Shiba tunneling is expected to show absolute spin selection in the absence of the magnetic field whose temperature dependency would also be an interesting topic.

9.2.3   Time resolved measurements in Shiba-Shiba systems

A YSR state consists of one ground state $|0\rangle$ and one excited level $|1\rangle$ in the many-body picture. A Shiba-Shiba system is thus a coupled system with four possible quantum states $|00\rangle$, $|01\rangle$, $|10\rangle$ and $|11\rangle$, like a coupled double qubit (alternatively, one effective qubit consisting of two YSR impurties is proposed in Ref. [142]). The direct Shiba-Shiba tunneling switches the system between $|00\rangle$ and $|11\rangle$ and the thermal Shiba-Shiba process switches the system between $|01\rangle$ and $|10\rangle$ (see Chapter 8). Beyond the measurement of a steady current, time resolved experiments might be beneficial for extracting the dynamics and further manipulating the quantum system. Such experiments require a time resolution in the nanosecond range given the YSR lifetime measured in Chapter 8, which corresponds to a frequency in the gigahertz

regime already realized in recent development of an ESR-STM in the group [143].

Pump-probe measurements At 10 mK, the thermal processes are absent. However, in case of different lifetimes of the tip and sample YSR states, we can excite the system at the direct Shiba-Shiba tunneling voltage (the pump pulse) and detect the current at the thermal Shiba-Shiba tunneling voltage (the probe pulse) after a short time interval which will give the dynamics of the relaxations. Alternatively, the YSR states may be excited individually at the YSR-BCS tunneling voltage.

Microwave assisted tunneling, coherent manipulation and operations In the presence of a continuous microwave radiation on the junction at low conductance, the Tien-Gordon equation predicts the emergence of replicas of the original signal at multiples of $\hbar\omega$, where ω is the angular frequency of the input microwave [143, 144] (Fig. 9.2). The microwave assisted tunneling in a Shiba-Shiba system is already interesting in this regard especially in the sublinear regime where back and forth tunneling happens.

In addition, another interesting topic is to coherently drive the YSR states between the ground state and the excited state and realize Rabi oscillations, which is recently predicted to be possible for a YSR dimer which is similar to the Shiba-Shiba system [142].

The next step after the realization of the coherent manipulation of the Shiba-Shiba system is realizing the operations of the quantum states like initializing, writing and reading out.

9.2.4 YSR-Majorana tunneling

The YSR-STM can be applied to discrete levels other than the sample YSR states, and one intriguing application is to probe topological bound states like the Majorana bound states (MBS). Both MBS and YSR states originate from the magnetic impurities on superconductors and are both discrete in-gap states, making it non-trivial to distinguish the MBS from zero energy YSR states. With the YSR tip as a new tool, more aspects of the MBS might be explored, including the lifetime.

Probing Majorana lifetime One direct extension of Chapter 8 is that the lifetime of a MBS may be directly probed through YSR-Majorana tunneling (Fig. 9.3 a)). One obstacle is that only the combined lifetime is measured, which might be solved if the lifetime of the MBS is very different from that of the YSR states, or if it is possible to characterize the tip YSR lifetime independently through Shiba-Shiba tunneling statistics for example.

Majorana tip, coherent manipulation and possible braiding If the coupling between the tip and the Majorana chain is adequate, the tip impurity effectively extends the Majorana chain
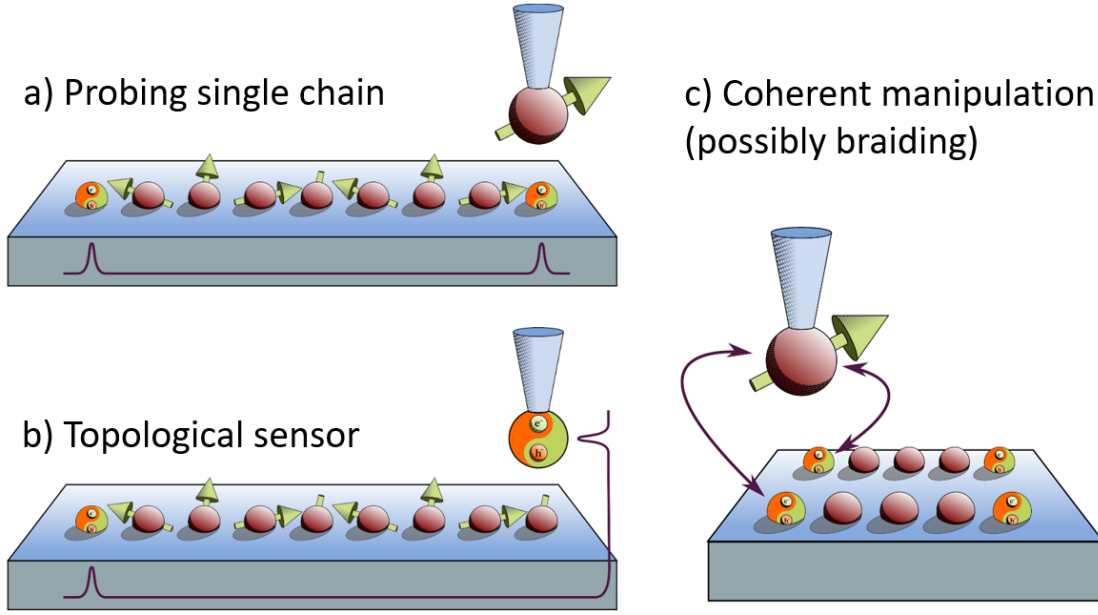
Figure 9.3 – **YSR-Majorana tunneling.** a) The YSR tip offers a new possibility to probe the Majorana bound state, for instance its lifetime. b) The tip YSR state is just an additional site of magnetic impurity. Under certain conditions (for example, the non-collinear spin orientation as observed already in the vanadium YSR tips), the Majorana bound state might move to the apex of the tip. c) The YSR tip as a movable magnetic site, might be further used to couple and exchange coherent information between two adjacent Majorana chains, possibly offering a pathway for Majorana braiding.

by one site and the MBS moves to the apex of the tip, resulting in a Majorana tip (Fig. 9.3 b)). Although once the tip moves too far away, the MBS goes back to the chain end on the surface, this might already give sufficient flexibility for coupling two nearby chains coherently and possible braiding of the MBS (Fig. 9.3 c)).

9.2.5 Phase sensitive measurements of unconventional superconductors

In Chapter 6, we have shown a rudimentary phase sensitivity through the Josephson measurement between a BCS superconductor and a YSR tip moving across the QPT upon tip approach. This phase sensitivity might be applied to study the symmetry of the anisotropic order parameters for p-wave and d-wave superconductors using either YSR states on the tip or on the sample. The sign of the order parameter is of special interest because it is not easy to detect otherwise from the conventional Josephson STM.

It is also predicted that a YSR state on the d-wave superconductor does not exhibit a QPT [71] which means that there is no $0 - \pi$ transition, so it would be interesting to repeat the measurement in Chapter 6 using YSR states on d-wave superconductors to verify this prediction.

Bibliography

[1] L. Yu. Bound state in superconductors with paramagnetic impurities. *Acta Phys. Sin.*, 21 (1):75–91, 1965.

[2] H. Shiba. Classical spins in superconductors. *Prog. Theor. Phys.*, 40(3):435–451, 1968.

[3] A. I. Rusinov. Superconductivity near a paramagnetic impurity. *JETP Lett.*, 9(2):85, 1969.

[4] J. Kondo. Resistance minimum in dilute magnetic alloys. *Prog. Theor. Phys.*, 32(1):37–49, 1964.

[5] R. Feynman. There's plenty of room at the bottom. In *Feynman and computation*, pages 63–76. CRC Press, 2018.

[6] K. G. Wilson. The renormalization group: Critical phenomena and the Kondo problem. *Rev. Mod. Phys.*, 47(4):773, 1975.

[7] A. C. Hewson. *The Kondo Problem to Heavy Fermions*. Cambridge Studies in Magnetism. Cambridge University Press, 1993.

[8] H. R. Krishna-Murthy, J. W. Wilkins, and K. G. Wilson. Renormalization-group approach to the Anderson model of dilute magnetic alloys. i. static properties for the symmetric case. *Phys. Rev. B*, 21(3):1003, 1980.

[9] H. R. Krishna-Murthy, J. W. Wilkins, and K. G. Wilson. Renormalization-group approach to the Anderson model of dilute magnetic alloys. ii. static properties for the asymmetric case. *Phys. Rev. B*, 21(3):1044, 1980.

[10] K. Satori, H. Shiba, O. Sakai, and Y. Shimizu. Numerical renormalization group study of magnetic impurities in superconductors. *J. Phys. Soc. Japan.*, 61(9):3239–3254, 1992.

[11] O. Sakai, Y. Shimizu, H. Shiba, and K. Satori. Numerical renormalization group study of magnetic impurities in superconductors. ii. dynamical excitation spectra and spatial variation of the order parameter. *J. Phys. Soc. Japan.*, 62(9):3181–3197, 1993.

[12] G. Binnig, H. Rohrer, C. Gerber, and E. Weibel. (111) facets as the origin of reconstructed Au(110) surfaces. *Surf. Sci.*, 131(1):L379–L384, 1983.

Bibliography

[13] G. Binnig, H. Rohrer, C. Gerber, and E. Weibel. 7× 7 reconstruction on Si(111) resolved in real space. *Phys. Rev. Lett.*, 50(2):120, 1983.

[14] G. Binnig and H. Rohrer. Scanning tunneling microscopy—from birth to adolescence. *Rev. Mod. Phys.*, 59(3):615, 1987.

[15] M. Ternes. Probing magnetic excitations and correlations in single and coupled spin systems with scanning tunneling spectroscopy. *Prog. Surf. Sci.*, 92(1):83–115, 2017.

[16] J. Li, W. D. Schneider, R. Berndt, and B. Delley. Kondo scattering observed at a single magnetic impurity. *Phys. Rev. Lett.*, 80(13):2893, 1998.

[17] V. Madhavan, W. Chen, T. Jamneala, M. F. Crommie, and N. S. Wingreen. Tunneling into a single magnetic atom: spectroscopic evidence of the Kondo resonance. *Science*, 280 (5363):567–569, 1998.

[18] G. C. Menard, S. Guissart, C. Brun, S. Pons, V. S. Stolyarov, F. Debontridder, M. V. Leclerc, E. Janod, L. Cario, D. Roditchev, P. Simon, and T. Cren. Coherent long-range magnetic bound states in a superconductor. *Nat. Phys.*, 11(12):1013–1016, 2015.

[19] M. Ruby, F. Pientka, Y. Peng, F. von Oppen, B. W. Heinrich, and K. J. Franke. Tunneling processes into localized subgap states in superconductors. *Phys. Rev. Lett.*, 115(8): 087001, 2015.

[20] N. Hatter, B. W. Heinrich, D. Rolf, and K. J. Franke. Scaling of Yu-Shiba-Rusinov energies in the weak-coupling Kondo regime. *Nat. Commun.*, 8(1):1–7, 2017.

[21] L. Farinacci, G. Ahmadi, G. Reecht, M. Ruby, N. Bogdanoff, O. Peters, B. W. Heinrich, F. von Oppen, and K. J. Franke. Tuning the coupling of an individual magnetic impurity to a superconductor: quantum phase transition and transport. *Phys. Rev. Lett.*, 121(19): 196803, 2018.

[22] S. Kezilebieke, M. Dvorak, T. Ojanen, and P. Liljeroth. Coupled Yu-Shiba-Rusinov states in molecular dimers on NbSe$_2$. *Nano Lett.*, 18(4):2311–2315, 2018.

[23] L. Malavolti, M. Briganti, M. Hänze, G. Serrano, I. Cimatti, G. McMurtrie, E. Otero, P. Ohresser, F. Totti, M. Mannini, R. Sessoli, and S. Loth. Tunable spin–superconductor coupling of spin 1/2 vanadyl phthalocyanine molecules. *Nano Lett.*, 18(12):7955–7961, 2018.

[24] M. Ruby, B. W. Heinrich, Y. Peng, F. von Oppen, and K. J. Franke. Wave-function hybridization in Yu-Shiba-Rusinov dimers. *Phys. Rev. Lett.*, 120(15), 2018.

[25] S. Kezilebieke, R. Žitko, M. Dvorak, T. Ojanen, and P. Liljeroth. Observation of coexistence of Yu-Shiba-Rusinov states and spin-flip excitations. *Nano Lett.*, 19(7):4614–4619, 2019.

[26] L. Schneider, M. Steinbrecher, L. Rózsa, J. Bouaziz, K. Palotás, M. dos Santos Dias, S. Lounis, J. Wiebe, and R. Wiesendanger. Magnetism and in-gap states of 3d transition metal atoms on superconducting Re. *npj Quantum Mater.*, 4(1):1–8, 2019.

[27] J. Senkpiel, C. Rubio-Verdú, M. Etzkorn, R. Drost, L. M. Schoop, S. Dambach, C. Padurariu, B. Kubala, J. Ankerhold, C. R. Ast, and K. Kern. Robustness of Yu-Shiba-Rusinov resonances in the presence of a complex superconducting order parameter. *Phys. Rev. B*, 100(1):014502, 2019.

[28] H. Huang, R. Drost, J. Senkpiel, C. Padurariu, B. Kubala, A. L. Yeyati, J. C. Cuevas, J. Ankerhold, K. Kern, and C. R. Ast. Quantum phase transitions and the role of impurity-substrate hybridization in Yu-Shiba-Rusinov states. *Commun. Phys.*, 3(1):199, 2020.

[29] Y. Wang, S. Arabi, K. Kern, and M. Ternes. Symmetry mediated tunable molecular magnetism on a 2D material. *Commun. Phys.*, 4(1):1–6, 2021.

[30] W. D. Schneider. A local view of the Kondo effect: Scanning tunneling spectroscopy. *Pramana*, 52(6):537–552, 1999.

[31] N. Knorr, M. A. Schneider, L. Diekhöner, P. Wahl, and K. Kern. Kondo effect of single Co adatoms on Cu surfaces. *Phys. Rev. Lett.*, 88(9):096804, 2002.

[32] K. Nagaoka, T. Jamneala, M. Grobis, and M. F. Crommie. Temperature dependence of a single Kondo impurity. *Phys. Rev. Lett.*, 88(7):077205, 2002.

[33] A. Zhao, Q. Li, L. Chen, H. Xiang, W. Wang, S. Pan, B. Wang, X. Xiao, J. Yang, J. G. Hou, and Q. Zhu. Controlling the Kondo effect of an adsorbed magnetic ion through its chemical bonding. *Science*, 309(5740):1542–1544, 2005.

[34] A. F. Otte, M. Ternes, K. Von Bergmann, S. Loth, H. Brune, C. P. Lutz, C. F. Hirjibehedin, and A. J. Heinrich. The role of magnetic anisotropy in the Kondo effect. *Nat. Phys.*, 4 (11):847–850, 2008.

[35] M. Ternes. *Scanning tunneling spectroscopy at the single atom scale*. PhD thesis, EPFL, Lausanne, 2006.

[36] M. Ternes, A. J. Heinrich, and W. D. Schneider. Spectroscopic manifestations of the Kondo effect on single adatoms. *J. Phys. Condens. Matter*, 21(5), 2009.

[37] Y. Zhang, S. Kahle, T. Herden, C. Stroh, M. Mayor, U. Schlickum, M. Ternes, P. Wahl, and K. Kern. Temperature and magnetic field dependence of a Kondo system in the weak coupling regime. *Nat. Commun.*, 4(1):1–6, 2013.

[38] K. von Bergmann, M. Ternes, S. Loth, C. P. Lutz, and A. J. Heinrich. Spin polarization of the split Kondo state. *Phys. Rev. Lett.*, 114(7):076601, 2015.

[39] M. Ternes, C. P. Lutz, A. J. Heinrich, and W. D. Schneider. Sensing the spin of an individual Ce adatom. *Phys. Rev. Lett.*, 124(16):167202, 2020.

Bibliography

[40] H. Suderow, M. Crespo, P. Martinez-Samper, J. G. Rodrigo, G. Rubio-Bollinger, S. Vieira, N. Luchier, J. P. Brison, and P. C. Canfield. Scanning tunneling microscopy and spectroscopy at very low temperatures. *Physica C: Supercond.*, 369(1-4):106–112, 2002.

[41] J. G. Rodrigo, H. Suderow, and S. Vieira. On the use of STM superconducting tips at very low temperatures. *Eur. Phys. J. B*, 40(4):483–488, 2004.

[42] I. Guillamon, H. Suderow, S. Vieira, and P. Rodiere. Scanning tunneling spectroscopy with superconducting tips of Al. *Physica C Supercond.*, 468(7-10):537–542, 2008.

[43] S. Ji, T. Zhang, Y. Fu, X. Chen, X. Ma, J. Li, W. Duan, J. Jia, and Q. Xue. High-resolution scanning tunneling spectroscopy of magnetic impurity induced bound states in the superconducting gap of Pb thin films. *Phys. Rev. Lett.*, 100(22):226801, 2008.

[44] K. J. Franke, G. Schulze, and J. I. Pascual. Competition of superconducting phenomena and Kondo screening at the nanoscale. *Science*, 332(6032):940–944, 2011.

[45] A. Kamlapure, L. Cornils, R. Žitko, M. Valentyuk, R. Mozara, S. Pradhan, J. Fransson, A. I. Lichtenstein, J. Wiebe, and R. Wiesendanger. Investigation of the Yu-Shiba-Rusinov states of a multi-impurity Kondo system. *arXiv:1911.03794*, 2019.

[46] A. Odobesko, D. Di Sante, A. Kowalski, S. Wilfert, F. Friedrich, R. Thomale, G. Sangiovanni, and M. Bode. Observation of tunable single-atom Yu-Shiba-Rusinov states. *Phys. Rev. B*, 102(17):174504, 2020.

[47] M. D. Upward, J. W. Janssen, L. Gurevich, A. F. Morpurgo, and L. P. Kouwenhoven. An ultralow-temperature scanning tunnelling microscope. *Appl. Phys. A*, 72(2):S253–S256, 2001.

[48] N. Moussy, H. Courtois, and B. Pannetier. A very low temperature scanning tunneling microscope for the local spectroscopy of mesoscopic structures. *Rev. Sci. Instrum.*, 72 (1):128–131, 2001.

[49] H. Kambara, T. Matsui, Y. Niimi, and H. Fukuyama. Construction of a versatile ultralow temperature scanning tunneling microscope. *Rev. Sci. Instrum.*, 78(7):073703, 2007.

[50] M. Marz, G. Goll, and H. v. Löhneysen. A scanning tunneling microscope for a dilution refrigerator. *Rev. Sci. Instrum.*, 81(4):045102, 2010.

[51] H. Suderow, I. Guillamon, and S. Vieira. Compact very low temperature scanning tunneling microscope with mechanically driven horizontal linear positioning stage. *Rev. Sci. Instrum.*, 82(3):033711, 2011.

[52] Y. J. Song, A. F. Otte, V. Shvarts, Z. Y. Zhao, Y. Kuk, S. R. Blankenship, A. Band, F. M. Hess, and J. A. Stroscio. Invited review article: A 10 mK scanning probe microscopy facility. *Rev. Sci. Instrum.*, 81(12), 2010.

[53] M. Assig. *Development of a millikelvin scanning tunneling microscope for applications in ultra high vacuum and high magnetic fields.* PhD thesis, EPFL, Lausanne, 2011.

[54] M. Assig, M. Etzkorn, A. Enders, W. Stiepany, C. R. Ast, and K. Kern. A 10 mK scanning tunneling microscope operating in ultra high vacuum and high magnetic fields. *Rev. Sci. Instrum.*, 84(3):033903, 2013.

[55] J. Senkpiel. *Scanning Tunneling Spectroscopy with Superconducting Junctions: From Single Channel Transport to Local Pair Breaking Potentials.* PhD thesis, EPFL, Lausanne, 2018.

[56] H. K. Onnes. Further experiments with liquid helium. c. on the change of electric resistance of pure metals at very low temperatures etc. iv. the resistance of pure mercury at helium temperatures. In *KNAW, Proceedings*, volume 13, pages 1910–1911, 1911.

[57] W. Meissner and R. Ochsenfeld. Ein neuer Effekt bei Eintritt der Supraleitfähigkeit. *Naturwissenschaften*, 21(44):787–788, 1933.

[58] V. V. Schmidt. *The physics of superconductors: Introduction to fundamentals and applications.* Springer Berlin/Heidelberg, 2013.

[59] M. Tinkham. *Introduction to superconductivity.* Dover Publications Inc., 2004.

[60] J. Bardeen, L. N. Cooper, and J. R. Schrieffer. Theory of superconductivity. *Phys. Rev.*, 108(5):1175, 1957.

[61] J. G. Bednorz and K. A. Müller. Possible high T_c superconductivity in the Ba- La- Cu- O system. *Z. Phys. B Condens. Matter*, 64(2):189–193, 1986.

[62] M. K. Wu, J. R. Ashburn, C. J. Torng, P. H. Hor, R. L. Meng, L. Gao, Z. J. Huang, Y. Q. Wang, and C. W. Chu. Superconductivity at 93 K in a new mixed-phase Y-Ba-Cu-O compound system at ambient pressure. *Phys. Rev. Lett.*, 58(9):908, 1987.

[63] Y. Kamihara, T. Watanabe, M. Hirano, and H. Hosono. Iron-based layered superconductor La[$O_{1-x}F_x$]FeAs ($x = 0.05 - 0.12$) with $T_c = 26$ K. *J. Am. Chem. Soc.*, 130(11): 3296–3297, 2008.

[64] H. Takahashi, K. Igawa, K. Arii, Y. Kamihara, M. Hirano, and H. Hosono. Superconductivity at 43 K in an iron-based layered compound $LaO_{1-x}F_x$FeAs. *Nature*, 453(7193): 376–378, 2008.

[65] K. Ishida, Y. Nakai, and H. Hosono. To what extent iron-pnictide new superconductors have been clarified: a progress report. *J. Phys. Soc. Japan.*, 78(6):062001, 2009.

[66] Y. Cao, V. Fatemi, S. Fang, K. Watanabe, T. Taniguchi, E. Kaxiras, and P. Jarillo-Herrero. Unconventional superconductivity in magic-angle graphene superlattices. *Nature*, 556 (7699):43–50, 2018.

[67] L. N. Cooper. Bound electron pairs in a degenerate fermi gas. *Phys. Rev.*, 104(4):1189, 1956.

[68] J. Zhu. *Bogoliubov-de Gennes method and its applications*, volume 924 of *The Lecture Notes in Physics*. Springer, 2016.

[69] M. Graham and D. K. Morr. Imaging the spatial form of a superconducting order parameter via Josephson scanning tunneling spectroscopy. *Phys. Rev. B*, 96(18), 2017.

[70] K. Björnson, A. V. Balatsky, and A. M. Black-Schaffer. Superconducting order parameter π-phase shift in magnetic impurity wires. *Phys. Rev. B*, 95(10):104521, 2017.

[71] M. I. Salkola, A. V. Balatsky, and J. R. Schrieffer. Spectral properties of quasiparticle excitations induced by magnetic moments in superconductors. *Phys. Rev. B*, 55(18): 12648–12661, 1997.

[72] A. V. Balatsky, I. Vekhter, and J. X. Zhu. Impurity-induced states in conventional and unconventional superconductors. *Rev. Mod. Phys.*, 78(2):373–433, 2006.

[73] G. J. Van den Berg and J. De Nobel. Les propriétés à basses températures des alliages des métaux normaux avec des solutés de transition. *J. phys. radium*, 23(10):665–671, 1962.

[74] W. J. De Haas, J. De Boer, and G. J. Van den Berg. The electrical resistance of gold, copper and lead at low temperatures. *Physica*, 1(7-12):1115–1124, 1934.

[75] W. J. De Haas and G. J. Van Den Berg. The electrical resistance of gold and silver at low temperatures. *Physica*, 3(6):440–449, 1936.

[76] M. Gruber, A. Weismann, and R. Berndt. The Kondo resonance line shape in scanning tunnelling spectroscopy: instrumental aspects. *J. Phys. Condens. Matter*, 30(42):424001, 2018.

[77] U. Fano. Effects of configuration interaction on intensities and phase shifts. *Phys. Rev.*, 124(6):1866, 1961.

[78] H. O. Frota. Shape of the Kondo resonance. *Phys. Rev. B*, 45(3):1096, 1992.

[79] R. Žitko, R. Peters, and T. Pruschke. Splitting of the Kondo resonance in anisotropic magnetic impurities on surfaces. *New J. Phys.*, 11(5):053003, 2009.

[80] P. Nozieres. A "Fermi-liquid" description of the Kondo problem at low temperatures. *J. Low Temp. Phys.*, 17(1):31–42, 1974.

[81] R. Bulla, T. A. Costi, and T. Pruschke. Numerical renormalization group method for quantum impurity systems. *Rev. Mod. Phys.*, 80(2):395, 2008.

[82] A. C. Hewson, A. Oguri, and D. Meyer. Renormalized parameters for impurity models. *Eur. Phys. J. B*, 40(2):177–189, 2004.

[83] D. R. Hamann. New solution for exchange scattering in dilute alloys. *Phys. Rev.*, 158(3): 570, 1967.

[84] Y. Nagaoka. Self-consistent treatment of Kondo's effect in dilute alloys. *Phys. Rev.*, 138 (4A):A1112, 1965.

[85] R. Žitko and T. Pruschke. Energy resolution and discretization artifacts in the numerical renormalization group. *Phys. Rev. B*, 79(8):085106, 2009.

[86] R. Žitko. *Many-particle effects in resonant tunneling of electrons through nanostructures.* PhD thesis, University of Ljubljana, Ljubljana, 2007.

[87] J. R. Schrieffer and P. A. Wolff. Relation between the Anderson and Kondo Hamiltonians. *Phys. Rev.*, 149(2):491, 1966.

[88] T. Yoshioka and Y. Ohashi. Numerical renormalization group studies on single impurity Anderson model in superconductivity: A unified treatment of magnetic, nonmagnetic impurities, and resonance scattering. *J. Phys. Soc. Japan.*, 69(6):1812–1823, 2000.

[89] L. V. Keldysh. Diagram technique for nonequilibrium processes. *Sov. Phys. JETP*, 20(4): 1018–1026, 1965.

[90] J. C. Cuevas, A. MartinRodero, and A. L. Yeyati. Hamiltonian approach to the transport properties of superconducting quantum point. *Phys. Rev. B*, 54(10):7366–7379, 1996.

[91] J. C. Cuevas. *Electronic transport in normal and superconducting nanocontacts.* PhD thesis, Universidad Autónoma, Madrid, 1999.

[92] E. Scheer and J. C. Cuevas. *Molecular electronics: an introduction to theory and experiment.* World Scientific, 2nd edition, 2017.

[93] A. A. Odintsov. Effect of dissipation on the characteristics of small-area tunnel junctions: application of the polaron model. *Sov. Phys. JETP*, 67:1265, 1988.

[94] M. H. Devoret, D. Esteve, H. Grabert, G. L. Ingold, H. Pothier, and C. Urbina. Effect of the electromagnetic environment on the Coulomb blockade in ultrasmall tunnel-junctions. *Phys. Rev. Lett.*, 64(15):1824–1827, 1990.

[95] C. R. Ast, B. Jack, J. Senkpiel, M. Eltschka, M. Etzkorn, J. Ankerhold, and K. Kern. Sensing the quantum limit in scanning tunnelling spectroscopy. *Nat. Commun.*, 7:13009, 2016.

[96] H. Grabert and M. H. Devoret. *Single charge tunneling: Coulomb blockade phenomena in nanostructures*, volume 294 of *Nato Science Series B.* Springer US, 2013.

[97] G. L. Ingold and H. Grabert. Finite-temperature current-voltage characteristics of ultrasmall tunnel-junctions. *EPL*, 14(4):371–376, 1991.

[98] G. L. Ingold, H. Grabert, and U. Eberhardt. Cooper-pair current through ultrasmall Josephson-junctions. *Phys. Rev. B*, 50(1):395–402, 1994.

Bibliography

[99] B. Jack, M. Eltschka, M. Assig, A. Hardock, M. Etzkorn, C. R. Ast, and K. Kern. A nanoscale gigahertz source realized with Josephson scanning tunneling microscopy. *Appl. Phys. Lett.,* 106(1), 2015.

[100] H. Huang, J. Senkpiel, C. Padurariu, R. Drost, A. Villas, R. L. Klees, A. L. Yeyati, J. C. Cuevas, B. Kubala, J. Ankerhold, K. Kern, and C. R. Ast. Spin-dependent tunneling between individual superconducting bound states. *Phys. Rev. Res.,* 3(3):L032008, 2021.

[101] B. D. Josephson. Possible new effects in superconductive tunnelling. *Phys. Lett.,* 1(7): 251–253, 1962.

[102] V. Ambegaokar and A. Baratoff. Tunneling between superconductors. *Phys. Rev. Lett.,* 10 (11):486–489, 1963.

[103] M. L. Della Rocca, M. Chauvin, B. Huard, H. Pothier, D. Esteve, and C. Urbina. Measurement of the current-phase relation of superconducting atomic contacts. *Phys. Rev. Lett.,* 99(12):127005, 2007.

[104] C. W. J. Beenakker. Universal limit of critical-current fluctuations in mesoscopic Josephson junctions. *Phys. Rev. Lett.,* 67(27):3836, 1991.

[105] J. Senkpiel, S. Dambach, M. Etzkorn, R. Drost, C. Padurariu, B. Kubala, W. Belzig, A. L. Yeyati, J. C. Cuevas, J. Ankerhold, C. R. Ast, and K. Kern. Single channel Josephson effect in a high transmission atomic contact. *Commun. Phys.,* 3(1):1–6, 2020.

[106] M. T. Randeria, B. E. Feldman, I. K. Drozdov, and A. Yazdani. Scanning Josephson spectroscopy on the atomic scale. *Phys. Rev. B,* 93(16):161115, 2016.

[107] J. Chen. *Introduction to Scanning Tunneling Microscopy,* volume 69 of *Monographs on the Physics and Chemistry of Materials.* Oxford University Press, USA, 3rd edition, 2021.

[108] B. Jäck. *Josephson Tunneling at the Atomic Scale: The Josephson Effect as a Local Probe.* PhD thesis, EPFL, Lausanne, 2015.

[109] M. A. Eltschka. *Scanning Tunneling Microscopy using Superconducting Tips to Probe Absolute Spin Polarization.* PhD thesis, EPFL, Lausanne, 2015.

[110] F. Pobell. *Matter and methods at low temperatures.* Springer Berlin Heidelberg, Dresden, 2007.

[111] R. Koller, W. Bergermayer, G. Kresse, E. L. D. Hebenstreit, C. Konvicka, M. Schmid, R. Podloucky, and P. Varga. The structure of the oxygen induced (1 x 5) reconstruction of V(100). *Surf. Sci.,* 480(1-2):11–24, 2001.

[112] V. Jensen, J. N. Andersen, H. B. Nielsen, and D. L. Adams. The surface-structure of V(100). *Surf. Sci.,* 116(1):66–84, 1982.

[113] F. Dulot, P. Turban, B. Kierren, J. Eugene, M. Alnot, and S. Andrieu. (001) V surface structures analysed by RHEED and STM. *Surf. Sci.*, 473(3):172–182, 2001.

[114] H. Huang, C. Padurariu, J. Senkpiel, R. Drost, A. L. Yeyati, J. C. Cuevas, B. Kubala, J. Ankerhold, K. Kern, and C. R. Ast. Tunnelling dynamics between superconducting bound states at the atomic limit. *Nat. Phys.*, 16(12):1227–1231, 2020.

[115] W. Bergermayer, R. Koller, C. Konvicka, M. Schmid, G. Kresse, J. Redinger, P. Varga, and R. Podloucky. Superstructures of carbon on V(100). *Surf. Sci.*, 497(1-3):294–304, 2002.

[116] M. M. J. Bischoff, C. Konvicka, A. J. Quinn, M. Schmid, J. Redinger, R. Podloucky, P. Varga, and H. van Kempen. Scanning tunneling spectroscopy on clean and contaminated V(001). *Surf. Sci.*, 513(1):9–25, 2002.

[117] M. M. J. Bischoff, C. Konvicka, A. J. Quinn, M. Schmid, J. Redinger, R. Podloucky, P. Varga, and H. van Kempen. Influence of impurities on localized transition metal surface states: Scanning tunneling spectroscopy on V(001). *Phys. Rev. Lett.*, 86(11):2396–2399, 2001.

[118] M. Kralj, P. Pervan, M. Milun, K. Wandelt, D. Mandrino, and M. Jenko. HRAES, STM and ARUPS study of (5 x 1) reconstructed V(100). *Surf. Sci.*, 526(1-2):166–176, 2003.

[119] M. B. Tsetlin and M. N. Mikheeva. Oscillations of energy gap of superconducting vanadium/carbon sandwiches. *JETP Lett.*, 27(3):178–181, 1978.

[120] J. L. Brewster, M. Levy, and I. Rudnick. Ultrasonic determination of the superconducting energy gap in vanadium. *Phys. Rev.*, 132(3):1062, 1963.

[121] R. S. Deacon, Y. Tanaka, A. Oiwa, R. Sakano, K. Yoshida, K. Shibata, K. Hirakawa, and S. Tarucha. Tunneling spectroscopy of Andreev energy levels in a quantum dot coupled to a superconductor. *Phys. Rev. Lett.*, 104(7), 2010.

[122] E. J. Lee, X. Jiang, M. Houzet, R. Aguado, C. M. Lieber, and S. De Franceschi. Spin-resolved Andreev levels and parity crossings in hybrid superconductor–semiconductor nanostructures. *Nat. Nanotechnol.*, 9(1):79–84, 2014.

[123] E. J. Lee, X. Jiang, Žitko R., R. Aguado, C. M. Lieber, and S. De Franceschi. Scaling of subgap excitations in a superconductor-semiconductor nanowire quantum dot. *Phys. Rev. B*, 95(18):180502, 2017.

[124] J. Brand, S. Gozdzik, N. Neel, J. L. Lado, J. Fernandez-Rossier, and J. Kroger. Electron and Cooper-pair transport across a single magnetic molecule explored with a scanning tunneling microscope. *Phys. Rev. B*, 97(19):195429, 2018.

[125] P. W. Anderson. Localized magnetic states in metals. *Phys. Rev.*, 124(1):41, 1961.

[126] A. Villas, R. L. Klees, H. Huang, C. R. Ast, G. Rastelli, W. Belzig, and J. C. Cuevas. Interplay between Yu-Shiba-Rusinov states and multiple Andreev reflections. *Phys. Rev. B*, 101 (23):235445, 2020.

Bibliography

[127] J. C. Cuevas, A. L. Yeyati, A. Martín-Rodero, G. R. Bollinger, C. Untiedt, and N. Agraït. Evolution of conducting channels in metallic atomic contacts under elastic deformation. *Phys. Rev. Lett.*, 81(14):2990, 1998.

[128] S. Karan, H. Huang, C. Padurariu, B. Kubala, G. Morrás, A. L. Yeyati, J. C. Cuevas, J. Ankerhold, K. Kern, and C. R. Ast. Superconducting quantum interference at the atomic scale. *arXiv:2102.12521*, 2021.

[129] J. A. Van Dam, Y. V. Nazarov, E. P. Bakkers, S. De Franceschi, and L. P. Kouwenhoven. Supercurrent reversal in quantum dots. *Nature*, 442(7103):667–670, 2006.

[130] Silvano De Franceschi, Leo Kouwenhoven, Christian Schönenberger, and Wolfgang Wernsdorfer. Hybrid superconductor–quantum dot devices. *Nat. Nanotechnol.*, 5(10): 703–711, 2010.

[131] V. V. Ryazanov, V. A. Oboznov, A. Y. Rusanov, A. V. Veretennikov, A. A. Golubov, and J. Aarts. Coupling of two superconductors through a ferromagnet: Evidence for a π junction. *Phys. Rev. Lett.*, 86(11):2427, 2001.

[132] T. Kontos, M. Aprili, J. Lesueur, F. Genêt, B. Stephanidis, and R. Boursier. Josephson junction through a thin ferromagnetic layer: negative coupling. *Phys. Rev. Lett.*, 89(13): 137007, 2002.

[133] B. I. Spivak and S. A. Kivelson. Negative local superfluid densities: The difference between dirty superconductors and dirty bose liquids. *Phys. Rev. B*, 43(4):3740, 1991.

[134] J. Bauer, A. Oguri, and A. C. Hewson. Spectral properties of locally correlated electrons in a Bardeen–Cooper–Schrieffer superconductor. *J. Phys. Condens. Matter*, 19(48):486211, 2007.

[135] J. Bauer, J. I. Pascual, and K. J. Franke. Microscopic resolution of the interplay of Kondo screening and superconducting pairing: Mn-phthalocyanine molecules adsorbed on superconducting Pb(111). *Phys. Rev. B*, 87(7):075125, 2013.

[136] L. Cornils, A. Kamlapure, L. Zhou, S. Pradhan, A. A. Khajetoorians, J. Fransson, J. Wiebe, and R. Wiesendanger. Spin-resolved spectroscopy of the Yu-Shiba-Rusinov states of individual atoms. *Phys. Rev. Lett.*, 119(19):197002, 2017.

[137] T. Fujisawa, T. H. Oosterkamp, W. G. van der Wiel, B. W. Broer, R. Aguado, S. Tarucha, and L. P. Kouwenhoven. Spontaneous emission spectrum in double quantum dot devices. *Science*, 282(5390):932–935, 1998.

[138] G. O. Steffensen, J. C. E. Saldaña, A. Vekris, P. Krogstrup, K. Grove-Rasmussen, J. Nygård, A. L. Yeyati, and J. Paaske. Direct transport between superconducting subgap states in a double quantum dot. *arXiv:2105.06815*, 2021.

[139] A. Villas, R. L. Klees, G. Morrás, H. Huang, C. R. Ast, G. Rastelli, W. Belzig, and J. C. Cuevas. Tunneling processes between Yu-Shiba-Rusinov bound states. *Phys. Rev. B*, 103(15): 155407, 2021.

[140] M. Eltschka, B. Jack, M. Assig, O. V. Kondrashov, M. A. Skvortsov, M. Etzkorn, C. R. Ast, and K. Kern. Probing absolute spin polarization at the nanoscale. *Nano Lett.*, 14(12): 7171–7174, 2014.

[141] L. Schneider, P. Beck, J. Wiebe, and R. Wiesendanger. Atomic-scale spin-polarization maps using functionalized superconducting probes. *Sci. Adv.*, 7(4):eabd7302, 2021.

[142] A. Mishra, P. Simon, T. Hyart, and M. Trif. A Yu-Shiba-Rusinov qubit. *arXiv:2106.01188*, 2021.

[143] P. Kot, R. Drost, M. Uhl, J. Ankerhold, J. C. Cuevas, and C. R. Ast. Microwave-assisted tunneling and interference effects in superconducting junctions under fast driving signals. *Phys. Rev. B*, 101(13):134507, 2020.

[144] O. Peters, N. Bogdanoff, S. A. González, L. Melischek, J. R. Simon, G. Reecht, C. B. Winkelmann, F. von Oppen, and K. J. Franke. Resonant Andreev reflections probed by photon-assisted tunnelling at the atomic scale. *Nat. Phys.*, 16(12):1222–1226, 2020.

Curriculum Vitae

Personal Information

Name	Haonan Huang
Date of Birth	November 1, 1993
Place of Birth	Wuhan, China
Nationality	Chinese

Education

Since Nov. 2017   **PhD student**
Doctoral School of Physics, École Polytechnique Fédérale de Lausanne
Thesis: *Tunneling processes through magnetic impurities on superconducting surfaces: Yu-Shiba-Rusinov states and the Josephson effect*
Supervisors: Prof. Klaus Kern and Dr. Christian R. Ast

Sep. 2015-Oct. 2017   **M.Sc. in Physics**
Max-Planck-Institute for Solid State Research & University of Stuttgart
Thesis: *Preparation of bismuth single atom on silicon (100) surface*
Supervisor: Dr. Christian R. Ast

Sep. 2011-Jul. 2015   **B.Sc. in Physics**
School of Physics, Peking University
Thesis: *The impedance spectrum of perovskite solar cell*
Supervisors: Prof. Dapeng Yu and Prof. Qing Zhao

Jul. 2015   **B.Sc. in Psychology**
(Double major)
School of Psychological and Cognitive Sciences, Peking University

Scientific Experience

Since Sep. 2016   **Research Assistant**
Max-Planck-Institute for Solid State Research, Stuttgart
Supervisors: Dr. Christian R. Ast and Prof. Klaus Kern

Oct. 2015-Aug. 2016   **Research Assistant**
Max-Planck-Institute for Intelligent System, Stuttgart
*Quantum kinetic theory for ultrafast demagnetization after femtosec-
ond laser pulse*
Supervisor: Prof. Manfred Fähnle

Oct. 2015-Dec. 2015   **Research Assistant**
1st Physikalisches Institut, University of Stuttgart, Stuttgart
LabVIEW and MATLAB programming
Supervisors: Dr. Yuan Yan and Prof. Martin Dressel

Jul. 2014-Sep. 2014   **Research Internship**
Max-Planck-Institute for Polymer Research, Mainz
Metal-Organic-Framework electroluminescent devices
Supervisors: Dr. Kamal Asadi and Prof. Dago de Leeuw

Sep. 2013-Sep. 2014   **Research Assistant**
*Nanostructure and Low dimensional Physics Laboratory, Peking Uni-
versity, Beijing*
*Large-scale fabrication of highly symmetrically organized ZnO
nanowire arrays using laser-interference lithography*
Supervisor: Prof. Dapeng Yu

Publications

1. **H. Huang** *et al.* Experimental connection between Yu-Shiba-Rusinov states and the Kondo effect using the numerical renormalization group theory (*in preparation*)

2. S. Karan, **H. Huang** *et al.* Remaining correlation effects in the superconducting state (*in preparation*)

3. M. Uhl, P. Kot, R. Drost, **H. Huang** *et al.* Multiband Josephson effect in a Pb tunnel junction (*in preparation*)

4. A. Villas, R.L. Klees, G. Morrás, **H. Huang**, C.R. Ast, G. Rastelli, W. Belzig and J.C. Cuevas, "Tunneling processes between Yu-Shiba-Rusinov bound states", *Phys. Rev. B*, **103**(15), 155407 (2021)

5. S. Karan, **H. Huang**, C. Padurariu, B. Kubala, G. Morrás, A.L. Yeyati, J.C. Cuevas, J. Ankerhold, K. Kern and C.R. Ast, "Superconducting Quantum Interference at the Atomic Scale", arXiv:2102.12521 (*in review*, 2021)

6. **H. Huang**, J. Senkpiel, C. Padurariu, R. Drost, A. Villas, R.L. Klees, A.L. Yeyati, J.C. Cuevas, B. Kubala, J. Ankerhold and K. Kern, "Spin-dependent tunneling between individual superconducting bound states", *Phys. Rev. Res.*, **3**(3), L032008 (2021)

7. **H. Huang**, C. Padurariu, J. Senkpiel, R. Drost, A.L. Yeyati, J.C. Cuevas, B. Kubala, J. Ankerhold, K. Kern and C.R. Ast, "Tunnelling dynamics between superconducting bound states at the atomic limit", *Nature Physics*, **16**(12), 1227-1231 (2020)

8. **H. Huang**, R. Drost, J. Senkpiel, C. Padurariu, B. Kubala, A.L. Yeyati, J.C. Cuevas, J. Ankerhold, K. Kern and C.R. Ast, "Quantum phase transitions and the role of impurity-substrate hybridization in Yu-Shiba-Rusinov states", *Commun. Phys.*, **3**, 199 (2020)

9. A. Villas, R.L. Klees, **H. Huang**, C.R. Ast, G. Rastelli, W. Belzig and J.C. Cuevas, "Interplay between Yu-Shiba-Rusinov states and multiple Andreev reflections", *Phys. Rev. B*, **101**(23), 235445 (2020)

10. M. Fähnle, M. Haag, C. Illg, B.Y. Müller, W. Weng, T. Tsatsoulis, **H. Huang**, J.Z. Briones Paz, N. Teeny, L. Zhang and T. Kuhn, "Review of ultrafast demagnetization after femtosecond

laser pulses: A complex interaction of light with quantum matter", *Am. J. Mod. Phys*, **7**(2), 68-74 (2018)

11. W. Weng, **H. Huang**, J. Briones, N. Teeny, B.Y. Mueller, M. Haag, T. Kuhn and M. Fähnle, "Unexpectedly marginal effect of electronic correlations on ultrafast demagnetization after femtosecond laser-pulse excitation", *Phys. Rev. B*, **95**(22), 224439 (2017)

12. **H. Huang**, M. Beuchel, Y. Park, P.J. Baesjou, S.C. Meskers, D.M. De Leeuw and K. Asadi, "Solvent-induced galvanoluminescence of metal organic framework electroluminescent diodes", *J. Phys. Chem. C*, **120**(20), 11045-11048 (2016)

13. W. Zhou, Y. Zhao, C. Shi, **H. Huang**, J. Wei, R. Fu, K. Liu, D. Yu and Q. Zhao, "Reversible healing effect of water molecules on fully crystallized metal–halide perovskite film", *J. Phys. Chem. C*, **120**(9), 4759-4765 (2016)